

# **Quantum Dots (QDs): Syntheses, Photo-Switching, Photocatalysis, and Spectroscopy**

By

Yucheng Yuan

B.S., Pharmaceutical Chemistry, Tianjin University, 2012

M.S., Pharmaceutical Chemistry, Tianjin University, 2015

M.A., Chemistry, Brown University, 2017

A Dissertation Submitted in Partial Fulfillment of the  
Requirements for the Degree of Doctor of Philosophy  
in the Department of Chemistry at Brown University

Providence, Rhode Island  
May 2020

© Copyright 2020  
by  
Yucheng Yuan



This dissertation by Yucheng Yuan is accepted in its present form by  
the Department of Chemistry as satisfying the dissertation requirement  
for the degree of Doctor of Philosophy.

Date \_\_\_\_\_

\_\_\_\_\_

Ou Chen, Advisor

Recommended to the Graduate Council by

Date \_\_\_\_\_

\_\_\_\_\_

Vicki L. Colvin, Reader

Date \_\_\_\_\_

\_\_\_\_\_

Jerome R. Robinson, Reader

Approved by the Graduate Council

Date \_\_\_\_\_

\_\_\_\_\_

Andrew G. Campbell,  
Dean of the Graduate School

# CURRICULUM VITAE

Yucheng Yuan grew up in Shandong, China. She attended Tianjin University in 2008, where she decided to major in Pharmacy. While keeping good academic records and participating school activities at the same time, Yucheng spent her time exploring synthetic organic chemistry research in the lab of Prof. Kang Zhao from 2010. She mastered to do organic reactions and started to do research independently. Yucheng graduated from Tianjin University in 2012 as BA in pharmacy and continue to enroll as a master student in Prof. Zhao's lab in Tianjin University, where she majored in pharmaceutical chemistry and continued to do research in organic synthesis. During this time, she was able to publish 4 papers and obtained National Scholarship in 2014. She joined Brown in 2015 after she obtained her master's degree. Although she has strong organic chemistry background, she decided to apply her synthetic skills into "nano" field, which was a totally new area for her. Yucheng joined Prof. Ou Chen's group and became one of his first batch of graduate students, starting to explore the fascinating field of quantum dots. She did excellent work during her PhD studies in Prof. Ou Chen's group with many publications on the synthesis and characterizations of quantum dots with novel properties. Later in her research, she combined organic molecules and organic synthesis with quantum dots to optimize her own strength. She has applied specially designed QDs in photo-switching and photocatalysis. She also has attended and presented posters at many national meetings during her time at Brown.

# PUBLICATIONS

(in reverse chronological order, \* corresponding author)

17. **Yuan, Y.**; Zhu, H.; Hills-Kimball, K.; Cai, T.; Shi, W.; Wei, Z.; Yang, H.; Candler, Y.; Wang, P.; He, J.; Chen, O.\*, Stereoselective C–C Oxidative Coupling Reactions Photocatalyzed by CsPbBr<sub>3</sub> Perovskite Nanocrystals. In preparation.
16. Cai, T.; Wang, J.; Li, W.; Hills-Kimball, K.; Yang, H.; Nagaoka, Y.; **Yuan, Y.**; Zia, R.; Chen, O.\*, Mn<sup>2+</sup>/Yb<sup>3+</sup> Codoped CsPbCl<sub>3</sub> Perovskite Nanocrystals with Triple-Wavelength Emission for Luminescent Solar Concentrators. Submitted.
15. Xu, J. X.; **Yuan, Y.**; Liu, M. Zou, S.; Chen, O.; Zhang, D\*., Quantification of the Photon Absorption, Scattering, and On-resonance Emission Properties of CdSe/CdS Core/Shell Quantum Dots: Effect of Shell Geometry and Volumes. *Anal. Chem.* **2020**, *92* (7), 5346-5353.
14. Zhu, H.; Cai, T.; **Yuan, Y.**; Wang, X.; Nagaoka, Y.; Zhao, J.; Liu, Z.; Li, R.; Chen, O\*., Pressure Induced Hetero-trimer Formation from CdS-Au<sub>2</sub>S-Au Janus Satellite Heterostructural Nanocrystals. *ACS Appl. Nano Mater.* **2019**, *2* (11), 6804-6808.
13. Wang, J.; **Yuan, Y.**; Zhu, H.; Cai, T.; Fang, Y.; Chen, O\*., Three-Dimensional Macroporous Photonic Crystal Enhanced Photon Collection for Quantum Dot-Based Luminescent Solar Concentrator. *Nano Energy* **2019**, *67*, 104217.
12. Yu, C.; Guo, X.; Yin, Z.; Zhao, Z.; Li, X.; Robinson, J.; Muzzio, M.; Barbosa, C.; Shen, M.; **Yuan, Y.**; Wang, J.; Antolik, J.; Lu, G.; Su, D.; Chen, O.; Guduru, P.; Seto, C.\* and Sun, S\*., Highly Efficient AuPd Nanoparticle Catalyst for Synthesizing Polybenzoxazole with Controlled Polymerization. *Matter* **2019**, *1* (6), 1631-1643.
11. Xu, J. X.; **Yuan, Y.**; Zou, S.; Chen, O.; Zhang, D\*., A Divide-and-Conquer Strategy for Quantification of Light Absorption, Scattering, and Emission Properties of Fluorescent Nanomaterials in Solutions. *Anal. Chem.* **2019**, *91* (13), 8540-8548.
10. **Yuan, Y.**; Zhu, H.; Wang, X.; Cui, D.; Gao, Z.; Su, D.; Zhao, J.; Chen, O\*., Cu-Catalyzed Synthesis of CdZnSe-CdZnS Alloy Quantum Dots with Highly Tunable Emission. *Chem. Mater.* **2019**, *31* (7), 2635-2643.
9. **Yuan, Y.**; Zhu, H.; Nagaoka, Y.; Tan, R.; Davis, A. H.; Zheng, W.; Chen, O\*., Reversible Photo-Switching of Dual Color Fluorescent Mn-Doped CdS-ZnS Quantum Dots Modulated by Diarylethene Molecules. *Front. Chem.* **2019**, *7*, 145. (Invited to Special Theme of Frontiers in Chemistry: Rising Stars)
8. Zhu, H.; Fan, Z.; **Yuan, Y.**; Wilson, M. A.; Hills-Kimball, K.; Wei, Z.; He, J.; Li, R.; Gruenwald, M.; Chen, O., Self-Assembly of Quantum Dot-Gold Heterodimer Nanocrystals with Orientational Order. *Nano Lett.* **2018**, *18* (8), 5049–5056.
7. Heine, M.; Fischer, A. W.; Schlein, C.; Jung, C.; Straub, L. G.; Gottschling, K.; Mangels, N.; **Yuan, Y.**; Nilsson, S. K.; Liebscher, G.; Chen, O.; Schreiber, R.; Zechner, R.; Scheja, L.; Heeren, J\*., Lipolysis Triggers a Systemic Insulin Response Essential for Efficient Energy Replenishment of Activated Brown Adipose Tissue in Mice. *Cell Metab.* **2018**, *28* (4), 644-655.
6. Tan, R.; Yuan, Y.; Nagaoka, Y.; Eggert, D.; Wang, X.; Thota, S.; Guo, P.; Yang, H.; Zhao, J.; Chen, O\*., Monodisperse Hexagonal Pyramidal and Bipyramidal Wurtzite CdSe-CdS Core-Shell Nanocrystals. *Chem. Mater.* **2017**, *29* (9), 4097–4108.

Before Brown University

5. Zheng, Z.; Dian, L.; **Yuan, Y.**; Zhang-Negrerie, D.; Du, Y. \*; Zhao, K.\*  $\text{PhI}(\text{OAc})_2$ -Mediated Intramolecular Oxidative Aryl-Aldehyde  $\text{Csp}^2$ - $\text{Csp}^2$  Bond Formation: Metal-Free Synthesis of Acridone Derivatives. *J. Org. Chem.* **2014**, *79* (16), 7451–7458.
4. **Yuan, Y.**; Hou, W.; Zhang-Negrerie, D.; Zhao, K.; Du, Y.\*; Direct Oxidative Coupling of Enamines and Electron-Deficient Amines: TBAI/ TBHP-Mediated Synthesis of Substituted Diaminoalkenes under Metal-Free Conditions. *Org. Lett.* **2014**, *16* (20), 5410–5413.
3. Du, Y.\* **Yuan, Y.**; Zhao, K., A Method for Synthesis of Substituted Diaminoalkenes through C–N Oxidative Coupling. *Chinese Patent*, NO. 2014104793464.
2. **Yuan, Y.**; Yang, R.; Zhang-Negrerie, D.; Wang, J.; Du, Y.; Zhao, K.\*; One-Pot Synthesis of 3-Hydroxyquinolin-2(1*H*)-ones from *N*-Phenylacetamide via  $\text{PhI}(\text{OCOCF}_3)_2$ -Mediated  $\alpha$ -Hydroxylation and  $\text{H}_2\text{SO}_4$ -Promoted Intramolecular Cyclization. *J. Org. Chem.* **2013**, *78* (11), 5385–5392. Cited by *ChemInform* **2013**, *44*(41).
1. Wang, J.; **Yuan, Y.**; Xiong, R.; Zhang-Negrerie, D.; Du, Y.; Zhao, K.\*; PhenyliodineBis(trifluoroacetate)-Mediated Oxidative C–C Bond Formation: Synthesis of 3-Hydroxy-2-oxindoles and Spirooxindoles from Anilides. *Org. Lett.* **2012**, *14* (9), 2210–2213. Cited by *ChemInform* **2012**, *43* (35).

# ACKNOWLEDGEMENTS

*“Life is like riding a bicycle. To keep your balance, you must keep moving.”* – Albert Einstein. It took me a while to learn to ride a bicycle when I was a child, and I still remember the experience that I fell over a lot when I was afraid and stopped pedaling. Finally, I figured out that I would not fall if I kept moving. Later I saw this quote from Einstein, I am really motivated by this and try to be a better researcher and a better person.

First, I want to thank my advisor, Prof. Ou Chen. I have been feeling so lucky to join your lab back in 2015 and I always feel perfectly free to explore science and knowledge in your lab. I really appreciate that you spent a huge amount of time discussing ideas and how to improve projects with me. I still remember the days you taught me how to synthesize nanocrystals in person. To me, you are one real advisor who guided me to propose a project, to find problems, and to solve problems.

I also appreciate Prof. Vicki L. Colvin and Prof. Jerome R. Robinson, who support me as members of my graduate committee. I really appreciate your advices for my research for all the time I spent here. You also always provide great questions, which make me think more and learn more for my research.

I must also thank my undergraduate and master research advisor at Tianjin University, Prof. Kang Zhao. As the very first research advisor in my life, you helped me to know how the world of research looks like and makes me feel passion about it. It was also you who encouraged me to come to Brown.

My appreciation to my collaborators, Prof. Dongmao Zhang, Prof. Jing Zhao, Prof. Jie He, who really showed me what interdisciplinary and reliable collaborative work is supposed to look like. You explain science in different ways, which make me know deeply about my research.

Further, I want to thank Prof. Sarah Delaney, who is the director of graduate studies. I appreciate the advice you provided during my every step of my PhD study. Speaking of support, I also want to thank all the staff in chemistry department. To Rose, Sheila, Melissa, Russ, Tunli, Al, Hess, Hector, Eric Ferarra, Eric Friedfeld and all members of the chemistry department that have facilitated every part of my PhD study. I appreciate it so much that all of you are always professional, friendly and eager to assist with my needs. Appreciation also goes to Anthony McCormick and Joseph Orchardo, who trained

me for TEM and ICP measurements.

My thanks to my wonderful group members, past and present of the Chen Lab. Dr. Yasutaka Nagaoka and Dr. Rui Tan, I have learned a lot of about quantum dots from you, thank you for encouraging me and helping me when I was stressed. To current group members, Hanjun, Junyu, Tong, Zhengyang, Wenwu, Lacie, Norah, thank you all for providing amazing advices as a team for my research. Special thanks to Katie and Hua, who are in the same year as mine, we have gone through our PhD together step by step. This special memory will be always in my head. Very special thanks to Hua, who I spent most of my time in and outside the lab. We have been encouraging and helping each other, it is beyond lucky to involve you in both of my research and life.

My thanks also go to Yue, Mengke, Muchun, Sen, and again Hua. We spent almost all the traditional Chinese festivals together. You make me feel at home, as a family. Your smiles will be always my valuables.

Finally, I want to thank my family, my mom, dad, sister and twin brother. Mom and dad, I have become is all because of your sacrifice, love, and unending support. Your passion and love have always inspired me, and I would hope it can last forever. My sister and brother, I spent most of my life with you two before I came here. Though sometimes we may have different ideas, I know you are the person who are willing to do anything for me. Now both of you have your own small families, but for me, it is just our family becomes larger. My love for you and I know your love for me will never change. No matter what happens, I know you are there, and I will be strong again.

Dedicated to my family

Abstract of “*Quantum Dots (QDs): Syntheses, Photo-Switching, Photocatalysis, and Spectroscopy*” by Yucheng Yuan, Ph.D., Brown University, May 2020

Semiconductor quantum dots (QDs) have garnered a significant amount of research effort for not only scientific advances but also a range of technological applications including bioimaging and labeling, solar energy harvesting, light-emitting diodes, and next-generation displays. In this dissertation, I report four different aspects for QDs, including syntheses, photo-switching, photocatalysis, and spectroscopy.

First, controlling the particle morphology and fabrication of QDs with emission covering a wide spectral region are vital in regulating the photophysical properties and the application potential of the QDs. Accordingly, for the first time, we have synthesized pyramidal shaped CdSe-CdS core-shell QDs with high morphological uniformity and epitaxial crystallinity through a two-step shell growth method. Then we report the synthesis of CdZnSe-CdZnS core-shell alloy QDs through a Cu-catalyzed solid solution alloying strategy starting from CdSe-CdS core-shell QDs. The resulting alloy QDs exhibit emission profiles covering a wide wavelength range of 470–650 nm while maintaining high PL QYs.

Second, the combination of QDs and light-responsive organic switches can generate novel photo-switchable materials for diverse applications. We established a highly reversible dynamic hybrid system by mixing dual-color emitting Mn-doped CdS-ZnS QDs with photo-switchable diarylethene molecules. The emission color switching between blue and pink of the system can be induced mainly by selective quenching/recovering of the Mn- PL of the QDs due to the switchable absorbance of the molecule.

Third, most recently, QDs have attracted tremendous attention in the field of



photocatalysis, owing to their superior optoelectronic properties for photocatalytic reactions. Herein, we demonstrate a series of stereoselective C-C oxidative homocoupling reactions of  $\alpha$ -aryl ketonitriles using the zwitterionic-capped CsPbBr<sub>3</sub> perovskite QDs under the illumination of visible light.

Fourth, reliable quantification of the optical properties of QDs is critical for their photochemical, physical, and biological applications. We experimentally quantify the photon scattering, absorption, and on-resonance-fluorescence activities of CdSe-CdS QDs as a function of the shell sizes and geometries. Effects of shell size and geometry on optical properties for both of cores and shells are discussed.

# Table of Contents

<b>Ch. 1. Introduction to QDs</b> .....	1
1.1 General Introduction to QDs.....	2
1.2 Synthetic Methods of QDs .....	4
1.3 Applications of QDs .....	11
Ch. 1 References.....	16
<b>Ch. 2. Monodisperse Hexagonal Pyramidal and Bipyramidal Wurtzite CdSe-CdS Core-Shell Nanocrystals</b> .....	23
2.1 Core-Shell QDs .....	24
2.2 Blinking of QDs .....	25
2.3 Synthesis of Characterization of HP- and HBP QDs .....	27
2.4 Ligand-Induced Particle Shape Evolution during the Shell Growth ...	39
2.5 Optical Properties of HP-HBP- Core-Shell QDs .....	43
2.6 <i>In Vitro</i> Biological Study.....	48
Ch. 2 Methods.....	52
Ch. 2 References.....	58
<b>Ch. 3. Cu-Catalyzed Synthesis of CdZnSe-CdZnS Alloy QDs with Highly Tunable Emission</b> .....	64
3.1 Limit of Current Synthetic Methods of QDs .....	65
3.2 Cu-Catalyzed Alloying Method to the Synthesis of Alloy QDs.....	66
3.3 Mechanism Study .....	74
3.4 Cu-catalyzed alloying method to the synthesis of alloy NRs.....	80
Ch. 3 Methods.....	83
Ch. 3 References.....	86

<b>Ch. 4.</b>	<b>Reversible Photo-Switching of Dual-Color Fluorescent Mn-Doped CdS-ZnS QDs Modulated by Diarylethene Molecules .....</b>	<b>92</b>
	4.1 Dynamic Materials.....	93
	4.2 Photo-Switchable Molecules .....	93
	4.3 Doping in QDs .....	94
	4.4 Energy Transfer Caused Photo-Switching in Mn-Doped CdS-ZnS QDs and Diarylethene Molecules Hybrid System .....	96
	Ch. 4 Methods.....	108
	Ch. 4 NMR Spectra.....	114
	Ch. 4 References.....	116
<b>Ch. 5.</b>	<b>Stereoselective C–C Oxidative Coupling Reactions Photocatalyzed by CsPbBr<sub>3</sub> Perovskite Nanocrystals.....</b>	<b>120</b>
	5.1 QDs as Catalysts in Organic Synthesis.....	121
	5.2 Optimization of Reaction Conditions .....	123
	5.3 Investigation of Reaction Scope .....	129
	5.4 Mechanism Study and Proposed Mechanism.....	133
	Ch. 5 Methods.....	137
	Ch. 5 NMR Characterization Data.....	146
	Ch. 5 NMR Spectra.....	156
	Ch. 5 References.....	176
<b>Ch. 6.</b>	<b>Quantification of the Photon Absorption, Scattering, and On-resonance Emission Properties of CdSe-CdS Core-Shell NC.....</b>	<b>182</b>
	6.1 Background of Quantification of NCs Optical Properties.....	183
	6.2 Quantification of Fluorescent Nanomaterials in Solutions.....	187
	6.3 Quantification of the QD Optical Spectra.....	197
	6.4 Effect of Shell Sizes and Geometries on Shell Scattering and Absorption Cross-sections.....	203
	6.5 Effect of Shell Sizes and Geometries on the Core Optical Properties	205

Ch. 6 Methods.....	209
Ch. 6 Reference.....	210
<b>Ch. 7. Conclusions and Future Directions.....</b>	<b>214</b>
Ch. 7 Reference.....	217

# List of Figures

<b>Fig. 1.1:</b>	Electronic energy levels of semiconductors and size dependent absorption and photoluminescence properties of QDs.....	3
<b>Fig. 1.2:</b>	Schematic representation of the energy-level alignment .....	5
<b>Fig. 1.3:</b>	Optical properties and TEM images for compact CdSe-CdS QDs .....	8
<b>Fig. 1.4:</b>	Evaporation-mediated self-assembly of CdSe-CdS NRs prepared by seeded growth .....	9
<b>Fig. 1.5:</b>	Schematic illustration of colloidal QDs for solar technologies .....	11
<b>Fig. 1.6:</b>	Schematic representation of the QD-based PC-LSC device .....	12
<b>Fig. 1.7:</b>	Schematic presentation of QDs bioconjugation using various methods of coupling reactions and interactions .....	14
<b>Fig. 1.8:</b>	Illustration and cross-sectional TEM image of the QD-LED device structure and EQE-luminance profile.....	15
<b>Fig. 2.1:</b>	Two-step synthesis of core-shell NCs.....	24
<b>Fig. 2.2:</b>	<i>quasi</i> -Type-II band structural alignment of CdSe-CdS core-shell QDs...	25
<b>Fig. 2.3:</b>	Fluorescence intensity versus time trace .....	26
<b>Fig. 2.4:</b>	A TEM image and size distribution of the CdSe-CdS core-shell QDs synthesized without the intermediate purification step.....	27
<b>Fig. 2.5:</b>	Optical spectra and TEM images of HP and HBP CdSe-CdS QDs.....	28
<b>Fig. 2.6:</b>	Comparisons of optical properties of HP-QDs vs spherical- QDs and HP-QDs vs spherical- QDs .....	29
<b>Fig. 2.7:</b>	HAADF-TEM images, elemental mapping and line-scan for Hp- and HBP- QDs.....	32
<b>Fig. 2.8:</b>	XRD spectra of the HP, HBP and the corresponding spherical CdSe-CdS core-shell QDs with the same particle volumes .....	33
<b>Fig. 2.9:</b>	Images of the reconstructed volumes via electron tomography for a HP- and HBP- CdSe-CdS core-shell QD .....	33
<b>Fig. 2.10:</b>	TEM images of HP-QDs at various magnifications .....	34

<b>Fig. 2.11:</b>	TEM images of HBP-QDs at various magnifications .....	35
<b>Fig. 2.12:</b>	HR-TEM images for core-shell HP-QDs .....	36
<b>Fig. 2.13:</b>	HR-TEM images for core-shell HBP-QDs .....	38
<b>Fig. 2.14:</b>	Mechanism of the HP and HBP shape evolutions of the CdSe-CdS QDs	40
<b>Fig. 2.15:</b>	FTIR spectra of CdSe core QDs, HP-QDs, and HBP-QDs.....	40
<b>Fig. 2.16:</b>	<sup>1</sup> H-NMR and <sup>31</sup> P-NMR for HP-, HBP-QDs.....	42
<b>Fig. 2.17:</b>	TEM images of the CdSe-CdS core-shell QDs synthesized with additional ODPAs during the 2nd-shell-growth reaction.....	43
<b>Fig. 2.18:</b>	The ensemble and single-QD PL spectra of the HP- and HBP-QDs.....	44
<b>Fig. 2.19:</b>	TEM images of the spherical CdSe-CdS core-shell QDs with the same core size and shell volumes to the HP- and HBP-QDs.....	45
<b>Fig. 2.20:</b>	Single particle PL blinking traces, “On” time fraction distribution and lifetimes of the HP-QDs and HBP-QDs.....	46
<b>Fig. 2.21:</b>	Excitation-intensity-dependent single-QD lifetimes of HBP-QD.....	46
<b>Fig. 2.22:</b>	Representative g <sup>(2)</sup> data for HBP-QDs.....	48
<b>Fig. 2.23:</b>	Absorption, PL emission, lifetime decays for Spherical QDs and HBP-QDs before and after ligand exchanges with Thiol-PEGs.....	49
<b>Fig. 2.24:</b>	Cytotoxicity and cell uptake tests for HBP-QDs and Spherical QDs.....	49
<b>Fig. 2.25:</b>	Cellular uptake of PEG-HBP-QDs and PEG-S-QDs.....	50
<b>Fig. 3.1:</b>	Characterization of CdSe-CdS core-shell QDs.....	67
<b>Fig. 3.2:</b>	Absorption and PL evolution during the synthesis of CdZnSe-CdZnS core-shell alloy QDs.....	67
<b>Fig. 3.3:</b>	TEM images and XRD spectra during the synthesis of CdZnSe-CdZnS core-shell alloy QDs.....	69
<b>Fig. 3.4:</b>	Size distribution histograms of CdZnSe-CdZnS core-shell alloy QDs ...	71
<b>Fig. 3.5:</b>	HAADF-STEM images and corresponding elemental mapping images for CdZnSe-CdZnS core-shell alloy QDs.....	72

<b>Fig. 3.6:</b>	Cd and Zn atomic percentage evolutions.....	73
<b>Fig. 3.7:</b>	The CdZnSe-CdZnS core-shell QDs emitting at different wavelength ...	74
<b>Fig. 3.8:</b>	Photograph image (top) and PL spectra (bottom) of QDs showing the fully coverage of the visible spectral range .....	75
<b>Fig. 3.9:</b>	Optical spectral evolution of the control reaction without an addition of Cu source .....	75
<b>Fig. 3.10:</b>	TEM images of the QDs synthesized in the control experiment without an addition of Cu source .....	76
<b>Fig. 3.11:</b>	The EPR spectra of Cu-doped CdSe-CdS QDs and CdZnSe-CdZnS alloy QDs .....	76
<b>Fig. 3.12:</b>	Schematic illustration for Cu-induced alloying process .....	78
<b>Fig. 3.13:</b>	Optical change of CdZnSe-CdZnS QDs after TOP treatment.....	79
<b>Fig. 3.14:</b>	PL lifetime evolution of CdZnSe-CdZnS QDs at different reaction time..	81
<b>Fig. 3.15:</b>	Characterization of CdZnSe-CdZnS core-shell NRs.....	82
<b>Fig. 4.1:</b>	nanoparticles that have been functionalized with switches.....	93
<b>Fig. 4.2:</b>	Chemical structures of some typical examples of molecular switches ....	94
<b>Fig. 4.3:</b>	Tunable dual-emission of Mn-doped CdS-ZnS QDs.....	95
<b>Fig. 4.4:</b>	Blue-shifting of the Mn PL for CdS-ZnS <sub>x</sub> ML-Mn-ZnS <sub>(7.5-x)</sub> ML with x increasing from 0 to 6.....	96
<b>Fig. 4.5:</b>	Chemical structures and photoisomerization of diarylethene <b>1</b> .....	97
<b>Fig. 4.6:</b>	Scheme and energy diagram of proposed mechanism for the selective Mn-PL quenching .....	98
<b>Fig. 4.7:</b>	Characterization of Mn-doped CdS-ZnS core-shell QDs .....	100
<b>Fig. 4.8:</b>	Photoswitching performance of Mn-doped CdS-ZnS QDs with diarylethene <b>1</b> .....	101
<b>Fig. 4.9:</b>	Optical spectral evolution in one cycle of mixture of Mn-doped CdS-ZnS QDs and diarylethene <b>1</b> .....	102
<b>Fig. 4.10:</b>	Evolution of absorption and PL properties of mixture of Mn-doped CdS-ZnS QDs and diarylethene <b>1</b> in solution of THF for ten cycles .....	103

<b>Fig. 4.11:</b>	BG-PL lifetime evolution in one cycle of mixture of Mn-doped CdS-ZnS QDs and diarylethene <b>1</b> .....	104
<b>Fig. 4.12:</b>	Photoswitching performance of Mn-doped CdS-ZnS QDs with diarylethene <b>2</b> and <b>3</b> .....	105
<b>Fig. 4.13:</b>	Evolution of absorption properties of mixture of Mn-doped CdS-ZnS QDs and diarylethene <b>2</b> in solution of THF for four cycles.....	105
<b>Fig. 4.14:</b>	Evolution of PL properties of mixture of Mn-doped CdS-ZnS QDs and diarylethene <b>2</b> in solution of THF for four cycles.....	106
<b>Fig. 4.15:</b>	Evolution of absorption properties of mixture of Mn-doped CdS-ZnS QDs and diarylethene <b>3</b> in solution of THF .....	106
<b>Fig. 5.1:</b>	Schematic illustration for different types of organic reactions photocatalyzed by semiconductor QDs .....	122
<b>Fig. 5.2:</b>	TEM images, and absorption and PL spectra for eight types of QDs.....	123
<b>Fig. 5.3:</b>	HR-TEM and XRD spectrum for zwitterionic ligands capped CsPbBr <sub>3</sub> ....	124
<b>Fig. 5.4:</b>	HPLC standard curve for product <b>2a</b> .....	126
<b>Fig. 5.5:</b>	Stability test of zwitterion capped CsPbBr <sub>3</sub> NCs .....	127
<b>Fig. 5.6:</b>	FTIR spectra of zwitterion and OLA/OAm capped CsPbBr <sub>3</sub> NCs .....	128
<b>Fig. 5.7:</b>	TGA spectra of zwitterion and OLA/OAm capped CsPbBr <sub>3</sub> NCs .....	128
<b>Fig. 5.8:</b>	Dynamic study for the model reaction.....	129
<b>Fig. 5.9:</b>	Reaction Scope of CsPbBr <sub>3</sub> photocatalyzed dimerization.....	130
<b>Fig. 5.10:</b>	Variable temperature <sup>1</sup> H NMR experiment for product <b>2c</b> .....	131
<b>Fig. 5.11:</b>	HSQC NMR spectrum of product <b>2c</b> at -40 °C .....	132
<b>Fig. 5.12:</b>	Mechanism study for the photocatalytic dimerization.....	133
<b>Fig. 5.13:</b>	EPR spectrum of DMPO-superoxide.....	134
<b>Fig. 5.14:</b>	XPS spectra for zwitterionic ligands capped CsPbBr <sub>3</sub> .....	135
<b>Fig. 5.15:</b>	Proposed mechanism for the stereoselective dimerization .....	136



<b>Fig. 6.1:</b>	Schematic illustration of PRS2.....	185
<b>Fig. 6.2:</b>	PAOS spectra for five different fluorophores .....	188
<b>Fig. 6.3:</b>	Decomposition of NP fluorophore UV–Vis extinction cross-section spectra into the absorption and scattering component spectra .....	189
<b>Fig. 6.4:</b>	Comparisons of as-acquired PAOS and PRS2 spectra .....	192
<b>Fig. 6.5:</b>	PRS2 fluorescence and scattering component spectra derived from the experimental PAOS spectra.....	194
<b>Fig. 6.6:</b>	Optical constants of fPSNP, RQD, and SQD in their respective red wavelength region.....	195
<b>Fig. 6.7:</b>	TEM images of SQD5.6, SQD7.4, SQD9.2, SQD10.8, RQD4.8, RQD9.3, RQD12.8, and RQD16.8.....	198
<b>Fig. 6.8:</b>	TGA thermograms of SQDs and RQDs .....	198
<b>Fig. 6.9:</b>	fluorescence depolarization and fluorescence excitation depolarization spectra of SQDs and RQDs.....	200
<b>Fig. 6.10:</b>	PRS2 spectra for RQDs and SQDs.....	202
<b>Fig. 6.11:</b>	Effect of shell sizes and geometries on shell scattering and absorption cross-sections.....	203
<b>Fig. 6.12:</b>	Experimental and fitting scattering cross-section spectra .....	204
<b>Fig. 6.13:</b>	Computational simulation of scattering depolarization spectra of RQDs and SQDs.....	205
<b>Fig. 6.14:</b>	Optical properties in QD core region.....	206
<b>Fig. 6.15:</b>	Absorption cross-sections of the 1st absorption peak of SQDs as a function of shell (a) monolayers and (b) thickness .....	207
<b>Fig. 7.1:</b>	New Generation Cadmium-Free QDs for Biophotonics and Nanomedicine .....	215

## List of Tables

<b>Table 1.1</b>	Material parameters of selected bulk semiconductors.....	6
<b>Table 2.1:</b>	Comparison of the three dimensions measured and calculated for both HP- and HBP-QDs .....	30
<b>Table 2.2:</b>	Volumes of small spherical, HP, large spherical, and HBP QDs .....	31
<b>Table 3.1:</b>	PL QYs of the CdZnSe-CdZnS core-shell alloy QDs before and after TOP treatment .....	68
<b>Table 3.2:</b>	Fitting results of the XRD patterns of CdZnSe-CdZnS alloy QDs. ....	70
<b>Table 3.3:</b>	EDX Elemental mapping data for <b>Fig. 3.5</b> .....	72
<b>Table 3.4:</b>	ICP-AES-determined Cd, Zn, and Cu percentages.....	80
<b>Table 5.1:</b>	Optimization of reaction conditions .....	125
<b>Table 6.1:</b>	Summary of QD dimensions and calculation of QD Molarity .....	199

# Chapter 1

## Introduction to QDs

Portions of this chapter are adapted and/or reprinted from the following works. Copyright belongs to the publisher.

Wang, J.; **Yuan, Y.**; Zhu, H.; Cai, T.; Fang, Y.; Chen, O.\*, Three-Dimensional Macroporous Photonic Crystal Enhanced Photon Collection for Quantum Dot-Based Luminescent Solar Concentrator. *Nano Energy* **2019**, *67*, 104217.

## 1.1 General Introduction to QDs

Colloidal semiconductor nanocrystals (NCs), also known as quantum dots (QDs), are tiny crystalline particles that commonly considered to have dimensions in the range of 1-100 nm, depending on the exciton Bohr radius (the distance between an electron and a hole) of different materials. Numerous efforts have been devoted to QDs since they were first discovered in 1981.<sup>1</sup> Colloidal QDs are composed of an inorganic core and an organic outer layer of surfactants, and they typically are referred to as ligands (**Fig. 1.1c**).<sup>2</sup> When excitation occurs, an electron in the valence band is transferred to the conduction band, leaving an orbital hole in the valence band. The electron-hole pair is called an exciton, and one typical relaxation process occurs when the excited electron goes back to the valence band, which is accompanied by the emission of a photon, a process that is known as radiative recombination. While bulk semiconductors have composition-dependent band gap energy (**Fig. 1.1a**),<sup>3</sup> which is the minimum energy required to excite an electron from the valence band to the conduction band, QDs display unique optical and electronic properties. Due to their small size, the excited electrons are confined inside the particles, and when the radius of a QD is smaller than the exciton Bohr radius, the charge carriers become spatially confined and their energy raises. Consequently, the band gap energy increases as the size of the QDs decreases, and, concurrently, more energy is released after excitation (**Fig. 1.1b**).<sup>4</sup> As a result, the emitted color can be tuned simply by changing the size of the QDs. **Fig. 1.1d** shows an example of CdSe QDs, the absorption and photoluminescence (PL) of which can be tuned by the size of the dots.<sup>2</sup> It has been shown that the PL of CdSe QDs can be tuned throughout the visible spectrum, making them appropriate candidates for applications in biological imaging and optoelectronic devices. Also, this material exhibits large extinction

coefficients and broad absorption spectra, which cannot be obtained from organic chromophores. To date, the PL quantum yield (QY) (the ratio of the number of photons emitted to the number of photons absorbed) of QDs has been engineered to near unity at room temperature, which is not possible for bulk materials.<sup>5,6</sup>

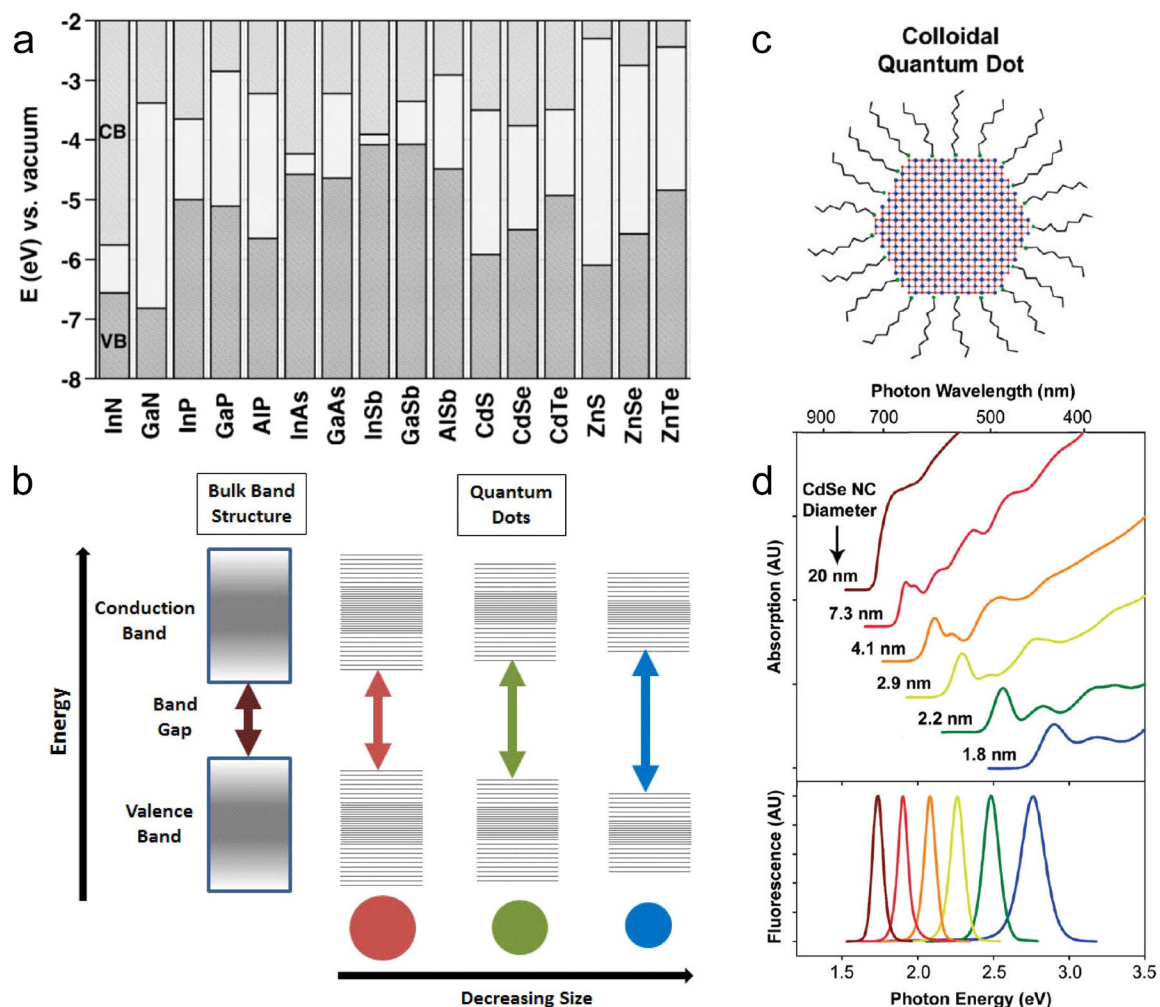


**Fig. 1.1:** (a) Electronic energy levels of selected III–V and II–VI semiconductors, reprinted from ref 3. VB = valence band, CB = conduction band. (b) Splitting of energy levels in QDs due to the quantum confinement effect, semiconductor band gap increases with decrease in size of the nanocrystal, reprinted from ref 4. (c) Schematic illustration of a colloidal QD, reprinted from ref 2. (d) Absorption (upper) and fluorescence (lower) spectra of CdSe QDs showing quantum confinement and size tunability, reprinted from ref 2. AU = arbitrary units.

Because of the unique properties of QDs, efforts have been made to synthesize them with uniform sizes, different shapes, high PL QYs, and tunable and narrow

emission spectra. Also, efforts have been made to apply QDs in diverse areas, including biology, medicine, photocatalysis (*e.g.*, the generation of H<sub>2</sub>, the reduction of CO<sub>2</sub>, organic syntheses, and others), harvesting solar energy, next-generation displays, and others. The methods used to synthesize QDs and some of their applications are discussed in Sections 1.2 and 1.3, respectively.

## 1.2 Methods Used to Synthesize QDs

Basically, chemists' approach to the synthesis of QDs is the "bottom-up" strategy, which is the process that utilizes ionic or molecular precursors to react in solution to produce NCs.<sup>7</sup> The hot injection method introduced by Murray *et al.* (1993) made it possible to obtain monodisperse spherical and highly-crystalline QDs of cadmium chalcogenides (CdSe, CdS, CdTe).<sup>8</sup> Subsequently, the chemistry involved in the synthesis of colloidal QDs has been developed rapidly, and currently it includes group II-VI QDs (*i.e.*, CdSe, CdS, CdTe, ZnSe, ZnS, and ZnTe), group III-V QDs (*i.e.*, InP and InAs), and group IV-VI QDs (*i.e.*, PbS and PbSe).

Because of their intrinsically high surface area-to-volume ratio, QDs can be very unstable in solution, causing them to aggregate because of the high surface energy. Thus, to stabilize QDs by minimizing the surface energy, capping ligands are always involved in the synthesis process. The system that is most often used is the formation of QDs in organic solvent that contains dissolved surfactants, which results in particles that are coated by surfactants. The commonly used capping ligands include trioctylphosphine/trioctylphosphine oxide (TOP/TOPO), oleylamine (OAm), oleic acid (OLA), octadecylphosphonic acid (ODPA), and hexylphosphonic acid (HPA). After the colloidal QDs are formed, the polar groups of the ligands attach to the surface of the particles, and the long, hydrophobic carbon chains protrude into the nonpolar organic

solvents (*e.g.*, toluene, hexanes, chloroform). By replacing the ligands with two polar head groups (*e.g.*, 11-mercaptoundecanoic acid (MUA) and 4-mercaptobenzoic acid (MBA)) or by coating with another layer with hydrophilic moieties (*e.g.*, polyethylene glycol (PEG)-thiol, PEG-carboxylic acid (PEG-AA), Poly(acrylic acid) (PAA)), the colloidal QDs can be transferred to the aqueous phase. Also, the ligands can also conjugate with biomolecules for bio applications, which will be discussed Section 1.3.

Since the crystals are extremely small, there are many atoms on the surface that are not completely bonded within in the crystal lattice, resulting in “dangling orbitals” on the atoms. The lower coordinated surface atoms may cause localized electronic states or highly reactive sites, which are susceptible to the surrounding conditions. Thus, these core-type QDs typically exhibit surface-related trap states that act as non-radiative exciton recombination channels that reduce PL QY, which is detrimental for QD-based optoelectronic applications. To solve this problem, one significant strategy is to engineer the core QDs with a shell of a second semiconductor, resulting in high PL efficiency and improving both the photo stability and chemical stability. In addition, by engineering the core-shell structure, it is possible to tune the optical properties of QDs in a larger spectral window.

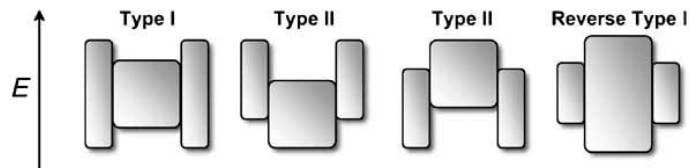


**Fig. 1.2:** Schematic representation of the energy-level alignment in different core-shell systems realized with semiconductor NCs to date. The upper and lower edges of the rectangles correspond to the positions of the conduction- and valence-band edge of the core (center) and shell materials, respectively, reprinted from ref 3.

There are three types of core-shell structures that can be engineered based on the bandgaps and the relative positions of electronic levels of the core and shell

semiconductors that are involved (**Fig. 1.2**).<sup>3</sup> For type I alignment, the conduction band energy level of the shell material is higher, while valance band energy level is lower than the core material, resulting in both the electrons and the holes being confined in the core. For type II alignment, only electrons or holes are confined in the core, resulting in spatial separation of the holes and electrons in the core-shell structure. For a reverse type I system, depending on the thickness of the shell, both the electrons and the holes are partially or completely confined in the shell. Since the growth of the heterostructure can generate strain and defect states at the interface, one should consider a small lattice mismatch for the core and shell materials when designing a core-shell structure. The material parameters of selected bulk semiconductors are listed in **Table 1.1**.<sup>3</sup>

*Table. 1.1: Material parameters of selected bulk semiconductors, reprinted from ref 3.*

Material	Structure [300K]	Type	$E_{\text{gap}}$ [eV]	Lattice parameter [ $\text{\AA}$ ]	Density [ $\text{kg m}^{-3}$ ]
ZnS	Zinc blende	II-VI	3.61	5.41	4090
ZnSe	Zinc blende	II-VI	2.69	5.668	5266
ZnTe	Zinc blende	II-VI	2.39	6.104	5636
CdS	Wurtzite	II-VI	2.49	4.136/6.714	4820
CdSe	Wurtzite	II-VI	1.74	4.3/7.01	5810
CdTe	Zinc blende	II-VI	1.43	6.482	5870
GaN	Wurtzite	III-V	3.44	3.188/5.185	6095
GaP	Zinc-blende	III-V	2.27	5.45	4138
GaAs	Zinc blende	III-V	1.42	5.653	5318
GaSb	Zinc blende	III-V	0.75	6.096	5614
InN	Wurtzite	III-V	0.8	3.545/5.703	6810
InP	Zinc blende	III-V	1.35	5.869	4787
InAs	Zinc blende	III-V	0.35	6.058	5667
InSb	Zinc blende	III-V	0.23	6.479	5774
PbS	Rocksalt	IV-VI	0.41	5.936	7597
PbSe	Rocksalt	IV-VI	0.28	6.117	8260
PbTe	Rocksalt	IV-VI	0.31	6.462	8219

The most studied core-shell systems are type I systems, as they can increase the PL QYs and improve the stability by the shell passivation. The first established system is CdSe-ZnS QDs, in which ZnS shell was grown by injection of a mixture of the organometallic precursors diethylzinc ( $\text{ZnEt}_2$ ) and hexamethyldisilathiane ( $(\text{TMS})_2\text{S}$ ) at



300 °C.<sup>9, 10</sup> Growth of the ZnS shell also accompanied by a small red shift (5–10 nm) of both excitonic peak in the UV-Vis absorption spectrum and the PL peak, which is attributed to a partial leakage of the exciton into the shell material. Later, CdSe-CdS core-shell system was established and studied more because of its high tunability. Compared to CdSe-ZnS system, epitaxial growth is favored for CdSe-CdS, benefitting from their less lattice mismatch (4% compared to 7%). Moreover, in the CdSe-CdS heterostructure, the band structural alignment is strongly confined holes with loosely confined electrons, thereby electrons can delocalize in the entire core-shell structure, indicated by the continuous PL red shifting upon CdS shell growth. Instead of using pyrophoric dimethylcadmium ( $\text{CdMe}_2$ ) and toxic  $(\text{TMS})_2\text{S}$ , air-stable precursors, cadmium oleate and elemental sulfur dissolved in 1-octadecene (ODE) were used for the CdS shell growth.<sup>11</sup> Successive ion layer adsorption and reaction (SILAR) method was exploited in the CdS shell synthesis, which was carried out by injection of cationic and anionic precursors alternatively into the core QDs monolayer by monolayer. The SILAR method has been extended to the synthesis of “giant” CdSe-CdS QDs, which could suppress the blinking of QDs by fully isolating the excited carriers from the QD surface (see detailed discussion in Section 2.2).<sup>12, 13</sup> The breakthrough for the CdSe-CdS core-shell QDs synthesis was the compact growth reported by Bawendi’s group in 2013.<sup>5</sup> Octanethiol (OCT) was chosen as the sulfur precursor in this strategy, the low reactivity of which ensured the slow epitaxial shell formation with a high crystallinity at high temperature (310 °C). During the CdS shell growth, the PL line widths decreased to 67.1 meV (full width at half-maximum, FWHM  $\sim$ 20 nm), the PL QYs increased to near unity, and monodispersity of the particles was maintained throughout the entire reaction (size distribution of  $\sim$  4%) ( **Fig. 1.3 a–h**). The compact high-quality core-shell QDs showed

significantly suppressed blinking (94% “on” time fractions) (**Fig. 1.3i–j**), and the blinking statistics aging induced ensemble luminescence photodarkening was eliminated (**Fig. 1.3k**).<sup>14</sup> Owing to the significant improvement of the CdSe-CdS core-shell QDs synthesis, synthesis of hexagonal pyramidal and bipyramidal CdSe-CdS core-shell QDs and synthesis of CdZnSe-CdZnS alloy QDs applied similar strategy, which are discussed in Ch. 2 and Ch. 3, respectively.<sup>15, 16</sup>

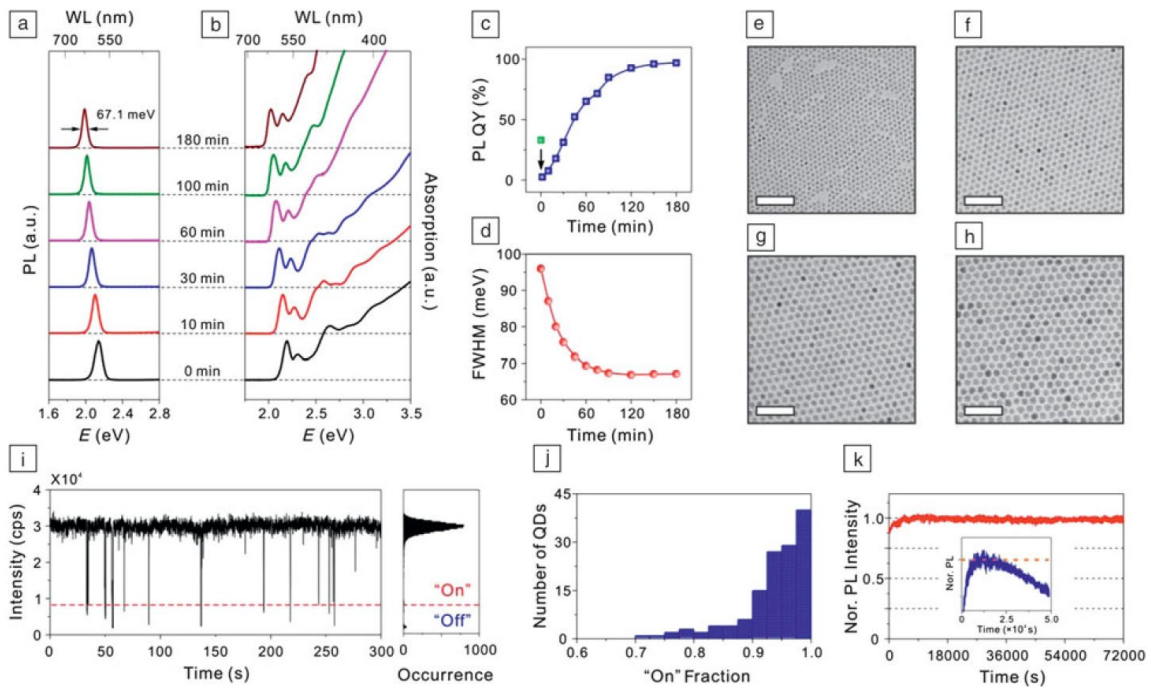


**Fig. 1.3:** Temporal evolution of (a) PL, (b) absorption, and (c) PL QYs. The green square shows the original PL QY of CdSe QDs and (d) FWHM of the PL peak of CdSe-CdS core-shell QDs during shell growth reaction. WL = wavelength. Transmission electron microscopy images of (e) 4.4 nm CdSe core and (f–h) CdSe-CdS core-shell QDs with a CdS shell thickness of 0.8 nm, 1.6 nm, and 2.4 nm, respectively. Scale bar is 50 nm. (i) Representative PL blinking trace of a single CdSe-CdS core-shell QD. The histogram shows the distribution of intensities observed in the trace. (j) Histogram of the blinking “on” time fraction. The average “on” time fraction is 0.94. (k) The normalized (Nor.) PL intensity trace obtained from a collection of QDs. The inset shows the Nor. PL intensity trace obtained from a collection of QDs synthesized through the conventional method, reprinted from ref 14.

Another well-established type I core-shell system is CdS-ZnS core-shell structure. Using zinc stearate and elemental sulfur as ZnS shell precursors, monodispersed CdS-ZnS QDs could be achieved emitting in the range of 410-480 nm (FWHM ~15-18 nm)

with QYs of 35-45%.<sup>17</sup> This system has further been used as a host matrix for Mn doping, see detailed discussion in Section 4.3.<sup>18-23</sup>

Due to the toxicity and thus low acceptability for practical applications of Cd-based QDs materials, InP is considered as the environmentally benign alternative as its bandgap can be tuned throughout the visible and near-infrared range by changing the particle size. However, InP QDs are much less developed compared to Cd-based QDs since the synthetic research started ~26 years ago.<sup>24, 25</sup> The properties of InP-based QDs did not approach those of CdSe-based QDs until Peng's group reported that InP-ZnSe-ZnS core-shell-shell QDs possess PL QY of 93% and narrow PL line width (FWHM ~42 nm) by introducing stoichiometry control with both core and shell.<sup>26</sup> Then Jang's group was able to prepare InP-ZnSe-ZnS QDs with almost-unity QY and even narrower PL line width (FWHM ~35 nm) by adding hydrofluoric acid to etch out the oxidative InP core surface, which is suspected to cause the poor optical properties of InP, followed by high-temperature ZnSe shell growth (340 °C).<sup>27</sup>

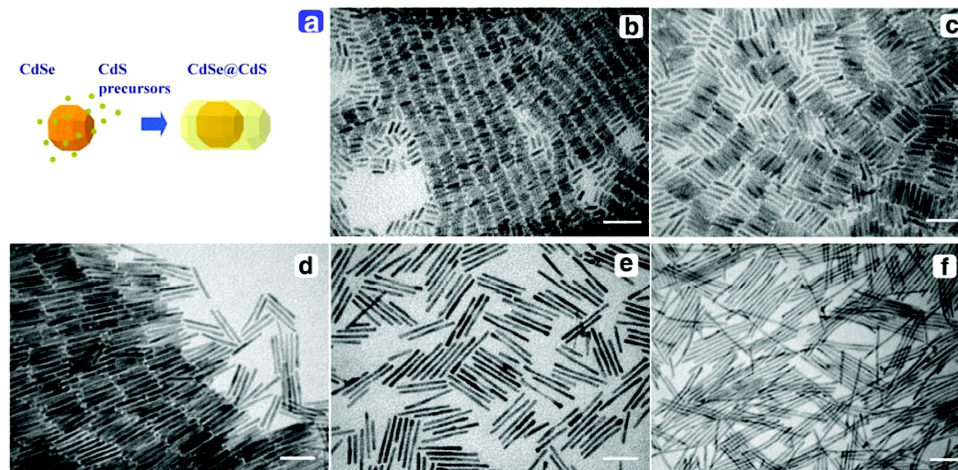


**Fig. 1.4:** Evaporation-mediated self-assembly of CdSe-CdS NRs prepared by seeded growth. (a) Sketch of the seeded growth approach. b–f) TEM images of self-assembled CdSe-CdS NRs. Small AR rods (b–d) tend to form locally ordered 2D smectic phases, while longer rods form either disordered assemblies, ribbons, or locally ordered 2D nematic phases. Average rod diameters and lengths, as determined by HRTEM, are: b)  $4.9 \times 19$  nm; c)  $4.2 \times 35$  nm; d)  $3.9 \times 53$  nm; e)  $3.8 \times 70$  nm; f)  $3.8 \times 111$  nm. All scale bars are 50 nm long. Reprinted from ref 28.

In addition to isotropic QD, anisotropic colloidal semiconductor nanorods (NRs) with elongated structures exhibiting an attractive set of emergent properties such as a large degree of fluorescence anisotropy, have received great attention in the past decade. So far, the most established system is the seeded growth of CdSe-CdS core-shell NRs, which was reported by Talapin *et al.* and Carbone *et al.* independently in 2007, both using preformed spherical semiconductor CdSe QDs as seeds (**Fig. 1.4a**).<sup>28, 29</sup> Carbone's method employed co-injected preformed spherical CdSe nanocrystal seeds and sulfur in TOP as precursor to the decomposed CdO in the presence of a mixture of TOPO, HPA and ODPa at a temperature of 350 °C–380 °C. Since the activation energy for heterogeneous nucleation is much lower than that for homogeneous nucleation, CdS tends to grow on the CdSe seeds rather than form self-nuclei in solution. NRs can be formed with a narrow distribution of lengths and diameters as the NCs undergo almost identical growth conditions. By tuning various parameters for this synthesis, including the diameter of the seeds, the growth temperature, and the amount of precursors and seeds, the morphology of the resulting NRs can be controlled (**Fig. 1.4b–f**). The aspect ratio (AR) of the NRs attained can go up to 30:1. PL QYs of the core-shell rods in solution for short AR rods are 70–75% and decay to about 10% for the largest AR rods in their syntheses. At the same time, Talapin *et al.* reported the seeded growth of CdSe-CdS NRs with only a slight difference that *n*-propylphosphonic acid (PPA) instead of HPA was used as one of the surfactants.<sup>29</sup> By changing wurtzite-CdSe cores to zinc blende-CdSe cores, nanotetrapods were obtained with QY ~50%.<sup>29</sup>

In addition to classical QDs, there are extremely rapid advancements in both of syntheses and device applications for perovskite NCs in the past few years,<sup>30</sup> since the prominent work of a colloidal synthesis of monodisperse CsPbX<sub>3</sub> (X = Cl, Br, I) was

reported by Protesescu *et al.* in 2015.<sup>31</sup> A hot injection method was employed to produce perovskite NCs, which exhibit remarkable properties, including high QYs (up to 90%), narrow PL peak width (FWHM < 100 meV), and tunable PL by simply changing the halides ratio.<sup>31</sup> In addition, the peculiar property of metal halide perovskite is defect-tolerant, as a result of that the defect states tend to be either localized in the valence band and conduction band, or to be essentially “inert”, resulting in perovskite QDs with high PL QYs. However, one of the most weakness for perovskite NCs are their poor stability under ambient conditions, which limit their practical use.<sup>32</sup> According, a lot works have been done to address this issue.<sup>33-35</sup> One of the strategies is to cap the particle surface with zwitterionic molecules, which can bind strongly on the surface, improving the stability.<sup>34</sup> We also found that the zwitterionic ligands capped CsPbBr<sub>3</sub> QDs show superior efficiency for photocatalytic organic synthesis, which will be discussed in Ch. 5.

### 1.3 Applications of QDs

With the advances of synthetic chemistry of QDs, they have been engineered in diverse practical applications including solar energy harvestings (**Fig. 1.5**),<sup>36-42</sup> biological imaging and labelling,<sup>43-49</sup> light-emitting diodes (LEDs) and next generation displays.<sup>50-59</sup>

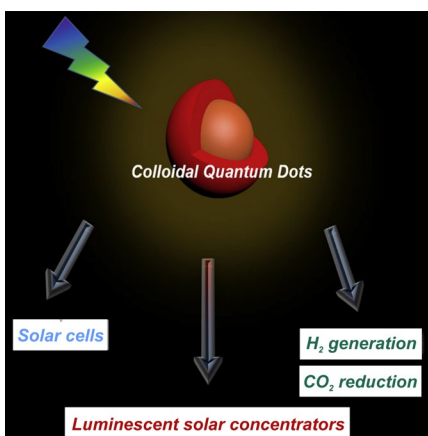


**Fig. 1.5:** Schematic illustration of colloidal QDs for solar technologies, adapted from ref 49.

Fabrication of QD solar cells (QDSC) is one strategy to convert solar energy to electricity via the creation of exciton.<sup>49</sup> Theoretically, the power-conversion efficiency (PCE) can be 45% in a single-junction QDSCs and 66% in multiple-junction QDSCs, which is higher than the Shockley-Queisser limit.<sup>60</sup> Along with the possibility of full-spectrum solar harvesting and easy fabrication conditions, QDSCs have drawn a lot of attentions over the past decades.<sup>36-41</sup> However, due to the poor long-term stability, limited PCE (state-of-art, ~12%),<sup>61</sup> and small active area, a lot of issues should be addressed before the QDSCs to be commercialized. Currently, researchers are focusing on improving the PCE and improving the long-term stability of QDSCs.

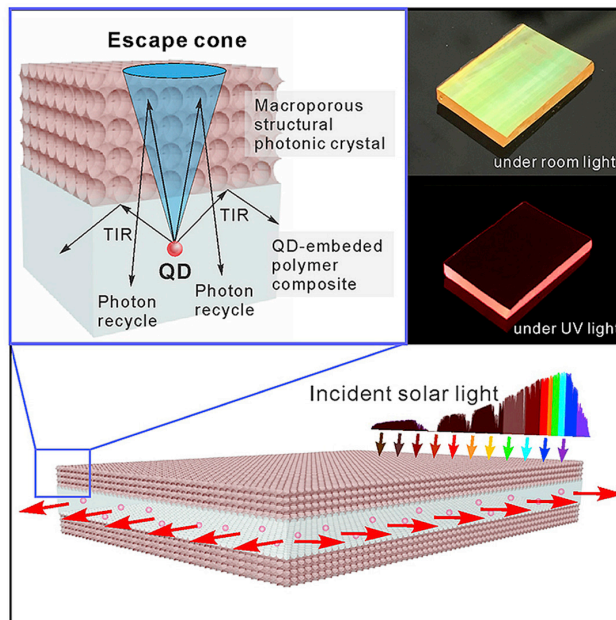


**Fig. 1.6:** Schematic representation of the QD-based PC-LSC device (bottom), and the zoomed-in schematic illustration of the top PC surface and the associated photon trapping mechanism (top left). TIR = total internal reflection. Photographs of a PC-LSC device (dimensions: 2.8 cm × 1.5 cm × 0.1 cm) illuminated under room light and UV light at 365 nm (top right).

Luminescent solar concentrator (LSC) another technology as a platform for solar energy harvesting. LSC is a photon managing device that can harvest, direct and concentrate solar light to small areas that are coupled with photovoltaics for solar energy

conversion.<sup>62-64</sup> However, the intrinsic photon loss through the so-called escape cone of the LSCs significantly limits their light harvesting and concentrating performance.<sup>65-67</sup> Recently, our group introduced a facile and low-cost approach for the fabrication of three-dimensional (3D) macroporous photonic crystal (PC) filter as efficient photon reflector, which can be coated on QD based LSC devices (**Fig. 1.6**).<sup>42</sup> We demonstrated that by controlling the PC reflection band to match the emission profile of the QD emitters, the light trapping efficiency of the PC coated LSC (PC-LSC) can be significantly improved from 73.3% to 95.1% as compared to the conventional PC-free LSC due to the reduced escape cone photon loss. In addition, we have developed simulation model with the consideration of PC reflector effect. Both experimental and simulation results show that the enhancement in LSC device performance induced by the PC reflector increases with increasing the dimension of the LSC. A maximum of 13.3-fold enhancement in external quantum efficiency (EQE) and concentration factor (C factor) of the PC-LSC can be achieved in our simulation when using ideal QD emitters and enhanced PC reflector. Moreover, the simulation result offers the relationship between photon output efficiencies and geometrical design of the PC-LSC. Our study sheds light on future design and fabrication of LSC devices with enhanced photon collection and concentrating efficiencies through novel and wavelength selective photon reflectors.

In addition to solar cell and LSC, QDs can also be used in photocatalysis, including photocatalytic H<sub>2</sub> generation,<sup>68, 69</sup> CO<sub>2</sub> reduction,<sup>70, 71</sup> and photoreforming,<sup>72, 73</sup> which will not be detailed discussed in this dissertation. And most recently, QDs have been exploited as good photocatalysts for organic reactions,<sup>74-76</sup> which will be discussed in Section 5.1.



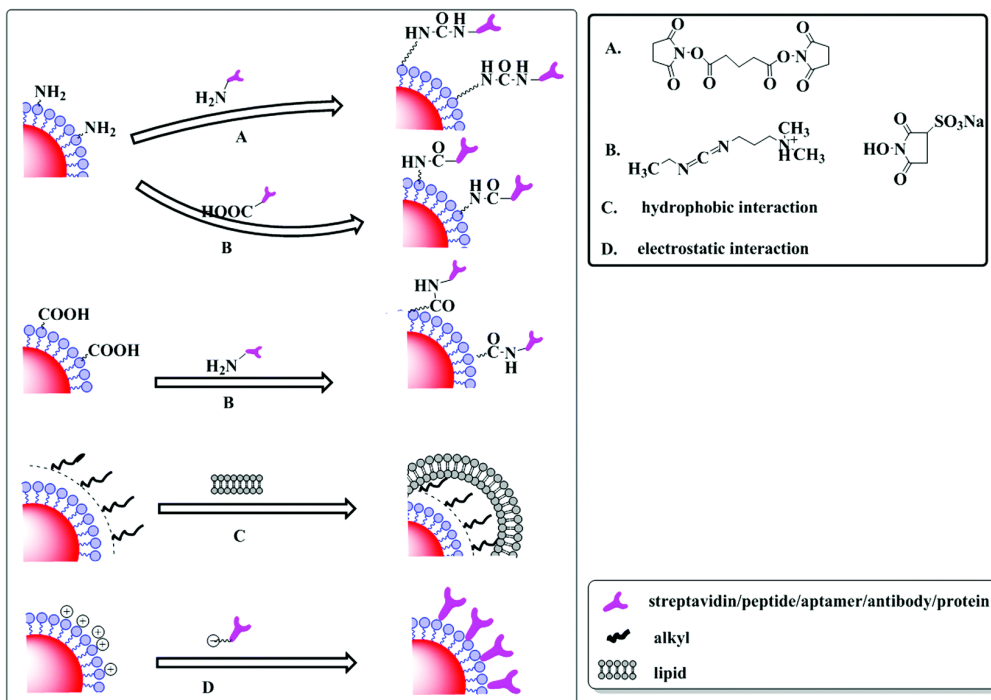


**Fig. 1.7:** Schematic presentation of QDs bioconjugation using various methods of coupling reactions and interactions, reprinted from ref 48.

Researchers have been investigating QDs as new probes for molecular, cellular, biosensing and *in vivo* imaging ever since the first example of using QDs for biological application was reported.<sup>77</sup> Typically, QDs as probes can be divided into two types regarding their specificity in the bio application: non-targeted and targeted probes. As non-targeted probes, colloidal QDs are engineered with an organic protective layer, commonly polymers, suppressing macrophage recognition and improving biocompatibility.<sup>5</sup> It is more complicated to fabricate targeted probes, which are QDs functionalized with biological molecules, for instances streptavidin, peptide, aptamer, antibody, and protein, which present specificity and selectivity to direct QDs to reaching effectively the diseased site (**Fig. 1.7**).<sup>48, 78</sup> As illustrated in **Fig. 1.7**, there are various crosslinking molecules (*e.g.*, 1-ethyl-3-(3-dimethylaminopropyl)carbodiimide (EDC) and 4-(N-maleimidomethyl)cyclohexane carboxylic acid N-hydroxyl succinimide ester



(SMCC)) can be used for QDs conjugation via covalent linkage, adsorption, hydrophobic interaction, and electrostatic interaction.<sup>79</sup> Then the prepared QD-biomolecules are ready to use in the bioimaging. However, there are still several significant issues should be addressed before QDs can be practically used in bio, including biocompatibility which may be caused by toxicity of Cd-based QDs, surface chemistry to stabilize the conjugate under *in vivo* conditions, and targeting efficacy, *etc.*

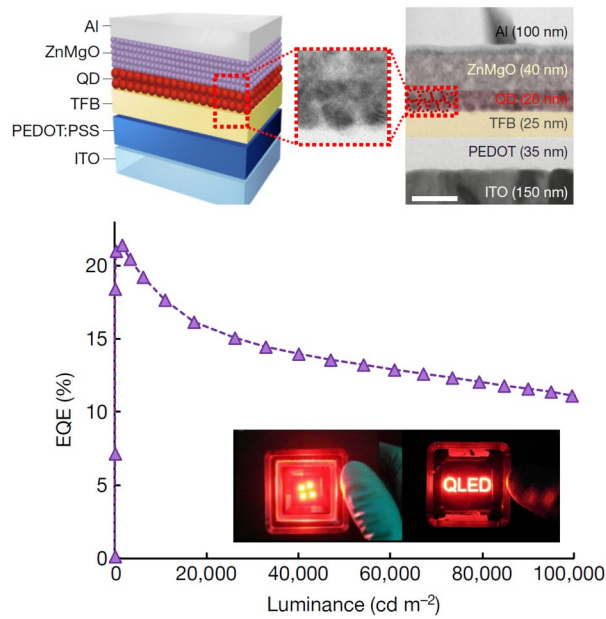


**Fig. 1.8:** (Top) Illustration and cross-sectional TEM image of the QD-LED device structure (scale bar, 50 nm). (Bottom) EQE–luminance profile. Inset, photographs of four-pixel QD-LED and text-patterned QD-LED, adapted from ref 27.

QDs are also ideal for LEDs and displays because of their color purity, high efficiency, and cost-effectiveness, therefore, intensive efforts have been done to improve the efficiencies of red-, green, and blue-emitting LEDs, the state-of-art EQEs for which are 20.5,<sup>80</sup> 24%,<sup>81</sup> and 19.8%,<sup>82</sup> respectively.<sup>50-59</sup> And recently, by dedicated design and synthesis of ZnCdSe-ZnSe-ZnS QDs with high QY (> 95%), the fabricated LEDs can exhibit peak (597 nm) EQE up to 30.9%.<sup>83</sup> Furthermore, as mentioned above, the quality of Cd-free InP-ZnSe-ZnS QDs (QY ~100%) have been largely improved recently, and

the EQE of LED produced from these QDs could be optimized up to 21.4% (**Fig. 1.8**).<sup>27</sup> The Cd-free QD-LEDs from this work could be fabricated in the next-generation displays for commercial use.

Chemists have made intensive efforts to improve the quality of QDs in order to make it possible for engineers and biologists to use these unique materials in various practical applications. In this thesis, four different aspects of QDs that I have evaluated in my PhD study are discussed. First, for the synthesis of QDs, CdSe-CdS core-shell QDs were synthesized with exclusive shape control (*i.e.*, hexagonal pyramid, HP, and hexagonal bipyramid, HBP), high morphological uniformity, and epitaxial crystallinity through a two-step, shell-growth method. Also, we synthesized CdZnSe-CdZnS core-shell alloy QDs with highly tunable emission (470–650 nm) through a Cu-catalyzed solid solution alloying strategy starting from CdSe-CdS core-shell QDs. Second, we established a highly-reversible, dynamic hybrid system with high fatigue resistance by mixing dual-color emitting, Mn-doped CdS-ZnS QDs with photo-switchable diarylethene molecules. Photo-switching between blue and pink of the system can be induced mainly by selective quenching/recovering of the Mn-PL of the QDs. Third, we demonstrated a series of stereoselective C-C oxidative homocoupling reactions of  $\alpha$ -aryl ketonitriles using the zwitterionic-capped CsPbBr<sub>3</sub> perovskite QDs illuminated by visible light. Fourth, we experimentally quantified the photon scattering, absorption, and on-resonance-fluorescence (ORF) activities of CdSe-CdS core-shell QDs as a function of the shell sizes and geometries. I believe our future work will result in more discoveries on QDs for various applications. Overall, with the research I have done and, of course, the excellent work that has been done by other researchers, there will be novel concepts for applications in different fields.

## References

1. Ekimov, A.; Onushchenko, A., Quantum Size Effect in Three-Dimensional Microscopic Semiconductor Crystals. *JETP Lett.* **1981**, *34*, 345-349.
2. Smith, A. M.; Nie, S., Semiconductor Nanocrystals: Structure, Properties, and Band Gap Engineering. *Acc. Chem. Res.* **2010**, *43* (2), 190-200.
3. Reiss, P.; Protière, M.; Li, L., Core/Shell Semiconductor Nanocrystals. *Small* **2009**, *5* (2), 154-168.
4. M G Bawendi; M L Steigerwald, a.; Brus, L. E., The Quantum Mechanics of Larger Semiconductor Clusters ("Quantum Dots"). *Annu. Rev. Phys. Chem.* **1990**, *41* (1), 477-496.
5. Chen, O.; Zhao, J.; Chauhan, V. P.; Cui, J.; Wong, C.; Harris, D. K.; Wei, H.; Han, H.-S.; Fukumura, D.; Jain, R. K.; Bawendi, M. G., Compact High-Quality CdSe–CdS Core–Shell Nanocrystals with Narrow Emission Linewidths and Suppressed Blinking. *Nat. Mater.* **2013**, *12*, 445.
6. Zhou, J.; Zhu, M.; Meng, R.; Qin, H.; Peng, X., Ideal CdSe/CdS Core/Shell Nanocrystals Enabled by Entropic Ligands and Their Core Size-, Shell Thickness-, and Ligand-Dependent Photoluminescence Properties. *J. Am. Chem. Soc.* **2017**, *139* (46), 16556-16567.
7. Mansur, H. S., Quantum Dots and Nanocomposites. *Wiley Interdiscip. Rev, Nanomed. Nanobiotechnol.* **2010**, *2* (2), 113-129.
8. Murray, C. B.; Norris, D. J.; Bawendi, M. G., Synthesis and Characterization of Nearly Monodisperse CdE (E = S, Se, Te) Semiconductor Nanocrystallites. *J. Am. Chem. Soc.* **1993**, *115* (19), 8706-8715.
9. Hines, M. A.; Guyot-Sionnest, P., Synthesis and Characterization of Strongly Luminescing ZnS-Capped CdSe Nanocrystals. *J. Phys. Chem.* **1996**, *100* (2), 468-471.
10. Dabbousi, B. O.; Rodriguez-Viejo, J.; Mikulec, F. V.; Heine, J. R.; Mattoussi, H.; Ober, R.; Jensen, K. F.; Bawendi, M. G., (CdSe)ZnS Core–Shell Quantum Dots: Synthesis and Characterization of a Size Series of Highly Luminescent Nanocrystallites. *J. Phys. Chem. B* **1997**, *101* (46), 9463-9475.
11. Li, J. J.; Wang, Y. A.; Guo, W.; Keay, J. C.; Mishima, T. D.; Johnson, M. B.; Peng, X., Large-Scale Synthesis of Nearly Monodisperse CdSe/CdS Core/Shell Nanocrystals Using Air-Stable Reagents via Successive Ion Layer Adsorption and Reaction. *J. Am. Chem. Soc.* **2003**, *125* (41), 12567-12575.
12. Chen, Y.; Vela, J.; Htoon, H.; Casson, J. L.; Werder, D. J.; Bussian, D. A.; Klimov, V. I.; Hollingsworth, J. A., "Giant" multishell CdSe nanocrystal quantum dots with suppressed blinking. *J. Am. Chem. Soc.* **2008**, *130* (15), 5026-5027.
13. Mahler, B.; Spinicelli, P.; Buil, S.; Quelin, X.; Hermier, J. P.; Dubertret, B., Towards non-blinking colloidal quantum dots. *Nat. Mater.* **2008**, *7* (8), 659-664.
14. Chen, O.; Wei, H.; Maurice, A.; Bawendi, M.; Reiss, P., Pure Colors from Core–Shell Quantum Dots. *MRS Bull.* **2013**, *38* (9), 696-702.
15. Tan, R.; Yuan, Y.; Nagaoka, Y.; Eggert, D.; Wang, X.; Thota, S.; Guo, P.; Yang, H.; Zhao, J.; Chen, O., Monodisperse Hexagonal Pyramidal and Bipyramidal Wurtzite CdSe–CdS Core–Shell Nanocrystals. *Chem. Mater.* **2017**, *29* (9), 4097-4108.
16. Yuan, Y.; Zhu, H.; Wang, X.; Cui, D.; Gao, Z.; Su, D.; Zhao, J.; Chen, O., Cu-Catalyzed Synthesis

- of CdZnSe–CdZnS Alloy Quantum Dots with Highly Tunable Emission. *Chem. Mater.* **2019**, *31* (7), 2635-2643.
17. Protière, M.; Reiss, P., Facile Synthesis of Monodisperse ZnS Capped CdS Nanocrystals Exhibiting Efficient Blue Emission. *Nanoscale Res. Lett.* **2006**, *1* (1), 62.
18. Yang, Y.; Chen, O.; Angerhofer, A.; Cao, Y. C., Radial-Position-Controlled Doping in CdS/ZnS Core/Shell Nanocrystals. *J. Am. Chem. Soc.* **2006**, *128* (38), 12428-12429.
19. Yang, Y.; Chen, O.; Angerhofer, A.; Cao, Y. C., On Doping CdS/ZnS Core/Shell Nanocrystals with Mn. *J. Am. Chem. Soc.* **2008**, *130* (46), 15649-15661.
20. Chen, O.; Shelby, D. E.; Yang, Y.; Zhuang, J.; Wang, T.; Niu, C.; Omenetto, N.; Cao, Y. C., Excitation-Intensity-Dependent Color-Tunable Dual Emissions from Manganese-Doped CdS/ZnS Core/Shell Nanocrystals. *Angew. Chem. Int. Ed. Engl.* **2010**, *122* (52), 10330-10333.
21. Chen, H.-Y.; Maiti, S.; Son, D. H., Doping Location-Dependent Energy Transfer Dynamics in Mn-Doped CdS/ZnS Nanocrystals. *ACS Nano* **2012**, *6* (1), 583-591.
22. Pradhan, N.; Das Adhikari, S.; Nag, A.; Sarma, D. D., Luminescence, Plasmonic, and Magnetic Properties of Doped Semiconductor Nanocrystals. *Angew. Chem. Int. Ed. Engl.* **2017**, *56* (25), 7038-7054.
23. Hofman, E.; Robinson, R. J.; Li, Z.-J.; Dzikovski, B.; Zheng, W., Controlled Dopant Migration in CdS/ZnS Core/Shell Quantum Dots. *J. Am. Chem. Soc.* **2017**, *139* (26), 8878-8885.
24. Micic, O. I.; Curtis, C. J.; Jones, K. M.; Sprague, J. R.; Nozik, A. J., Synthesis and Characterization of InP Quantum Dots. *J. Phys. Chem.* **1994**, *98* (19), 4966-4969.
25. Guzelian, A. A.; Katari, J. E. B.; Kadavanich, A. V.; Banin, U.; Hamad, K.; Juban, E.; Alivisatos, A. P.; Wolters, R. H.; Arnold, C. C.; Heath, J. R., Synthesis of Size-Selected, Surface-Passivated InP Nanocrystals. *J. Phys. Chem.* **1996**, *100* (17), 7212-7219.
26. Li, Y.; Hou, X.; Dai, X.; Yao, Z.; Lv, L.; Jin, Y.; Peng, X., Stoichiometry-Controlled InP-Based Quantum Dots: Synthesis, Photoluminescence, and Electroluminescence. *J. Am. Chem. Soc.* **2019**, *141* (16), 6448-6452.
27. Won, Y.-H.; Cho, O.; Kim, T.; Chung, D.-Y.; Kim, T.; Chung, H.; Jang, H.; Lee, J.; Kim, D.; Jang, E., Highly Efficient and Stable InP/ZnSe/ZnS Quantum Dot Light-Emitting Diodes. *Nature* **2019**, *575* (7784), 634-638.
28. Carbone, L.; Nobile, C.; De Giorgi, M.; Sala, F. D.; Morello, G.; Pompa, P.; Hytch, M.; Snoeck, E.; Fiore, A.; Franchini, I. R.; Nadasan, M.; Silvestre, A. F.; Chiodo, L.; Kudera, S.; Cingolani, R.; Krahn, R.; Manna, L., Synthesis and Micrometer-Scale Assembly of Colloidal CdSe/CdS Nanorods Prepared by a Seeded Growth Approach. *Nano Lett.* **2007**, *7* (10), 2942-2950.
29. Talapin, D. V.; Nelson, J. H.; Shevchenko, E. V.; Aloni, S.; Sadtler, B.; Alivisatos, A. P., Seeded Growth of Highly Luminescent CdSe/CdS Nanoheterostructures with Rod and Tetrapod Morphologies. *Nano. Lett.* **2007**, *7* (10), 2951-9.
30. Shamsi, J.; Urban, A. S.; Imran, M.; De Trizio, L.; Manna, L., Metal Halide Perovskite Nanocrystals: Synthesis, Post-Synthesis Modifications, and Their Optical Properties. *Chem. Rev.* **2019**, *119* (5), 3296-3348.

31. Protesescu, L.; Yakunin, S.; Bodnarchuk, M. I.; Krieg, F.; Caputo, R.; Hendon, C. H.; Yang, R. X.; Walsh, A.; Kovalenko, M. V., Nanocrystals of Cesium Lead Halide Perovskites (CsPbX<sub>3</sub>, X = Cl, Br, and I): Novel Optoelectronic Materials Showing Bright Emission with Wide Color Gamut. *Nano Lett.* **2015**, *15* (6), 3692-3696.
32. Yuan, L.; Patterson, R.; Wen, X.; Zhang, Z.; Conibeer, G.; Huang, S., Investigation of Anti-Solvent Induced Optical Properties Change of Cesium Lead Bromide Iodide Mixed Perovskite (CsPbBr<sub>3-x</sub>I<sub>x</sub>) Quantum Dots. *J. Colloid Interface Sci.* **2017**, *504*, 586-592.
33. Woo, J. Y.; Kim, Y.; Bae, J.; Kim, T. G.; Kim, J. W.; Lee, D. C.; Jeong, S., Highly Stable Cesium Lead Halide Perovskite Nanocrystals through in Situ Lead Halide Inorganic Passivation. *Chem. Mater.* **2017**, *29* (17), 7088-7092.
34. Krieg, F.; Ochsenbein, S. T.; Yakunin, S.; ten Brinck, S.; Aellen, P.; Süess, A.; Clerc, B.; Guggisberg, D.; Nazarenko, O.; Shynkarenko, Y.; Kumar, S.; Shih, C.-J.; Infante, I.; Kovalenko, M. V., Colloidal CsPbX<sub>3</sub> (X = Cl, Br, I) Nanocrystals 2.0: Zwitterionic Capping Ligands for Improved Durability and Stability. *ACS Energy Lett.* **2018**, *3* (3), 641-646.
35. Zhong, Q.; Cao, M.; Xu, Y.; Li, P.; Zhang, Y.; Hu, H.; Yang, D.; Xu, Y.; Wang, L.; Li, Y.; Zhang, X.; Zhang, Q., L-Type Ligand-Assisted Acid-Free Synthesis of CsPbBr<sub>3</sub> Nanocrystals with Near-Unity Photoluminescence Quantum Yield and High Stability. *Nano Lett.* **2019**.
36. Nozik, A. J., Quantum Dot Solar Cells. *Phys. E* **2002**, *14* (1), 115-120.
37. Kamat, P. V., Quantum Dot Solar Cells. Semiconductor Nanocrystals as Light Harvesters. *J. Phys. Chem. C* **2008**, *112* (48), 18737-18753.
38. Lee, H.; Wang, M.; Chen, P.; Gamelin, D. R.; Zakeeruddin, S. M.; Grätzel, M.; Nazeeruddin, M. K., Efficient CdSe Quantum Dot-Sensitized Solar Cells Prepared by an Improved Successive Ionic Layer Adsorption and Reaction Process. *Nano Lett.* **2009**, *9* (12), 4221-4227.
39. Lee, Y.-L.; Lo, Y.-S., Highly Efficient Quantum-Dot-Sensitized Solar Cell Based on Co-Sensitization of CdS/CdSe. *Adv. Funct. Mater.* **2009**, *19* (4), 604-609.
40. Chuang, C.-H. M.; Brown, P. R.; Bulović, V.; Bawendi, M. G., Improved Performance and Stability in Quantum Dot Solar Cells through Band Alignment Engineering. *Nat. Mater.* **2014**, *13* (8), 796-801.
41. Carey, G. H.; Abdelhady, A. L.; Ning, Z.; Thon, S. M.; Bakr, O. M.; Sargent, E. H., Colloidal Quantum Dot Solar Cells. *Chem. Rev.* **2015**, *115* (23), 12732-12763.
42. Wang, J.; Yuan, Y.; Zhu, H.; Cai, T.; Fang, Y.; Chen, O., Three-Dimensional Macroporous Photonic Crystal Enhanced Photon Collection for Quantum Dot-Based Luminescent Solar Concentrator. *Nano Energy* **2020**, *67*, 104217.
43. Dahan, M.; Laurence, T.; Pinaud, F.; Chemla, D. S.; Alivisatos, A. P.; Sauer, M.; Weiss, S., Time-Gated Biological Imaging by Use of Colloidal Quantum Dots. *Opt. Lett.* **2001**, *26* (11), 825-827.
44. Han, M.; Gao, X.; Su, J. Z.; Nie, S., Quantum-Dot-Tagged Microbeads for Multiplexed Optical Coding of Biomolecules. *Nat. Biotechnol.* **2001**, *19*, 631-635.
45. Medintz, I. L.; Uyeda, H. T.; Goldman, E. R.; Mattoussi, H., Quantum Dot Bioconjugates for Imaging, Labelling and Sensing. *Nat. Mater.* **2005**, *4*, 435-446.

46. Franke, D.; Harris, D. K.; Chen, O.; Bruns, O. T.; Carr, J. A.; Wilson, M. W. B.; Bawendi, M. G., Continuous Injection Synthesis of Indium Arsenide Quantum Dots Emissive in the Short-Wavelength Infrared. *Nat. Commun.* **2016**, *7*, 12749.
47. Panthani, M. G.; Khan, T. A.; Reid, D. K.; Hellebusch, D. J.; Rasch, M. R.; Maynard, J. A.; Korgel, B. A., In Vivo Whole Animal Fluorescence Imaging of a Microparticle-Based Oral Vaccine Containing (CuInSe<sub>x</sub>S<sub>2-x</sub>)/ZnS Core/Shell Quantum Dots. *Nano Lett.* **2013**, *13* (9), 4294-4298.
48. Girma, W. M.; Fahmi, M. Z.; Permadi, A.; Abate, M. A.; Chang, J.-Y., Synthetic Strategies and Biomedical Applications of I–III–VI Ternary Quantum Dots. *J. Mater. Chem. B* **2017**, *5* (31), 6193-6216.
49. Zhao, H.; Rosei, F., Colloidal Quantum Dots for Solar Technologies. *Chem* **2017**, *3* (2), 229-258.
50. Colvin, V. L.; Schlamp, M. C.; Alivisatos, A. P., Light-Emitting Diodes Made from Cadmium Selenide Nanocrystals and a Semiconducting Polymer. *Nature* **1994**, *370*, 354-357.
51. Liu, W.; Howarth, M.; Greytak, A. B.; Zheng, Y.; Nocera, D. G.; Ting, A. Y.; Bawendi, M. G., Compact Biocompatible Quantum Dots Functionalized for Cellular Imaging. *J. Am. Chem. Soc.* **2008**, *130* (4), 1274-1284.
52. Pimpulkar, S.; Speck, J. S.; DenBaars, S. P.; Nakamura, S., Prospects for LED Lighting. *Nat. Photon.* **2009**, *3*, 180-182.
53. Jang, E.; Jun, S.; Jang, H.; Lim, J.; Kim, B.; Kim, Y., White-Light-Emitting Diodes with Quantum Dot Color Converters for Display Backlights. *Adv. Mater.* **2010**, *22* (28), 3076-3080.
54. Shirasaki, Y.; Supran, G. J.; Bawendi, M. G.; Bulović, V., Emergence of Colloidal Quantum-Dot Light-Emitting Technologies. *Nat. Photon.* **2012**, *7*, 13-23.
55. Bae, W. K.; Park, Y.-S.; Lim, J.; Lee, D.; Padilha, L. A.; McDaniel, H.; Robel, I.; Lee, C.; Pietryga, J. M.; Klimov, V. I., Controlling the Influence of Auger Recombination on the Performance of Quantum-Dot Light-Emitting Diodes. *Nat. Commun.* **2013**, *4*, 2661.
56. Mashford, B. S.; Stevenson, M.; Popovic, Z.; Hamilton, C.; Zhou, Z.; Breen, C.; Steckel, J.; Bulovic, V.; Bawendi, M.; Coe-Sullivan, S.; Kazlas, P. T., High-Efficiency Quantum-Dot Light-Emitting Devices with Enhanced Charge Injection. *Nat. Photon.* **2013**, *7*, 407-412.
57. Yang, Y.; Zheng, Y.; Cao, W.; Titov, A.; Hyvonen, J.; Manders, J. R.; Xue, J.; Holloway, P. H.; Qian, L., High-Efficiency Light-Emitting Devices Based on Quantum Dots with Tailored Nanostructures. *Nat. Photon.* **2015**, *9* (4), nphoton. 2015.36.
58. Li, X.; Zhao, Y.-B.; Fan, F.; Levina, L.; Liu, M.; Quintero-Bermudez, R.; Gong, X.; Quan, L. N.; Fan, J.; Yang, Z.; Hoogland, S.; Voznyy, O.; Lu, Z.-H.; Sargent, E. H., Bright Colloidal Quantum Dot Light-Emitting Diodes Enabled by Efficient Chlorination. *Nat. Photon.* **2018**, *12* (3), 159-164.
59. Pinaud, F.; Clarke, S.; Sittner, A.; Dahan, M., Probing Cellular Events, One Quantum Dot at a Time. *Nat. Methods* **2010**, *7*, 275-285.
60. Nozik, A. J.; Beard, M. C.; Luther, J. M.; Law, M.; Ellingson, R. J.; Johnson, J. C., Semiconductor Quantum Dots and Quantum Dot Arrays and Applications of Multiple Exciton Generation to Third-Generation Photovoltaic Solar Cells. *Chem. Rev.* **2010**, *110* (11), 6873-6890.
61. Jiao, S.; Du, J.; Du, Z.; Long, D.; Jiang, W.; Pan, Z.; Li, Y.; Zhong, X., Nitrogen-Doped

- Mesoporous Carbons as Counter Electrodes in Quantum Dot Sensitized Solar Cells with a Conversion Efficiency Exceeding 12%. *J. Phys. Chem. Lett.* **2017**, *8* (3), 559-564.
62. Batchelder, J. S.; Zewai, A. H.; Cole, T., Luminescent Solar Concentrators. 1: Theory of Operation and Techniques for Performance Evaluation. *Appl. Opt.* **1979**, *18* (18), 3090-3110.
63. McKenna, B.; Evans, R. C., Towards Efficient Spectral Converters through Materials Design for Luminescent Solar Devices. *Adv. Mater.* **2017**, *29* (28), 1606491.
64. Meinardi, F.; Bruni, F.; Brovelli, S., Luminescent Solar Concentrators for Building-Integrated Photovoltaics. *Nat. Rev. Mater.* **2017**, *2* (12), 1-9.
65. Debije, M. G.; Verbunt, P. P. C.; Rowan, B. C.; Richards, B. S.; Hoeks, T. L., Measured Surface Loss from Luminescent Solar Concentrator Waveguides. *Appl. Opt.* **2008**, *47* (36), 6763-6768.
66. McDowall, S.; Butler, T.; Bain, E.; Scharnhorst, K.; Patrick, D., Comprehensive Analysis of Escape-Cone Losses from Luminescent Waveguides. *Appl. Opt.* **2013**, *52* (6), 1230-1239.
67. Xu, L.; Yao, Y.; Bronstein, N. D.; Li, L.; Alivisatos, A. P.; Nuzzo, R. G., Enhanced Photon Collection in Luminescent Solar Concentrators with Distributed Bragg Reflectors. *ACS Photonics* **2016**, *3* (2), 278-285.
68. Han, Z.; Qiu, F.; Eisenberg, R.; Holland, P. L.; Krauss, T. D., Robust Photogeneration of H<sub>2</sub> in Water Using Semiconductor Nanocrystals and a Nickel Catalyst. *Science* **2012**, *338* (6112), 1321-1324.
69. Kandi, D.; Martha, S.; Parida, K. M., Quantum Dots as Enhancer in Photocatalytic Hydrogen Evolution: A Review. *Int. J. Hydrog. Energy* **2017**, *42* (15), 9467-9481.
70. Wu, H.-L.; Li, X.-B.; Tung, C.-H.; Wu, L.-Z., Semiconductor Quantum Dots: An Emerging Candidate for CO<sub>2</sub> Photoreduction. *Adv. Mater.* **2019**, *31* (36), 1900709.
71. Guo, Q.; Liang, F.; Li, X.-B.; Gao, Y.-J.; Huang, M.-Y.; Wang, Y.; Xia, S.-G.; Gao, X.-Y.; Gan, Q.-C.; Lin, Z.-S.; Tung, C.-H.; Wu, L.-Z., Efficient and Selective CO<sub>2</sub> Reduction Integrated with Organic Synthesis by Solar Energy. *Chem* **2019**, *5* (10), 2605-2616.
72. Uekert, T.; Kuehnel, M. F.; Wakerley, D. W.; Reisner, E., Plastic Waste as A Feedstock for Solar-Driven H<sub>2</sub> Generation. *Energy & Environ. Sci.* **2018**, *11* (10), 2853-2857.
73. Uekert, T.; Kasap, H.; Reisner, E., Photoreforming of Nonrecyclable Plastic Waste over a Carbon Nitride/Nickel Phosphide Catalyst. *J. Am. Chem. Soc.* **2019**, *141* (38), 15201-15210.
74. Caputo, J. A.; Frenette, L. C.; Zhao, N.; Sowers, K. L.; Krauss, T. D.; Weix, D. J., General and Efficient C–C Bond Forming Photoredox Catalysis with Semiconductor Quantum Dots. *J. Am. Chem. Soc.* **2017**, *139* (12), 4250-4253.
75. Xie, S.; Shen, Z.; Deng, J.; Guo, P.; Zhang, Q.; Zhang, H.; Ma, C.; Jiang, Z.; Cheng, J.; Deng, D.; Wang, Y., Visible Light-Driven C–H Activation and C–C Coupling of Methanol into Ethylene Glycol. *Nat. Commun.* **2018**, *9* (1), 1181.
76. Jiang, Y.; Wang, C.; Rogers, C. R.; Kodaimati, M. S.; Weiss, E. A., Regio- and Diastereoselective Intermolecular [2+2] Cycloadditions Photocatalysed by Quantum Dots. *Nat. Chem.* **2019**, *11* (11), 1034-1040.
77. Michalet, X.; Pinaud, F.; Lacoste, T. D.; Dahan, M.; Bruchez, M. P.; Alivisatos, A. P.; Weiss, S.,

- Properties of Fluorescent Semiconductor Nanocrystals and Their Application to Biological labeling. *Single Mol.* **2001**, 2 (4), 261-276.
78. Medintz, I. L.; Uyeda, H. T.; Goldman, E. R.; Mattoussi, H., Quantum Dot Bioconjugates for Imaging, Labelling and Sensing. *Nat. Mater.* **2005**, 4 (6), 435-446.
79. Chen, Y.; Cordero, J. M.; Wang, H.; Franke, D.; Achorn, O. B.; Freyria, F. S.; Coropceanu, I.; Wei, H.; Chen, O.; Mooney, D. J., A Ligand System for the Flexible Functionalization of Quantum Dots via Click Chemistry. *Angew. Chem. Int. Ed.* **2018**, 57 (17), 4652-4656.
80. Dai, X.; Zhang, Z.; Jin, Y.; Niu, Y.; Cao, H.; Liang, X.; Chen, L.; Wang, J.; Peng, X., Solution Processed, High-Performance Light-Emitting Diodes Based on Quantum Dots. *Nature* **2014**, 515 (7525), 96-99.
81. Fu, Y.; Jiang, W.; Kim, D.; Lee, W.; Chae, H., Highly Efficient and Fully Solution-Processed Inverted Light-Emitting Diodes with Charge Control Interlayers. *ACS Appl. Mater. Interfaces* **2018**, 10 (20), 17295-17300.
82. Wang, L.; Lin, J.; Hu, Y.; Guo, X.; Lv, Y.; Tang, Z.; Zhao, J.; Fan, Y.; Zhang, N.; Wang, Y.; Liu, X., Blue Quantum Dot Light-Emitting Diodes with High Electroluminescent Efficiency. *ACS Appl. Mater. Interfaces* **2017**, 9 (44), 38755-38760.
83. Song, J.; Wang, O.; Shen, H.; Lin, Q.; Li, Z.; Wang, L.; Zhang, X.; Li, L. S., Over 30% External Quantum Efficiency Light-Emitting Diodes by Engineering Quantum Dot-Assisted Energy Level Match for Hole Transport Layer. *Adv. Funct. Mater.* **2019**, 29 (33), 1808377.



## Chapter 2

# Monodisperse Hexagonal Pyramidal and Bipyramidal Wurtzite CdSe-CdS Core–Shell Nanocrystals

Portions of this chapter are adapted and/or reprinted from the following works. Copyright belongs to the publisher.

Tan, R.; **Yuan, Y.**; Nagaoka, Y.; Eggert, D.; Wang, X.; Thota, S.; Guo, P.; Yang, H.; Zhao, J.; Chen, O.\*, Monodisperse Hexagonal Pyramidal and Bipyramidal Wurtzite CdSe-CdS Core-Shell Nanocrystals. *Chem. Mater.* **2017**, *29* (9), 4097–4108.

## 2.1 Core-Shell QDs

As discussed in Ch.1, QDs materials exhibit exceptional properties, including high absorption cross sections, tunable absorption and emission profiles, high PL QYs and stable PL output against photo- and physical- degradations, making them great candidates for a range of applications, such as new-generation displays, lasers, photodetectors, biological sensing, tracking and imaging. To realize these properties and utilize them in potential applications, QDs with a core-shell hetero-structure have proven to be not only beneficial, but necessary.<sup>1-3</sup> Ever since the first report of the synthesis of high-quality monodispersed CdSe-CdS core-shell QDs by Alivisatos *et al.* in 1997,<sup>4</sup> this particular system has been emerging arguably as one of the most studied model systems among all the known hetero-structural QDs (hetero-QDs). This could be due to the established syntheses and extensive knowledge in CdSe QD materials,<sup>5-7</sup> and the common crystal structures (i.e., wurtzite, WZ and zinc-blende, ZB) with a minimal crystal lattice mismatch (3.9%) between CdSe core and CdS shell materials.<sup>4, 8</sup> The core-shell QDs are mostly fabricated using a two-step procedure: first synthesis of core QDs, then the growth

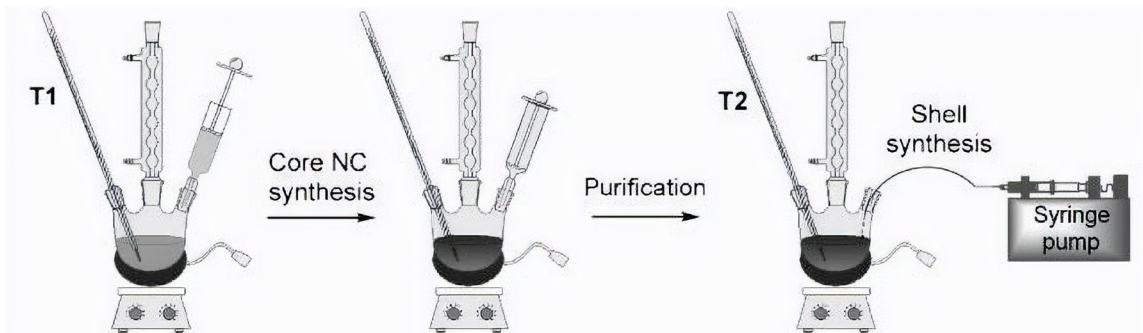


*Fig. 2.1: Two-step synthesis of core-shell NCs, adapted from reference 3.*

of shell with the purified core QDs (**Fig. 2.1**). Moreover, given by the band gap of bulk CdSe ( $\sim 1.74\text{eV}$ ) and the quasi-Type-II band structural alignment (strongly confined “hole” and loosely confined “electron”) between the CdSe core and CdS shell,<sup>9</sup> the tunable

emission color of the CdSe-CdS hetero-QDs covers a large portion of the visible spectrum. The dramatically different exciton dynamics (electron *vs* hole) fuel additional interests for this hetero-QD system.

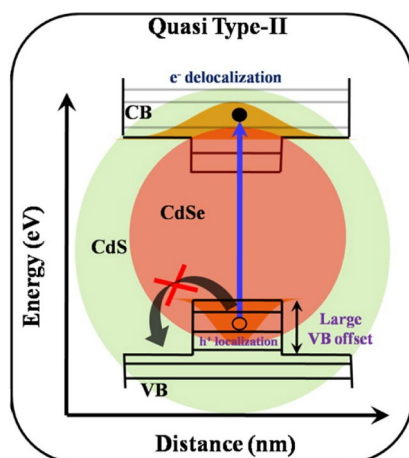


*Fig. 2.2: Schematic presentation of quasi-Type-II band structural alignment of CdSe-CdS core-shell QDs, reproduced from ref 9.*

Discoveries made in this system have played important roles in the hetero-QD field over the past two decades. For example, the SILAR technique was first introduced to the field for growing CdS shell on CdSe core by a layer-by-layer manner.<sup>10</sup> This SILAR concept has later been applied to a variety of hetero-QD syntheses.<sup>11-14</sup> Additionally, shape-controlled syntheses for hetero-QDs taking advantage of the different crystal symmetry characteristics were pioneered using CdSe-CdS QDs as a model system.<sup>15-18</sup>

## 2.2 Blinking of QDs

Fluorescence intermittency (also known as blinking) is a property that under continuous excitation, single-QDs exhibit switching between bright (ON) and dark (OFF) states randomly, which was discovered in 1996 (**Fig. 2.3**).<sup>19</sup> It has long been recognized as a potential limitation of QDs in applications at not only the single-QD level but also at

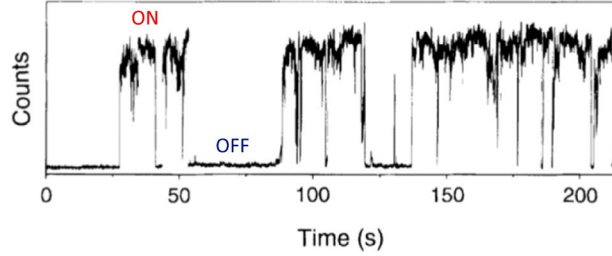


**Fig. 2.3:** Fluorescence intensity versus time trace of a single  $\sim 21\text{-\AA}$ -radius CdSe nanocrystal, recorded using a multichannel scaler with a 40-ms sampling interval and an excitation intensity of  $\sim 0.52\text{ kW/cm}^2$ . Reproduced from ref 19.

ensemble scales.<sup>20, 21</sup> More recently, despite the controversy on the physical origin (Auger effects, surface trap states, or defects at interface) of PL “blinking”, the chemical synthetic strategies designed for the core-shell system to overcome this intrinsic property limitation were developed.<sup>8, 22, 23</sup> These seminal discoveries, along with yet to be fully understood make studying the CdSe-CdS core-shell QDs persistently intriguing. Furthermore, within the hetero-QD family, “giant” core-shell QDs (g-QDs), typically defined as the QDs with a shell thickness equals to or larger than 15-monolayer (ML) of the shell material, have gradually developed into a distinct category of QD materials since their first demonstration.<sup>22, 23</sup> Many unique and interesting properties of g-QDs have been discovered including suppressed single-QD blinking,<sup>22-25</sup> reduced Auger recombination,<sup>26, 27</sup> efficient multi-exciton generation,<sup>28-30</sup> unusual dual-band emission,<sup>31, 32</sup> large stokes shift,<sup>33, 34</sup> and *etc.* These advanced photophysical properties enable g-QDs to have superior performances in applications such as light-emitting diodes and luminescence solar concentrators.<sup>26, 33-35</sup> However, due to extremely large shell volume deposition, synthesizing g-QDs simultaneously exhibiting high particle uniformity, narrow emission profile with minimized inhomogeneous linewidth broadening and high PL QYs remains a challenge. Additionally, to date, most developments have been focused on studying g-QDs with a spherical or quasi-spherical shape. Bals *et al.* showed

a very recent example of synthesizing CdSe-CdS g-QDs with a bullet shape.<sup>36</sup> Unfortunately, in their study, very limited ensemble and no single-particle optical data were provided.

### 2.3 Synthesis of Characterization of HP- and HBP-QDs

In order to form atomically flat crystal facets for the final core-shell QDs, three major factors have been taken into consideration for the experimental design: 1) precursors with relatively low reactivity (i.e., Cd-oleate and OCT as Cd and S sources) are needed to ensure a slow epitaxial shell formation with a high crystallinity; 2) in contrast to the spherical core-shell QD synthesis using the same combination of the shell precursors, neither oleic acid addition nor further high temperature thermal annealing should be performed, both of which will round the developed flat atomic facets and lead to a thermodynamically favored spherical shape as reported previously;<sup>8, 34</sup> 3) to form large core-shell QDs with flat crystal facets, an intermediate purification step is necessary to remove the unreacted precursors and by-products accumulated during the shell growth reaction. This intermediate purification step has been found to be critical for the formation of high-quality HBP-QDs. Indeed, the core-shell QDs synthesized without the intermediate purification step showed poly-dispersed sizes and shapes (**Fig. 2.4**).

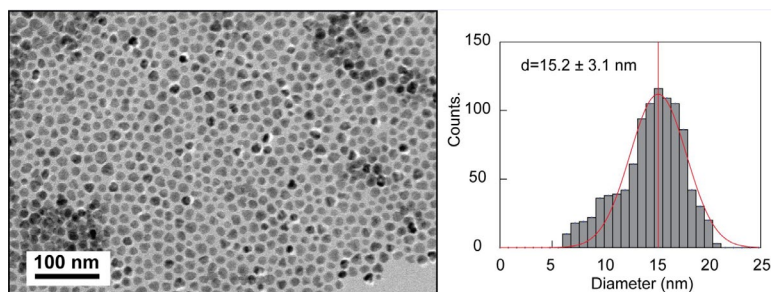


**Fig. 2.4:** A TEM image and size distribution of the CdSe-CdS core-shell QDs synthesized without the intermediate purification step shows poly-dispersed sizes and shapes of the sample.

On the basis of the above considerations, we have designed a two-step shell

growth method separated by an intermediate purification step for synthesizing pyramidal-shaped core-shell QDs (see Method for the detailed procedure). The entire shell growth reaction was monitored by absorption and PL spectroscopies. During the reaction, the absorption features and the PL peak shifted to a longer wavelength region (**Fig. 2.5a–c**) as a result of the quasi-Type-II band structure alignment (weak exciton confinement with largely delocalized electron) of the CdSe-CdS hetero-QDs.<sup>8, 10</sup> The large increase of the

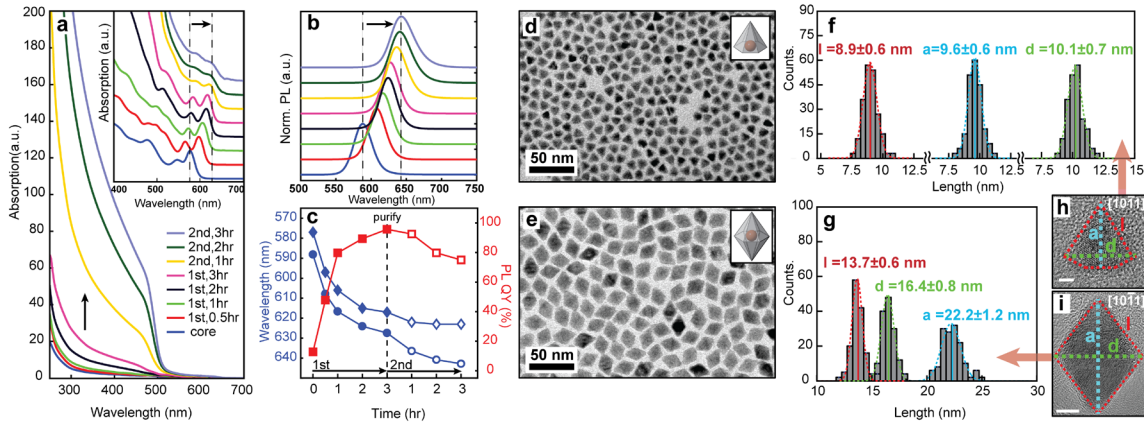


**Fig. 2.5:** (a) Absorption and (b) PL spectral evolution during the shell growth reaction. (c) Variations of Absorption peaks (blue diamond), PL peaks (blue circle) and PL QYs (red square) during the shell growth reaction, empty markers indicate the 2<sup>nd</sup> growth after purification. TEM images of CdSe-CdS HP-QDs (d) and CdSe-CdS HBP-QDs (e). Distributions of three characteristic dimensions of HP-QDs (f) and HBP-QDs (g). High-resolution TEM (HR-TEM) images of HP-QDs (h) and HBP-QDs (i) in  $[10\bar{1}1]$  projection labelled with three characteristic dimensions.

absorbance in the wavelength range below 500 nm during the 2<sup>nd</sup>-growth step indicated a thick CdS shell formation (**Fig. 2.5a**), consistent with the band-edge of CdS bulk material (2.42eV,  $\sim$ 512 nm).<sup>8, 10</sup> Interestingly, the high energy photon absorbance for the samples synthesized here is dramatically stronger than their spherical counterparts containing the same core and shell volumes (**Fig. 2.6a, b**). The PL excitation measurement ruled out the possibility of non-emissive organic ligands contribution, indicating the particle shape (i.e., the shape of the CdS shell) was at play (**Fig. 2.6 a, b**). The PL QY measurement showed a monotone increase during the 1<sup>st</sup>-shell-growth reaction, followed by a slight decrease

during the 2<sup>nd</sup>-shell-growth process (**Fig. 2.5c**). The PL QYs for the samples obtained from the 1<sup>st</sup>- and 2<sup>nd</sup>-shell-growth reactions are 94% and 73%, respectively. In addition, the PL decay measurements showed an ensemble lifetime of 49.7 ns for the first-shell-growth sample and 242 ns for the second-shell-growth sample (**Fig. 2.6c, d**). Both PL decays were dramatically slower than that of the spherical QDs with the same core and shell volumes (**Fig. 2.6c, d**).

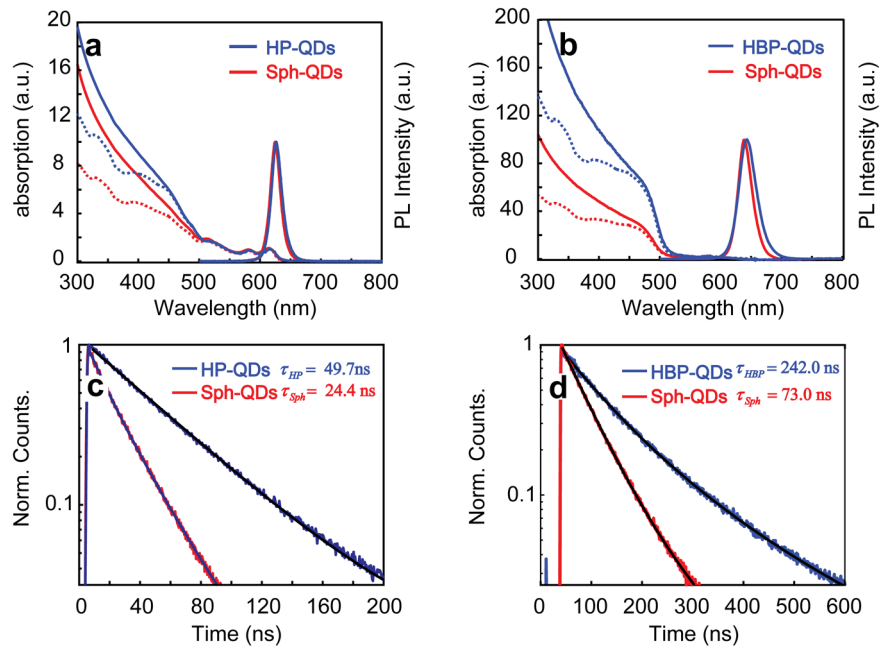


**Fig. 2.6:** Comparisons of absorption (solid lines), PL excitation (dotted lines) and PL emission spectra of (a) HP-QDs vs Spherical QDs (Spherical-QDs) of the same volume; (b) HBP-QDs vs. Spherical-QDs of the same volume. (c) Ensemble PL lifetimes of HP-QDs and the Spherical-QDs with the same particle volume. (d) Ensemble PL lifetimes of HBP-QDs and the Spherical-QDs with the same particle volume.

TEM images show that the resultant core-shell QDs displayed two-dimensional (2D) outlines of a combination of triangular/truncated triangular (rhombus) and hexagonal shapes after the 1<sup>st</sup>-shell-growth (2<sup>nd</sup>-shell-growth) reaction (**Fig. 2.5d, e**). Considering the different 2D outlines observed in TEM images are from different projections of the 3D QDs, we proposed the most possible 3D shapes of the obtained core-shell QDs after the 1<sup>st</sup>- and 2<sup>nd</sup>-shell-growth reactions are hexagonal pyramid (HP)

and hexagonal bipyramid (HBP), respectively (**Fig. 2.5d** and **e**, insets). The verifications

**Table 2.1:** Comparison of the three dimensions measured and calculated for both HP- and HBP-QDs:

Hexagonal Pyramid NCs	Measured (nm)	Calculated (nm)	Hexagonal Bipyramid NCs	Measured (nm)	Calculated (nm)
<i>a</i>	9.6±0.6	--	<i>d</i>	16.4±0.8	--
<i>d</i>	10.1±0.7	10.4±0.6	<i>a</i>	22.2±1.2	23.6±1.2
<i>l</i>	8.9±0.6	9.1±0.6	<i>l</i>	13.7±0.6	14.4±0.7

for the HP and HBP shapes, as well as atomic facet determinations of the obtained core-shell QDs are discussed in greater detail in the following section. Unlike spherical QDs, the size and size distribution of the HP and HBP hetero-QDs were determined by measuring three characteristic dimensions: *d*, diagonal of the hexagonal base; *l*, the projection of side length (the length between one corner of hexagonal base and the pyramid apex) for the QDs with one of the triangular faces lying on the TEM substrate; and *a*, slant height for the HP-QDs, or the projected distance between two apexes for the HBP-QDs (**Fig. 2.5h, i**, and Methods). Distributions of these three dimensions of the HP- and HBP-QDs are shown in **Fig. 2.5f, g** and **Table 2.1**, demonstrating high uniformities with typical standard deviations of 5~7% for all measured dimensions for both samples (**Table 2.1**). The calculated individual particle volumes of HP- and HBP-QDs are  $189 \pm 27 \text{ nm}^3$  and  $1480 \pm 170 \text{ nm}^3$ , respectively (**Table 2.2**). It is worth mentioning that the shell volume of the HBP-QDs ( $\sim 1450 \text{ nm}^3$ ) is equivalent to a thickness of  $\sim 16$ -ML of CdS shell when converted to a spherical core-shell QD. Given this large shell volume, the HBP core-shell QDs can be classified as g-QDs, but with a HBP shape and high morphological uniformities.<sup>22, 37</sup>



**Table 2.2:** Volumes of small spherical, HP, large spherical, and HBP QDs:

NC	$d^a$ (nm)	$a$ (nm)	$\theta^b$ (°)	Volume (nm <sup>3</sup> )	Surface area (nm <sup>2</sup> )
Hexagonal Pyramid	10.1±0.7	9.6±0.6	62.8±2.5	189±27 <sup>c</sup>	212±21 <sup>c</sup>
Spherical_1	7.1±0.4	-	-	187±32	158±18
Hexagonal Bipyramid	16.4±0.8	22.2±1.2	60.8±1.4	1481±171 <sup>d</sup>	717±54 <sup>d</sup>
Spherical_2	14.1±0.7	-	-	1468±219	643±62

<sup>a</sup>: diagonal of the hexagonal base for HP- and HBP-QDs; diameter for spherical QDs.

<sup>b</sup>:  $\theta$  is the included angle between (0001) and (10 $\bar{1}$ 1) crystal planes, theoretical value of 61.92°.

<sup>c</sup>: Applying  $a$  and  $d$  in the **HP model**:  $V_{HP} = \frac{3}{32} d^3 \tan\theta$  ;

where:

$$\tan\theta = \frac{\sqrt{16a^2 - 3d^2}}{\sqrt{3}d}$$

then,

$$V_{HP} = \frac{\sqrt{3}}{32} d^2 \sqrt{16a^2 - 3d^2}$$

$$S_{HP} = \frac{3\sqrt{3}}{8} d^2 + \frac{3}{2} ad$$

<sup>d</sup>: Applying  $a$  and  $d$  in the **HBP model**:  $V_{HBP} = \frac{3}{16} d^3 \tan\theta$  ;

where:

$$\tan\theta = \frac{\sqrt{2a^2 + 2a\sqrt{a^2 + 3d^2}}}{\sqrt{3}d}$$

then,

$$V_{HBP} = \frac{\sqrt{6a^2 + 6a\sqrt{a^2 + 3d^2}}}{16} d^2$$

$$S_{HBP} = \frac{3}{4} d \sqrt{2a^2 + 3d^2 + 2a\sqrt{a^2 + 3d^2}}$$

To verify the core-shell hetero-structure of the HP- and HBP-QDs, high-angle annular dark-field scanning TEM (HAADF-STEM) was used to map out the atomic distributions of Cd, S and Se atoms. The elemental mapping results clearly show that the

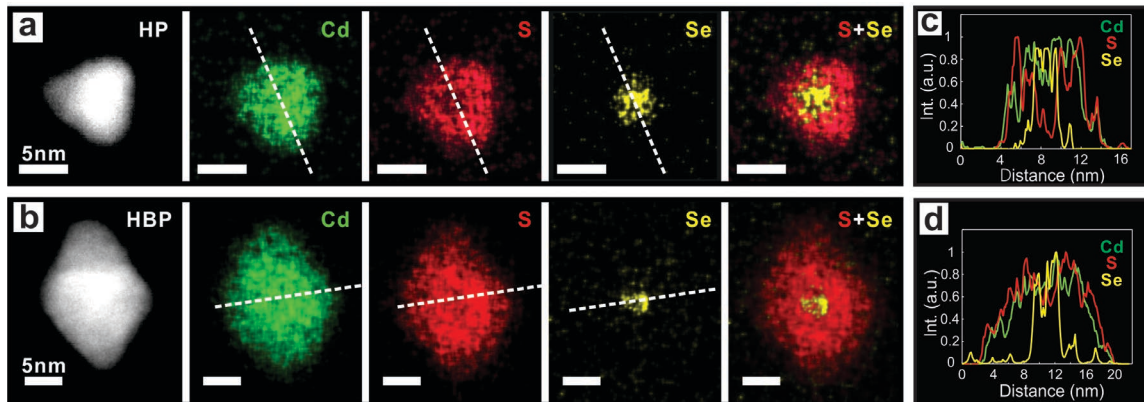


**Fig. 2.7:** HAADF-TEM images, elemental mapping and line-scan for a HP (a, c) and a HBP (b, d) CdSe-CdS core-shell hetero-QD.

Cd and S atoms are distributed in the entire QD, while Se atoms are only located at the center of the particle (**Fig. 2.7a, b**). The line-scans show that the Se atoms distribute across a distance of  $\sim 3.8$  nm for both samples (**Fig. 2.7c, d**), in good agreement with the CdSe core diameter of 3.9 nm used for the shell growth reactions. This result indicates an epitaxy rather than alloying was formed in the core-shell QDs, consistent with continuous red-shifts of both absorption and PL features (**Fig. 2.5a, b**) and a relatively short reaction time. However, slight inter-diffusion of anions at the core-shell interface, which is difficult to identify, may still occur during the high temperature (i.e., 310 °C) reactions performed here.

The crystal structures of the final HP and HBP hetero-QDs were determined by XRD measurements (**Fig. 2.8**). For comparisons, the XRD patterns of two spherical QD samples with the same CdSe core size and CdS shell volumes as the HP- and HBP-QDs were also measured (**Fig. 2.8**). The XRD spectra unambiguously show that all four samples possess a WZ crystal structure with the fingerprint Bragg peaks of  $(10\bar{1}2)$  and  $(10\bar{1}3)$  (**Fig. 2.8a**), consistent with a WZ crystal structure of the starting CdSe cores, demonstrating epitaxial CdS shell formation in all cases. Notably, the  $(0002)$  Bragg peaks

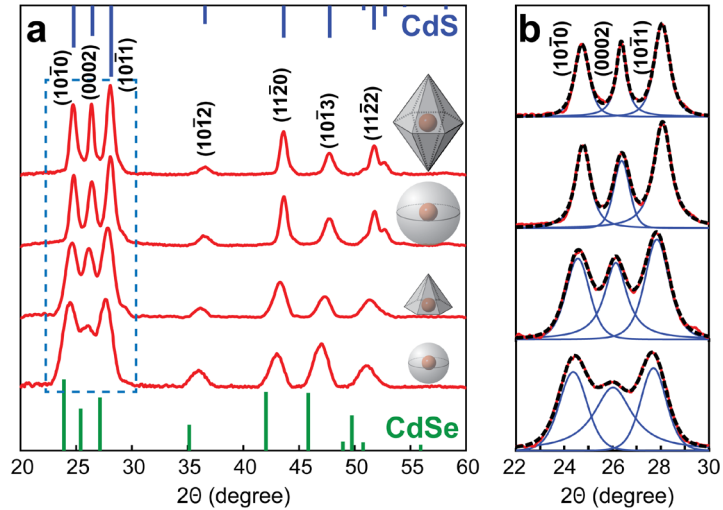


**Fig. 2.8:** (a) XRD spectra of the HP, HBP and the corresponding spherical CdSe-CdS core-shell QDs with the same particle volumes. The green and blue stick patterns show the positions of standard XRD peaks for bulk WZ-CdSe and WZ-CdS, respectively. (b) The zoomed-in XRD spectra for the highlighted area in (a) to show the  $(10\bar{1}0)$ ,  $(0002)$  and  $(10\bar{1}1)$  peaks. Red lines: XRD spectra; Black dotted-lines: fitted XRD spectra; Blue lines: fitted peaks.

for both samples are narrower than the peaks for spherical QD samples with the same particle volumes, suggesting larger domain sizes in  $(0002)$  direction for both the HP- and HBP-QDs. These results reveal that the fastest growth direction of the HP- and HBP-QDs is along the  $(0002)$  direction ( $Z$ -direction of the WZ crystal structure), consistent with previous reports for WZ nanorod growth.<sup>15-17, 38</sup>

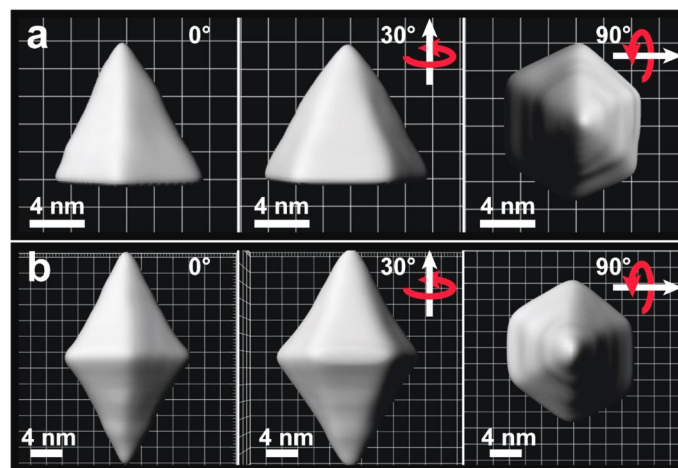


**Fig. 2.9:** Images of the reconstructed volumes via electron tomography for a HP CdSe-CdS core-shell QD (a) and an HBP CdSe-CdS core-shell QD (b) along three different viewing directions.

Regular TEM images only display 2D projection outlines of the 3D QDs. In order to accurately determine the 3D shape of the QDs, volume reconstructions were carried out using electron tomography techniques. For the 3D electron tomography, a set of TEM images was acquired by tilting the specimens over an angle range of  $\pm 65^\circ$  at a  $1^\circ$  increment. The 3D volume reconstructions were performed using the sequential iterative reconstruction technique (SIRT) algorithm and visualized using a Bitplane Imaris software (see details in Methods). As shown in **Fig. 2.9**, the 3D shapes of the QDs

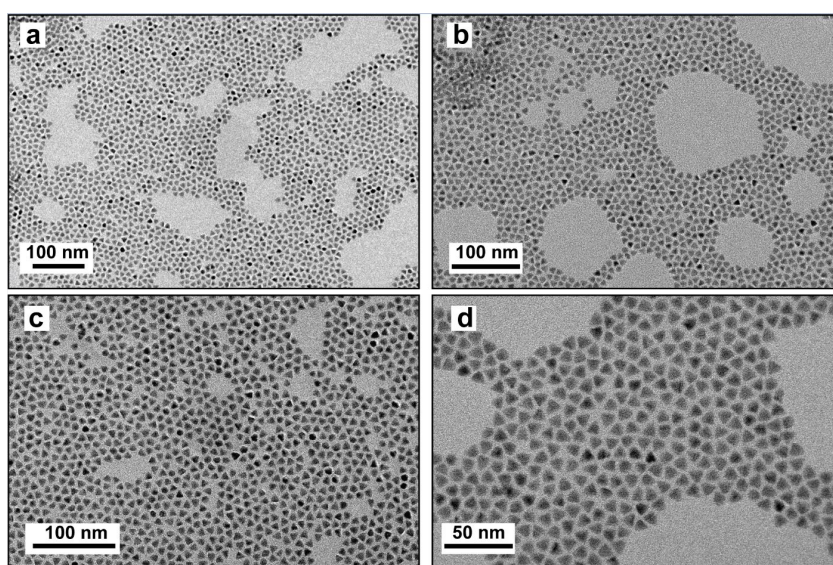


**Fig. 2.10:** TEM images of HP-QDs at various magnifications showing a high particle uniformity in size and shape.

resulted from the first- and second-shell growth reactions were unambiguously determined to be HP and HBP, respectively. These reconstructed 3D geometries show a high consistency with the particle shape 2D outlines observed in the regular TEM images (**Fig. 2.5d, e**, and **Fig. 2.10** and **2.11**). In order to fully understand the shape, crystal facets, and atomic orientations of these core-shell QDs, detailed crystallographic analyses based on a series of high-resolution TEM (HR-TEM) measurements have been performed and discussed as follows.

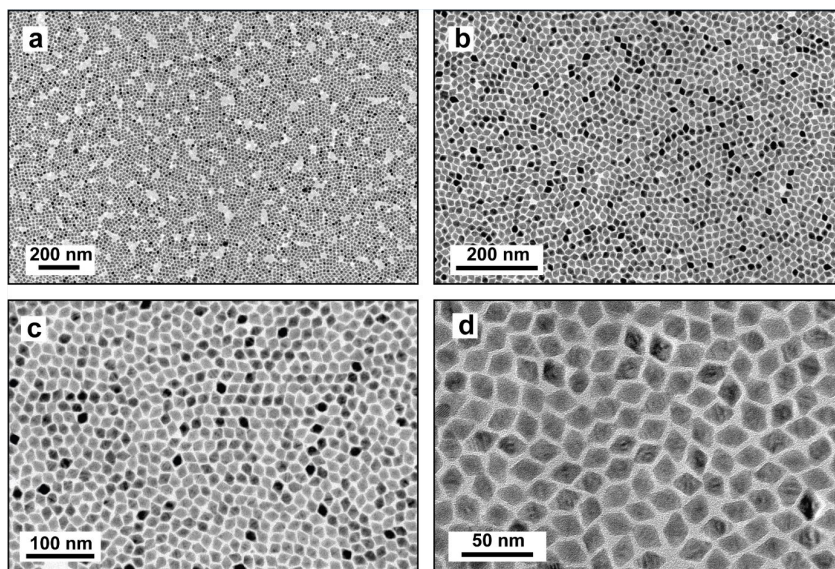


*Fig. 2.11: TEM images of HBP-QDs at various magnifications showing a high particle uniformity in size and shape.*

HR-TEM measurements of the HP-QDs clearly demonstrate the existence of different particle projections (**Fig. 2.12**). Statistical analysis shows that only  $\sim 5\%$  of the HPQDs display the projection with a hexagonal-shaped outline, while the majority of the QDs display a truncated-triangular outline (**Fig. 2.5d, h**). The center of **Fig. 2.12** shows the proposed HP-QD model with four defined directions (i.e.,  $a_1$ ,  $a_2$ ,  $a_3$ , and  $Z$ , **Fig. 2.12**, center left) and a computer generated atomic model of the HP WZ crystal with one hexagonal (0002) facet as a base and six equivalent  $\{10\bar{1}1\}$  facets on the lateral sides (**Fig. 2.12**, center right). Each of the four panels in **Fig. 2.12** (**Fig. 2.12a–d**) is composed of a representative HR-TEM image of an individual QD with a certain projection (left), the corresponding fast-Fourier transform (FFT) pattern (right top), the atomic model (right bottom), and its simulated electron diffraction pattern (right middle) after a one- or twostep rotation along the  $Z$  and  $X$  axes from the central atomic model.

**Fig. 2.12a** shows a clear hexagonal outline and atomic cross-fringes with a measured  $d$ -spacing of  $3.6 \text{ \AA}$ , which is associated with the  $\{10\bar{1}0\}$  planes of WZ CdS



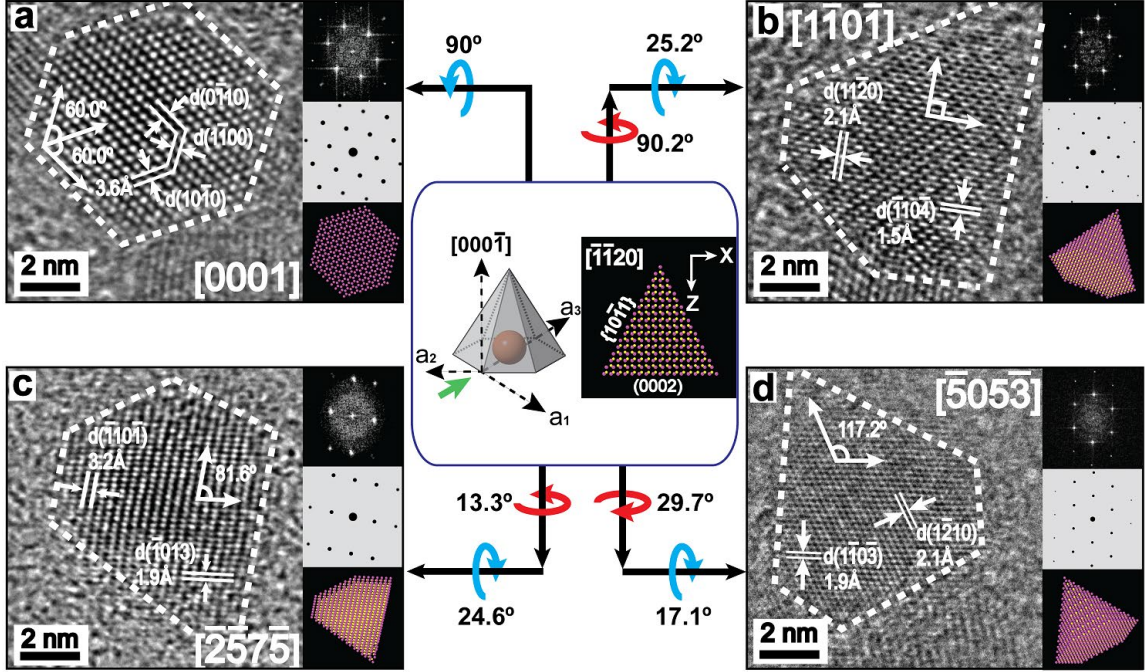


**Fig. 2.12:** HR-TEM images for core-shell HP-QDs. Center models define the shape (left) and atomic orientation (right) of the HP-QDs. The  $[\bar{1}\bar{1}20]$  projection (viewing along the green arrow in center left model) is set as the starting point of rotations. Each of the four panels (a-d) is composed of one representative HR-TEM image (left image) for an individual QD with a certain projection, the corresponding FFT pattern of the HR-TEM image (top right), and the computer generated atomic model (bottom right) and its corresponding simulated electron diffraction pattern (middle right) after a one- or two-step rotation from the center atomic model. The detailed rotations are indicated by the red and blue arrows along the Z axis and X axis (the axis normal to both Z and  $a_2$  axes), respectively. (a)-(d) show the HP QDs viewed along  $[0001]$ ,  $[110\bar{1}]$ ,  $[257\bar{5}]$ , and  $[505\bar{3}]$  zone axes, respectively.

material, suggesting that the particle is viewed along the  $[0001]$  zone axis. When viewed along the  $[110\bar{1}]$  zone axis (**Fig. 2.12b**), the particle instead shows characteristic rectangular cross-fringes from its  $(11\bar{2}0)$  and  $(\bar{1}10\bar{4})$  plane families with measured  $d$ -spacings of 2.1 and 1.5 Å, respectively. Both the outline of the HR-TEM image and the corresponding FFT pattern perfectly match the computer-generated atomic model (**Fig. 2.12b**). Furthermore, we also observed a low population ( $\sim 4\%$ ) of QDs with high-order projections (**Fig. 2.12c, d**). For example, **Fig. 2.12c** shows the particle viewed along the  $[257\bar{5}]$  zone axis, displaying the  $(\bar{1}10\bar{1})$  and  $(\bar{1}013)$  planes. The cross-fringes in this projection exhibit an angle of  $80.6^\circ$  (**Fig. 2.12c**), which is in good agreement with the

theoretically calculated value of  $80.50^\circ$  between the  $(\bar{1}10\bar{1})$  and  $(\bar{1}013)$  planes. In addition, **Fig. 2.12d** shows the particle viewed from the  $[\bar{5}05\bar{3}]$  projection with the characteristic cross-fringe angle of  $117.2^\circ$ , matching well to the theoretical value of  $117.32^\circ$  between the  $(1\bar{1}0\bar{3})$  and  $(1\bar{2}10)$  planes. The measured  $d$ -spacings of  $1.9\text{\AA}$  and  $2.1\text{\AA}$  match the  $d$ -spacings of  $(1\bar{1}0\bar{3})$  and  $(1\bar{2}10)$  planes perfectly. These results unequivocally validate the 3D HP shape, as well as crystal facets and atomic orientations of the CdSe-CdS core-shell QDs synthesized from the first-shell-growth reaction.

Similar crystallographic analyses have been applied to the HBP-QDs. The model was generated by cutting a bulk WZ CdS crystal into an HBP-shape with 12 equivalent  $\{10\bar{1}1\}$  surfaces merging into two apexes (**Fig. 2.13**, center). Most of the HBP-QDs seen on the TEM substrate display a rhombus outline, while only a low population ( $\sim 1\%$ ) show hexagonal outlines (**Fig. 2.13g**). **Fig. 2.13** shows a series of HR-TEM images of the HBP-QDs and the corresponding computer simulated atomic models. The particles with three common projections viewed along the  $[\bar{1}100]$ ,  $[\bar{1}101]$ , and  $[0001]$  zone axes are shown in **Fig. 2.13b**, **c**, **g**, respectively. The atomic fringes, FFT patterns, as well as the measured lattice distances can all be precisely matched to the model (**Fig. 2.13**, center) after completing certain rotations (**Fig. 2.13b**, **c**, **g**). For example, the  $[\bar{1}101]$  projection model can be achieved by rotating  $30^\circ$  along the Z axis, followed by a rotation of  $25.11^\circ$  along the X axis from the center model (**Fig. 2.13c**). In this projection,  $(01\bar{1}\bar{2})$ ,  $(\bar{1}01\bar{2})$  and  $(11\bar{2}0)$  planes can be seen with  $d(01\bar{1}\bar{2}) = d(\bar{1}01\bar{2}) = 2.5\text{\AA}$ , and  $d(11\bar{2}0) = 2.1\text{\AA}$ . The cross-fringe angles of  $126.2^\circ$  between  $(01\bar{1}\bar{2})$  and  $(11\bar{2}0)$  planes and  $107.6^\circ$  between  $(01\bar{1}\bar{2})$  and  $(\bar{1}01\bar{2})$  planes match well with the theoretical calculated values of  $126.32^\circ$  and  $107.36^\circ$ , respectively. The HBP-QDs projected from  $[10\bar{1}\bar{1}]$  and  $[\bar{1}01\bar{1}]$  directions can also be frequently seen in HR-TEM images (**Fig. 2.13d**, **h**).

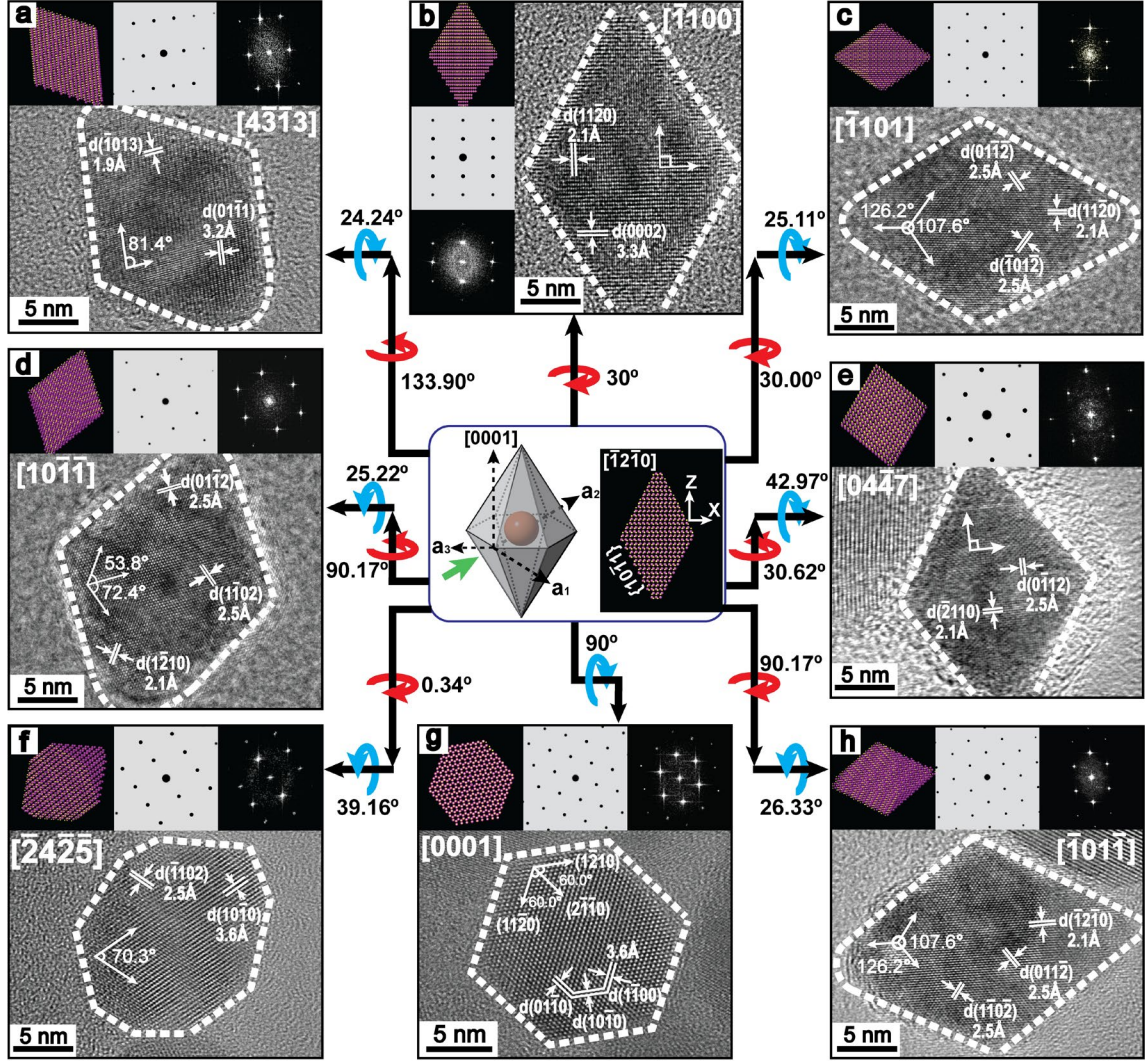


**Fig. 2.13:** HR-TEM images for core-shell HBP-QDs. Center models define the shape (left) and atomic orientation (right) of the HBP-QDs. The  $[\bar{1}2\bar{1}0]$  projection (viewing along the green arrow in center left model) is set as the starting point of rotations. Each of the eight panels (a-h) is composed of one representative HR-TEM image for an individual QD with a certain projection, the corresponding FFT pattern of the HR-TEM image, and the computer generated atomic model and its corresponding simulated electron diffraction pattern after a one- or two-step rotation from the center atomic model. The detailed rotations are indicated by the red and blue arrows along the Z axis and X axis (the axis normal to both Z and  $a_2$  axes), respectively. (a)-(h) show the HBP-QDs viewed along  $[4\bar{3}13]$ ,  $[\bar{1}100]$ ,  $[\bar{1}101]$ ,  $[10\bar{1}\bar{1}]$ ,  $[04\bar{4}7]$ ,  $[\bar{2}4\bar{2}\bar{5}]$ ,  $[0001]$ , and  $[\bar{1}01\bar{1}]$  zone axes, respectively.

Furthermore, we have also observed a low population (<5%) of the HBP-QDs viewed from high-order projections (Fig. 2.13a, e, f). For example, in Fig. 2.13a, the  $(\bar{1}013)$  and  $(01\bar{1}\bar{1})$  planes with  $d(\bar{1}013) = 1.9 \text{ \AA}$ ,  $d(01\bar{1}\bar{1}) = 3.2 \text{ \AA}$  were observed with



a measured cross-fringe angle of  $81.4^\circ$  (theoretical calculated angle of  $81.48^\circ$ ), suggesting the  $[4\bar{3}\bar{1}3]$  projection. The coexistence of the orthogonal planes of  $(0\bar{1}12)$  and  $(\bar{2}110)$  in **Fig. 2.13e** and the  $(\bar{1}102)$  and  $(10\bar{1}0)$  planes with an angle of  $70.3^\circ$  in **Fig. 2.13f** were observed for the particles viewed along the  $[04\bar{4}7]$  and  $[\bar{2}4\bar{2}\bar{5}]$  zone axes, respectively. The particles with these unusual high-order projections are likely due to squeezing by nearby particles or laying on an uneven surface of the TEM substrate.<sup>39-41</sup>

Taken together, 2D projection outlines, atomic lattice fringes, and the corresponding FFT patterns of the HR-TEM images for individual core-shell hetero-QDs can all be perfectly matched to the computer generated atomic models and the corresponding simulated electron diffraction patterns at different viewing projections (**Fig. 2.12** and **2.13**). These results explicitly prove the correctness of the proposed models shown in **Fig. 2.12** and **2.13**, demonstrating a high degree of agreement between the proposed models and the shape, facet, and atomic orientation of the obtained hetero-QDs.

#### **2.4 Ligand-Induced Particle Shape Evolution during the Shell Growth**

The complete characterization and analysis of the crystal facets and atomic orientations of the HP- and HBP-QDs allowed us to suggest a mechanism and reconstruct the particle shape evolution. **Fig. 2.14** shows a scheme of the formation mechanism for HP- and HBP-QDs in the two-step growth procedure (**Fig. 2.14a**) and the TEM images of the QD samples collected at the corresponding growth stages (**Fig. 2.14b-f**).

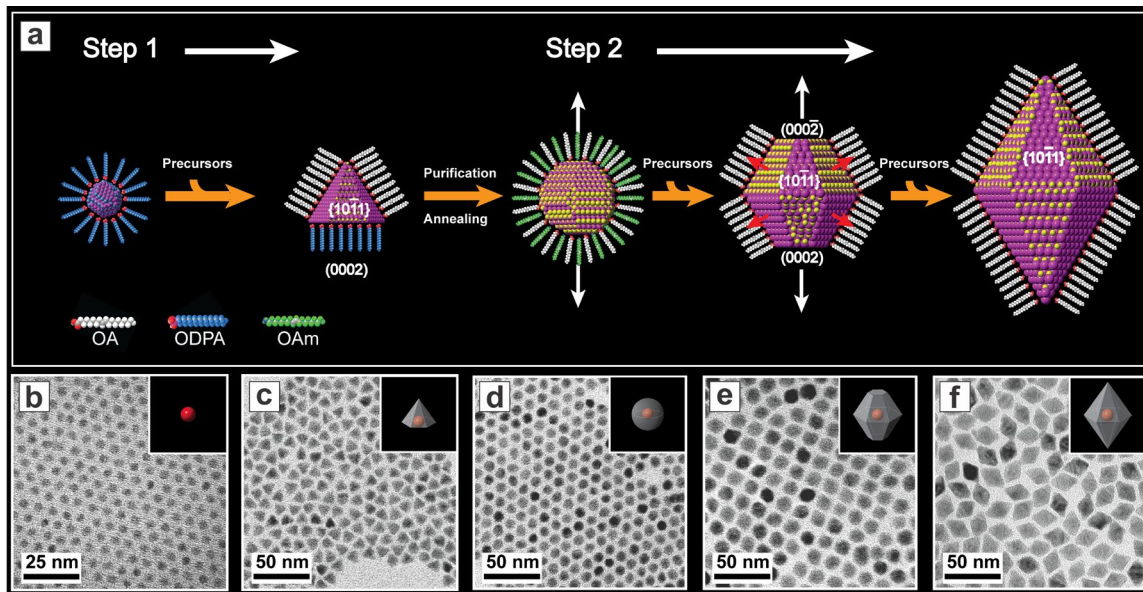


**Fig. 2.14:** (a) Mechanism of the HP and HBP shape evolutions of the CdSe-CdS core-shell QDs during the shell formation process. (b-f) The corresponding TEM images of the QD samples at different shell-growth stages: (b) starting CdSe cores; (c) HP-QDs after the 1st-shell-growth step; (d-f) QD samples taken at different time points during the 2nd-shell-growth step, 20 min (d), 120 min (e), and 180 min (f).

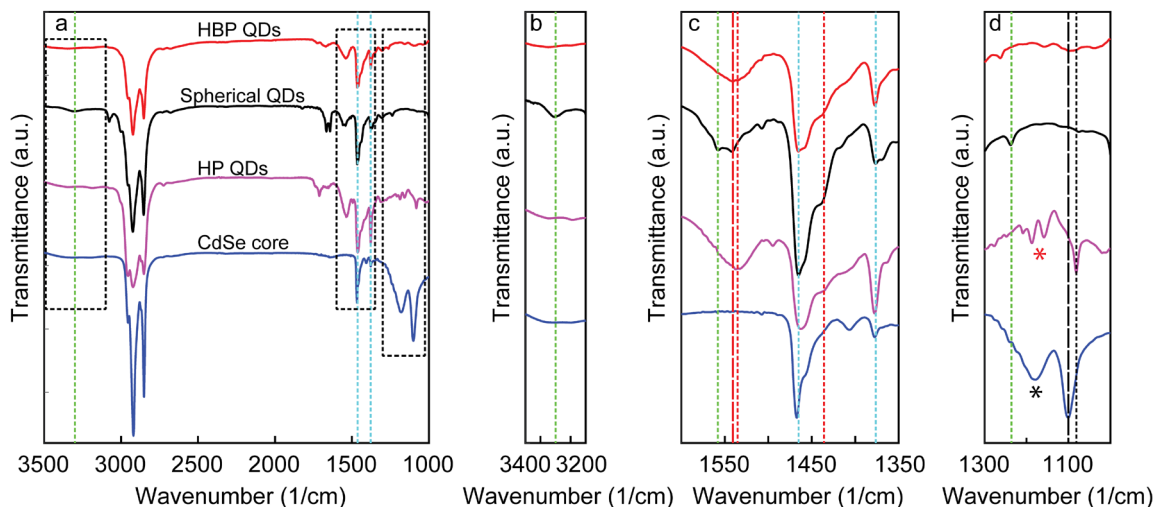


**Fig. 2.15:** FTIR spectra of CdSe core QDs, HP-QDs, the sample took at the early stage of 2<sup>nd</sup>-shell-growth reaction (Spherical QDs), and final HBP-QDs. (a) Full FTIR spectra; (b-d) Zoomed-in rectangular area in (a).

It is known that Cd-chalcogenide QDs can be well-passivated by efficient bonding ligands such as ODPA, OLA, and OAm through the interactions with surface

Cd-sites.<sup>42-45</sup> Particularly, the CdSe cores used in this study are surface-coated by ODPa ligands (**Fig. 2.15**).<sup>17</sup> During the first-shell-growth reaction, the Cd-rich (0002) facet was stabilized by strong ODPa bonding to Cd<sup>2+</sup> cations,<sup>15, 43, 44</sup> which led to a slow shell deposition that consequently developed into an atomically flat hexagonal base (**Fig. 2.14a-c**). In contrast, the less stable chalcogenide-rich (000 $\bar{2}$ ) facet exhibited a fast-epitaxial shell growth that subsequently developed to an apex (**Fig. 2.14a-c**). Concomitantly, Cd-rich {10 $\bar{1}$ 1} facets, which were stabilized by oleate ligands (from the Cd precursor) through covalent chelating bidentate interactions (**Fig. 2.15**), emerged on the lateral sides of the particle (**Fig. 2.14, Step 1**).<sup>46, 47</sup> The overall growth fashion led to a HP particle shape during the first-shell-growth (**Fig. 2.14a-c**). The coexistence of OA and ODPa ligands on the HP-QD surface was also proved by <sup>1</sup>H (nuclear magnetic resonance) NMR and <sup>31</sup>P NMR (**Fig. 2.16a, c**). Unlike CdSe-CdS nanorod or nanobullet syntheses,<sup>15-17, 36</sup> the absence of the {10 $\bar{1}$ 0} and {11 $\bar{2}$ 0} facets indicates their instability as compared to the {10 $\bar{1}$ 1} facets under the present growth conditions. Next, an intermediate purification step is essential for the following development of the HBP shape as it removes the excess ODPa ligands from the reaction solution (**Fig. 2.16d**). In the second shell-growth reaction, a particle shape conversion from HP to sphere was observed at the initial stage (**Fig. 2.14a, d**). A similar QD shape conversion has been observed recently by Peng *et al.*<sup>39</sup>s Importantly, during this shape conversion associated with surface atom rearrangement processes, the remaining surface-bonded ODPa ligands from the first-step were totally removed due to the presence of a large excess of fresh OAm (solvent) and the addition of Cd-oleate and OLA in the shell precursor solution (**Fig. 2.15**). As a result, the QDs' surface was covered by both oleate and OAm but no ODPa as proved by the FT-IR measurements (**Fig. 2.15**). In contrast to the first-shell-

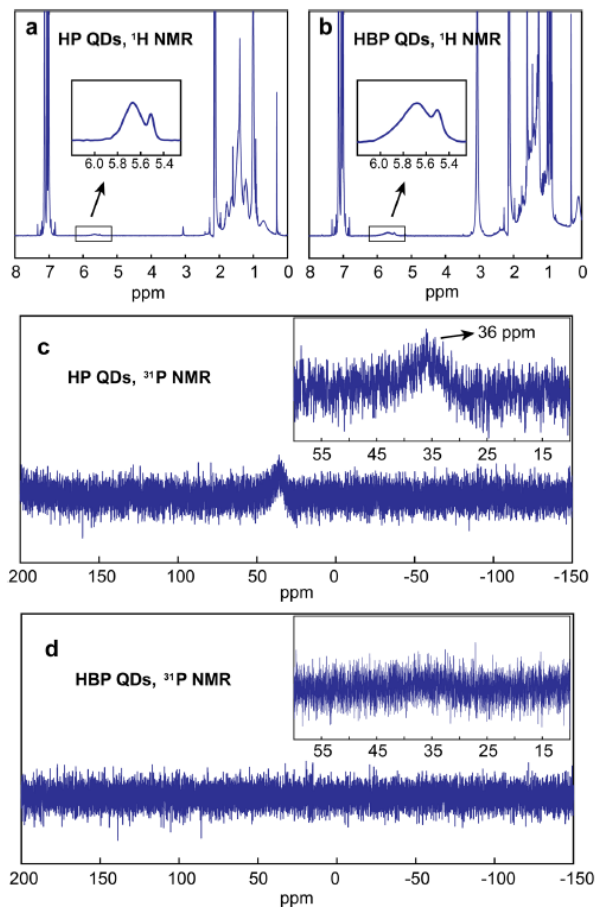


**Fig. 2.16:** (a, b)  $^1\text{H}$ -NMR and (c, d)  $^{31}\text{P}$ -NMR for HP-, HBP-QDs. The  $^1\text{H}$ -NMR spectra show broad peaks between 5~6 ppm which correspond to the proton of double bond in OLA molecule, proving the existence of oleate as the surface passivating ligand (The small sharp peak is associated to the double bond proton from solvent ODE); in the meantime,  $^{31}\text{P}$ -NMR spectrum of HP-QDs shows a broad peak at ~36 ppm, which is associated to the bonded ODPA on HP-QD surfaces.  $^{31}\text{P}$ -NMR spectrum of HBP-QDs shows no obvious phosphonate peak from ODPA. Both the  $^1\text{H}$ -NMR and  $^{31}\text{P}$ -NMR results are consistent with the proposed model.

growth reaction, the absence of the surface ODPA ligands and the presence of excess OAm and OLA diminished the growth preference between the (0002) and (000 $\bar{2}$ ) directions (**Fig. 2.15** and **2.16**).<sup>43, 48</sup> Thus, the CdS shell grew simultaneously in both directions during the second-shell-growth (**Fig. 2.14**). At the same time, the oleate stabilized {10 $\bar{1}$ 1} facets gradually dominated the particle surface, resulting in first a hexagonal bipyramid shape (**Fig. 2.14a, e**) and finally a HBP shape (**Fig. 2.14a, f**). Evidently, the Fourier-transform infrared-spectroscopy (FTIR) characterizations and NMR

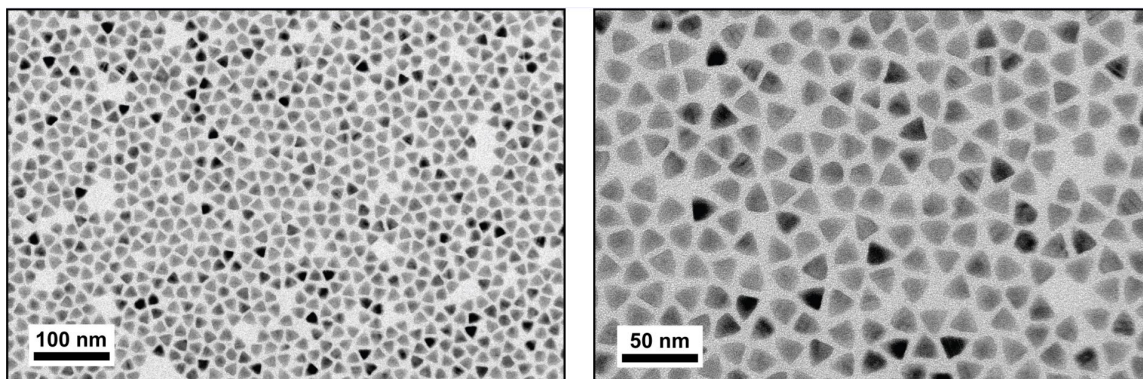


*Fig. 2.17: TEM images of the CdSe-CdS core-shell QDs synthesized with additional ODPA during the 2nd-shell-growth reaction. It shows that the final QDs maintain the HP shape instead of HBP shape due to the presence of extra ODPA.*

measurements show that the final HBP-QDs' surface is solely passivated by bidentate oleate ligand without OAm and ODPA (Fig. 2.15 and 2.16), consistent with the proposed mechanism. Moreover, if additional ODPA was added to the second-shell growth solution, instead of developing into the HBP shape, particles preserved the HP shape (Fig. 2.17). This result strongly supports the proposed mechanism of ligand-induced particle shape evolution.

## 2.5 Optical Properties of HP-HBP- Core-Shell QDs

To further study the optical properties of these HP and HBP core-shell QDs, we monitored the PL line width and the global Stokes shift evolutions during the CdS shell growth (Fig. 2.18a, b). Both the ensemble PL line width (FWHM) and global Stokes shift decreased, respectively, from 86.6 to 65.6 meV and 41.2 to 33.6 meV during the first-shell-growth. The PL measurements at the single-QD level show that the PL line width of single-HP-QDs fluctuated around the ensemble PL line width (Fig. 2.18c, d). This suggested the PL line width narrowing effect was due to the minimization of inhomogeneous broadening with improved particle uniformities in size and shape, shell crystallinity, as well as surface passivation.<sup>8</sup> However, during the course of second shell-

growth reaction while developing the HBP shaped QDs, both the PL line width and the Stokes shift increased significantly from 65.6 to 101.5 meV and 33.6 to 66.2 meV, respectively. The PL line width of the final HBP-QDs is  $\sim 23\%$  larger than that of the spherical QDs with the same core size and shell volume (101.5 meV vs 78.2 meV, **Fig. 2.6**). Single-HBP-QD PL measurements revealed nearly overlapped PL profiles (**Fig. 2.18e**) and almost identical PL line widths for the single-HBP-QD and the ensemble sample (**Fig. 2.18f**). These results lead to the conclusion that the PL broadening effect during the second-shell-growth step was solely due to the homogeneous broadening of the average single-QD PL line width rather than the inhomogeneous broadening caused

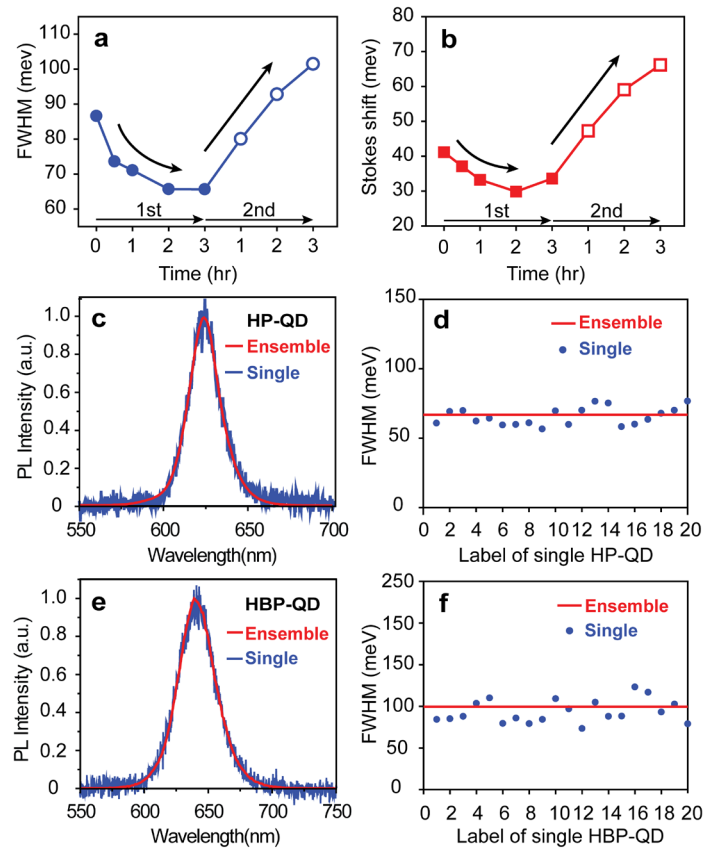


**Fig. 2.18:** Temporal evolutions of the PL linewidth (a) and Stokes shift (b) of the CdSe-CdS core-shell QDs during the shell growth reactions. The ensemble and single-QD PL spectra of the HP- (c) and HBP-QDs (e). The distributions of single-QD PL linewidth (FWHM) of HP- (d) and HBP-QDs (f). The ensemble PL linewidth values are shown as the red lines in (d) and (f).



from losing particle uniformity.<sup>8, 49</sup> Given the minimal excitonic fine structure contribution ( $< 8$  meV) to line width changes an negligible spectral diffusion on submillisecond time scales at room temperature,<sup>50, 51</sup> this homogeneous broadening can be attributed to two major factors that are directly related to the thick HBP CdS shell: (1) enhanced longitudinal optical (LO) phonon coupling with excitons through increased Fröhlich interactions induced by reduced electron–hole wave function overlap during the CdS shell formation;<sup>52, 53</sup> (2) a strong internal electrical field and large dipole moment induced by a spontaneous polarization of a WZ crystal structure and the HBP particle shape.<sup>54-57</sup> In addition, a  $\sim 43\%$  larger Stokes shift (66.2 meV vs 46.3 meV) was measured for the HBP-QDs than for spherical QDs with the same particle volume ( $\sim 1480$  nm<sup>3</sup>, **Fig. 2.19** and **Table 2.2**), further providing strong indication of increased

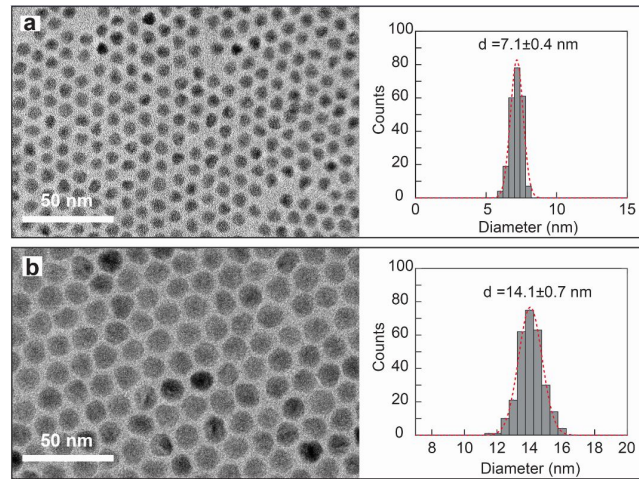


**Fig. 2.19:** TEM images of the spherical CdSe-CdS core-shell QDs with the same core size and shell volumes to the HP- and HBP-QDs and the corresponding histograms of size distributions.

net exciton–phonon coupling for the HBP-QDs.<sup>58</sup> Because of the lack of direct experimental evidence and characterization tools, other factors that may affect the single-QD PL line width changes cannot be completely ruled out, such as localized charges, surface reconstruction, and the piezoelectric effect on local electrical fields.<sup>46, 59, 60</sup>

To further characterize our HP- and HBP-QDs as single-emitters, we studied single-QD blinking behavior of both samples. **Fig. 2.20** shows representative PL blinking

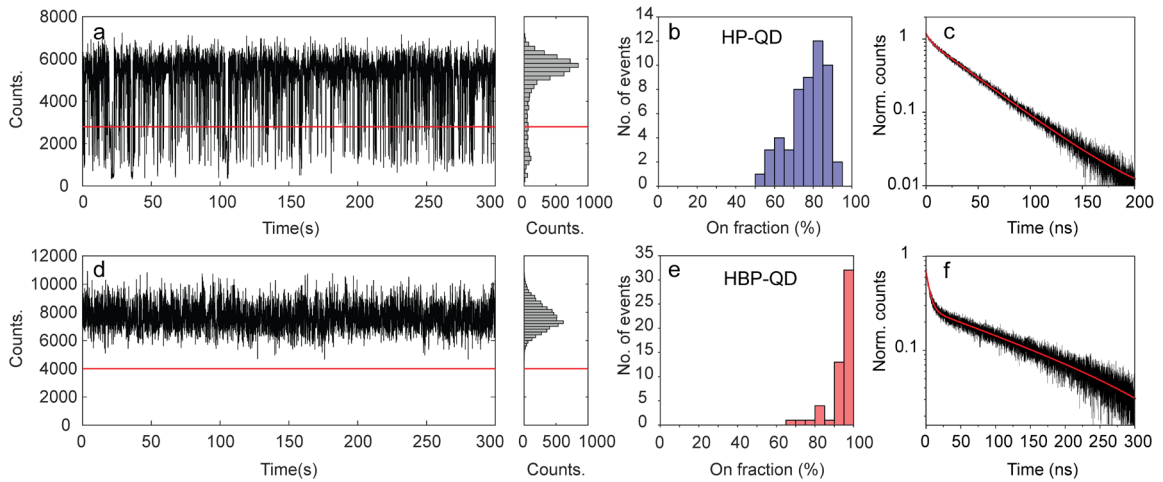


**Fig. 2.20:** Single particle PL blinking traces, histogram of PL intensity distributions, “On” time fraction distribution and lifetimes of the HP-QDs (a-c) and HBP-QDs (d-f).

traces, histograms of PL intensity distributions, and the “On” time fraction distribution of the measured HP- and HBP-QDs. The average “On” time fraction is 80% for HP-QDs and 96% for HBP-QDs. More than 50% of the HBP-QDs we measured were completely nonblinking (**Fig. 2.20**). Such high “On” time fractions for the HBP-QDs can be attributed to the thick and highly crystalline CdS shell, proven by the XRD and TEM measurements (**Fig. 2.8, 2.12, and 2.13**) and also in good accordance to previous studies

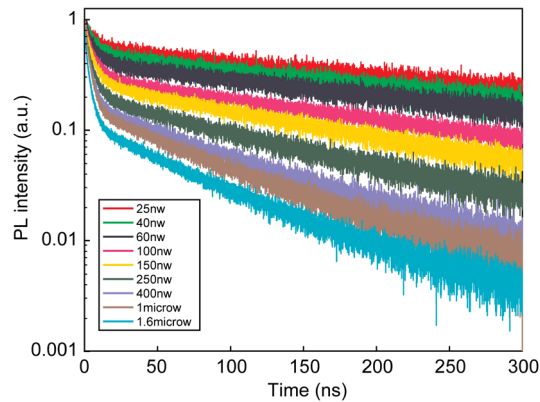


**Fig. 2.21:** Excitation-intensity-dependent single-QD lifetimes of HBP-QD.



with similar growth conditions for spherical core–shell QDs.<sup>8</sup>

In addition to the high “On” fraction, we also measured the PL decay of single HP- and HBP-QDs. A representative decay profile is shown in **Fig. 2.20c, f**. The PL decays of single HP-QDs can be fitted to a single exponential function with an average single-QD lifetime of  $\sim 36.0$  ns, which is consistent with the ensemble measurements (**Fig. 2.20c**). In contrast, the PL decay curve of single HBP-QDs clearly contains two components and can be well-fitted to a double exponential decay function (**Fig. 2.20f**). The slow component is attributed to the radiative recombination of single excitons, which is consistent with the slow PL decay from ensemble PL lifetime measurements ( $\sim 242$  ns, **Fig. 2.6**). The fast decay component has an average lifetime of  $\sim 6$  ns, which is ascribed to the PL decay of biexciton (BX). Since the HBP-QDs have a thick shell and, therefore, high absorption cross section, there is high probability of generating BX in the QD even under low power excitation (40 nW).<sup>26, 61</sup> Moreover, this fast decay component showed an excitation intensity dependence (**Fig. 2.21**), further proving its origin is due to BXs.<sup>26</sup> This long BX decay lifetime indicates a strong suppression of the Auger recombination, which has been previously observed in spherical g-QDs (**Fig. 2.20d**).<sup>29, 62</sup> Additionally, this suppression of Auger recombination should result in a high BX QY of the QDs. Previously, Nair *et al.* showed that the BX QY of a single-QD can be determined from the size of the 0-time feature in the second order photon correlation function ( $g^{(2)}$ ) of the QD.<sup>63</sup> The  $g^{(2)}$  function of a single-HBP-QD showed a high 0-time feature (**Fig. 2.22**), suggesting the HBP-QDs have a high BX QY. A high BX QY has also been observed in conventional g-QDs.<sup>29, 62</sup> In all, the thick and high crystalline CdS shell prevents the electron/hole from reaching to the QD surface, thus limiting their accessibility to the defect and surface-related nonradiative pathways in the HBP-QDs. Furthermore, the

reduced spatial overlap due to the large HBP CdS shell formation also results in a

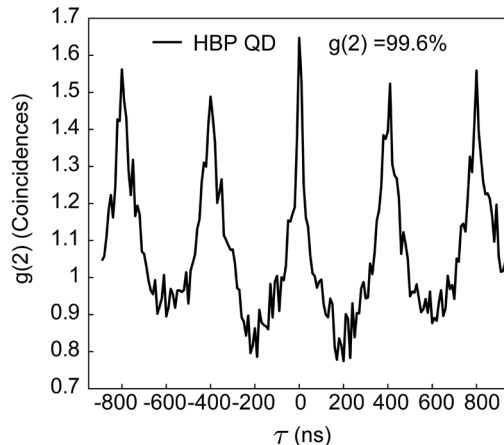


*Fig. 2.22: Representative  $g^{(2)}$  data for HBP-QDs.*

suppressed nonradiative Auger recombination.<sup>64</sup> Both factors contribute to the observed high QY and long lifetime of BXs in this HBP-QDs.

## 2.6 *In Vitro* Biological Study

Recent discoveries reveal that the shape of nanomaterials is an important parameter when interacting with living biological systems (e.g., living cells, organisms, tumors).<sup>65-67</sup> To demonstrate the shape effect of pyramidal QDs on in vitro cellular uptake and intracellular imaging, samples of spherical QDs (SQDs, as a reference sample) and HBP-QDs underwent the same ligand exchange reaction with methoxy-polyethylene-glycol thiol (PEG-SH, MW5000) (details in the Methods). After ligand exchange, both samples were successfully transferred into aqueous solutions and showed similar hydrodynamic diameters of  $\sim 26.7$  nm and  $\sim 25.8$  nm for the PEGylated HBP-QDs (PEG-HBP-QDs) and SQDs (PEG-SQDs), respectively, suggesting no aggregations in aqueous solution.<sup>68, 69</sup> No measurable variations in absorption and PL spectral profiles of the QDs were observed after the ligand exchange reaction (**Fig. 2.23**). A  $\sim 30\%$  PL QY decrease was measured for both PEG-HBP-QD and PEG-SQD samples, consistent with the

reported PL quenching effect caused by a monothiol group.<sup>70-72</sup>

The obtained water-soluble QDs were incubated with three different cell lines: Non-neoplastic human mammary epithelial MCF10A cells and two types of human breast cancer cells (MDA-MB-231 and MCF7). Minimal cell toxicities for all three cell lines were detected for both QD samples, indicating robust surface protection with sufficient PEG coating (**Fig. 2.24**).<sup>69</sup> To quantify the amount of QD cellular uptake,

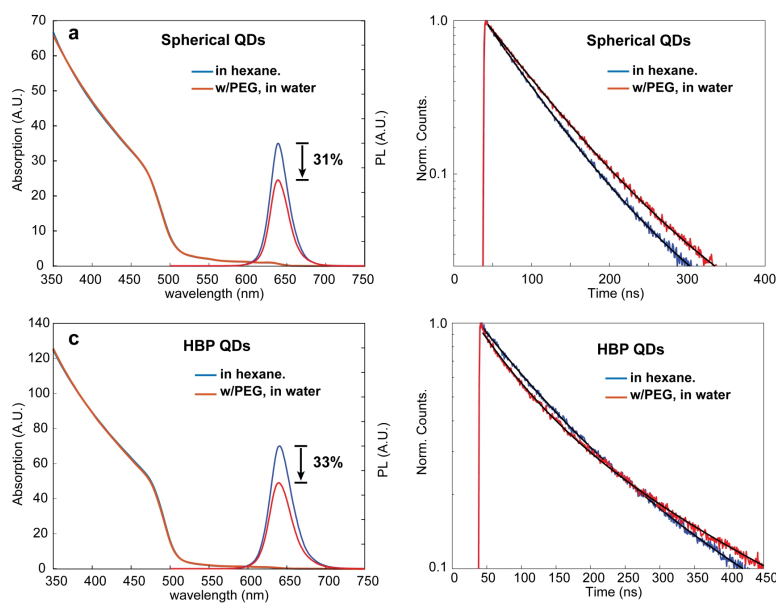


**Fig. 2.23:** Absorption, PL emission, lifetime decays for Spherical QDs and HBP-QDs before and after ligand exchanges with Thiol-PEGs.

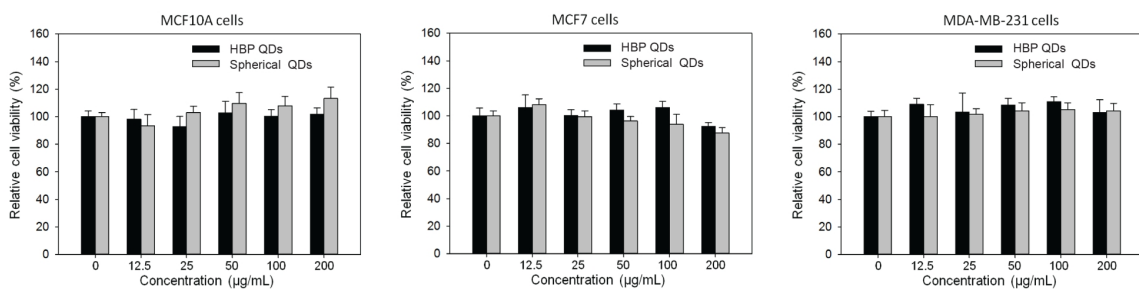


**Fig. 2.24:** Cytotoxicity and cell uptake tests for HBP-QDs and Spherical QDs. Cell line: MDA-MB-231 and MCF7 are human breast cancer cells; MCF10A is a non-neoplastic human mammary epithelial cell.

confocal fluorescence imaging was carried out and the relative amount of cell uptaken

QDs were determined based on the fluorescence intensity quantification method. Interestingly, we found that the PEG-HBP-QDs uptake was  $\sim 3$  times as much as the PEG-S-QDs under the same experimental conditions for all three cell lines tested here (Fig. 2.25,  $p < 0.02$  with Student's t test,  $n = 3$ ). This is likely caused by a slightly higher hydrodynamic AR and a dramatically increased contacting curvature (i.e., sharp apexes of the HBP-QDs) of the PEG-HBP-QDs compared to the PEG-S-QDs.<sup>66, 73, 74</sup> When attached on the cell surface with the apex, the PEG-HBP-QDs could readily “puncture” into the lipid bilayer and break the integrity of the cell membrane, leading to a significant increased cellular internalization.<sup>73, 75, 76</sup>

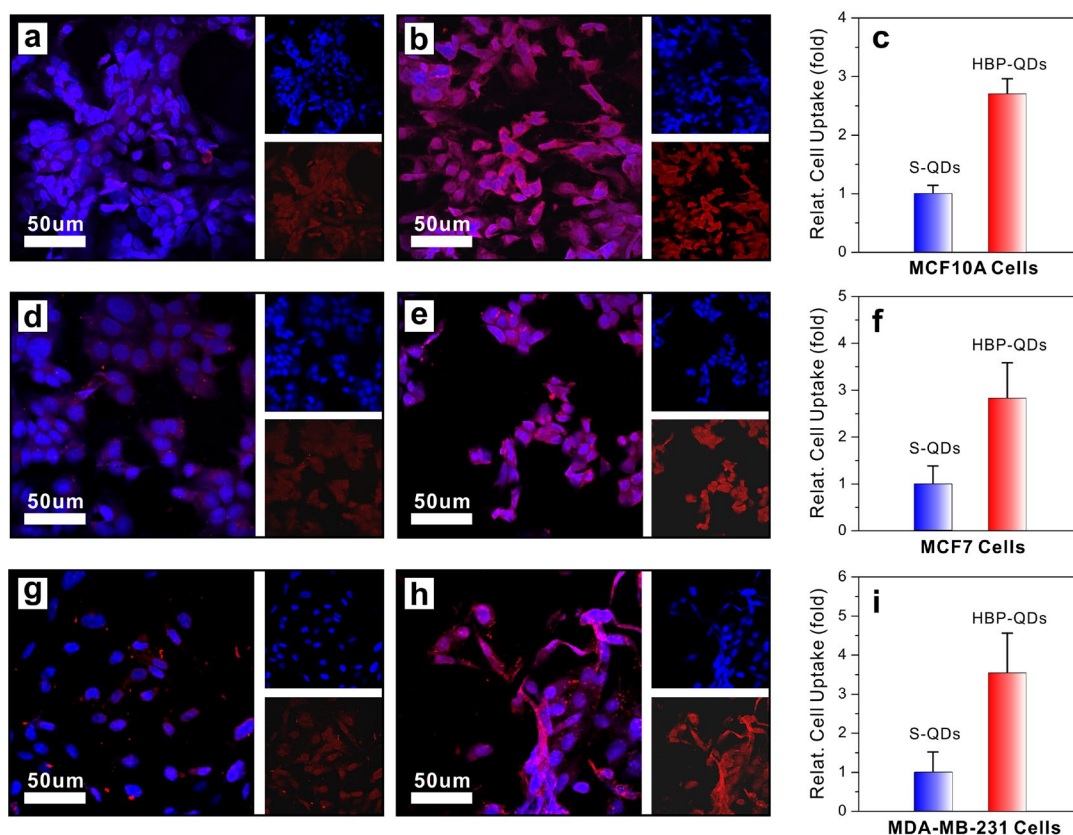


**Fig. 2.25:** Cellular uptake of PEG-HBP-QDs and PEG-S-QDs. Representative confocal fluorescent microscope images show the cellular uptake of PEG-S-QDs (a, d, and g) and PEG-HBP-QDs (b, e, h) in MCF10A, MCF7, and MDA-MB-231 cells, respectively. Quantified amount of uptaken PEG-S-QDs and PEG-HBP-QDs in MCF10A (c), MCF7 (f), and MDA-MB-231 (i) cells. ( $p < 0.02$  with Student's T-test,  $n=3$ ).

The results provided here manifest potential applications of these HBP-QDs in cellular internalization processes and provide further insights for drug deliveries, therapeutic design, and intracellular activities under fluorescence imaging and tracking. Moreover, the largely prolonged emission lifetime and significantly suppressed single-dot PL blinking of the HBP-QDs can further enable more characterization dimensions (e.g., fluorescence lifetime imaging microscopy, single-particle sensing and tracking) for biological imaging down to the single-molecule scale both *in vitro* and *in vivo*.<sup>77, 78</sup>

In summary, we have demonstrated, for the first time, the syntheses of HP and HBP CdSe-CdS core-shell hetero-QDs. Through detailed crystallographic analyses using HR-TEM as well as the volume reconstruction *via* electron tomography, we have unambiguously identified the HP and HBP shapes as well as the atomic facets of the obtained hetero-QDs. While the HP-QDs contain one (0002) hexagonal base and six equivalent low-index  $\{10\bar{1}1\}$  facets on the lateral sides, the HBP-QDs' surface is dominated only by twelve equivalent  $\{10\bar{1}1\}$  facets, which merge into two apexes at the (0002) and (000 $\bar{2}$ ) directions. We attributed this pyramidal shape development to a ligand-induced growth model during the CdS shell formation process. The resultant HP and HBP core-shell hetero-QDs exhibit high morphological uniformity, perfect epitaxial WZ crystallinity, and superior optical properties including high PL QYs, minimal inhomogeneous PL linewidth broadening, significantly suppressed single-QD blinking, and prolonged ensemble and single-QD PL lifetimes as compared to spherical QDs with the same core and shell volumes. Given the large CdS shell volume ( $\sim 1450 \text{ nm}^3$ ,  $\sim 16 \text{ ML}$  equivalent CdS shell for spherical core-shell QDs), the HBP-QDs can be categorized as conventional g-QDs, but with flat atomic facets and high morphological uniformity. Furthermore, the HBP-QDs were successfully transferred to an aqueous solution without

aggregation while retaining their optical properties. The obtained water-soluble HBP-QDs showed low-cytotoxicity and greatly enhanced cellular uptake for different cell-lines, demonstrating their potentials in biological intracellular labeling and imaging applications.

## **Methods**

### *Chemicals:*

Cadmium oxide (CdO, 99.998%), 1-octadecene (ODE, 90%), trioctylphosphine oxide (TOPO 99%), trioctylphosphine (TOP, 97%), oleylamine (OAm, 70%), 1-octanethiol (> 98.5%), were obtained from Sigma Aldrich. Selenium powder (99.999%), oleic acid (OLA, 90%) were purchased from Alfa Aesar. Octadecylphosphonic acid (ODPA, 99%) were purchased from PCI Synthesis. Methoxy-polyethylene-glycol thiol (PEG-SH), MW 5k was purchased from Creative PEGWorks.

### *Synthesis of CdSe core QDs:*

The synthesis of CdSe core QDs is followed by a hot-injection method as previously reported.<sup>8</sup> Typically, 120 mg CdO (99.998%), 560 mg ODPA (99%) and 6 g TOPO (99%) were loaded to a 100 mL flask. The mixture was degassed and heated to 150 °C for 1 hour under vacuum. The reaction solution was then heated to 360 °C under nitrogen to form a colorless clear solution. After adding 4.0 mL TOP (97%), the temperature was brought up to 380 °C and a freshly prepared Se/TOP (120 mg Se in 1.0 mL TOP) solution was swiftly injected into the flask. The reaction was quenched by removing heating mantle and blowing cool air when a desired CdSe core size was reached. The resulting CdSe core QDs were diluted in hexane as stock.

### *Synthesis of CdSe-CdS core-shell pyramidal-shaped QDs:*

In a typical synthesis of HP QDs, 100 nmol of CdSe cores (purified one time by acetone) were loaded into a 100mL 3-neck flask with a solvent mixture of 2 mL ODE and 2mL OAm. The reaction mixture was degassed under vacuum at room temperature for 1 hour and 120 °C for 10 min to remove hexane, water and oxygen. The reaction mixture was then heated to 310 °C under nitrogen for shell growth. When temperature reached 240 °C, a desired amount (typically calculated 6 monolayer CdS shell equivalent) of Cd-oleate (0.1M, balanced by ODE,  $w/V_{\text{tot}} = 6\text{mL}$ ) and 1.2 equivalent of 1-octanethiol balanced by ODE  $w/V_{\text{tot}} = 6\text{mL}$  were injected dropwisely into the reaction mixture simultaneously by a syringe pump with an injection rate of 2mL/hr. Aliquots were taken during the reaction for absorption and photoluminescence characterizations. The reaction was stopped by removing the heating mantle and cooled down to room temperature after finishing the injection. The synthesized CdSe-CdS core-shell HP-QDs were purified by three rounds of precipitation and redispersion using acetone/methanol and hexane. The particles were finally suspended in ~2 ml hexane as stock.

HBP QDs are achieved by a 2<sup>nd</sup>-shell-growth step using the purified HP QDs. In a typical synthesis, the purified HP QDs were loaded in a 100 mL 3-neck flask with a solvent mixture of 2 mL ODE and 2 mL OAm. The reaction mixture was degassed under vacuum at room temperature for 1 hour and 120 °C for 10 min to remove hexane, water and oxygen, and then heated to 310 °C under nitrogen for the 2<sup>nd</sup>-shell-growth. The amount of shell precursors (Cd-oleate and 1.2 equivalent of 1-octanethiol) were determined by calculating the desired CdS shell volume. The desired amount of Cd-oleate and 1-octanethiol were balanced with ODE into the same total volume of 6 mL (typically, the next 7<sup>th</sup>-12<sup>th</sup> monolayer equivalent amount of cadmium-oleate and 1-octanethiol were used to achieve hexagonal bipyramid NPs). When the temperature

reached 240 °C, the precursors were injected into the reaction solution simultaneously using a syringe pump with an injection rate of 2 mL/hr. Aliquots were taken during the reaction for absorption and photoluminescence characterizations. After the injection was completed, the reaction was stopped by removing heating mantle and allowed to cool to room temperature. The synthesized CdSe-CdS core-shell HBP-QDs were purified by three rounds of precipitation and redispersion using acetone/methanol and hexane. The particles were finally suspended in ~2 mL hexane as stock.

*UV-Vis absorption measurements of HP and HBP QDs:*

UV-Vis absorption spectra were measured using an Agilent Technologies Cary 5000 UV-Vis Spectrophotometer. HP- and HBP-QDs were dissolved in hexane for the measurements.

*PL, lifetime and QY measurements of HP and HBP QDs:*

The solution PL, lifetime and QY measurements were performed on an Edinburgh Instruments Fluorescence Spectrometer FS5. The HP- and HBP-QDs were dissolved in hexane for measurements. The PL lifetime were measured with excitation at 360 nm, with an average acquisition time of 15 min. The PL QYs were measured by FS5 Spectrometer with a built-in integrating sphere.

*TEM measurements of HP and HBP QDs:*

TEM measurements were performed on a JEOL 2100F operated at 200 kV. The QDs were diluted in hexane after purification, then drop cast on a 300-mesh copper TEM grid and dried at ambient condition before TEM measurements. High angle annular dark field-scanning transmission electron microscopy (HAADF-STEM) images, energy dispersive X-ray (EDX) elemental mapping data were acquired using a Thermo Fisher Scientific -Talos



microscope operated at an accelerating voltage of 200 kV. The high-resolution STEM (HR-STEM) imaging and STEM-EELS mappings were performed on a Hitachi-2700C aberration corrected STEM at 200 kV with a cold-field emission gun in Brookhaven.

*Powder X-ray diffraction (XRD) measurements:*

XRD spectra were obtained on a Bruker D8 Discovery 2D X-ray diffractometer equipped with a Vantec 500 2D area detector operating with Cu K $\alpha$  ( $\lambda = 1.541 \text{ \AA}$ ) radiation. Samples were drop-casted on glass slides and the solvent evaporated under room temperature.

*FTIR Measurements:*

FTIR measurements were performed on a Jasco FT/IR 4100 with attenuated total reflectance (ATR) attachment. Dried samples were directly placed on the ATR crystal for measurements.

*Preparation for water-soluble QDs:*

The CdSe-CdS core-shell spherical QDs and HBP-QDs solutions (1 nmol in 100  $\mu\text{L}$  chloroform) was added to a freshly prepared chloroform solution of PEG-SH (60 mg in 100  $\mu\text{L}$ ). The solution mixture was stirred at room temperature for  $\sim 10$  hrs. The QDs were precipitated by adding hexane solution. After centrifuging for 2 min at 300 rcf, QDs were then re-dissolved in 2 mL of PBS buffer solution and stored at 4  $^{\circ}\text{C}$ .

*Cell culture:*

Human breast cancer cells (MDA-MB-231 and MCF7) and non-neoplastic human mammary epithelial MCF10A cells were obtained from American Type Culture Collection (ATCC, Manassas, VA, USA), and cultured in DMEM (MDA-MB-231 and MCF7) and DMEM/F12 media with supplements, respectively. All cells were maintained

at 37 °C in a humidified incubator with 5% CO<sub>2</sub>.

*In vitro cytotoxicity test:*

*In vitro* cytotoxicity of PEG-HBP-QDs and PEG-S-QDs were evaluated using a cell viability assay. 5,000 cells (MDA-MB-231, MCF7 and MCF10A) were seeded in each well of a 96 well plate and incubated for 24 h. Then cells were treated with sample-1 or sample-2 at different particle concentrations of 0, 12.5 25, 50, 100 and 200 µg/mL for 24 hours. Cell viability was determined by a Dojindo cell counting kit using the protocol from the manufacturer (Rockville, MD, USA).

*In vitro cell uptake test:*

10,000 cells (MDA-MB-231, MCF7 and MCF10A) were seeded in each well of a 96 well plate and incubated for 24 h. Then cells were treated with PEG-HBP-QDs or PEG-S-QDs at a concentration of 100 µg/mL in DMEM with 10% FBS for 4 hours. Cells were rinsed with PBS twice to remove free QDs, and the fluorescence intensity of cell uptaken QDs was quantified using a Synergy H4 Microplate reader (Winooski, VT, USA) at excitation/emission wavelengths of 400 and 632 nm, respectively.

*Fluorescent cell imaging:*

100,000 cells (MDA-MB-231, MCF7 and MCF10A) were seeded in each well of Nunc Lab-Tek II Chamber Slide system (4 wells) and incubated for 24 h. Then cells were treated with sample-1 or sample-2 at a concentration of 100 µg/mL in DMEM with 10% FBS for 4 hours. Cells were rinsed with PBS twice to remove free QDs, and fixed with 4% paraformaldehyde solutions for 15 min. Fixed cells were rinsed with PBS, and DAPI dye solution was applied to stain cell nucleus, and dried overnight in the dark. The fluorescent cell images were taken using a Leica TCS SP5 confocal fluorescent

microscope (Buffalo Grove, IL, USA).

*Electron tomography:*

Tilt series were acquired in 1 degree increments from -65 to + 65 degrees on a transmission electron microscope (Tecnai G2, FEI company, Eindhoven, The Netherlands) using an acceleration voltage of 200 KV. Tilt series were acquired at magnifications of 29,000 x and 50,000 x. A bottom mounted 4K CCD camera (Eagle 4K, FEI company) was used for image acquisition.

The Inspect 3D Xpress software package (v. 3.0.0.3478, FEI company) was used for image alignment and reconstruction of 3D datasets from the tilt series. The reconstructions were performed using the sequential iterative reconstruction techniques (SIRT) algorithm with 20 iterations computed on a graphics processing unit (QUADRO 5000, NVIDIA Corporation, Santa Clara, CA, USA).

Rendering of 3D datasets was performed in the image analysis and visualization software package Bitplane Imaris (v. 8.2.1., Bitplane AG, Zurich, Switzerland) using a combination of automated thresholding and manual segmentation.

*Single-QDs optical property measurements:*

All the single particle measurements were performed with a home-built confocal fluorescence microscope. The samples for single particle study were prepared by spin-coating highly diluted QD solutions in hexane on No 1.5 glass coverslip to make the density of QDs on glass low enough to observe isolated QDs under microscope. QDs were excited with a supercontinuum laser (SOLEA, Picoquant) at 530 nm with a repetition of 2.5 MHz. Fluorescence signal was collected by an avalanche photodiodes ( $\tau$ -SPAD, Picoquant) with appropriate bandpass filter. The PL decay was measured by a

single photon counting module (PicoHarp 300, Picoquant) with a time resolution of 32 ps. The PL intensity time traces and time-dependent PL decays were collected at an excitation power of 40 nW. The single-QD emission spectra were collected by a spectrograph (Isoplane SCT 320, Princeton Instruments) equipped with a CCD camera (PIXIS 1024 BR, Princeton Instruments). All measurements were performed under ambient conditions.

## References

1. Cui, J.; Beyler, A. P.; Bischof, T. S.; Wilson, M. W.; Bawendi, M. G., Deconstructing the Photon Stream from Single Nanocrystals: from Binning to Correlation. *Chem. Soc. Rev.* **2014**, *43* (4), 1287-310.
2. Chen, O.; Wei, H.; Maurice, A.; Bawendi, M.; Reiss, P., Pure Colors from Core–Shell Quantum Dots. *MRS Bull.* **2013**, *38* (09), 696-702.
3. Reiss, P.; Protiere, M.; Li, L., Core/Shell Semiconductor Nanocrystals. *Small* **2009**, *5* (2), 154-168.
4. Peng, X. G.; Schlamp, M. C.; Kadavanich, A. V.; Alivisatos, A. P., Epitaxial Growth of Highly Luminescent CdSe/CdS Core/Shell Nanocrystals with Photostability and Electronic Accessibility. *J. Am. Chem. Soc.* **1997**, *119* (30), 7019-7029.
5. Murray, C. B.; Norris, D. J.; Bawendi, M. G., Synthesis and Characterization of Nearly Monodisperse Cde (E = S, Se, Te) Semiconductor Nanocrystallites. *J. Am. Chem. Soc.* **1993**, *115* (19), 8706-8715.
6. Peng, Z. A.; Peng, X. G., Formation of High-Quality CdTe, CdSe, and CdS Nanocrystals Using CdO as Precursor. *J. Am. Chem. Soc.* **2001**, *123* (1), 183-184.
7. Chen, O.; Chen, X.; Yang, Y. A.; Lynch, J.; Wu, H. M.; Zhuang, J. Q.; Cao, Y. C., Synthesis of Metal-Selenide Nanocrystals Using Selenium Dioxide as the Selenium Precursor. *Angew. Chem. Int. Ed.* **2008**, *47* (45), 8638-8641.
8. Chen, O.; Zhao, J.; Chauhan, V. P.; Cui, J.; Wong, C.; Harris, D. K.; Wei, H.; Han, H. S.; Fukumura, D.; Jain, R. K.; Bawendi, M. G., Compact High-Quality CdSe-CdS Core-Shell Nanocrystals with Narrow Emission Linewidths and Suppressed Blinking. *Nat. Mater.* **2013**, *12* (5), 445-451.
9. Maity, P.; Debnath, T.; Ghosh, H. N., Ultrafast Charge Carrier Delocalization in CdSe/CdS Quasi-Type II and CdS/CdSe Inverted Type I Core–Shell: A Structural Analysis through Carrier-Quenching Study. *J. Phys. Chem. C* **2015**, *119* (46), 26202-26211.
10. Li, J. J.; Wang, Y. A.; Guo, W. Z.; Keay, J. C.; Mishima, T. D.; Johnson, M. B.; Peng, X. G., Large-Scale Synthesis of Nearly Monodisperse CdSe/CdS Core/Shell Nanocrystals Using Air-Stable Reagents via Successive Ion Layer Adsorption and Reaction. *J. Am. Chem. Soc.* **2003**, *125* (41), 12567-12575.
11. Li, J. J.; Tsay, J. M.; Michalet, X.; Weiss, S., Wavefunction Engineering: From Quantum Wells to Near-Infrared Type-II Colloidal Quantum Dots Synthesized by Layer-by-Layer Colloidal Epitaxy. *Chem. Phys.* **2005**, *318* (1-2), 82-90.

12. Xie, R. G.; Kolb, U.; Li, J. X.; Basche, T.; Mews, A., Synthesis and Characterization of Highly Luminescent CdSe-Core CdS/Zn<sub>0.5</sub>Cd<sub>0.5</sub>S/ZnS Multishell Nanocrystals. *J. Am. Chem. Soc.* **2005**, *127* (20), 7480-7488.
13. Nemchinov, A.; Kirsanova, M.; Hewa-Kasakarage, N. N.; Zamkov, M., Synthesis and Characterization of Type II ZnSe/CdS Core/Shell Nanocrystals. *J. Phys. Chem. C* **2008**, *112* (25), 9301-9307.
14. Yang, Y. A.; Chen, O.; Angerhofer, A.; Cao, Y. C., Radial-Position-Controlled Doping in CdS/ZnS Core/Shell Nanocrystals. *J. Am. Chem. Soc.* **2006**, *128* (38), 12428-12429.
15. Talapin, D. V.; Koeppel, R.; Gotzinger, S.; Kornowski, A.; Lupton, J. M.; Rogach, A. L.; Benson, O.; Feldmann, J.; Weller, H., Highly Emissive Colloidal CdSe/CdS Heterostructures of Mixed Dimensionality. *Nano Lett.* **2003**, *3* (12), 1677-1681.
16. Talapin, D. V.; Nelson, J. H.; Shevchenko, E. V.; Aloni, S.; Sadtler, B.; Alivisatos, A. P., Seeded Growth of Highly Luminescent CdSe/CdS Nanoheterostructures with Rod and Tetrapod Morphologies. *Nano Lett.* **2007**, *7* (10), 2951-2959.
17. Carbone, L.; Nobile, C.; De Giorgi, M.; Sala, F. D.; Morello, G.; Pompa, P.; Hytch, M.; Snoeck, E.; Fiore, A.; Franchini, I. R.; Nadasan, M.; Silvestre, A. F.; Chiodo, L.; Kudera, S.; Cingolani, R.; Krahn, R.; Manna, L., Synthesis and Micrometer-Scale Assembly of Colloidal CdSe/CdS Nanorods Prepared by a Seeded Growth Approach. *Nano Lett.* **2007**, *7* (10), 2942-2950.
18. Cassette, E.; Mahler, B.; Guigner, J. M.; Patriarche, G.; Dubertret, B.; Pons, T., Colloidal CdSe/CdS Dot-in-Plate Nanocrystals with 2D-Polarized Emission. *ACS Nano* **2012**, *6* (8), 6741-6750.
19. Nirmal, M.; Dabbousi, B. O.; Bawendi, M. G.; Macklin, J. J.; Trautman, J. K.; Harris, T. D.; Brus, L. E., Fluorescence Intermittency in Single Cadmium Selenide Nanocrystals. *Nature* **1996**, *383* (6603), 802-804.
20. Frantsuzov, P.; Kuno, M.; Janko, B.; Marcus, R. A., Universal Emission Intermittency in Quantum Dots, Nanorods and Nanowires. *Nat. Phys.* **2008**, *4* (7), 519-522.
21. Brokmann, X.; Hermier, J. P.; Messin, G.; Desbieres, P.; Bouchaud, J. P.; Dahan, M., Statistical Aging and Nonergodicity in the Fluorescence of Single Nanocrystals. *Phys. Rev. Lett.* **2003**, *90* (12), 120601.
22. Chen, Y.; Vela, J.; Htoon, H.; Casson, J. L.; Werder, D. J.; Bussian, D. A.; Klimov, V. I.; Hollingsworth, J. A., "Giant" Multishell CdSe Nanocrystal Quantum Dots with Suppressed Blinking. *J. Am. Chem. Soc.* **2008**, *130* (15), 5026-5027.
23. Mahler, B.; Spinicelli, P.; Buil, S.; Quelin, X.; Hermier, J. P.; Dubertret, B., Towards Non-Blinking Colloidal Quantum Dots. *Nat. Mater.* **2008**, *7* (8), 659-664.
24. Vela, J.; Htoon, H.; Chen, Y.; Park, Y. S.; Ghosh, Y.; Goodwin, P. M.; Werner, J. H.; Wells, N. P.; Casson, J. L.; Hollingsworth, J. A., Effect of Shell Thickness and Composition on Blinking Suppression and the Blinking Mechanism in 'Giant' CdSe/CdS Nanocrystal Quantum Dots. *J. Biophotonics* **2010**, *3* (10-11), 706-717.
25. Malko, A. V.; Park, Y. S.; Sampat, S.; Galland, C.; Vela, J.; Chen, Y.; Hollingsworth, J. A.;

- Klimov, V. I.; Htoon, H., Pump-Intensity- and Shell-Thickness-Dependent Evolution of Photoluminescence Blinking in Individual Core/Shell CdSe/CdS Nanocrystals. *Nano Lett.* **2011**, *11* (12), 5213-5218.
26. Garcia-Santamaria, F.; Chen, Y.; Vela, J.; Schaller, R. D.; Hollingsworth, J. A.; Klimov, V. I., Suppressed Auger Recombination in "Giant" Nanocrystals Boosts Optical Gain Performance. *Nano Lett.* **2009**, *9* (10), 3482-3488.
27. Ji, B. T.; Giovanelli, E.; Habert, B.; Spinicelli, P.; Nasilowski, M.; Xu, X. Z.; Lequeux, N.; Hugonin, J. P.; Marquier, F.; Greffet, J. J.; Dubertret, B., Non-Blinking Quantum Dot with a Plasmonic Nanoshell Resonator. *Nat. Nanotechnol.* **2015**, *10* (2), 170-175.
28. Htoon, H.; Malko, A. V.; Bussian, D.; Vela, J.; Chen, Y.; Hollingsworth, J. A.; Klimov, V. I., Highly Emissive Multiexcitons in Steady-State Photoluminescence of Individual "Giant" CdSe/CdS Core/Shell Nanocrystals. *Nano Lett.* **2010**, *10* (7), 2401-2407.
29. Park, Y. S.; Malko, A. V.; Vela, J.; Chen, Y.; Ghosh, Y.; Garcia-Santamaria, F.; Hollingsworth, J. A.; Klimov, V. I.; Htoon, H., Near-Unity Quantum Yields of Biexciton Emission from CdSe/CdS Nanocrystals Measured Using Single-Particle Spectroscopy. *Phys. Rev. Lett.* **2011**, *106* (18), 187401.
30. Nasilowski, M.; Spinicelli, P.; Patriarche, G.; Dubertret, B., Gradient CdSe/CdS Quantum Dots with Room Temperature Biexciton Unity Quantum Yield. *Nano Lett.* **2015**, *15* (6), 3953-3958.
31. Brovelli, S.; Bae, W. K.; Galland, C.; Giovanella, U.; Meinardi, F.; Klimov, V. I., Dual-Color Electroluminescence from Dot-in-Bulk Nanocrystals. *Nano Lett.* **2014**, *14* (2), 486-494.
32. Cirloganu, C. M.; Padilha, L. A.; Lin, Q. L.; Makarov, N. S.; Velizhanin, K. A.; Luo, H. M.; Robel, I.; Pietryga, J. M.; Klimov, V. I., Enhanced Carrier Multiplication in Engineered Quasi-Type-II Quantum Dots. *Nat. Commun.* **2014**, *5*, 4148.
33. Meinardi, F.; Colombo, A.; Velizhanin, K. A.; Simonutti, R.; Lorenzon, M.; Beverina, L.; Viswanatha, R.; Klimov, V. I.; Brovelli, S., Large-Area Luminescent Solar Concentrators Based on 'Stokes-Shift-Engineered' Nanocrystals in a Mass-Polymerized PMMA Matrix. *Nat. Photon.* **2014**, *8* (5), 392-399.
34. Coropceanu, I.; Bawendi, M. G., Core/Shell Quantum Dot Based Luminescent Solar Concentrators with Reduced Reabsorption and Enhanced Efficiency. *Nano Lett.* **2014**, *14* (7), 4097-101.
35. Li, H.; Wu, K.; Lim, J.; Song, H.-J.; Klimov, V. I., Doctor-Blade Deposition of Quantum Dots onto Standard Window Glass for Low-Loss Large-Area Luminescent Solar Concentrators. *Nat. Energy* **2016**, *1*, 16157.
36. Bladt, E.; van Dijk-Moes, R. J.; Peters, J.; Montanarella, F.; de Mello Donega, C.; Vanmaekelbergh, D.; Bals, S., Atomic Structure of Wurtzite CdSe (Core)/CdS (Giant Shell) Nanobullets Related to Epitaxy and Growth. *J. Am. Chem. Soc.* **2016**, *138* (43), 14288-14293.
37. Pal, B. N.; Ghosh, Y.; Brovelli, S.; Laocharoensuk, R.; Klimov, V. I.; Hollingsworth, J. A.; Htoon, H., 'Giant' CdSe/CdS Core/Shell Nanocrystal Quantum Dots as Efficient Electroluminescent Materials: Strong Influence of Shell Thickness on Light-Emitting Diode Performance. *Nano Lett.* **2012**, *12* (1), 33133-6.

38. Peng, Z. A.; Peng, X. G., Mechanisms of the Shape Evolution of CdSe Nanocrystals. *J. Am. Chem. Soc.* **2001**, *123* (7), 1389-1395.
39. Zhou, J.; Pu, C.; Jiao, T.; Hou, X.; Peng, X., A Two-Step Synthetic Strategy toward Monodisperse Colloidal CdSe and CdSe/CdS Core/Shell Nanocrystals. *J. Am. Chem. Soc.* **2016**, *138* (20), 6475-6483.
40. Ghosh, S.; Gaspari, R.; Bertoni, G.; Spadaro, M. C.; Prato, M.; Turner, S.; Cavalli, A.; Manna, L.; Brescia, R., Pyramid-Shaped Wurtzite CdSe Nanocrystals with Inverted Polarity. *ACS Nano* **2015**, *9* (8), 8537-46.
41. Cheng, Y.; Wang, Y.; Bao, F.; Chen, D., Shape Control of Monodisperse CdS Nanocrystals: Hexagon and Pyramid. *J. Phys. Chem. B* **2006**, *110* (19), 9448-9451.
42. Gomes, R.; Hassinen, A.; Szczygiel, A.; Zhao, Q. A.; Vantomme, A.; Martins, J. C.; Hens, Z., Binding of Phosphonic Acids to CdSe Quantum Dots: A Solution NMR Study. *J. Phys. Chem. Lett.* **2011**, *2* (3), 145-152.
43. Rempel, J. Y.; Trout, B. L.; Bawendi, M. G.; Jensen, K. F., Density Functional Theory Study of Ligand Binding on CdSe (0001), (0001), and (1120) Single Crystal Relaxed and Reconstructed Surfaces: Implications for Nanocrystalline Growth. *J. Phys. Chem. B* **2006**, *110* (36), 18007-18016.
44. Owen, J. S.; Park, J.; Trudeau, P. E.; Alivisatos, A. P., Reaction Chemistry and Ligand Exchange at Cadmium-Selenide Nanocrystal Surfaces. *J. Am. Chem. Soc.* **2008**, *130* (37), 12279-12281.
45. Tan, R.; Blom, D. A.; Ma, S. G.; Greytak, A. B., Probing Surface Saturation Conditions in Alternating Layer Growth of CdSe/CdS Core/Shell Quantum Dots. *Chem. Mater.* **2013**, *25* (18), 3724-3736.
46. Chen, O.; Yang, Y.; Wang, T.; Wu, H.; Niu, C.; Yang, J.; Cao, Y. C., Surface-Functionalization-Dependent Optical Properties of II-VI Semiconductor Nanocrystals. *J. Am. Chem. Soc.* **2011**, *133* (43), 17504-17512.
47. Wu, N. Q.; Fu, L.; Su, M.; Aslam, M.; Wong, K. C.; Dravid, V. P., Interaction of Fatty Acid Monolayers with Cobalt Nanoparticles. *Nano Lett.* **2004**, *4* (2), 383-386.
48. Cirillo, M.; Aubert, T.; Gomes, R.; Van Deun, R.; Emplit, P.; Biermann, A.; Lange, H.; Thomsen, C.; Brainis, E.; Hens, Z., "Flash" Synthesis of CdSe/CdS Core-Shell Quantum Dots. *Chem. Mater.* **2014**, *26* (2), 1154-1160.
49. Cui, J.; Beyler, A. P.; Marshall, L. F.; Chen, O.; Harris, D. K.; Wanger, D. D.; Brokmann, X.; Bawendi, M. G., Direct Probe of Spectral Inhomogeneity Reveals Synthetic Tunability of Single-Nanocrystal Spectral Linewidths. *Nat. Chem.* **2013**, *5* (7), 602-606.
50. Cui, J.; Beyler, A. P.; Coropceanu, I.; Cleary, L.; Avila, T. R.; Chen, Y.; Cordero, J. M.; Heathcote, S. L.; Harris, D. K.; Chen, O.; Cao, J.; Bawendi, M. G., Evolution of the Single-Nanocrystal Photoluminescence Linewidth with Size and Shell: Implications for Exciton-Phonon Coupling and the Optimization of Spectral Linewidths. *Nano Lett.* **2016**, *16* (1), 289-296.
51. Marshall, L. F.; Cui, J.; Brokmann, X.; Bawendi, M. G., Extracting Spectral Dynamics from Single Chromophores in Solution. *Phys. Rev. Lett.* **2010**, *105* (5), 053005.
52. Chernikov, A.; Bornwasser, V.; Koch, M.; Chatterjee, S.; Böttge, C. N.; Feldtmann, T.; Kira, M.; Koch, S. W.; Wassner, T.; Lautenschläger, S.; Meyer, B. K.; Eickhoff, M., Phonon-Assisted

- Luminescence of Polar Semiconductors: Fröhlich Coupling versus Deformation-Potential Scattering. *Phys. Rev. B* **2012**, *85* (3), 035201.
53. Tessier, M. D.; Mahler, B.; Nadal, B.; Heuclin, H.; Pedetti, S.; Dubertret, B., Spectroscopy of Colloidal Semiconductor Core/Shell Nanoplatelets with High Quantum Yield. *Nano Lett.* **2013**, *13* (7), 3321-3328.
54. Rosenthal, S. J.; McBride, J.; Pennycook, S. J.; Feldman, L. C., Synthesis, Surface Studies, Composition and Structural Characterization of CdSe, Core/Shell, and Biologically Active Nanocrystals. *Surf. Sci. Rep.* **2007**, *62* (4), 111-157.
55. Shim, M.; Guyot-Sionnest, P., Permanent Dipole Moment and Charges in Colloidal Semiconductor Quantum Dots. *J. Chem. Phys.* **1999**, *111* (15), 6955-6964.
56. Rabani, E., Structure and Electrostatic Properties of Passivated CdSe Nanocrystals. *J. Chem. Phys.* **2001**, *115* (3), 1493-1497.
57. Li, L. S.; Alivisatos, A. P., Origin and Scaling of the Permanent Dipole Moment in CdSe Nanorods. *Phys. Rev. Lett.* **2003**, *90* (9), 097402.
58. Kelley, A. M., Electron-Phonon Coupling in CdSe Nanocrystals from an Atomistic Phonon Model. *ACS Nano* **2011**, *5* (6), 5254-5262.
59. Jiang, Z. J.; Kelley, D. F., Surface Charge and Piezoelectric Fields Control Auger Recombination in Semiconductor Nanocrystals. *Nano Lett.* **2011**, *11* (10), 4067-4073.
60. Takagahara, T., Electron-Phonon Interactions and Excitonic Dephasing in Semiconductor Nanocrystals. *Phys. Rev. Lett.* **1993**, *71* (21), 3577-3580.
61. Garcia-Santamaria, F.; Brovelli, S.; Viswanatha, R.; Hollingsworth, J. A.; Htoon, H.; Crooker, S. A.; Klimov, V. I., Breakdown of Volume Scaling in Auger Recombination in CdSe/CdS Heteronanocrystals: The Role of the Core-Shell Interface. *Nano Lett.* **2011**, *11* (2), 687-693.
62. Garcia-Santamaria, F.; Chen, Y. F.; Vela, J.; Schaller, R. D.; Hollingsworth, J. A.; Klimov, V. I., Suppressed Auger Recombination in "Giant" Nanocrystals Boosts Optical Gain Performance. *Nano Lett.* **2009**, *9* (10), 3482-3488.
63. Nair, G.; Zhao, J.; Bawendi, M. G., Biexciton Quantum Yield of Single Semiconductor Nanocrystals from Photon Statistics. *Nano Lett.* **2011**, *11* (3), 1136-1140.
64. Oron, D.; Kazes, M.; Banin, U., Multiexcitons in Type-II Colloidal Semiconductor Quantum Dots. *Phys. Rev. B* **2007**, *75* (3), 035330.
65. Florez, L.; Herrmann, C.; Cramer, J. M.; Hauser, C. P.; Koynov, K.; Landfester, K.; Crespy, D.; Mailander, V., How Shape Influences Uptake: Interactions of Anisotropic Polymer Nanoparticles and Human Mesenchymal Stem Cells. *Small* **2012**, *8* (14), 2222-2230.
66. Chauhan, V. P.; Popovic, Z.; Chen, O.; Cui, J.; Fukumura, D.; Bawendi, M. G.; Jain, R. K., Fluorescent Nanorods and Nanospheres for Real-Time In Vivo Probing of Nanoparticle Shape-Dependent Tumor Penetration. *Angew. Chem. Int. Ed.* **2011**, *50* (48), 11417-11420.
67. Fratila, R. M.; Rivera-Fernandez, S.; de la Fuente, J. M., Shape Matters: Synthesis and Biomedical Applications of High Aspect Ratio Magnetic Nanomaterials. *Nanoscale* **2015**, *7* (18), 8233-8260.



68. Popovic, Z.; Liu, W. H.; Chauhan, V. P.; Lee, J.; Wong, C.; Greytak, A. B.; Insin, N.; Nocera, D. G.; Fukumura, D.; Jain, R. K.; Bawendi, M. G., A Nanoparticle Size Series for In Vivo Fluorescence Imaging. *Angew. Chem. Int. Ed.* **2010**, *49* (46), 8649-8652.
69. Chen, O.; Riedemann, L.; Etoc, F.; Herrmann, H.; Coppey, M.; Barch, M.; Farrar, C. T.; Zhao, J.; Bruns, O. T.; Wei, H.; Guo, P.; Cui, J.; Jensen, R.; Chen, Y.; Harris, D. K.; Cordero, J. M.; Wang, Z. W.; Jasanoff, A.; Fukumura, D.; Reimer, R.; Dahan, M.; Jain, R. K.; Bawendi, M. G., Magneto-Fluorescent Core-Shell Supernanoparticles. *Nat. Commun.* **2014**, *5*, 5093.
70. Wuister, S. F.; Donega, C. D.; Meijerink, A., Influence of Thiol Capping on the Exciton Luminescence and Decay Kinetics of CdTe and CdSe Quantum. *J. Phys. Chem. B* **2004**, *108* (45), 17393-17397.
71. Munro, A. M.; Jen-La Plante, I.; Ng, M. S.; Ginger, D. S., Quantitative Study of the Effects of Surface Ligand Concentration on CdSe Nanocrystal Photoluminescence. *J. Phys. Chem. C* **2007**, *111* (17), 6220-6227.
72. Uyeda, H. T.; Medintz, I. L.; Jaiswal, J. K.; Simon, S. M.; Mattoussi, H., Synthesis of Compact Multidentate Ligands to Prepare Stable Hydrophilic Quantum Dot Fluorophores. *J. Am. Chem. Soc.* **2005**, *127* (11), 3870-3878.
73. Gratton, S. E. A.; Ropp, P. A.; Pohlhaus, P. D.; Luft, J. C.; Madden, V. J.; Napier, M. E.; DeSimone, J. M., The Effect of Particle Design on Cellular Internalization Pathways. *Proc. Natl. Acad. Sci. U.S.A.* **2008**, *105* (33), 11613-11618.
74. Wang, T.; Wang, X.; LaMontagne, D.; Wang, Z.; Wang, Z.; Cao, Y. C., Shape-Controlled Synthesis of Colloidal Superparticles from Nanocubes. *J. Am. Chem. Soc.* **2012**, *134* (44), 18225-18228.
75. Shi, X. H.; von dem Bussche, A.; Hurt, R. H.; Kane, A. B.; Gao, H. J., Cell Entry of One-Dimensional Nanomaterials Occurs by Tip Recognition and rotation. *Nat. Nanotechnol.* **2011**, *6* (11), 714-719.
76. Huang, C. J.; Zhang, Y.; Yuan, H. Y.; Gao, H. J.; Zhang, S. L., Role of Nanoparticle Geometry in Endocytosis: Laying Down to Stand Up. *Nano Lett.* **2013**, *13* (9), 4546-4550.
77. Dahan, M.; Laurence, T.; Pinaud, F.; Chemla, D. S.; Alivisatos, A. P.; Sauer, M.; Weiss, S., Time-Gated Biological Imaging by Use of Colloidal Quantum Dots. *Optics Lett.* **2001**, *26* (11), 825-827.
78. Pinaud, F.; Clarke, S.; Sittner, A.; Dahan, M., Probing Cellular Events, One Quantum Dot at a Time. *Nat. Methods* **2010**, *7* (4), 275-285.

## Chapter 3

# Cu-Catalyzed Synthesis of CdZnSe-CdZnS Alloy QDs with Highly Tunable Emission

Portions of this chapter are adapted and/or reprinted from the following works. Copyright belongs to the publisher.

**Yuan, Y.;** Zhu, H.; Wang, X.; Cui, D.; Gao, Z.; Su, D.; Zhao, J.; Chen, O.\*, Cu-Catalyzed Synthesis of CdZnSe-CdZnS Alloy Quantum Dots with Highly Tunable Emission. *Chem. Mater.* **2019**, *31* (7), 2635-2643.

### 3.1 Limit of Current Synthetic Methods of QDs

Semiconductor QDs exhibit unique properties including high absorbance cross section, broad excitation spectrum, tunable emission profile, high PL QYs and superior photo-chemical/physical stabilities.<sup>1, 2</sup> These properties offer QDs great potential in diverse practical applications including solar energy harvestings,<sup>3-8</sup> biological imaging and labelling,<sup>9-13</sup> light-emitting diodes (LEDs) and next generation displays.<sup>14-23</sup> As a result, synthesizing QDs with uniform size, different shape, high PL QY, and tunable and narrow emission spectrum has been a long-lasting active research topic and largely investigated in the past three decades.<sup>24-49</sup> One of the most profound discoveries towards improving the optical properties of QDs is through epitaxial deposition of shell semiconductor materials, especially with a wider bandgap than that of the core QDs (also known as type-I core-shell QDs).<sup>1, 35, 50</sup> To date, various type-I core-shell QD systems have been synthesized and reported,<sup>35</sup> among which CdSe-ZnS, CdSe-CdS and CdS-ZnS core-shell QDs are arguably the most studied ones with great synthetic control and superior optical performance.<sup>39, 51, 52</sup> However, due to the intrinsic properties of the core and shell materials, those core-shell systems either can only emit photons covering a limited range of the visible spectrum (i.e., CdSe-CdS and CdS-ZnS systems),<sup>39, 52, 53</sup> or possess a large lattice mismatch between core and shell materials (i.e., CdSe-ZnS system) which usually limits the morphological uniformity and optical properties of the obtained core-shell QDs.<sup>51, 54</sup> To this extent, alloying core and/or shell compositions of QDs has later been realized as an efficient mean to enlarge spectral coverage as required in many of their potential applications.<sup>55, 56</sup> In addition, by choosing appropriate alloy compositions, the bandgap alignment and lattice mismatch between core and shell materials can be widely tuned and optimized for desired optical properties.<sup>57-67</sup> To date, a

variety of alloy QD systems has been reported through either simultaneous injection of the required precursors<sup>55, 58, 61, 62, 64</sup> or post-core-synthetic cation exchanges.<sup>56, 63, 65</sup> Especially, it is known that when CdZnSe alloy QDs serving as cores, a wide range of spectral tunability from deep blue to dark red can be achieved by altering the ratio of Cd and Zn compositions.<sup>65, 68</sup> However, unlike CdSeS alloy QDs which are relatively easy to fabricate due to minimal lattice mismatch (3.9%), the synthesis of CdZnSe QDs has proven challenging due to its relatively large crystal lattice mismatch (8.0%) between CdSe and ZnSe materials, and unbalanced reactivities of commonly used Cd and Zn precursors.<sup>55, 56</sup>

### **3.2 Cu-Catalyzed Alloying Method to the Synthesis of Alloy QDs**

In this work, we report a new synthetic paradigm for the fabrication of CdZnSe-CdZnS core-shell alloy QDs through a Cu-catalyzed solid-solution alloying strategy. Taking advantage of the high mobility of Cu cation, we demonstrate that Zn component can be transported into the starting CdSe-CdS core-shell QDs even using a relatively less reactive Zn precursor (i.e., Zn-oleate). We show that the obtained CdZnSe-CdZnS alloy QDs can emit at a wide range of wavelength with the peak center covering nearly full visible spectral region (470–650 nm) while maintaining high PL QYs (> 50%). By monitoring the reaction process, we propose a new alloying mechanism highlighting the unique “catalytic” role Cu cations played in the process. In addition, we demonstrate that the surface defects caused by the remaining Cu cations in the CdZnSe-CdZnS alloy QDs can be effectively removed through a post-synthetic treatment with trioctylphosphine (TOP) based on hard and soft acids and bases (HSAB) theory. Finally, this approach can be easily adapted to the synthesis of CdZnSe-CdZnS alloy nanorods system, suggesting its generality.

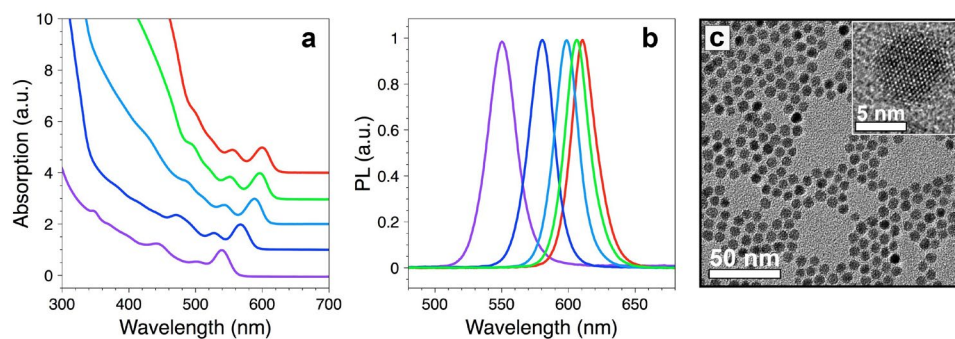


**Fig. 3.1:** Absorption (a) and PL (b) spectral evolution during the synthesis of starting CdSe-CdS core-shell QDs. (c) TEM image of starting CdSe-CdS core-shell QDs, inset: a HR-TEM image of starting QDs.

The starting CdSe-CdS core-shell QDs were synthesized following a previous reported method with minor modification (see Methods and **Fig. 3.1**).<sup>39</sup> For the typical synthesis of alloy QDs (see Methods), 10 mg (~11.5 nmol) CdSe-CdS core-shell QDs, 2.5 mL 1-octadecene (ODE) and 2.5 mL OAm were treated with 0.1 mL 0.5 mM Cu(acac)<sub>2</sub>/OAm (~ 4 Cu per QD) at 240 °C for 20 min, followed by a slow injection of Zn-oleate (0.1 M in ODE) and 1-dodecanethiol (0.1 M in ODE) with a rate of 0.4 mL/hr

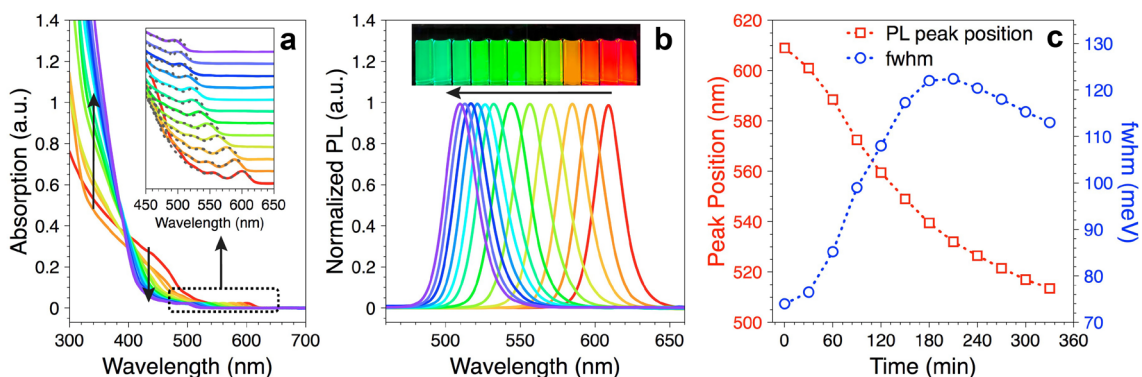


**Fig. 3.2:** (a) Absorption spectral evolution during the synthesis of CdZnSe-CdZnS core-shell alloy QDs. Inset: zoomed-in spectra showing the blueshift of core absorption feature (solid line) and the corresponding photoluminescence excitation (PLE) (dashed line). (b) The PL spectral evolution during the synthesis. Inset: photograph of the aliquots taken during the synthesis under UV light illumination. (c) Peak position (red open square) and full width at the half maximum (FWHM, blue open circle) of the PL profile as a function of reaction time.

at 330 °C, simultaneously. The alloying process was monitored by absorption and PL

spectroscopy measurements. During the process, the first absorption feature (PL peak) continuously blue-shifted from 600 nm to 493 nm (610 nm to 509 nm) (**Fig. 3.2a, b**), indicating an increase of the bandgap of QDs, which was attributed to the incorporation of  $Zn^{2+}$  cation into the CdSe-CdS core-shell QDs. The decrease (increase) of absorbance in the wavelength range of 400-500 nm (below 400 nm) indicated the incorporation of ZnS with a larger bandgap (i.e., 3.91 eV) in the CdSe-CdS QDs. While the PL QY of the QDs remained above 50% (**Table 3.1**), the FWHM of the PL peak increased from ~22 nm (~74 meV) to ~28 nm (~122 meV) and then decreased to ~23 nm (~113 meV) (**Fig. 3.2c**). The initial increase of the PL FWHM was unlikely due to inhomogeneous broadening effect as a high morphological uniformity of the core-shell QDs was

**Table 3.1:** PL QYs of the CdZnSe-CdZnS core-shell alloy QDs before and after TOP treatment.

Time (min)	Original QY (%)	QY after TOP treatment (%)
0	24	63
30	43	61
90	44	68
180	47	57
330	57	61

preserved during the entire alloying process evidenced by both transmission electron microscopy (TEM) and PL excitation measurements (**Fig. 3.2a**, inset and **Fig. 3.3a-f**).<sup>39</sup>,

<sup>69</sup> Accordingly, we attribute this PL broadening effect to the homogeneous broadening caused from Cu-induced defects (e.g., crystal defects, unbalanced charges) inside the particles, as well as enhanced internal electrical field and enlarged dipole moment caused by a spontaneous polarization of the Wurtzite (WZ) crystal structure while developing particle shape anisotropy (discussed below).

To further confirm the alloying process and characterize the final QDs, X-ray

diffraction (XRD) measurements were performed. The QDs unambiguously showed a WZ crystal structure with the fingerprint Bragg diffraction peaks of  $(10\bar{1}2)$  and  $(10\bar{1}3)$ , demonstrating the epitaxial incorporation of ZnS (**Fig. 3.3g**). However, all Bragg peaks red-shifted to higher angles during the growth, indicating a continuous shrinkage of the unit cell lattice (**Table 3.2**), consistent with the smaller WZ lattice parameters ( $a = 3.82 \text{ \AA}$ ,  $c = 6.26 \text{ \AA}$ ) of ZnS. In addition, the  $(0002)$  diffraction peak became narrower during the reaction (**Fig. 3.3h**), indicating the preferential growth along the  $[0002]$  direction.<sup>30-32, 70</sup> The ZnS growth was further confirmed by the increase of particle size from  $7.7 \pm 0.6 \text{ nm}$  for the starting QDs to  $11.9 \pm 0.9 \text{ nm}$  for the final particles determined by the TEM measurements (**Fig. 3.3a-f** and **3.4**). Instead of retaining the spherical shape, the particles became elongated with an AR of  $\sim 1.2$  for the final obtained QDs (**Fig. 3.3f**), in

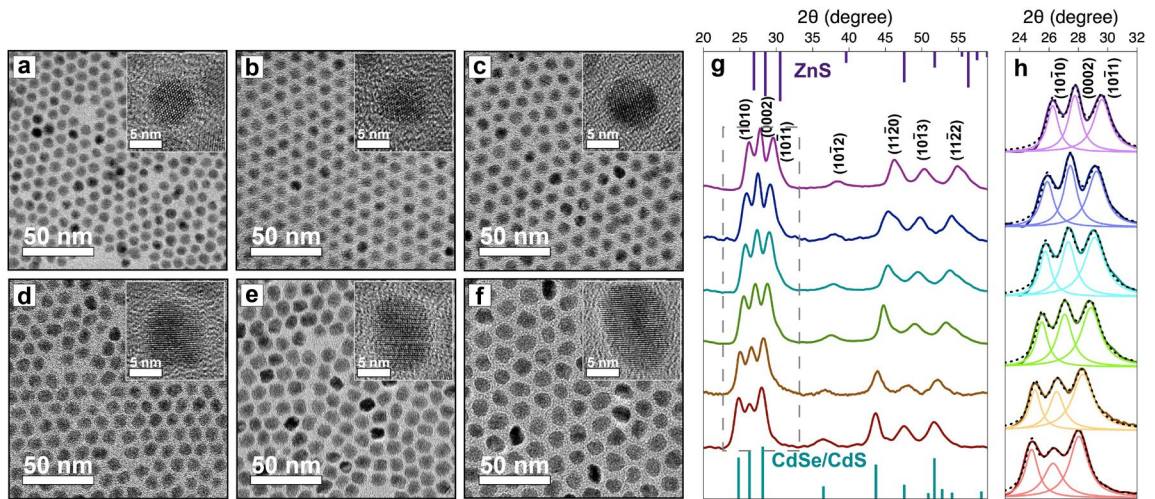


**Fig. 3.3:** TEM images of starting CdSe-CdS core-shell QDs (a) and CdZnSe-CdZnS core-shell alloy QDs (b-f) with different amount of Zn precursor addition (b, 0.02 mmol; c, 0.06 mmol; d, 0.10 mmol; e, 0.12 mmol; f, 0.22 mmol). Insets are high-resolution TEM (HR-TEM) images of these QDs. (g) XRD spectral evolution during the synthesis of CdZnSe-CdZnS alloy QDs. The green and purple sticks show the positions of XRD peaks for the starting CdSe-CdS QDs and bulk WZ-ZnS, respectively. (h) Zoomed-in XRD spectra of the rectangular area in (g) to show  $(10\bar{1}0)$ ,  $(0002)$  and  $(10\bar{1}1)$  peaks with the fitted constituent peaks.

accordance with the favored  $[0002]$  growth direction. To verify the alloy core-shell structure of the QDs, high-angle-annular dark-field scanning TEM (HAADF-STEM) was

employed to map out the atomic distributions of Cd, S, Se, and Zn atoms. The EDX elemental mapping result clearly showed that Cd and S atoms were distributed in the entire QDs, while Se atoms were located at the center of the particles throughout the alloying process, suggesting an intact anionic core-shell framework (**Fig. 3.5, Table 3.3**).<sup>71</sup> Interestingly, unlike traditional core-shell growth, Zn atoms were also distributed in the entire particles and not only at the outer layer as a shell (**Fig. 3.5e**). These results unambiguously led to the conclusion that a Zn alloying process instead of epitaxial shell

**Table 3.2:** Fitting results of the XRD patterns (**Fig. 3.3**) of CdZnSe-CdZnS core-shell alloy QDs. Unit cell parameters are determined by:

$$\frac{1}{d_{hkl}^2} = \frac{4}{3} \frac{h^2 + hk + k^2}{a^2} + \frac{l^2}{c^2}$$

Time (min)	0	30	90	150	180	330	ZnS
2 theta (10 $\bar{1}$ 0) (°)	24.828	25.030	25.538	25.750	25.907	26.250	26.914
d (10 $\bar{1}$ 0) (Å)	3.583	3.555	3.485	3.457	3.436	3.392	3.310
a (10 $\bar{1}$ 0) (Å)	4.138	4.105	4.024	3.992	3.968	3.917	3.822
2 theta (11 $\bar{2}$ 0) (°)	43.624	43.915	44.700	45.309	45.364	46.169	47.561
d (11 $\bar{2}$ 0) (Å)	2.073	2.060	2.026	2.000	1.998	1.965	1.910
a (11 $\bar{2}$ 0) (Å)	4.146	4.120	4.051	4.000	3.995	3.929	3.821
average a (Å)	4.142	4.112	4.038	3.996	3.982	3.923	3.821
% of Zn	0.000	9.202	32.456	45.593	50.019	68.254	100.000
2 theta (0002) (°)	26.303	26.595	27.094	27.359	27.491	27.782	28.500
d (0002) (Å)	3.386	3.349	3.288	3.257	3.242	3.209	3.129
c (0002) (Å)	6.771	6.698	6.577	6.514	6.484	6.417	6.259
% of Zn	0.000	14.252	37.891	50.090	56.078	69.076	100.000
average % of Zn	0.000	11.727	35.173	47.842	53.049	68.665	100.000

growth took place during the reaction. This conclusion was in accordance to the continuous blueshift of both absorption and PL features as shown in **Fig. 3.2a, b**.



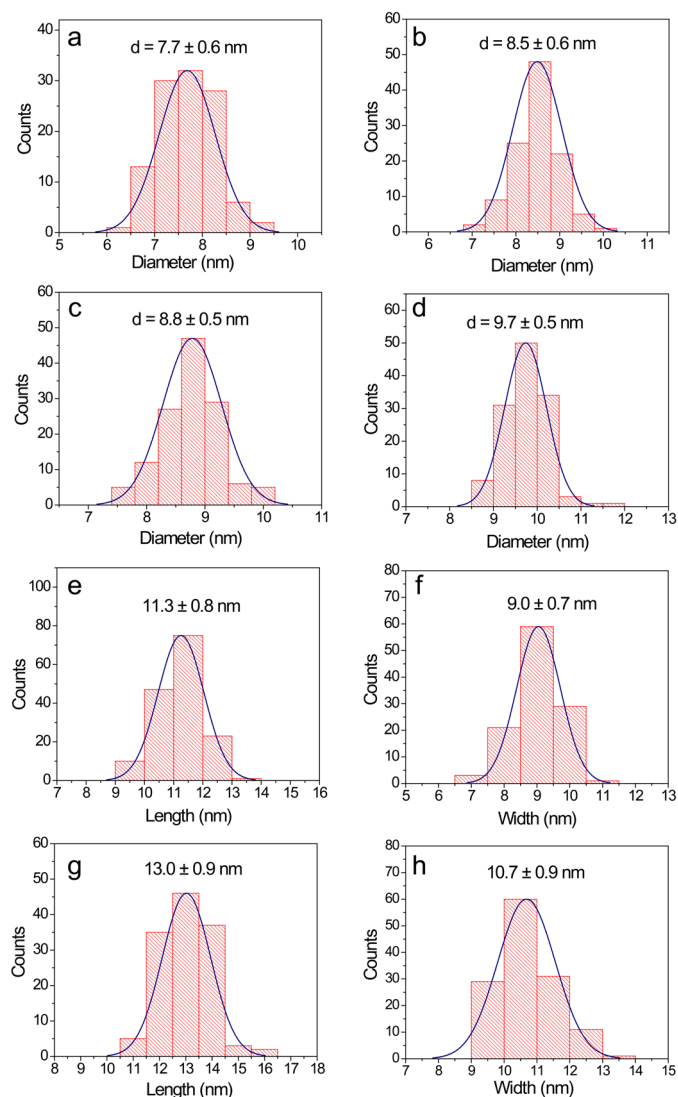


**Fig. 3.4:** Size distribution histograms of CdZnSe-CdZnS core-shell alloy QDs with different amount of Zn precursor addition corresponding to the QDs shown in Fig. 3.3. (a-d) Size distributions for particles shown in Fig. 3.3a-d, respectively. (e-f) Long (e) and short (f) dimension distributions for the particles shown in Fig. 3.3e. (g-h) Long (g) and short (h) dimension distributions for particles in Fig. 3.3f.

Inductively coupled plasma atomic emission spectroscopy (ICP-AES) and EDX were employed to further determine the atomic percentages of Cd and Zn components for the core-shell QDs. As shown in Fig. 3.6a, the atomic percentages of Cd and Zn measured by ICP-AES and EDX showed a high consistency. ICP data showed an increase of Zn percentage from 0% to ~74.3%, and a corresponding decrease of Cd

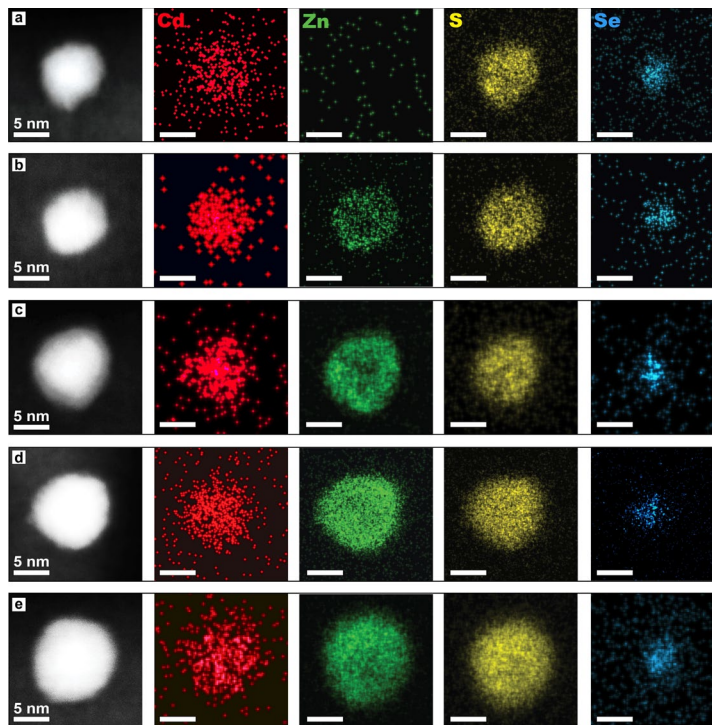


**Fig. 3.5:** High-angle-annular dark-field scanning TEM (HAADF-STEM) images and corresponding elemental mapping images for a CdSe-CdS QD (a), and CdZnSe-CdZnS QDs (b-e) at different reaction time of 30 (0.02 mmol), 90 (0.06 mmol), 180 (0.12 mmol), and 330 (0.22 mol) min after Zn and S precursors injection.

**Table 3.3:** EDX Elemental mapping data for **Fig. 3.5:**

Time (min)		0	30	90	180	330
[Norm. at%]	Cd	51.31	35.28	24.82	18.59	13.29
	Zn	0.00	15.57	26.89	33.43	36.73
	Se	4.00	3.65	2.45	1.95	1.14
	S	44.69	45.50	45.84	46.03	48.84
(Cd+Zn)/(S+Se)		1.05	1.03	1.07	1.08	1.00

percentage from unity to  $\sim 25.7\%$  as reaction progressed (**Fig. 3.6a**). To evaluate if the final particles were homogeneous or gradient alloys, the experimentally determined Cd and Zn atomic percentages were compared with the calculated values from the corresponding XRD patterns (**Table 3.2**) on the basis of Vegard's law.<sup>72</sup> The percentage

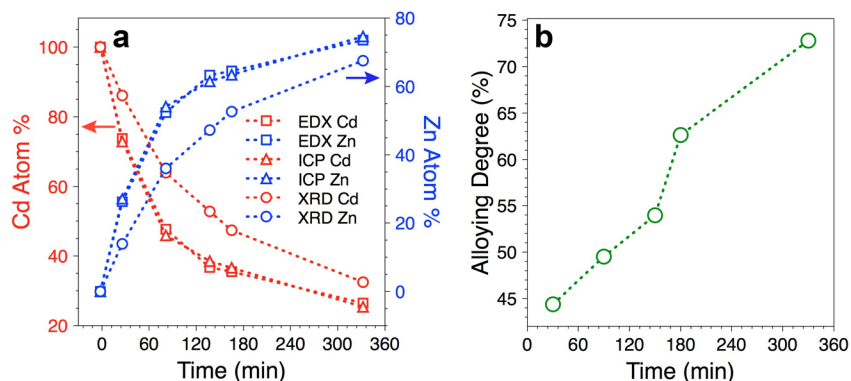


**Fig. 3.6:** (a) Cd (red dotted lines) and Zn (blue dotted lines) atomic percentage evolutions based on EDX (open square), ICP (open triangle), XRD (open circle) analyses. See detailed analysis data in Method. (b) Zn-alloying degree evolution in the CdZnSe-CdZnS alloy QDs as a function of reaction time.

offsets between the calculated and the experimentally-determined values indicated that the core-shell QDs were not a homogenous cationic solid-solution, but a partial gradient alloy of Zn component instead (**Fig. 3.6a**). To quantify the partial alloying level, we express the cation alloying degree ( $A$ ) of CdZnSe-CdZnS QDs as:  $A = (X_{Zn}/X_{Cd})/(Zn/Cd)_{nom}$ , where,  $X_{Zn}$  and  $X_{Cd}$  are the percentages of Zn and Cd atoms calculated based on the XRD data, and  $(Zn/Cd)_{nom}$  is the atomic ratio of Zn and Cd obtained from ICP-AES measurements.<sup>73</sup> Note that the core and core-shell interface effects were ignored due to the relative small volume of the CdSe or CdZnSe cores (less than 5% of the total particle volume). Based on this calculation, the alloying degree of the CdZnSe-CdZnS QDs increased from 44.4% after 30-min injection of Zn and S precursor injection, to 72.8% of the final core-shell QDs. This increase of alloying degree can be ascribed to the high temperature (i.e., 330 °C) and long-time annealing effect during the course of the reaction (**Fig. 3.6b**).<sup>74</sup>

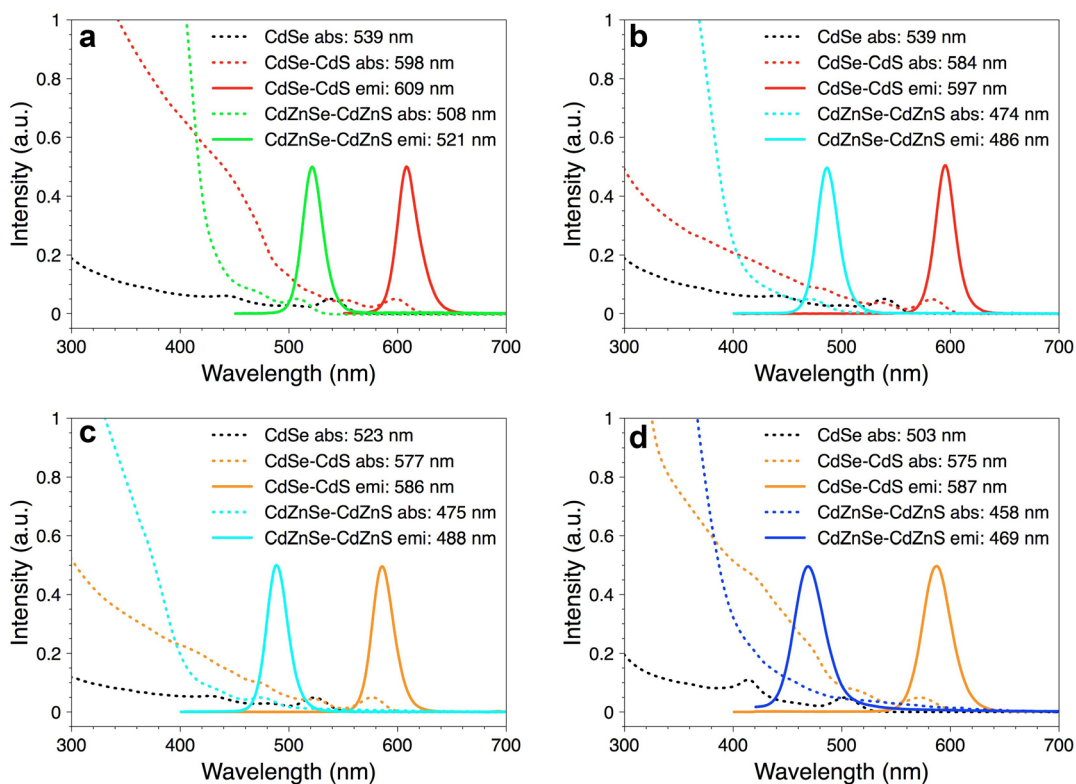


**Fig. 3.7:** The CdZnSe-CdZnS core-shell alloy QDs emitting at different wavelength synthesized from the CdSe-CdS QDs with different CdSe core size and CdS shell thickness.

We then applied this Cu-catalyzed alloying method to the synthesis of alloy QDs starting from the CdSe-CdS QDs with different CdSe core sizes and CdS shell thicknesses. A wide spectral coverage from 470-650 nm (for the center of the PL peaks) with high PL QYs (50-80%) of the obtained CdZnSe-CdZnS core-shell alloy QDs was achieved by tuning the amount of Zn and S precursors (**Fig. 3.7** and **3.8**).

### 3.3 Mechanism Study

It is very interesting that unlike conventional core-shell QD growth,<sup>39, 52</sup> a concurrent alloying process occurred during the addition of Zn and S precursors in our reaction system. The obvious difference as compared to the reaction conditions for conventional core-shell growth was a Cu precursor treatment of the starting core-shell QDs (see Methods). Therefore, it is straightforward to hypothesize that Cu cations play

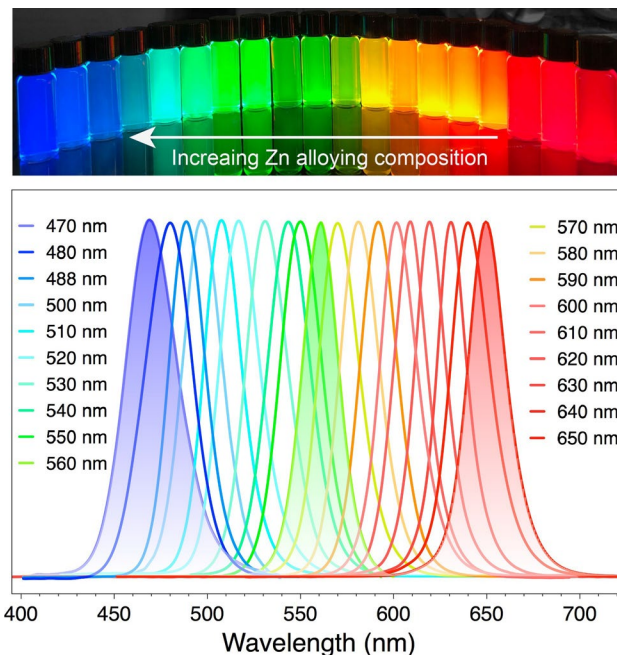


**Fig. 3.8:** Photograph image (top) and PL spectra (bottom) of the CdSe-CdS core-shell QDs and CdZnSe-CdZnS core-shell alloy QDs showing the fully coverage of the visible spectral range from 470 nm to 650 nm.

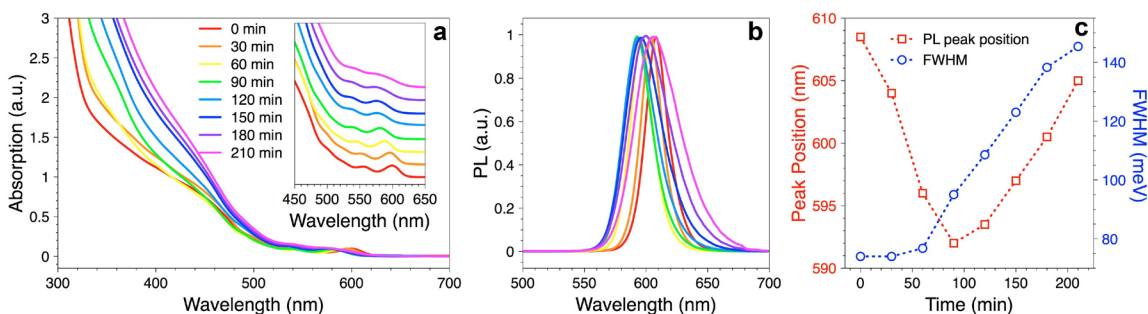


**Fig. 3.9:** Absorption (a) and PL (b) spectral evolution of the control reaction without an addition of Cu source. Inset: zoomed-in absorption spectra. (c) PL peak position (red square) and FWHM (blue circle) evolutions as a function of the reaction time.

the vital role of the observed alloying process. To confirm the necessity of Cu cations in the reaction, a control experiment without adding the Cu precursor was carried out while maintaining other reaction conditions for the growth of ZnS (see details in Methods). No obvious Zn-alloying effect was observed during the reaction as proved by both optical and TEM measurements (**Fig. 3.9** and **3.10**). The emission blue-shifted 18 nm (609 nm to 591 nm) and then red-shifted to 605 nm, while the FWHM kept broadening, indicating



the poor quality of generated QDs (**Fig. 3.9b,c**), which also was confirmed by the TEM images (**Fig. 3.10**).

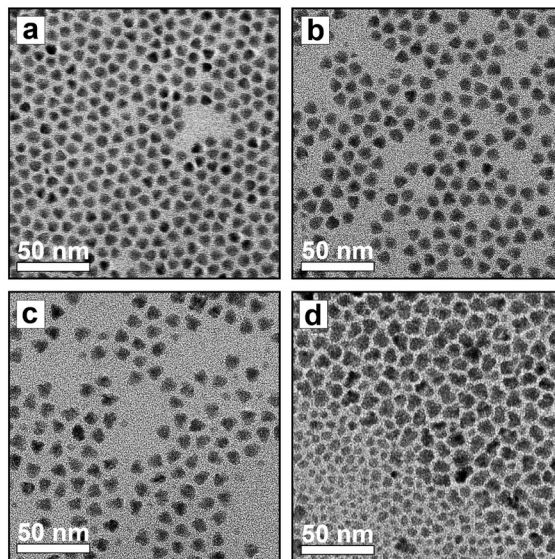


**Fig. 3.10:** (a-d) TEM images of the QDs synthesized in the control experiment without an addition of Cu source at different reaction time of 0, 90 (0.06 mmol), 150 (0.10 mmol), and 210 (0.14 mmol) min after Zn and S precursors injection.

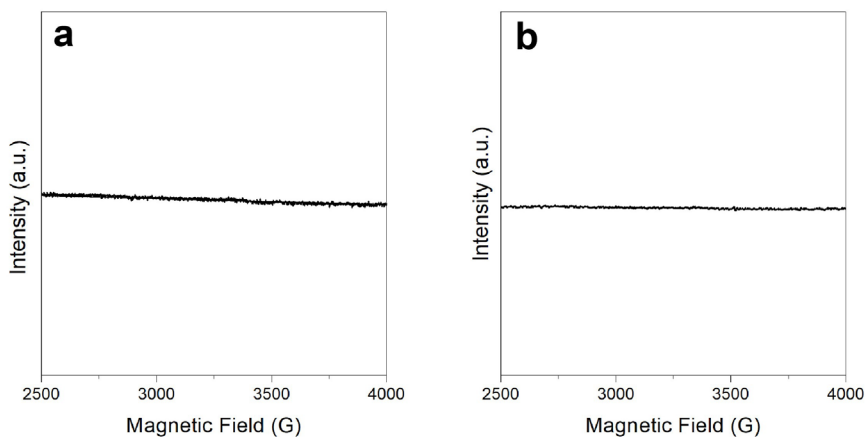


**Fig. 3.11:** The EPR spectra of Cu-doped CdSe-CdS QDs (a) and obtained CdZnSe-CdZnS alloy QDs (b) showing complete silence of signal.

It was remarkable that only about 4 Cu per CdSe-CdS QD in average could make such a difference in achieving the CdZnSe-CdZnS core-shell alloy QDs, which

stimulated us to further investigate the mechanism of this alloying process. First, the sample kept electron paramagnetic resonance (EPR) silent throughout the entire reaction (Fig. 3.11), suggesting that  $\text{Cu}^{2+}$  was quickly reduced to  $\text{Cu}^+$  in the presence of electron-rich solvent and ligand (i.e., ODE and OAm) under the synthetic condition used in this study.<sup>78-80</sup> These  $\text{Cu}^+$  cations can occupy Cd-sites substitutionally in the CdSe-CdS QDs rather to be in interstitial positions.<sup>77</sup> Second, the effective ionic radius of  $\text{Cu}^+$  (77 ppm) is nearly identical to the  $\text{Zn}^{2+}$  (74 ppm) and is  $\sim 20\%$  smaller than the radius of  $\text{Cd}^{2+}$  (95 ppm), suggesting a possible two-step process of Cd-to-Cu followed by Cu-to-Zn exchanges.<sup>81</sup> Last, the diffusion coefficient of  $\text{Cu}^+$  ions in CdS single crystal can be calculated based on the Equation (1):<sup>77</sup>

$$D = 2.1 \times 10^{-3} e^{-(0.96 \text{ eV}/kT)} \text{ cm}^2/\text{s} \quad \text{Equation (1)}$$

Where,  $k$  is Boltzmann constant,  $8.617 \times 10^{-5} \text{ eV/K}$ , and  $T$  is temperature. At the reaction temperature of  $330 \text{ }^\circ\text{C}$ , the diffusion coefficient of Cu ion was calculated to be  $\sim 2,000 \text{ nm}^2/\text{s}$ . The sizes of our QDs are of  $d = 7.7\text{-}11.9 \text{ nm}$ , so the time for  $\text{Cu}^+$  ions diffuse across the entire QDs,  $t = d^2/4D = (7.4\text{-}17.7) \times 10^{-3} \text{ s}$ . This calculated result suggested that  $\text{Cu}^+$  ions can diffuse across the entire QDs in only  $\sim 7$  milliseconds (ms) for the initial CdSe-CdS QDs (a diameter of  $7.7 \text{ nm}$ ) and  $\sim 18 \text{ ms}$  for the final CdZnSe-CdZnS alloy QDs (a diameter of  $11.9 \text{ nm}$ ) under the reaction condition. Meanwhile, When  $T = 25 \text{ }^\circ\text{C} = 298.15 \text{ K}$ ,  $D = 1.2 \times 10^{-19} \text{ cm}^2/\text{s} = 1.2 \times 10^{-5} \text{ nm}^2/\text{s}$ , which is about 8 orders of magnitude smaller at room temperature than at the reaction temperature (i.e.,  $330 \text{ }^\circ\text{C}$ ). Accordingly, the time for  $\text{Cu}^+$  ions diffuse across the entire QDs is 8 orders of magnitude longer at room temperature, which implies the need of the high reaction temperature.<sup>77</sup> All the statements listed above lead us to hypothesize a possible Cu-

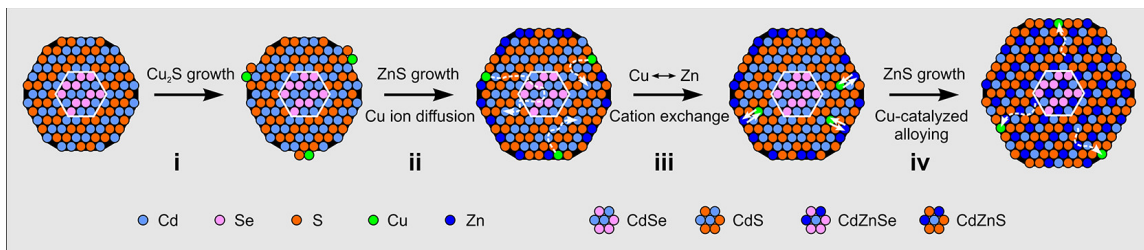


**Fig. 3.12:** Schematic illustration for Cu-induced alloying process during the synthesis of CdZnSe-CdZnS core-shell alloy QDs.

catalyzed solid-solution alloying mechanism for the formation of CdZnSe-CdZnS core-shell alloy QDs (**Fig. 3.12**). In this process, initially, a small amount of  $\text{Cu}_2\text{S}$  can grow on the surface of CdSe-CdS QDs (**Fig. 3.12 i**), followed by the growth of a layer of ZnS (**Fig. 3.12 ii**). Subsequently, Cu ions can diffuse into the particles through Cd-to-Cu cation exchanges (**Fig. 3.12 ii**), followed by the occurrence of Cu-to-Zn cation exchange (**Fig. 3.12 iii**). In this two-step cation exchange process, the Cu ions served as transporting agents to continuously transport Zn ions across the entire core-shell QDs, germinating the alloying process (**Fig. 3.12 iv**). By repeating this process, Zn component can be transferred into the CdS shell and then CdSe core eventually. This core alloying process (from CdSe to CdZnSe) was in line with the fact that the final positions of first absorption feature (493 nm) and PL peak (509 nm) were located at shorter wavelengths than those of the starting CdSe QDs (absorption: 539 nm, and PL at 550 nm). We did not observe any noticeable Cu-impurity emission in the alloy QDs, which was likely due to the minimal amount of Cu addition ( $\sim 4$  Cu per QD),<sup>75,76</sup> and commonly observed “self-purification” mechanism in QD systems owing to their finite particle size, thus the increased formation energy of substitutional impurities.<sup>77</sup> So the Cu ions can “self-purify” and be expelled to the surface of QDs during the cooling process after the reaction.<sup>78</sup> Therefore, overall, Cu ions play as catalysts in this alloying process.



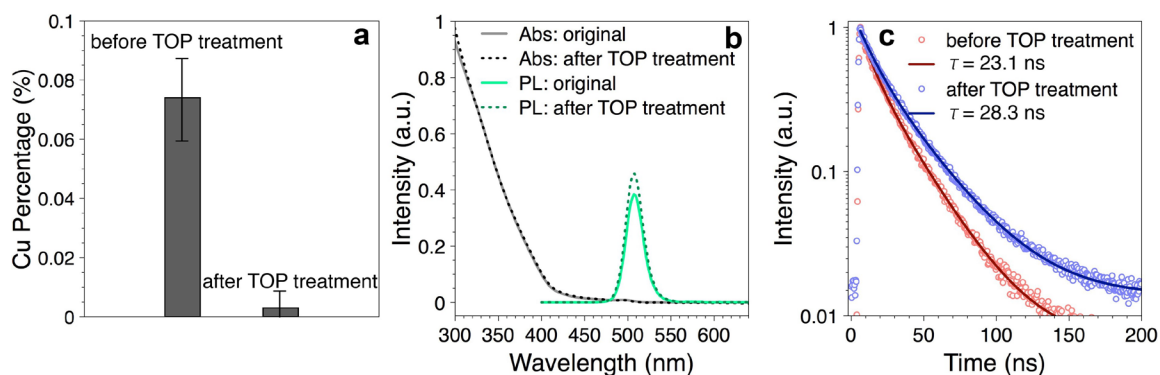


**Fig. 3.13:** (a) Cu amounts determined by ICP-AES in the as-synthesized alloy QDs before and after TOP treatment. (b) Absorption and PL spectra of the CdZnSe-CdZnS QDs before (solid line) and after (dashed line) TOP treatment. (c) Decay curves of PL lifetimes of the CdZnSe-CdZnS alloy QDs before and after TOP treatment.

To prove the existence of Cu atoms in CdZnSe-CdZnS core-shell alloy QDs, ICP-AES measurement was performed to quantify the Cu amount in the final alloy QDs after purification (see details in Methods). The ratio between Cu and Cd accessed from ICP-AES was 0.074%, which approximately equaled to the feeding ratio of 0.090%, suggesting the preservation of Cu in the QDs (**Fig. 3.13a**). As  $\text{Cu}^+$  ion is soft acid (absolute hardness,  $\eta = 6.28$  eV) compared to  $\text{Cd}^{2+}$  ( $\eta = 10.29$  eV) and  $\text{Zn}^{2+}$  ( $\eta = 10.88$  eV) cations,<sup>79</sup> it could be expected that Cu would be removed by employing soft bases, such as TOP ( $\eta \approx 6$  eV),<sup>80, 81</sup> relying on Pearson's HSAB theory.<sup>79, 80, 82</sup> To examine this speculation, the final CdZnSe-CdZnS QDs were treated with TOP at 250 °C for 5 min (see Methods).<sup>37</sup> As expected, the amount of Cu in the CdZnSe-CdZnS alloy QDs after the treatment decreased drastically to nearly background level (**Fig. 3.13a**, **Table 3.4**). This result further supported our hypothesis that Cu ions self-purified to the surface of the QDs.<sup>77</sup> The absorption spectrum of CdZnSe-CdZnS QDs showed nearly no change after TOP treatment, indicating the intact structural integrity of the QDs (**Fig. 3.13b**). While the PL peak position remained the same, its intensity increased by  $\sim 7\%$  (the PL QY increased from 57% to 61%), which can be attributed to the reduced trap states by

removing Cu impurities (**Fig. 3.13b**). This removal of defects was further evidenced by the prolonged PL lifetime of the QDs (from 23.1 ns to 28.3 ns) after the TOP treatment (**Fig. 3.13c and 3.14**).

*Table 3.4: ICP-AES-determined Cd, Zn, and Cu percentages of CdSe-CdS and CdZnSe-CdZnS QDs before and after TOP treatment.*

	Time (min)	Cu atom (%)	Cd atom (%)	Zn atom (%)	Cu atom (% of Cd)
Original	0	0.000	99.919	0.081	0.000
	30	0.055	71.223	28.722	0.077
	90	0.028	46.017	53.955	0.061
	150	0.026	38.156	61.818	0.073
	180	0.019	35.862	64.119	0.050
	330	0.022	25.652	74.326	0.086
After TOP Treatment	0	0.000	99.919	0.081	0.000
	30	0.000	91.460	8.540	0.000
	90	0.000	47.554	52.446	0.000
	150	0.000	40.113	59.887	0.000
	180	0.000	37.994	62.006	0.000
	330	0.005	28.078	71.922	0.018

### 3.4 Cu-catalyzed alloying method to the synthesis of alloy NRs

To further explore the generality of the Cu-induced alloy synthesis, CdSe-CdS core-shell NRs were also examined.<sup>32</sup> A sample of CdSe-CdS NRs with an AR of 9.4 and emitting at 602 nm was successfully converted to CdZnSe-CdZnS alloy NRs with a reduced AR of 6.2 and blue-shifted PL peak centered at 534 nm (**Fig. 3.15a**). Correspondingly, absorption features of NRs blue-shifted to shorter wavelength region, accompanied by the decrease of absorption for CdS and increase of absorption for ZnS

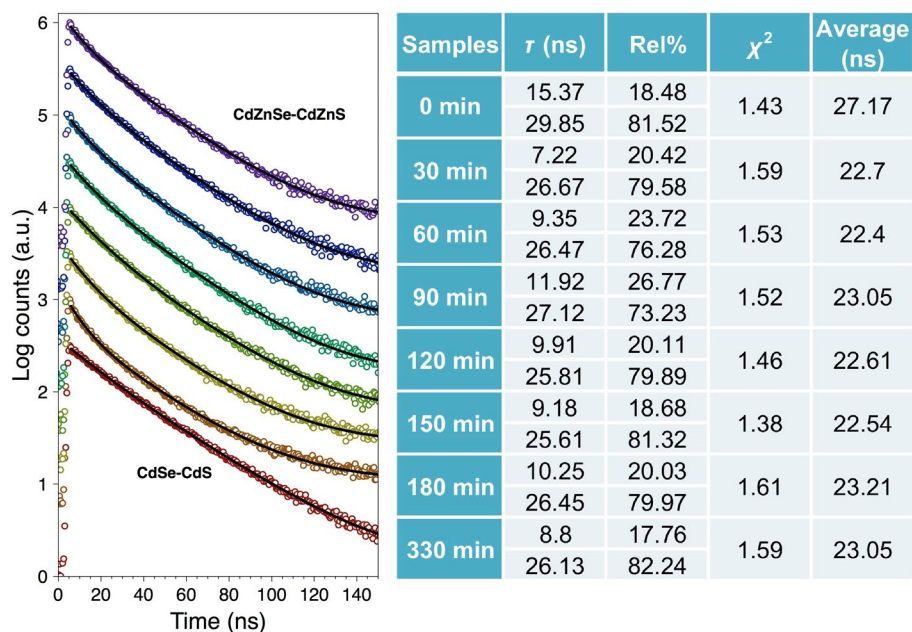


**Fig. 3.14:** PL lifetime evolution of CdZnSe-CdZnS QDs at different reaction time.

(**Fig. 3.15a, b**). TEM and XRD measurements indicated the preservation of shape, uniformity, and WZ crystal structure of the NRs (**Fig. 3.15c-g**). HR-STEM images showed cross-fringes of  $(10\bar{1}0)$  and  $(0002)$  planes with  $d$ -spacings of 3.4 Å and 3.2 Å, respectively (**Fig. 3.15f**). The slightly smaller lattices were caused by Zn alloying into the CdSe-CdS NRs, in good agreement with the XRD data showing red-shifted Bragg diffraction peaks (**Fig. 3.15g**). Additionally, the formation of CdZnSe-CdZnS alloy NRs was confirmed indisputably by STEM-electron energy-loss spectroscopy (EELS) elemental mapping results, showing that Zn atoms were fully distributed in the entire NRs (**Fig. 3.15h**). Time-resolved PL measurements showed that the average PL lifetime increased from 18.7 ns for CdSe-CdS NRs to 30.2 ns for CdZnSe-CdZnS alloy NRs, in line with the increased average volume of single NRs from  $\sim 3,900 \text{ nm}^3$  to  $\sim 6,700 \text{ nm}^3$  (**Fig. 3.15i**). The successful employment of CdSe-CdS NRs suggested that this Cu-induced alloying process is independent of the shape of the starting QDs.

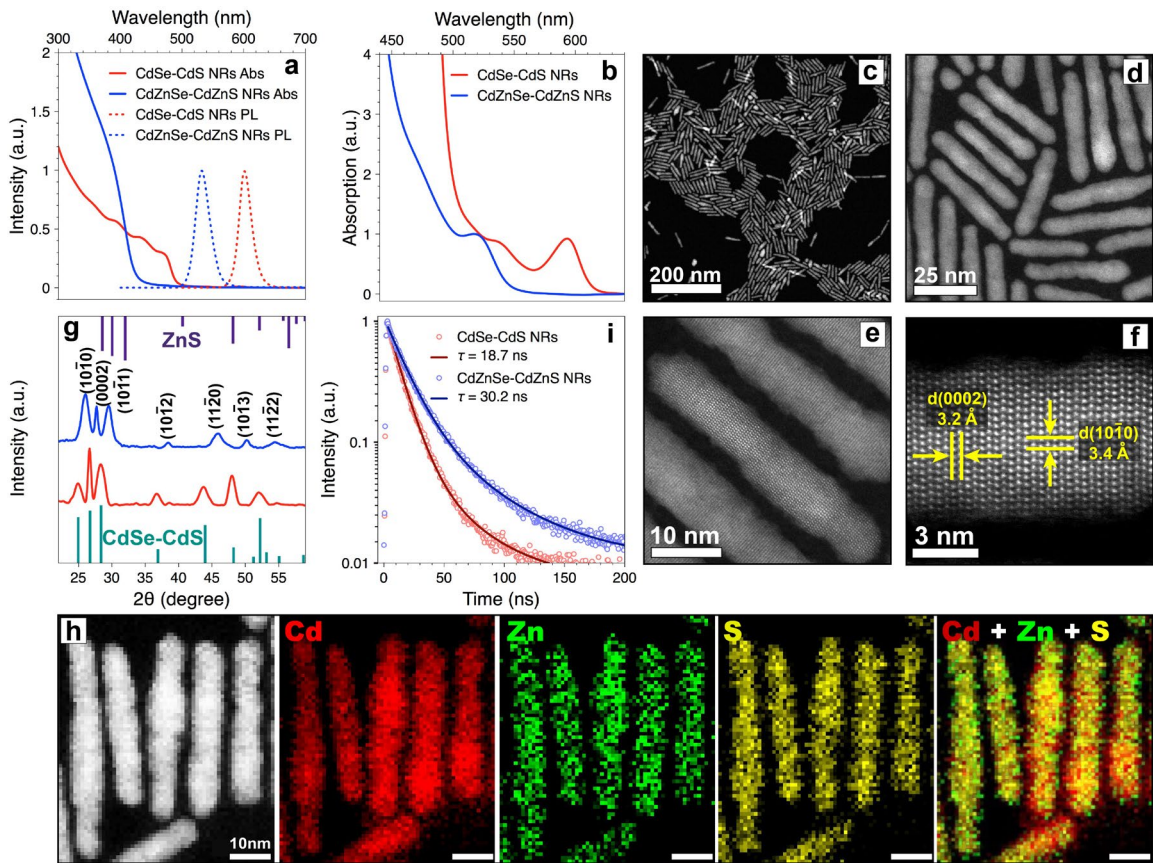


**Fig. 3.15:** (a) Absorption (solid lines) and PL (dashed lines) spectra of the starting CdSe-CdS nanorods (NRs, red) and CdZnSe-CdZnS alloy NRs (blue). (b) Zoomed-in spectrum to show the first absorption peak shift comparing the CdSe-CdS NRs to the CdZnSe-CdZnS alloy NRs. (c-f) HAADF-STEM images of the final CdZnSe-CdZnS alloy NRs at different magnifications. (g) XRD spectra of CdSe-CdS NRs and CdZnSe-CdZnS alloy NRs. The green and purple sticks show the positions of XRD peaks for starting CdSe-CdS NRs and bulk WZ-ZnS, respectively. (h) HAADF-STEM image and the corresponding STEM-EELS elemental mappings for Cd, Zn and S atoms. (i) Decay curves of PL lifetimes of CdSe-CdS NRs and CdZnSe-CdZnS NRs.

In conclusion, we demonstrate a new way of fabricating CdZnSe-CdZnS core-shell alloy QDs by using Cu cations as transporting catalysts to effectively transfer Zn component into CdSe-CdS core-shell QDs. The morphological uniformity, core-shell structure, and crystal phase can be well-preserved from the starting CdSe-CdS QDs during the synthesis. By employing this methodology, high-quality core-shell alloy QDs with high PL QYs and narrow emission profiles covering nearly the full range of visible spectrum have been synthesized. The mechanistic investigation attributes the alloying

process to highly diffusive Cu ions acting as alloying catalysts to transfer Zn component across the whole CdSe-CdS QDs. Moreover, we show that the remaining surface Cu can be removed with TOP treatment based on the HSAB theory, affording QDs with less surface defects, thus higher QYs. Finally, we demonstrate this approach can be easily adapted to the synthesis of CdZnSe-CdZnS NRs, suggesting a generality of this alloying process. Our study sheds light on a new synthetic paradigm of generating various alloy nanocrystals with desired properties through Cu-catalyzed ion diffusion and solid-solution alloying processes.

## Methods

\* (for synthesis of CdSe core QDs, CdSe-CdS core-shell QDs see Ch. 2)

\* (for UV-Vis absorption measurements, PL, lifetime and QY measurements, TEM measurements, and XRD measurements, see Ch.2)

### *Chemicals:*

Cadmium oxide (CdO, 99.998%), 1-octadecene (ODE, 90%), trioctylphosphine oxide (TOPO 99%), trioctylphosphine (TOP, 97%), oleylamine (OAm, 70%), 1-octanethiol (> 98.5%), 1-dodecanethiol (> 98%), and Cu(acac)<sub>2</sub> (> 99.9%) were obtained from Sigma Aldrich. Selenium powder (99.999%), oleic acid (OLA, 90%) were purchased from Alfa Aesar. N-octadecylphosphonic acid (ODPA, > 99%) and n-hexylphosphonic acid (HPA, > 99%) were purchased from PCI Synthesis.

### *Synthesis of CdSe-CdS core-shell NRs:*

CdSe-CdS NRs were prepared following previous published seeded growth approach with minor modification.<sup>32</sup> Typically, CdO (91 mg) was mixed in a flask together with TOPO (3 g), ODPA (290 mg), and HPA (80 mg). After pumping under vacuum for about 1 hour at 150 °C, the resulting solution was heated to 350 °C under

nitrogen, followed by injection of 1.5 g of TOP. After which the temperature could recover to 350 °C, then a solution of 200 nmol CdSe/120 mg S/1.5 mL TOP was quickly injected into the flask. The NRs were allowed to grow for 8 minutes after the injection (see Table 1 and Table 2), after which the heating mantle was removed. Purification of CdSe-CdS NRs is same as for CdSe-CdS QDs as mentioned above.

*Synthesis of CdZnSe-CdZnS alloy QDs and NRs:*

In a typical synthesis of CdZnSe-CdZnS alloy QDs, 10 mg of CdSe-CdS QDs (~11.5 nmol for a diameter of 7.7 nm) were loaded into a 50 mL 3-neck flask with a solvent mixture of 2.5 mL ODE and 2.5 mL OAm. The reaction mixture was degassed under vacuum at room temperature for 1 hour and 120 °C for 10 min to remove hexane, water and oxygen. The reaction mixture was then heated to 240 °C under nitrogen, followed by injection of 0.1 mL 0.5 mM Cu(acac)<sub>2</sub>/OAm dropwise. The reaction mixture was maintained at the same temperature for 20 min. Then Zn-oleate (0.1 M in ODE) and 1-dodecanethiol (0.1 M in ODE) were injected dropwise with a rate of 0.4 mL/hr into the reaction mixture simultaneously using a syringe pump. At the same time, the temperature was increased to 330 °C. It was started to count time zero at the starting point of injection of Zn and S precursors. 0.2 mL of OLA was injected to the reaction mixture every 15 min starting from 30 min. Aliquots were taken during the reaction for absorption and PL characterizations. The reaction was stopped by removing the heating mantle and cooling down to room temperature after finishing the injection. The synthesized CdZnSe-CdZnS core-shell alloy QDs were purified by three rounds of precipitation and redispersion using acetone/methanol and hexane. The particles were finally suspended in ~4 mL hexane as stock. CdZnSe-CdZnS NRs were prepared using the same conditions starting from CdSe-CdS NRs.

*TOP treatment:*

Cu residual in synthesized CdZnSe-CdZnS QDs was removed by treatment with TOP as a soft base.<sup>37</sup> Typically, CdZnSe-CdZnS alloy QDs in hexanes were dispersed in 5 mL of TOP in a 25 mL three-neck flask, then the resulting mixture was degassed at room temperature for 1 hr and at 80 °C for 20 min. Then the solution was increased to 240 °C under N<sub>2</sub> and maintained for 5 min at this temperature. After cooling down, the alloy particles were purified used the same purification methods as mentioned above.

*Control experiment without the addition of Cu precursor:*

Control experiments were done at the same conditions for synthesis of CdZnSe-CdZnS except without the addition of Cu(acac)<sub>2</sub> precursor.

*ICP–AES measurements:*

For ICP–AES analysis, the dried QDs were digested in warm nitric acid (~70 °C, overnight) to ensure their complete dissolution into the acid. The solution was then diluted with 2% HNO<sub>3</sub> solution. The measurements were carried out on a Thermo Scientific iCAP 7400 DUO ICP–AES equipped with a Teledyne ASX-560 240 position autosampler.

*EPR measurement:*

EPR spectrum was measured using a Bruker EMX Premium-X EPR spectrometer. Measurements were taken at room temperature with a 9.86 GHz microwave frequency and a power of 2 mW. Sample was dissolved in hexanes for the measurement.

*Cu diffusion rate calculation:*

The diffusion coefficient was obtained in the previous paper studying on Cu diffusion in bulk CdS single crystals.<sup>74</sup> The equation of Cu diffusion coefficient is:

$$D = 2.1 \times 10^{-3} e^{-(0.96 \text{ eV}/kT)} \text{ cm}^2/\text{s}$$

In which,  $k = 8.617 \times 10^{-5} \text{ eV/K}$ . When  $T = 330 \text{ }^\circ\text{C} = 603.15 \text{ K}$ ,  $D = 2.0 \times 10^{-11} \text{ cm}^2/\text{s} = 2.0 \times 10^3 \text{ nm}^2/\text{s}$ .

The sizes of our QDs are of  $d = 7.7\text{-}11.9 \text{ nm}$ , so  $t = d^2/4D = (7.4\text{-}17.7) \times 10^{-3} \text{ s}$ .  
When  $T = 25 \text{ }^\circ\text{C} = 298.15 \text{ K}$ ,  $D = 1.2 \times 10^{-19} \text{ cm}^2/\text{s} = 1.2 \times 10^{-5} \text{ nm}^2/\text{s}$ ,  $t = d^2/4D = (1.2\text{-}3.0) \times 10^6 \text{ s}$ .

## References

1. Chen, O.; Wei, H.; Maurice, A.; Bawendi, M.; Reiss, P., Pure Colors from Core–Shell Quantum Dots. *MRS Bull.* **2013**, *38* (9), 696-702.
2. Kovalenko, M. V.; Manna, L.; Cabot, A.; Hens, Z.; Talapin, D. V.; Kagan, C. R.; Klimov, V. I.; Rogach, A. L.; Reiss, P.; Milliron, D. J.; Guyot-Sionnest, P.; Konstantatos, G.; Parak, W. J.; Hyeon, T.; Korgel, B. A.; Murray, C. B.; Heiss, W., Prospects of Nanoscience with Nanocrystals. *ACS Nano* **2015**, *9* (2), 1012-1057.
3. Nozik, A. J., Quantum Dot Solar Cells. *Phys. E* **2002**, *14* (1), 115-120.
4. Kamat, P. V., Quantum Dot Solar Cells. Semiconductor Nanocrystals as Light Harvesters. *J. Phys. Chem. C* **2008**, *112* (48), 18737-18753.
5. Lee, H.; Wang, M.; Chen, P.; Gamelin, D. R.; Zakeeruddin, S. M.; Grätzel, M.; Nazeeruddin, M. K., Efficient CdSe Quantum Dot-Sensitized Solar Cells Prepared by an Improved Successive Ionic Layer Adsorption and Reaction Process. *Nano Lett.* **2009**, *9* (12), 4221-4227.
6. Lee, Y.-L.; Lo, Y.-S., Highly Efficient Quantum-Dot-Sensitized Solar Cell Based on Co-Sensitization of CdS/CdSe. *Adv. Funct. Mater.* **2009**, *19* (4), 604-609.
7. Chuang, C.-H. M.; Brown, P. R.; Bulović, V.; Bawendi, M. G., Improved Performance and Stability in Quantum Dot Solar Cells through Band Alignment Engineering. *Nat. Mater.* **2014**, *13* (8), 796-801.
8. Carey, G. H.; Abdelhady, A. L.; Ning, Z.; Thon, S. M.; Bakr, O. M.; Sargent, E. H., Colloidal Quantum Dot Solar Cells. *Chem. Rev.* **2015**, *115* (23), 12732-12763.
9. Dahan, M.; Laurence, T.; Pinaud, F.; Chemla, D. S.; Alivisatos, A. P.; Sauer, M.; Weiss, S., Time-Gated Biological Imaging by Use of Colloidal Quantum Dots. *Opt. Lett.* **2001**, *26* (11), 825-827.
10. Han, M.; Gao, X.; Su, J. Z.; Nie, S., Quantum-Dot-Tagged Microbeads for Multiplexed Optical Coding of Biomolecules. *Nat. Biotechnol.* **2001**, *19*, 631-635.
11. Medintz, I. L.; Uyeda, H. T.; Goldman, E. R.; Mattoussi, H., Quantum Dot Bioconjugates for Imaging, Labelling and Sensing. *Nat. Mater.* **2005**, *4*, 435-446.
12. Franke, D.; Harris, D. K.; Chen, O.; Bruns, O. T.; Carr, J. A.; Wilson, M. W. B.; Bawendi, M. G., Continuous Injection Synthesis of Indium Arsenide Quantum Dots Emissive in the Short-Wavelength Infrared. *Nat. Commun.* **2016**, *7*, 12749.



13. Panthani, M. G.; Khan, T. A.; Reid, D. K.; Hellebusch, D. J.; Rasch, M. R.; Maynard, J. A.; Korgel, B. A., In Vivo Whole Animal Fluorescence Imaging of a Microparticle-Based Oral Vaccine Containing (CuInSe<sub>x</sub>S<sub>2-x</sub>)/ZnS Core/Shell Quantum Dots. *Nano Lett.* **2013**, *13* (9), 4294-4298.
14. Colvin, V. L.; Schlamp, M. C.; Alivisatos, A. P., Light-Emitting Diodes Made from Cadmium Selenide Nanocrystals and a Semiconducting Polymer. *Nature* **1994**, *370*, 354-357.
15. Liu, W.; Howarth, M.; Greytak, A. B.; Zheng, Y.; Nocera, D. G.; Ting, A. Y.; Bawendi, M. G., Compact Biocompatible Quantum Dots Functionalized for Cellular Imaging. *J. Am. Chem. Soc.* **2008**, *130* (4), 1274-1284.
16. Pimputkar, S.; Speck, J. S.; DenBaars, S. P.; Nakamura, S., Prospects for LED Lighting. *Nat. Photon.* **2009**, *3*, 180-182.
17. Jang, E.; Jun, S.; Jang, H.; Lim, J.; Kim, B.; Kim, Y., White-Light-Emitting Diodes with Quantum Dot Color Converters for Display Backlights. *Adv. Mater.* **2010**, *22* (28), 3076-3080.
18. Shirasaki, Y.; Supran, G. J.; Bawendi, M. G.; Bulović, V., Emergence of Colloidal Quantum-Dot Light-Emitting Technologies. *Nat. Photon.* **2012**, *7*, 13-23.
19. Bae, W. K.; Park, Y.-S.; Lim, J.; Lee, D.; Padilha, L. A.; McDaniel, H.; Robel, I.; Lee, C.; Pietryga, J. M.; Klimov, V. I., Controlling the Influence of Auger Recombination on the Performance of Quantum-Dot Light-Emitting Diodes. *Nat. Commun.* **2013**, *4*, 2661.
20. Mashford, B. S.; Stevenson, M.; Popovic, Z.; Hamilton, C.; Zhou, Z.; Breen, C.; Steckel, J.; Bulovic, V.; Bawendi, M.; Coe-Sullivan, S.; Kazlas, P. T., High-Efficiency Quantum-Dot Light-Emitting Devices with Enhanced Charge Injection. *Nat. Photon.* **2013**, *7*, 407-412.
21. Yang, Y.; Zheng, Y.; Cao, W.; Titov, A.; Hyvonen, J.; Manders, J. R.; Xue, J.; Holloway, P. H.; Qian, L., High-Efficiency Light-Emitting Devices Based on Quantum Dots with Tailored Nanostructures. *Nat. Photon.* **2015**, *9* (4), nphoton. 2015.36.
22. Li, X.; Zhao, Y.-B.; Fan, F.; Levina, L.; Liu, M.; Quintero-Bermudez, R.; Gong, X.; Quan, L. N.; Fan, J.; Yang, Z.; Hoogland, S.; Voznyy, O.; Lu, Z.-H.; Sargent, E. H., Bright Colloidal Quantum Dot Light-Emitting Diodes Enabled by Efficient Chlorination. *Nat. Photon.* **2018**, *12* (3), 159-164.
23. Pinaud, F.; Clarke, S.; Sittner, A.; Dahan, M., Probing Cellular Events, One Quantum Dot at a Time. *Nat. Methods* **2010**, *7*, 275-285.
24. Nagaoka, Y.; Zhu, H.; Eggert, D.; Chen, O., Single-component quasicrystalline nanocrystal superlattices through flexible polygon tiling rule. *Science* **2018**, *362* (6421), 1396-1400.
25. Nagaoka, Y.; Tan, R.; Li, R.; Zhu, H.; Eggert, D.; Wu, Y. A.; Liu, Y.; Wang, Z.; Chen, O., Superstructures Generated from Truncated Tetrahedral Quantum Dots. *Nature* **2018**, *561* (7723), 378-382.
26. Murray, C.; Norris, D. J.; Bawendi, M. G., Synthesis and Characterization of Nearly Monodisperse CdE (E= Sulfur, Selenium, Tellurium) Semiconductor Nanocrystallites. *J. Am. Chem. Soc.* **1993**, *115* (19), 8706-8715.
27. Alivisatos, A. P., Semiconductor Clusters, Nanocrystals, and Quantum Dots. *Science* **1996**, *271* (5251), 933-937.
28. Peng, X.; Manna, L.; Yang, W.; Wickham, J.; Scher, E.; Kadavanich, A.; Alivisatos, A. P., Shape

- Control of CdSe Nanocrystals. *Nature* **2000**, *404* (6773), 59-61.
29. Buhro, W. E.; Colvin, V. L., Shape Matters. *Nat. Mater.* **2003**, *2*, 138-139.
30. Talapin, D. V.; Koeppel, R.; Götzinger, S.; Kornowski, A.; Lupton, J. M.; Rogach, A. L.; Benson, O.; Feldmann, J.; Weller, H., Highly Emissive Colloidal CdSe/CdS Heterostructures of Mixed Dimensionality. *Nano Lett.* **2003**, *3* (12), 1677-1681.
31. Talapin, D. V.; Nelson, J. H.; Shevchenko, E. V.; Aloni, S.; Sadtler, B.; Alivisatos, A. P., Seeded Growth of Highly Luminescent CdSe/CdS Nanoheterostructures with Rod and Tetrapod Morphologies. *Nano Lett.* **2007**, *7* (10), 2951-2959.
32. Carbone, L.; Nobile, C.; De Giorgi, M.; Sala, F. D.; Morello, G.; Pompa, P.; Hytch, M.; Snoeck, E.; Fiore, A.; Franchini, I. R.; Nadasan, M.; Silvestre, A. F.; Chiodo, L.; Kudera, S.; Cingolani, R.; Krahn, R.; Manna, L., Synthesis and Micrometer-Scale Assembly of Colloidal CdSe/CdS Nanorods Prepared by a Seeded Growth Approach. *Nano Lett.* **2007**, *7* (10), 2942-2950.
33. Zhong, H. Z.; Zhou, Y.; Ye, M. F.; He, Y. J.; Ye, J. P.; He, C.; Yang, C. H.; Li, Y. F., Controlled Synthesis and Optical Properties of Colloidal Ternary Chalcogenide CuInS<sub>2</sub> Nanocrystals. *Chem. Mater.* **2008**, *20* (20), 6434-6443.
34. Chen, Y.; Vela, J.; Htoon, H.; Casson, J. L.; Werder, D. J.; Bussian, D. A.; Klimov, V. I.; Hollingsworth, J. A., "Giant" Multishell CdSe Nanocrystal Quantum Dots with Suppressed Blinking. *J. Am. Chem. Soc.* **2008**, *130* (15), 5026-5027.
35. Reiss, P.; Protière, M.; Li, L., Core/Shell Semiconductor Nanocrystals. *Small* **2009**, *5* (2), 154-168.
36. Cassette, E.; Mahler, B.; Guigner, J.-M.; Patriarche, G.; Dubertret, B.; Pons, T., Colloidal CdSe/CdS Dot-in-Plate Nanocrystals with 2D-Polarized Emission. *ACS Nano* **2012**, *6* (8), 6741-6750.
37. Li, H.; Brescia, R.; Krahn, R.; Bertoni, G.; Alcocer, M. J. P.; D'Andrea, C.; Scotognella, F.; Tassone, F.; Zanella, M.; De Giorgi, M.; Manna, L., Blue-UV-Emitting ZnSe(Dot)/ZnS(Rod) Core/Shell Nanocrystals Prepared from CdSe/CdS Nanocrystals by Sequential Cation Exchange. *ACS Nano* **2012**, *6* (2), 1637-1647.
38. Morris-Cohen, A. J.; Malicki, M.; Peterson, M. D.; Slavin, J. W. J.; Weiss, E. A., Chemical, Structural, and Quantitative Analysis of the Ligand Shells of Colloidal Quantum Dots. *Chem. Mater.* **2013**, *25* (8), 1155-1165.
39. Chen, O.; Zhao, J.; Chauhan, V. P.; Cui, J.; Wong, C.; Harris, D. K.; Wei, H.; Han, H.-S.; Fukumura, D.; Jain, R. K.; Bawendi, M. G., Compact High-Quality CdSe-CdS Core-Shell Nanocrystals with Narrow Emission Linewidths and Suppressed Blinking. *Nat. Mater.* **2013**, *12*, 445.
40. Xie, R.; Zhou, M., Zinc Chalcogenide Seed-Mediated Synthesis of CdSe Nanocrystals: Nails, Chesses and Tetrahedrons. *Chem. Mater.* **2015**, *27* (8), 3055-3064.
41. Bladt, E.; van Dijk-Moes, R. J. A.; Peters, J.; Montanarella, F.; de Mello Donega, C.; Vanmaekelbergh, D.; Bals, S., Atomic Structure of Wurtzite CdSe (Core)/CdS (Giant Shell) Nanobullets Related to Epitaxy and Growth. *J. Am. Chem. Soc.* **2016**, *138* (43), 14288-14293.
42. Zhou, J.; Pu, C.; Jiao, T.; Hou, X.; Peng, X., A Two-Step Synthetic Strategy toward Monodisperse Colloidal CdSe and CdSe/CdS Core/Shell Nanocrystals. *J. Am. Chem. Soc.* **2016**, *138* (20), 6475-6483.

43. Leach, A. D. P.; Macdonald, J. E., Optoelectronic Properties of CuInS<sub>2</sub> Nanocrystals and Their Origin. *J. Phys. Chem. Lett.* **2016**, *7* (3), 572-583.
44. Tan, R.; Yuan, Y.; Nagaoka, Y.; Eggert, D.; Wang, X.; Thota, S.; Guo, P.; Yang, H.; Zhao, J.; Chen, O., Monodisperse Hexagonal Pyramidal and Bipyrarnidal Wurtzite CdSe-CdS Core-Shell Nanocrystals. *Chem. Mater.* **2017**, *29* (9), 4097-4108.
45. Chen, P. E.; Anderson, N. C.; Norman, Z. M.; Owen, J. S., Tight Binding of Carboxylate, Phosphonate, and Carbamate Anions to Stoichiometric CdSe Nanocrystals. *J. Am. Chem. Soc.* **2017**, *139* (8), 3227-3236.
46. Ritchhart, A.; Cossairt, B. M., Templated Growth of InP Nanocrystals with a Polytwistane Structure. *Angew. Chem. Int. Ed. Engl.* **2018**, *57* (7), 1908-1912.
47. Dennis, A. M.; Mangum, B. D.; Piryatinski, A.; Park, Y.-S.; Hannah, D. C.; Casson, J. L.; Williams, D. J.; Schaller, R. D.; Htoon, H.; Hollingsworth, J. A., Suppressed Blinking and Auger Recombination in Near-Infrared Type-II InP/CdS Nanocrystal Quantum Dots. *Nano Lett.* **2012**, *12* (11), 5545-5551.
48. Tan, R.; Shen, Y.; Roberts, S. K.; Gee, M. Y.; Blom, D. A.; Greytak, A. B., Reducing Competition by Coordinating Solvent Promotes Morphological Control in Alternating Layer Growth of CdSe/CdS Core/Shell Quantum Dots. *Chem. Mater.* **2015**, *27* (21), 7468-7480.
49. Liu, Y.-H.; Wang, F.; Hoy, J.; Wayman, V. L.; Steinberg, L. K.; Loomis, R. A.; Buhro, W. E., Bright Core-Shell Semiconductor Quantum Wires. *J. Am. Chem. Soc.* **2012**, *134* (45), 18797-18803.
50. Peng, X.; Schlamp, M. C.; Kadavanich, A. V.; Alivisatos, A. P., Epitaxial Growth of Highly Luminescent CdSe/CdS Core/Shell Nanocrystals with Photostability and Electronic Accessibility. *J. Am. Chem. Soc.* **1997**, *119* (30), 7019-7029.
51. Dabbousi, B. O.; Rodriguez-Viejo, J.; Mikulec, F. V.; Heine, J. R.; Mattoussi, H.; Ober, R.; Jensen, K. F.; Bawendi, M. G., (CdSe) ZnS Core-Shell Quantum Dots: Synthesis and Characterization of a Size Series of Highly Luminescent Nanocrystallites. *J. Phys. Chem. B* **1997**, *101* (46), 9463-9475.
52. Steckel, J. S.; Zimmer, J. P.; Coe-Sullivan, S.; Stott, N. E.; Bulović, V.; Bawendi, M. G., Blue Luminescence from (CdS)ZnS Core-Shell Nanocrystals. *Angew. Chem. Int. Ed.* **2004**, *43* (16), 2154-2158.
53. Li, J. J.; Wang, Y. A.; Guo, W.; Keay, J. C.; Mishima, T. D.; Johnson, M. B.; Peng, X., Large-Scale Synthesis of Nearly Monodisperse CdSe/CdS Core/Shell Nanocrystals Using Air-Stable Reagents via Successive Ion Layer Adsorption and Reaction. *J. Am. Chem. Soc.* **2003**, *125* (41), 12567-12575.
54. Hines, M. A.; Guyot-Sionnest, P., Synthesis and Characterization of Strongly Luminescing ZnS-Capped CdSe Nanocrystals. *J. Phys. Chem.* **1996**, *100* (2), 468-471.
55. Cao, H.; Ma, J.; Huang, L.; Qin, H.; Meng, R.; Li, Y.; Peng, X., Design and Synthesis of Antiblinking and Antibleaching Quantum Dots in Multiple Colors via Wave Function Confinement. *J. Am. Chem. Soc.* **2016**, *138* (48), 15727-15735.
56. Susumu, K.; Field, L. D.; Oh, E.; Hunt, M.; Delehanty, J. B.; Palomo, V.; Dawson, P. E.; Huston, A. L.; Medintz, I. L., Purple-, Blue-, and Green-Emitting Multishell Alloyed Quantum Dots: Synthesis, Characterization, and Application for Ratiometric Extracellular pH Sensing. *Chem. Mater.* **2017**, *29* (17), 7330-7344.

57. Zhong, X. H.; Han, M. Y.; Dong, Z. L.; White, T. J.; Knoll, W., Composition-tunable  $Zn_xCd_{1-x}Se$  nanocrystals with high luminescence and stability. *J. Am. Chem. Soc.* **2003**, *125* (28), 8589-8594.
58. Zhong, X.; Feng, Y.; Knoll, W.; Han, M., Alloyed  $Zn_xCd_{1-x}S$  Nanocrystals with Highly Narrow Luminescence Spectral Width. *J. Am. Chem. Soc.* **2003**, *125* (44), 13559-13563.
59. Kim, S.-W.; Zimmer, J. P.; Ohnishi, S.; Tracy, J. B.; Frangioni, J. V.; Bawendi, M. G., Engineering  $InAs_xP_{1-x}/InP/ZnSe$  III–V Alloyed Core/Shell Quantum Dots for the Near-Infrared. *J. Am. Chem. Soc.* **2005**, *127* (30), 10526-10532.
60. Steckel, J. S.; Snee, P.; Coe-Sullivan, S.; Zimmer, J. P.; Halpert, J. E.; Anikeeva, P.; Kim, L.-A.; Bulovic, V.; Bawendi, M. G., Color-Saturated Green-Emitting QD-LEDs. *Angew. Chem. Int. Ed.* **2006**, *45* (35), 5796-5799.
61. Swafford, L. A.; Weigand, L. A.; Bowers, M. J.; McBride, J. R.; Rapaport, J. L.; Watt, T. L.; Dixit, S. K.; Feldman, L. C.; Rosenthal, S. J., Homogeneously Alloyed  $CdS_xSe_{1-x}$  Nanocrystals: Synthesis, Characterization, and Composition/Size-Dependent Band Gap. *J. Am. Chem. Soc.* **2006**, *128* (37), 12299-12306.
62. Protière, M.; Reiss, P., Highly Luminescent  $Cd_{1-x}Zn_xSe/ZnS$  Core/Shell Nanocrystals Emitting in the Blue–Green Spectral Range. *Small* **2007**, *3* (3), 399-403.
63. Zhong, X.; Feng, Y.; Zhang, Y.; Gu, Z.; Zou, L., A Facile Route to Violet- to Orange-Emitting  $Cd_xZn_{1-x}Se$  Alloy Nanocrystals via Cation Exchange Reaction. *Nanotechnology* **2007**, *18* (38), 385606.
64. Bae, W. K.; Nam, M. K.; Char, K.; Lee, S., Gram-Scale One-Pot Synthesis of Highly Luminescent Blue Emitting  $Cd_{1-x}Zn_xS/ZnS$  Nanocrystals. *Chem. Mater.* **2008**, *20* (16), 5307-5313.
65. Groeneveld, E.; Witteman, L.; Lefferts, M.; Ke, X.; Bals, S.; Van Tendeloo, G.; de Mello Donega, C., Tailoring  $ZnSe$ – $CdSe$  Colloidal Quantum Dots via Cation Exchange: From Core/Shell to Alloy Nanocrystals. *ACS Nano* **2013**, *7* (9), 7913-7930.
66. Lee, K.-H.; Lee, J.-H.; Song, W.-S.; Ko, H.; Lee, C.; Lee, J.-H.; Yang, H., Highly Efficient, Color-Pure, Color-Stable Blue Quantum Dot Light-Emitting Devices. *ACS Nano* **2013**, *7* (8), 7295-7302.
67. Shen, H.; Bai, X.; Wang, A.; Wang, H.; Qian, L.; Yang, Y.; Titov, A.; Hyvonen, J.; Zheng, Y.; Li, L. S., High-Efficient Deep-Blue Light-Emitting Diodes by Using High Quality  $Zn_xCd_{1-x}S/ZnS$  Core/Shell Quantum Dots. *Adv. Funct. Mater.* **2014**, *24* (16), 2367-2373.
68. Anikeeva, P. O.; Halpert, J. E.; Bawendi, M. G.; Bulović, V., Quantum Dot Light-Emitting Devices with Electroluminescence Tunable over the Entire Visible Spectrum. *Nano Lett.* **2009**, *9* (7), 2532-2536.
69. Cui, J.; Beyler, A. P.; Marshall, L. F.; Chen, O.; Harris, D. K.; Wanger, D. D.; Brokmann, X.; Bawendi, M. G., Direct Probe of Spectral Inhomogeneity Reveals Synthetic Tunability of Single-Nanocrystal Spectral Linewidths. *Nat. Chem.* **2013**, *5* (7), 602-606.
70. Peng, Z. A.; Peng, X., Mechanisms of the Shape Evolution of  $CdSe$  Nanocrystals. *J. Am. Chem. Soc.* **2001**, *123* (7), 1389-1395.
71. Jain, P. K.; Amirav, L.; Aloni, S.; Alivisatos, A. P., Nanoheterostructure Cation Exchange: Anionic Framework Conservation. *J. Am. Chem. Soc.* **2010**, *132* (29), 9997-9999.
72. Denton, A. R.; Ashcroft, N. W., Vegard's Law. *Phys. Rev. A* **1991**, *43* (6), 3161-3164.

73. McClelland, K. P.; Weiss, E. A., Selective Photocatalytic Oxidation of Benzyl Alcohol to Benzaldehyde or C–C Coupled Products by Visible-Light-Absorbing Quantum Dots. *ACS Appl. Energy Mater.* **2019**, *2* (1), 92-96.
74. Sullivan, G. A., Diffusion and Solubility of Cu in CdS Single Crystals. *Phys. Rev.* **1969**, *184* (3), 796-805.
75. Jawaid, A. M.; Chattopadhyay, S.; Wink, D. J.; Page, L. E.; Snee, P. T., Cluster-Seeded Synthesis of Doped CdSe:Cu<sub>4</sub> Quantum Dots. *ACS Nano* **2013**, *7* (4), 3190-3197.
76. Yang, L.; Knowles, K. E.; Gopalan, A.; Hughes, K. E.; James, M. C.; Gamelin, D. R., One-Pot Synthesis of Monodisperse Colloidal Copper-Doped CdSe Nanocrystals Mediated by Ligand–Copper Interactions. *Chem. Mater.* **2016**, *28* (20), 7375-7384.
77. Dalpian, G. M.; Chelikowsky, J. R., Self-Purification in Semiconductor Nanocrystals. *Phys. Rev. Lett.* **2006**, *96* (22), 226802.
78. Erwin, S. C.; Zu, L.; Haftel, M. I.; Efros, A. L.; Kennedy, T. A.; Norris, D. J., Doping semiconductor nanocrystals. *Nature* **2005**, *436*, 91.
79. Pearson, R. G., Absolute Electronegativity and Hardness: Application to Inorganic Chemistry. *Inorg. Chem.* **1988**, *27* (4), 734-740.
80. Pearson, R. G., Chemical Hardness and Bond Dissociation Energies. *J. Am. Chem. Soc.* **1988**, *110* (23), 7684-7690.
81. Jain, P. K.; Beberwyck, B. J.; Fong, L.-K.; Polking, M. J.; Alivisatos, A. P., Highly Luminescent Nanocrystals From Removal of Impurity Atoms Residual From Ion-Exchange Synthesis. *Angew. Chem. Int. Ed.* **2012**, *51* (10), 2387-2390.
82. Parr, R. G.; Pearson, R. G., Absolute Hardness: Companion Parameter to Absolute Electronegativity. *J. Am. Chem. Soc.* **1983**, *105* (26), 7512-7516.

## Chapter 4

# Reversible Photo-Switching of Dual-Color Fluorescent Mn-Doped CdS-ZnS QDs Modulated by Diarylethene Molecules

Portions of this chapter are adapted and/or reprinted from the following works. Copyright belongs to the publisher.

**Yuan, Y.;** Zhu, H.; Nagaoka, Y.; Tan, R.; Davis, A. H.; Zheng, W.; Chen, O.\*, Reversible Photo-Switching of Dual Color Fluorescent Mn-Doped CdS-ZnS Quantum Dots Modulated by Diarylethene Molecules. *Front. Chem.* **2019**, *7*, 145. (Invited to Special Theme of Frontiers in Chemistry: Rising Stars)

## 4.1 Dynamic Materials

Dynamic materials have attracted attention of chemists in the past two decades owing to their potentials to be used for generating responsive materials for various applications.<sup>1-3</sup> Meanwhile, there is comprehensive development in the syntheses of nanocrystals with controlled size, shape, structure and compositions in various material systems (**Fig. 4.1**).<sup>4-7</sup> Combining organic molecular switches with inorganic nanocrystals can therefore afford dynamic hybrid systems with switchable properties.<sup>8-11</sup> Compared to static counterparts, dynamic materials exhibit intriguing advantages including selectively reversible properties with external stimuli, and thus potential applications in various fields including self-erasing paper<sup>12</sup> or self-healing coating,<sup>13</sup> bio-imaging *etc.*<sup>14</sup>

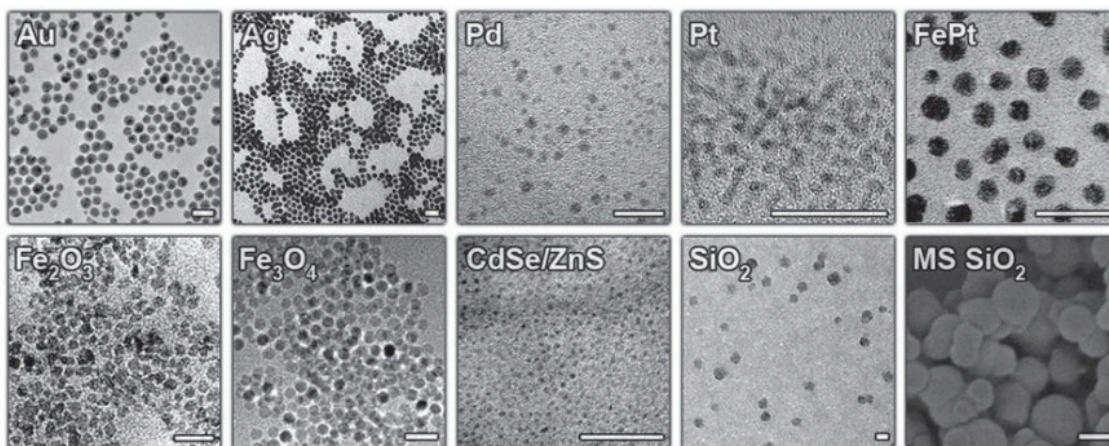


*Fig. 4.1: examples of nanoparticles that have been functionalized with molecular, supramolecular, or mechanically interlocked switches (from left to right, top to bottom): Au, Ag, Pd, Pt, FePt, Fe<sub>2</sub>O<sub>3</sub>, Fe<sub>3</sub>O<sub>4</sub>, CdSe-ZnS, SiO<sub>2</sub>, and mesoporous (MS) SiO<sub>2</sub>. Reproduced from ref 8.*

## 4.2 Photo-Switchable Molecules

Among diverse stimuli, light has been favored as an external input to tune the state of materials on account of its non-chemical contaminations, convenient delivery and specificity of desired wavelengths. As a result, a variety of photo-switchable molecules such as azobenzenes,<sup>15</sup> spiropyrans,<sup>16</sup> dithienylethenes,<sup>17, 18</sup> stilbene<sup>19</sup>, coumarins<sup>20</sup> *etc.*

(Fig. 4.2) have been employed to functionalize different nanomaterials<sup>8, 21, 22</sup> to construct light-responsive systems spanning from metal nanocrystals,<sup>12, 23, 24</sup> metal oxide nanocrystals,<sup>25, 26</sup> to quantum dots (QDs)<sup>27-30</sup>) and metal-organic frameworks (MOFs).<sup>31</sup> Upon irradiation of UV light, the switchable molecules can change from one isomer to another (azobenzenes and dithienylethenes) or undergo photodimerization (coumarins) and photocleavage (spiropyrans); while upon absorption with visible light, the molecules can undergo reverse process.

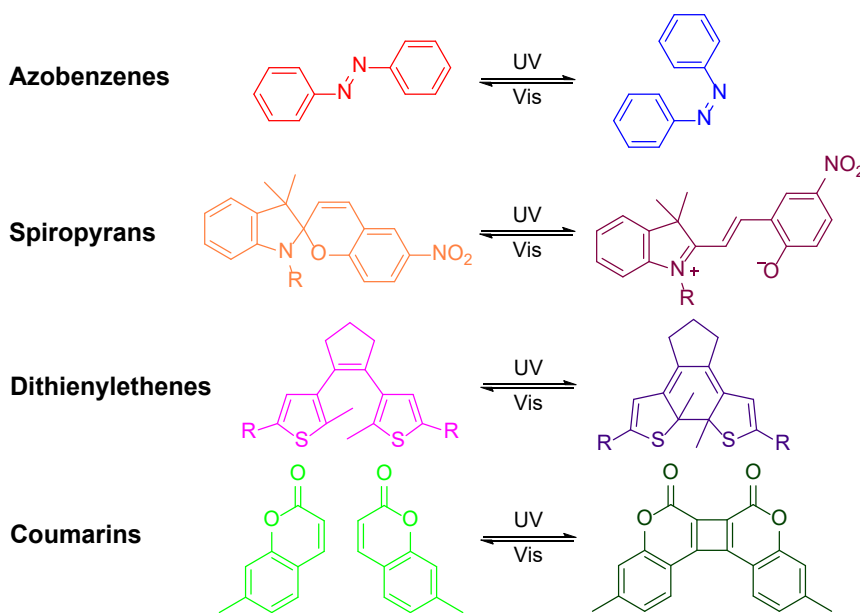


*Fig. 4.2: Chemical structures of some typical examples of molecular switches.*

### 4.3 Doping in QDs

In materials science, doping is a process that intentionally introduces impurity atoms as dopants to host lattices, thus providing unique properties inaccessible to conventional materials.<sup>32</sup> In this regard, doping in semiconductor QDs may exhibit improved optical, magnetic and electronic properties as compared to their undoped counterparts.<sup>33-40</sup> For example, when introducing transition metals or rare earth elements



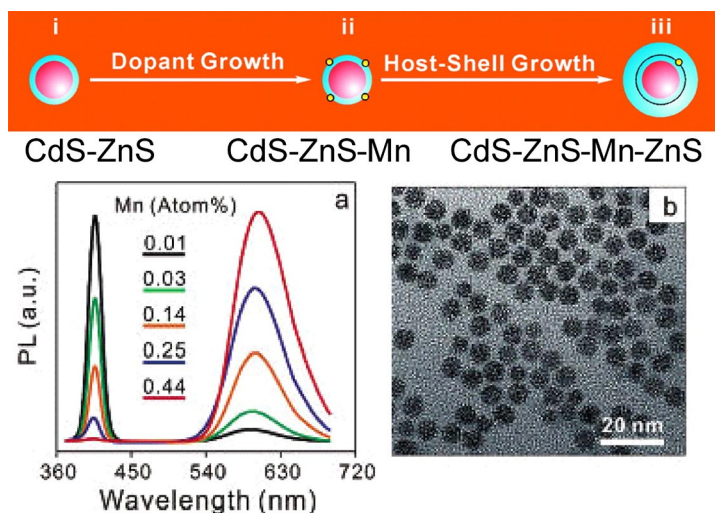


**Fig. 4.3:** The scheme shows two-step synthesis of Mn-doped CdS-ZnS core-shell QDs. (a) Normalized PL spectra of Mn-doped CdS-ZnS core-shell QDs with different doping levels. These core-shell QDs have a CdS core diameter of 3.1 nm ( $\sigma \sim 6\%$ ), ZnS-shell thickness is 1.5 nm ( $\sim 4.8$  ML), and the Mn dopants are located at 1.6 ML in the shell. (b) A typical TEM image of the Mn-doped core-shell QDs. Reproduced from ref 38.

to the QDs, a new emission band may emerge, resulting a dual-color emission property with two tunable non-overlapping PL peaks.<sup>41</sup> To this extent, Mn-doped CdS-ZnS QDs have been extensively studied as a model system for both fundamental understanding of host-to-dopant energy transfer processes and practical applications that are utilizing their dual-color emission properties.<sup>38, 42-46</sup> The intensity of Mn PL can be controlled by tuning doping level of Mn atoms in the CdS-ZnS QDs. **Fig. 4.3** shows a well-established strategy that can afford high quality of Mn-doped CdS-ZnS core-shell QDs, in which Mn PL increases with the increase of Mn doping level.<sup>38</sup> The Mn PL position is strongly dependent on Mn radial positions inside the CdS-ZnS. With increasing ZnS shell thickness before deposition of Mn atoms, Mn PL keeps blue shifting (**Fig. 4.4**).<sup>50</sup>

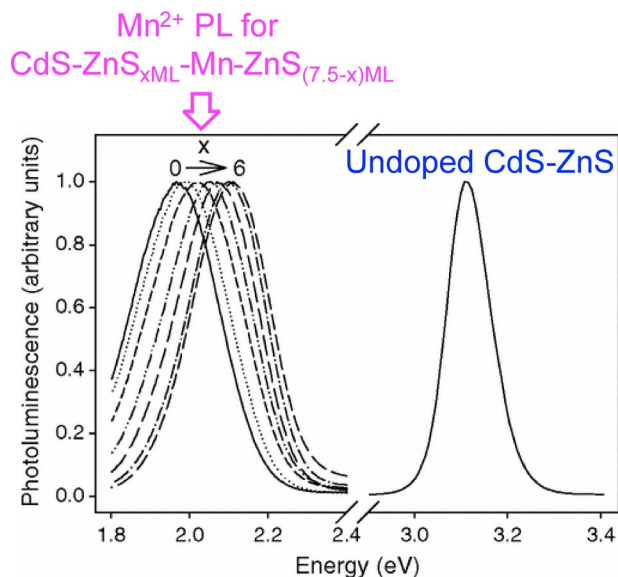


**Fig. 4.4:** Left: blue-shifting of the Mn PL for CdS-ZnS<sub>xML</sub>-Mn-ZnS<sub>(7.5-x)ML</sub> with  $x$  increasing from 0 to 6. Right: emission of undoped CdS-ZnS (7.5 ML). Reproduced from ref 50.

#### 4.4 Energy Transfer Caused Photo-Switching in Mn-Doped CdS-ZnS QDs and Diarylethene Molecules Hybrid System

Taking advantages of the dynamic switchable absorbance of diarylethene molecules and the dual-color emission property of Mn-doped CdS-ZnS QDs, in this work, we demonstrate a photo-switchable hybrid system by selectively quenching/recovering the Mn dopant emission. The quenching process is shown to include FRET from Mn-PL to closed isomer of diarylethenes as well as reabsorption processes. Three diarylethene switches with different electron-withdrawing groups were exploited to examine the performances of the photo-switching process. We demonstrate that the switch diarylethene molecule with substituent of 3,5-bis(trifluoromethyl)phenyl (switch 1) afford the best fatigue-resistant performance. PL color switching between blue and pink can be obtained by sequential illumination of UV (365 nm) and visible (590 nm) light. This switchable dual-color dynamic system could be potentially useful in a broad range of applications.

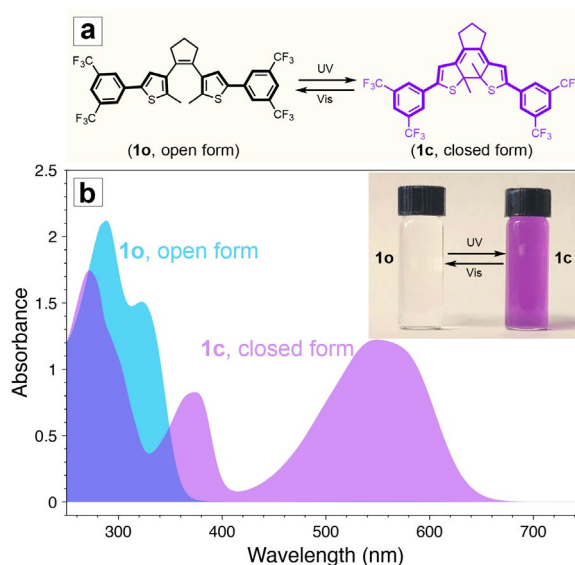


**Fig. 4.5:** (a) Chemical structures and photoisomerization of diarylethene **1** (Vis = visible). (b) UV-Vis absorption spectra of **1** at open (**1o**) and closed (**1c**) forms. Inset: photographs for the THF solution of **1o** (left) and **1c** (right).

We have synthesized diarylethene switch molecule featuring with electron withdrawing group of 3,5-bis(trifluoromethyl)benzene (**1**) as shown in **Fig. 4.5a**. The ring-open isomer (**1o**) and ring-closed isomer (**1c**) can be interconverted by illumination with UV and visible light showing drastically different absorption feature. Specifically, compared to the open form (**1o**), whose  $\pi$ -conjugation is restricted to each half of the molecule, the closed form (**1c**) possesses extended  $\pi$ -conjugation across the entire molecule. This extended conjugation places the highest occupied molecular orbital (HOMO) and lowest unoccupied molecular orbital (LUMO) of the molecule closer, thus allowing the absorption profile red-shift correspondingly.<sup>47</sup> UV-visible absorption spectra of the open and closed isomers (**1o** and **1c**) of diarylethene **1** are shown in **Fig. 4.5b**. The open form (**1o**) as prepared shows the absorbance in the wavelength range of shorter than 380 nm and negligible at longer wavelength. After illumination with UV light, the molecule turns into the closed isomer (**1c**) and a pronounced absorption peak appears in the visible range (420 - 650nm). It should be noted that there is minimal absorbance from

both isomers (**Fig. 4.5b**), indicating a nearly transparent window in the range of 400-420 nm. This photo-switchable absorption feature motivated us that a dynamic emitting architectural construct can be achieved when modulated with appropriate dual-color emitting fluorophores.

As mentioned above, high-quality dual-color emitters can be obtained by doping transition metals or rare earth elements in QD lattices. Among them, Mn-doped CdS-ZnS QDs have been robustly synthesized and extensively studied.<sup>38, 42-44, 48</sup> When excited with high energy photons, an electron-hole pair (an “exciton”) is created and confined inside the Mn-doped QD. This exciton can be radiatively deactivated through either recombination at the CdS-ZnS core-shell QD band edge to give a corresponding blue bandgap (BG) emission, or energy transfer to Mn dopants and subsequently emit a lower energy photon from the  ${}^4T_1$  to  ${}^6A_1$  states of the Mn ions (**Fig. 4.6**).<sup>48, 49</sup> Most importantly,

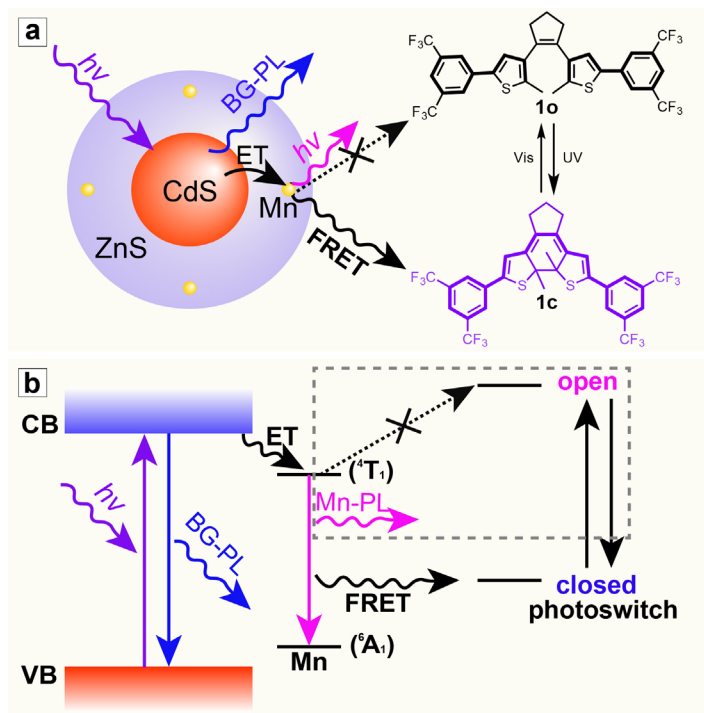


**Fig. 4.6:** Scheme (a) and energy diagram (b) of proposed mechanism for the selective Mn-PL quenching between Mn-doped CdS-ZnS core-shell QDs and diarylethene 1 molecules.

their dual-color emission bands can be adjusted to match the dynamic absorption windows of the diarylethene **1** (Fig. 4.5).<sup>43, 44, 50</sup> Therefore, we hypothesize that when mixing the well-designed Mn-doped CdS-ZnS core-shell QDs and the photo-switchable diarylethene molecules together, FRET from the excited state (i.e.,  $^4T_1$ ) of Mn to the switches can be turned on and off in the closed (**1c**) and open (**1o**) forms, respectively (Fig. 4.6). Thus, the system would show a combined color of both BG- and Mn-PL of the QDs while the diarylethene **1** stays at the open form (**1o**) and show the emission color mostly from BG-PL when the diarylethene **1** turns into the closed form (**1c**) (Fig. 4.6). This color switching process could be simply modulated by illuminating with UV or visible light.

To test our hypothesis, we designed and synthesized Mn-doped CdS-ZnS core-shell QDs with desired emission bands to match with the absorption profiles of the diarylethene **1**. In particular, the BG-PL centered at 413 nm with a FWHM of 16 nm (PL QY of 38.5%) was achieved by controlling the CdS core size and ZnS shell thickness (see Methods for details) (Fig. 4.7a). This BG-PL lays in the transmission window of the switch molecule disregarding to the open or closed form (Fig. 4.5b). Meanwhile, in order to achieve a large spectral overlap between the Mn-PL and absorption feature of the **1c**, Mn-PL centered at 592 nm (PL QY of 30.0%) was accessed by doping Mn ions closer to the surface of the QDs, thus minimizing the local strain of Mn impurities (Fig. 4.7a).<sup>50</sup> The Mn-to-BG PL intensity ratio was determined to be 0.24 (Fig. 4.7a). TEM measurements showed the resultant QDs exhibited a spherical shape and a high morphological uniformity with an average diameter of  $7.4 \pm 0.6$  nm (Fig. 4.7b and c). HR-TEM image showed (111) plane with  $d$ -spacing of 3.2 Å (Fig. 4.7d).

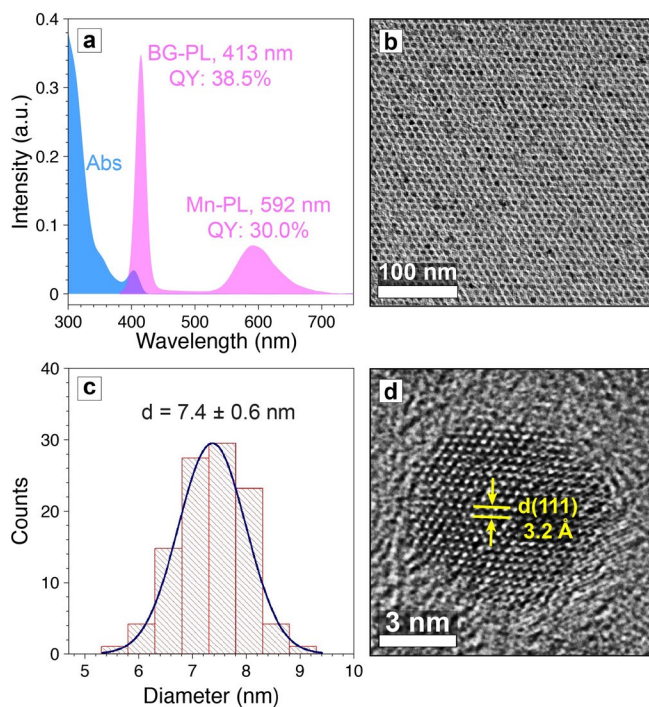


**Fig. 4.7:** (a) Absorption (blue) PL (pink) spectra, and (b) TEM image of Mn-doped CdS-ZnS core-shell QDs. (c) Size distribution histogram of Mn-doped CdS-ZnS core-shell QDs. (d) HR-TEM image for a Mn-doped CdS-ZnS core-shell QD.

The prepared Mn-doped CdS-ZnS QDs and diarylethene **1** were employed to test the photo-switching property. It is shown that while both the BG- and Mn-PL are disjoint from the absorbance of **1o**, the BG-PL locates at the absorbance depression area and most of the Mn-PL overlaps with visible-range absorbance of **1c** (Fig. 4.8a). We first tested the Mn-doped CdS-ZnS QDs under illumination of either UV or visible light without mixing with diarylethene **1** switches. Both BG- and Mn-PL intensities remained without any variation, indicating the robustness of the QD samples under light illumination. However, when mixing the same QDs with **1o** at a molar ratio of 1:500 in THF, the QD solution showed a pink color from the intact emission due to a minimal spectral overlap between the QD emission and the **1o** absorbance (Fig. 4.8a, b). When illuminated with UV light

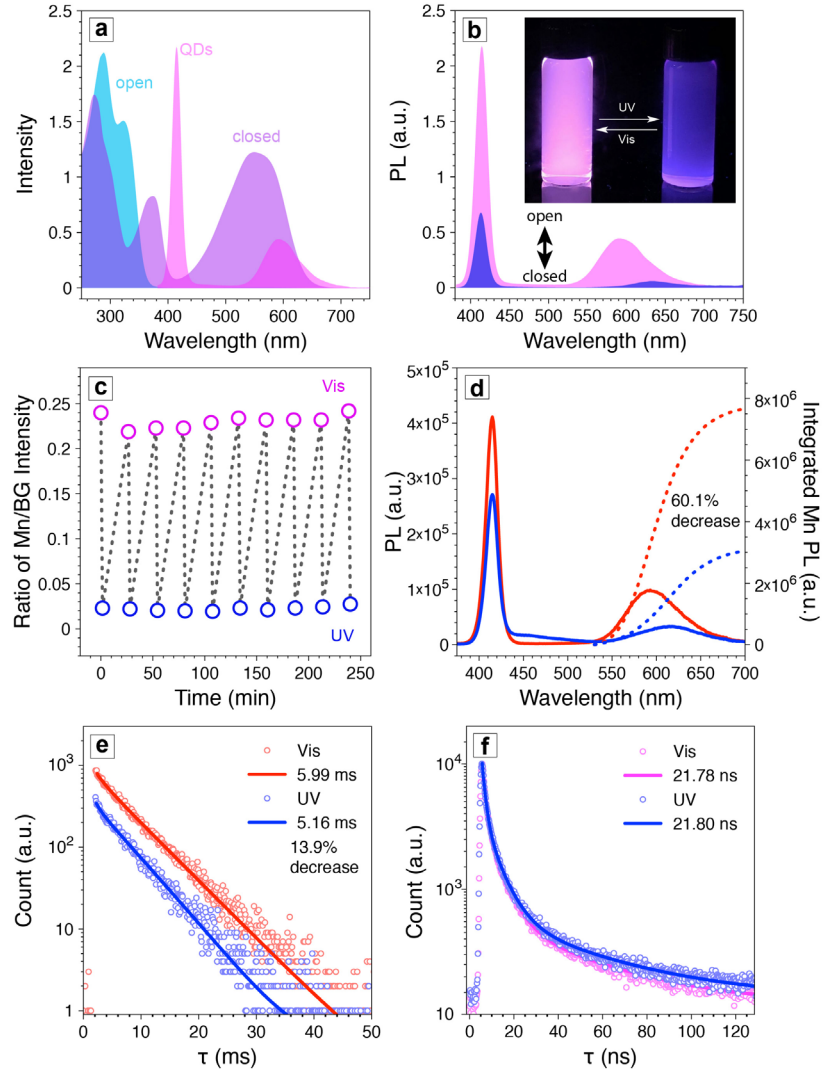


**Fig. 4.8:** (a) Overlay of the PL spectrum of the Mn-doped CdS-ZnS QDs with the absorption spectra of the **1o** and **1c**. (b) PL spectra of the mixture of Mn-doped CdS-ZnS QDs with **1o** (pink) and **1c** (blue). Inset: photographs for the mixture solution under UV light after UV (right) and visible (left) light illumination. (c) The ratio of Mn/BG PL intensity during repetitive switching cycles with sequential UV (blue open circle) and visible (pink open circle) light illumination. (d) The PL intensity (solid lines) and integrated Mn PL intensity (dotted lines) and (e) the corresponding Mn-PL lifetime changes during one switching cycle. (f) BG-PL lifetime decays after UV (blue) and visible (pink) light illumination.

(365 nm) for 90 seconds, a strong absorption feature arose in the visible range (420-650 nm, **Fig. 4.9a**), accompanying the decrease of the ratio of Mn/BG PL intensities from 0.24 to 0.02, corresponding to a change of the emission color from pink to blue (**Fig. 4.8b** and **Fig. 4.9b**). The change of the PL intensity ratio is largely due to the dynamic Mn-PL



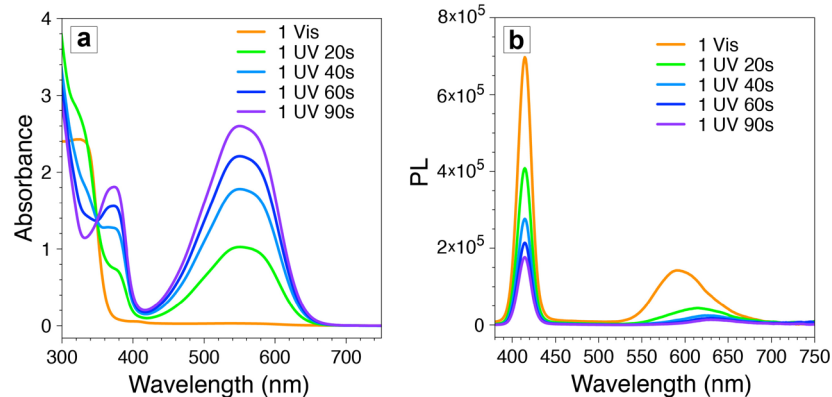


**Fig. 4.9:** Absorption (a) and PL (b) spectral evolution at different time in one cycle of mixture of Mn-doped CdS-ZnS QDs (BG-PL of 413 nm, Mn-PL of 592 nm) and diarylethene **1** in solution of THF under UV irradiation (365 nm).

quenching and recovering effect when the switch molecule alternates between closed (**1c**, quenching) and open (**1o**, recovering) forms (**Fig. 4.8b**). Importantly, this observed photo-switching process is highly reversible. Ten photo-switching cycles were carried out to test the fatigue resistance of the switch molecule (i.e., diarylethene **1**), and the stability of the entire system. During these cycles, both the absorption spectra and the intensity ratios of the Mn/BG PL peaks showed excellent reversibility (**Fig. 4.8c** and **4.10**), indicating a reliable photo-switching property of our designed system.

Two possible Mn-PL quenching/recovering mechanisms are attributable to the observed photo-switching property: 1) FRET from the excited state (i.e.,  $^4T_1$ ) of Mn dopant ions to the **1c** non-radiatively; 2) radiated photons of Mn-PL can be reabsorbed by the surrounding **1c**. To explore the origin of the observed Mn-PL quenching effect and their contributions, time-resolved PL lifetime measurements were carried out at different stage of the photo-switching process. When the integrated intensity of the Mn-PL decreased 60.1% of its initial value, the Mn-PL lifetime decreased from 5.99 ms to 5.16 ms, indicating that a 13.9% of the Mn-PL quenching can be attributed to FRET for the Mn-PL to the switch **1c** molecule in the measuring conditions (**Fig. 4.7a**, and **4.8 d, e**).<sup>51-</sup>



<sup>54</sup> Consequently, the rest 46.2% of Mn-PL quenching can be explained by the radiative

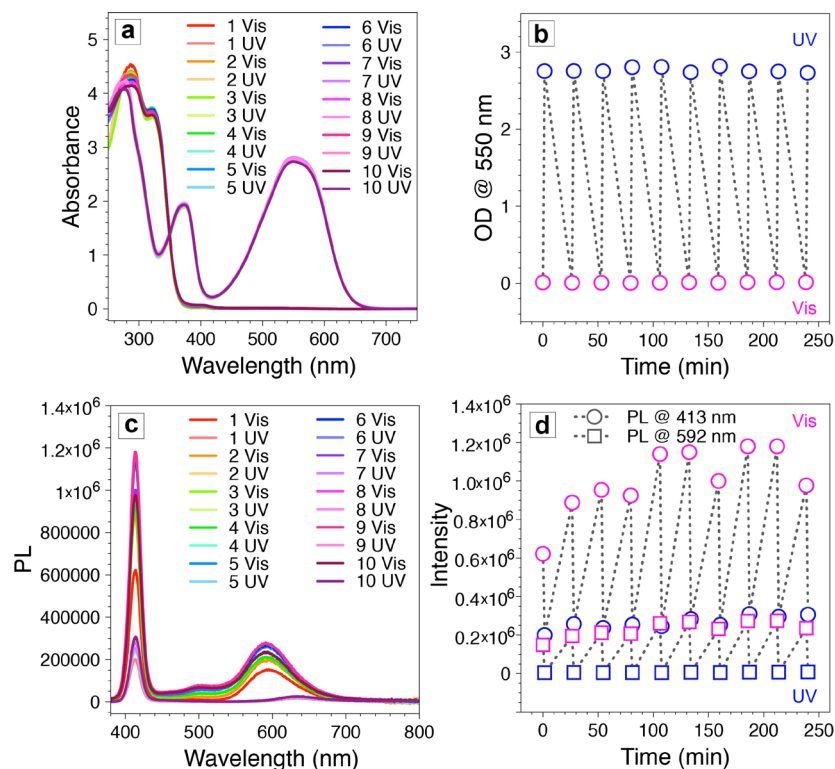


**Fig. 4.10:** Evolution of absorption and PL properties of mixture of Mn-doped CdS-ZnS QDs (BG-PL of 413 nm, Mn-PL of 592 nm) and diarylethene **1c** in solution of THF for ten cycles. (a) Absorption and (c) PL spectra during repetitive switching cycles consisting of alternating UV (365 nm, 90 s) and visible irradiation (590 nm, 25 min). (b) Evolution of absorbance at the wavelength of 550 nm. (d) Evolution of PL at wavelength of 413 nm (open circle) and 592 nm (open square).

photon reabsorption by surrounding **1c** molecule. A 31.0% of BG-PL integrated intensity decrease was also observed which again was contributed to the photon reabsorption due to the slight increase of the absorbance from the switch molecule (from **1o** to **1c**). No variance in PL lifetime ( $\sim 21$  ns) of the BG-PL further confirmed the reabsorption process (Fig. 4.8f and 4.11) without influencing the radiative photon recombination dynamics.<sup>51</sup> It is known that the efficiency of FRET process is strongly sensitive to the distance between donors and acceptors (inverse sixth power of the distance between donor and acceptor, typically within 1-10nm).<sup>55</sup> FRET process can happen only when the **1c** molecules reach to a close proximity (less than 10 nm) of the QD surface, which is in

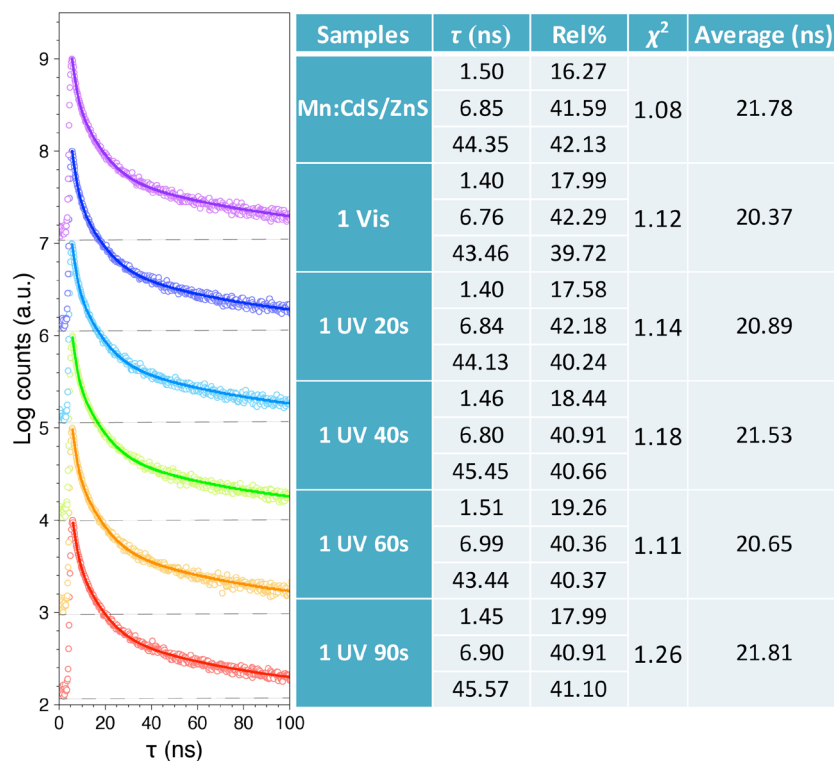


**Fig. 4.11:** BG-PL lifetime evolution at different time in one cycle of mixture of Mn-doped CdS-ZnS QDs (BG-PL of 413 nm, Mn-PL of 592 nm) and diarylethene **1** in solution of THF under UV irradiation.

line with our experimental observation that only a small portion (13.9% of the total quenching) of the Mn-PL quenching is caused by FRET. Moreover, given the size of the QDs (i.e., 7.4 nm) and the doping radial location of the Mn dopants inside the QDs (at the interface between the 5<sup>th</sup> and the 6<sup>th</sup> monolayer of the ZnS shell), the distances between the photo-generated exciton (electron-hole pair, the exciton center is determined at the center of core-shell QDs) and the **1c** is 3.2 nm larger than that between the Mn ion and the **1c**.<sup>48</sup> This larger distance will dramatically decrease the FRET efficiency between the exciton and **1c** as compared to that from Mn ion to **1c**. This again agrees well with the fact that the decrease of BG-PL was mostly attributable to the photon reabsorption processes.

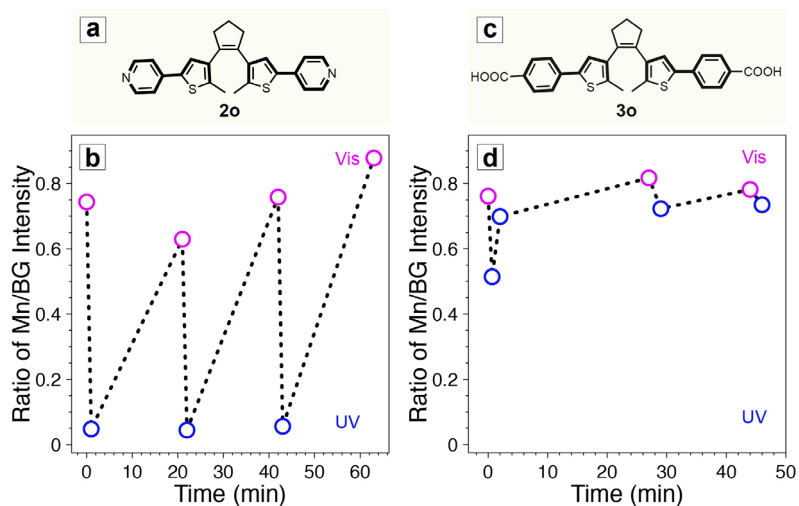


**Fig. 4.12:** Chemical structures of **2o** (a) and **3o** (c). The ratio of Mn/BG PL intensity of the mixture of Mn-doped CdS-ZnS QDs with **2o** (b) or **3o** (d) during repetitive switching cycles with sequential UV (blue open circle) and visible (pink open circle) light illumination.

Recently, it was reported that a series of diarylethene switch molecules with electron withdrawing substituents on the adjacent phenyl rings could provide fatigue resistance due to minimized formation of annulated isomers.<sup>56</sup> According to the study, two other diarylethene-based switches terminated with electron withdrawing groups of pyridine (diarylethene **2**) and 4-benzoic acid (diarylethene **3**) were synthesized and tested

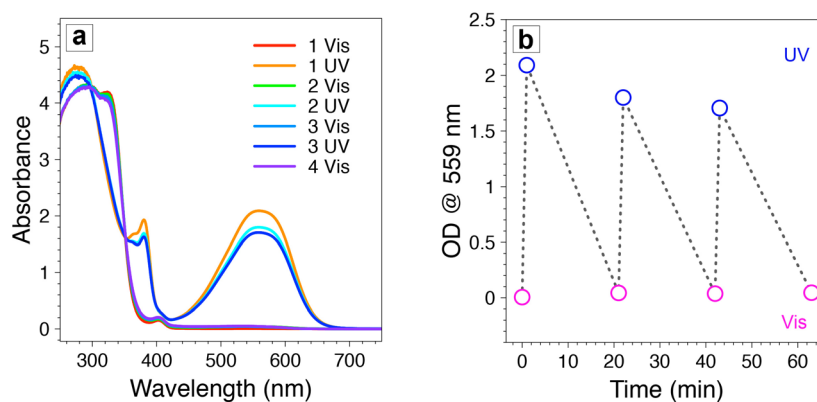


**Fig. 4.13:** Evolution of absorption property of mixture of Mn-doped CdS-ZnS QDs (BG-PL of 414 nm, Mn-PL of 600 nm) and diarylethene **2** in solution of THF for four cycles. (a) Absorption spectra during repetitive switching cycles consisting of alternating UV (365 nm, 90 s) and visible irradiation (590 nm, 25 min). (b) Evolution of absorbance at the wavelength of 559 nm.

in our system (**Fig. 4.12**). Diarylethene **2** was mixed with Mn-doped CdS-ZnS core-shell

QDs possessing BG- and Mn-PL peaks at 414 nm and 600 nm, respectively. The absorption spectral evolution clearly indicated fatigue effect over only 3 cycles (**Fig. 4.13**). Accordingly, the BG- and Mn-PL were quenched after visible light illumination

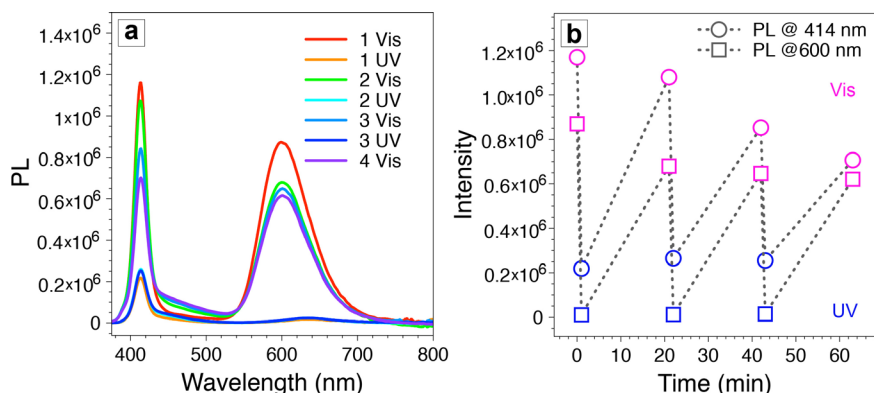


**Fig. 4.14:** Evolution of PL property of mixture of Mn-doped CdS-ZnS QDs (BG-PL of 414 nm, Mn-PL of 600 nm) and diarylethene 2 in solution of THF for four cycles. (a) PL spectra during repetitive switching cycles consisting of alternating UV (365 nm, 90 s) and visible irradiation (590 nm, 25 min). (b) Evolution of PL at wavelength of 414 nm (open circle) and 600 nm (open square).

whereas the quenching effect was reduced after UV irradiation after cycles (**Fig. 4.14**). Since the BG-PL was more affected by the fatigue of diarylethene 2, the ratio of Mn/BG intensity increased with 3 cycles (**Fig. 4.12b**). Diarylethene photo-switch 3, which

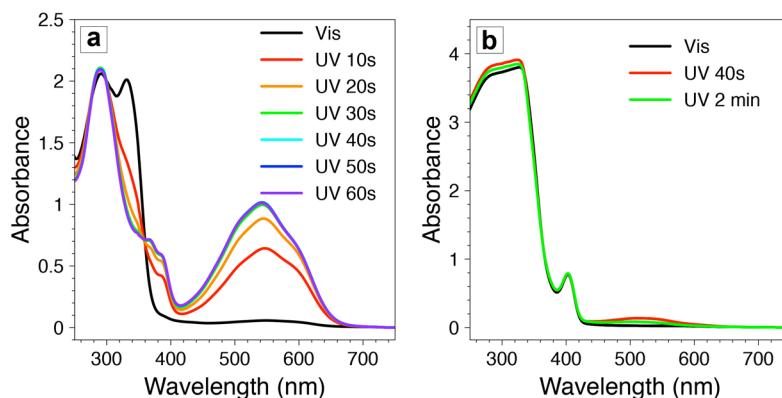


**Fig. 4.15:** (a) Absorption spectral evolution for diarylethene 3 at different time of UV irradiation (365 nm). (b) Absorption spectral evolution for the mixture of Mn-doped CdS-ZnS QDs (BG-PL of 414 nm, Mn-PL of 600 nm) and diarylethene 3 at different time of UV irradiation (365 nm).

possesses carboxylic groups at the para position of the phenyl rings, was expected to

attach on the surface of QDs covalently. This direct attachment of the switch **3** molecules would significantly reduce the mean distance between QDs donor and switch acceptor, thus facilitate the FRET from QD to the **3** molecules. However, our result showed that while **3o** itself can be isomerized to the closed form (**3c**) under UV illumination, it irreversibly stays at its open form (**3o**) mostly after mixing with Mn-doped CdS-ZnS QDs (**Fig. 4.15**). It is shown that while the Mn/BG PL intensity decreased with 40 s of UV illumination, it increased back with further UV illumination (**Fig. 4.12d**). This phenomenon can be ascribed to the direct attachment of switch **3** to the surface of the QDs through the carboxylate functional group, thus leading to a close proximity of switch **3** to the QD surface constantly rather than a dynamic on-and-off process as for switches **1** and **2** cases. In this case, the visible Mn-PL of the QDs can trap the switch molecule **3** in its open form (**3o**), preventing them from turning into the closed form (**3c**). Consequently, no reversible photo-switching phenomenon can be observed as shown in **Fig. 4.12d**, in good agreement with our experimental observations.

To conclude, we demonstrate a photo-switchable hybrid system with a reliable dual-color performance. This system combines photo-switchable diarylethene **1** molecule functionalized with strong electron withdrawing group of 3,5-bis(trifluoromethyl)benzene, and Mn-doped CdS-ZnS QDs with dual-emission band. Selective quenching/recovering of Mn-PL was achieved effectively, resulting in a pink and blue dual-color switching behavior under UV and visible light illumination. This photo-switching process is highly reversible and shows superior fatigue-resistance for at least ten switching cycles. The mechanism studies using both steady-state and time-resolved PL spectroscopy reveal the PL quenching contributions from both FRET and photo-reabsorption processes. Moreover, we show that the involvements of other electron

withdrawing functional groups (i.e., pyridine and carboxylate groups) limit the photo-switching property by significant molecular fatigue or irreversible optical effects. Our study sheds light on the fabrications of highly dynamic and photo-switchable hybrid systems that hold the potential in a broad range of applications spanning from self-erasing paper, biological-imaging to single molecule sensing/tracking and super-resolution imaging/localization microscopy.

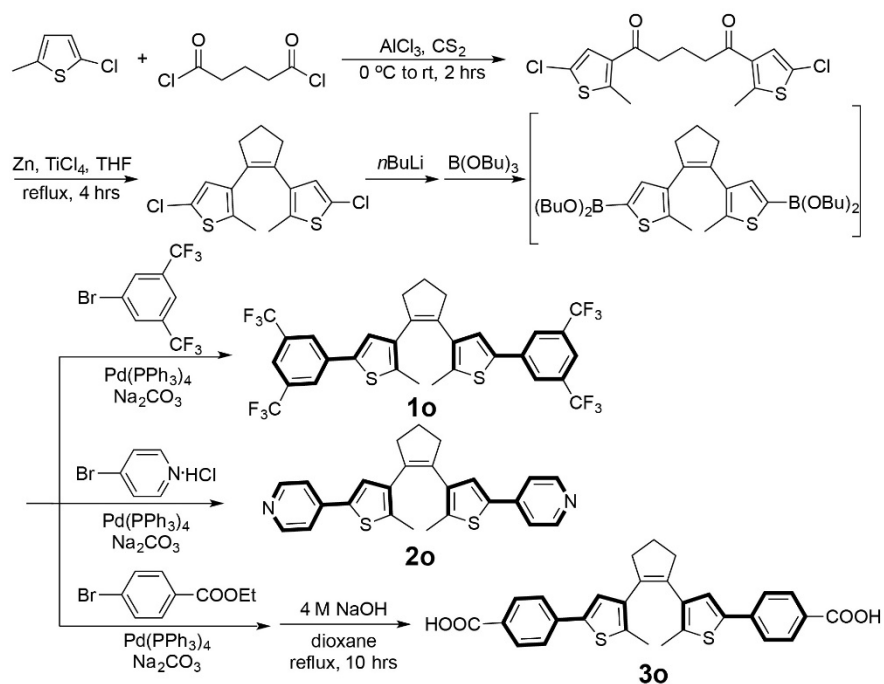
## Methods

\* (for UV-Vis absorption measurements, PL, lifetime and QY measurements, TEM measurements, see Ch.2)

### *Materials:*

All chemicals were used without further purification. 2-Chloro-5-methylthiophene (> 96.0%) was purchased from TCI Chemicals. Tributyl borate (98%) was purchased from Strem Chemicals. 1-Bromo-3,5-bis(trifluoromethyl)benzene (99%), *n*-butyllithium (1.6 M solution in hexanes, AcroSeal), zinc dust (98+%), and tetrahydrofuran (THF, 99.9%, extra dry, stabilized, anhydrous, SC, AcroSeal) were purchased from Acros Organics. Tetrakis(triphenylphosphine) palladium(0) (Pd(PPh<sub>3</sub>)<sub>4</sub>, 99%), glutaryl chloride (97%), TiCl<sub>4</sub> (99.9% trace metals basis), sulfur powder (99.999%), 1-octadecene (ODE, tech. 90%), and oleylamine (OAm, tech. 70%) were purchased from Aldrich. Manganese acetate tetrahydrate (99%), sodium carbonate (99.8%), and all the solvents were purchased from Fisher Scientific Company. Ethyl 4-bromobenzoate (98+%), AlCl<sub>3</sub> (anhydrous, 99.985%), cadmium acetate hydrate (99.999%), cadmium oxide (99.998%), zinc stearate (count as ZnO%  $\approx$  14%), oleic acid (OLA, 90%) and selenium (200 mesh, 99.999%) were purchased from Alfa Aesar. Nitric acid ( $\geq$  69.5%, TraceSELECT) was purchased from Fluka. 4-bromo-pyridine hydrochloride (98%) was purchased from Matrix Scientific. Cadmium myristate was self-made according to the literature method.<sup>57</sup>

*Synthesis of diarylethene molecules:*



The synthesis of 1,2-Bis(5-chloro-2-methylthiophen-3-yl)cyclopent-1-ene followed previous reported method with minor modifications<sup>58</sup>. To an ice-cooled mixture of 2-chloro-5-methylthiophene (298 mmol) and glutaryl dichloride (150 mmol) in  $\text{CS}_2$ ,  $\text{AlCl}_3$  (360 mmol) was added under vigorous stirring. Then the mixture was stirred for 2 hrs at room temperature. Afterwards, ice-cold water (100 mL) was added to the reaction mixture and the resulting solution was extracted with  $\text{CH}_2\text{Cl}_2$  ( $3 \times 150$  mL). The combined organic layer was washed with brine (100 mL) and then dried over  $\text{Na}_2\text{SO}_4$ . Then the solvent was evaporated to yield 1,5-Bis-3-(2-chloro-5-dimethylthienyl)-1,5-pentadione as a brown tar and used for next step without further purification.

THF (50 mL) and Zn dust (38 mmol) were added to a three-neck flask under  $\text{N}_2$  flow. Then  $\text{TiCl}_4$  (29 mmol) was injected cautiously with syringe. The solution turned yellow and was reflux for 45 min. After cooled using an ice bath, 1,5-Bis-3-(2-chloro-5-dimethylthienyl)-1,5-pentadione (19.2 mmol) was added and the reaction mixture was reheated and refluxed for 4 hrs. 10%  $\text{K}_2\text{CO}_3$  solution (50 mL) was added to the mixture

followed by filtration over Celite and washing with EtOAc ( $3 \times 20$  mL), and the filtrate was dried over anhydrous  $\text{Na}_2\text{SO}_4$ . After the solvent was evaporated, the crude product was purified by column chromatography (silica, pure hexanes) to afford 1,2-Bis(5-chloro-2-methylthiophen-3-yl)cyclopent-1-ene as a white solid.

Diarylethenes were synthesized using a previous established route with minor modifications.<sup>59</sup> The reactions were carried out using Schlenk line under dry  $\text{N}_2$  flow. *n*-Butyllithium (1.6 M in hexane, 1.3 mL) was added to a solution of 1,2-bis(5-chloro-2-methyl-3-thienyl)cyclopentene (1.0 mmol) in THF (15 mL) at room temperature. After stirring for 15 min, tributyl borate (3.0 mmol) was added and followed by stirring for another 1 hr. In another flask, DMSO (25 mL) was added and degassed, then 1-bromo-3,5-bis(trifluoromethyl)benzene (2.2 mmol) and  $\text{Pd}(\text{PPh}_3)_4$  (0.02 mmol) were added. After stirring for 15 min, aqueous  $\text{Na}_2\text{CO}_3$  (2 M, 5 mL) and ethylene glycol (0.5 mL) were added. The mixture was heated up to 60 °C after stirring for 15 min, then was added the above prepared solution. The resulting mixture was stirred at 80 °C overnight. solution of the borylated bithienylcyclopentene were added and the mixture was stirred at 80 °C for 16 h. After cooling to room temperature, 50 mL of water was added and the mixture was extracted with 20 mL of ethyl acetate three times. The combined organic phases were washed with brine, dried over  $\text{Na}_2\text{SO}_4$  and evaporated. Purification by flash column chromatography afforded compound 1,2-bis(5-(3,5-bis(trifluoromethyl)phenyl)-2-methylthiophen-3-yl)cyclopent-1-ene (**1o**) (32 %) as a pale white solid<sup>56</sup>. **<sup>1</sup>H-NMR (400 MHz,  $\text{CDCl}_3$ ):**  $\delta$  (ppm) = 7.86 (br s, 4 H,  $\text{CH}_{\text{ar}}$ ), 7.71 (br s, 2 H,  $\text{CH}_{\text{ar}}$ ), 7.14 (s, 2 H,  $\text{CH}_{\text{th}}$ ), 2.88 (t,  $J_{\text{H,H}} = 7.4$  Hz, 4 H,  $\text{CH}_2$ ), 2.14 (p,  $J_{\text{H,H}} = 7.2$  Hz, 2 H,  $\text{CH}_2$ ), 2.06 (s, 6 H,  $\text{CH}_3$ ). Compound 1,2-bis(2-methyl-5-(pyridin-4-yl)thiophen-3-yl)cyclopent-1-ene (**2o**) was prepared by exchanging 1-bromo-3,5-bis(trifluoromethyl)benzene with 4-bromo-



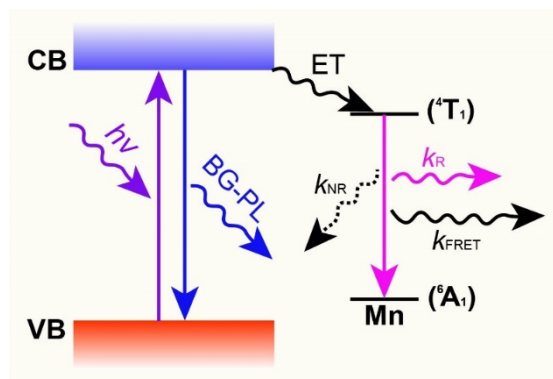
pyridine hydrochloride<sup>59</sup>. <sup>1</sup>H-NMR (400 MHz, CDCl<sub>3</sub>):  $\delta$  (ppm) = 8.53 (d,  $J_{H,H}$  = 6.0 Hz, 4H, CH<sub>ar</sub>), 7.39 (d,  $J_{H,H}$  = 6.4 Hz, 4H, CH<sub>ar</sub>), 7.25 (s, 2H, CH<sub>th</sub>), 2.86 (t,  $J_{H,H}$  = 7.4 Hz, 4H, CH<sub>2</sub>), 2.12 (m, 2H, CH<sub>2</sub>), 2.03 (s, 6H, CH<sub>3</sub>). Compound 4,4'-(cyclopent-1-ene-1,2-diylbis(5-methylthiophene-4,2-diyl))dibenzoic acid (**30**) was obtained by switching 1-bromo-3,5-bis(trifluoromethyl)benzene to ethyl 4-bromobenzoate to perform the Suzuki reaction and followed by hydrolysis with 4 M NaOH aqueous solution in dioxane<sup>56,60</sup>. **<sup>1</sup>H-NMR (400 MHz, CDCl<sub>3</sub>):**  $\delta$  (ppm) = 7.99 (d,  $J_{H,H}$  = 8.8 Hz, 4 H, CH<sub>ar</sub>), 7.53 (d,  $J_{H,H}$  = 8.8 Hz, 4 H, CH<sub>ar</sub>), 7.14 (s, 2 H, CH<sub>th</sub>), 4.37 (q,  $J_{H,H}$  = 7.2 Hz, 4 H, CH<sub>3</sub>CH<sub>2</sub>O), 2.85 (t,  $J_{H,H}$  = 7.4 Hz, 4 H, CH<sub>2</sub>), 2.10 (p,  $J_{H,H}$  = 7.4 Hz, 2 H, CH<sub>2</sub>), 2.01 (s, 6 H, CH<sub>3</sub>), 1.39 (t,  $J_{H,H}$  = 7.2 Hz, 6 H, CH<sub>3</sub>CH<sub>2</sub>O). **<sup>1</sup>H NMR (400 MHz, DMSO-*d*<sup>6</sup>):**  $\delta$  (ppm) = 12.86 (s, 2H), 7.92 (d,  $J_{H,H}$  = 8.0 Hz, 4 H, CH<sub>ar</sub>), 7.67 (d,  $J_{H,H}$  = 8.0 Hz, 4 H, CH<sub>ar</sub>), 7.48 (s, 2H, CH<sub>th</sub>), 2.84 (t,  $J_{H,H}$  = 7.6 Hz, 4 H, CH<sub>2</sub>), 2.07 (m, 2H), 1.92 (s, 6H).

*Synthesis of Mn-doped CdS-ZnS core-shell QDs:*

Mn-doped CdS-ZnS core-shell QDs were prepared following the reported method with minor modifications<sup>42</sup>. First, CdS core QDs were prepared using a direct heating-up method. In a typical synthesis, cadmium myristate (1.0 mmol), sulfur (0.5 mmol), and ODE (50 mL) were added to a 100 mL-flask. The resulting mixture was degassed at room temperature for 10 min, and then was heated to 240 °C under N<sub>2</sub> flow. The reaction was stopped by removing heating mantle and cooling to room temperature. The resulting CdS QDs were precipitated with addition of acetone, following by centrifugation and then were redispersed in hexane. A small amount of OLA can be added to assist QDs to disperse in hexane. The CdS QDs were dispersed in hexane as a stock after purified for three times. Second, ZnS shells were grown on the CdS cores using a layer by layer injection method. Typically, CdS cores (100 nmol) were mixed with ODE (3 mL) and

OAm (1 mL), and the resulting mixture was degassed for 1 hr at room temperature and then heat up to 220 °C under N<sub>2</sub> flow for ZnS growth. Zinc-stearate in ODE (0.1 M) and sulfur in ODE (0.1 M) were injected simultaneously for each monolayer growth of ZnS shell. The reaction time was 10 min after each injection. The growth for first two monolayers ZnS shells was at 220 °C and then was at 280 °C for later growth. Third, dopant growth was performed in the same pot with ZnS shells growth. Freshly made Mn(OAc)<sub>2</sub> solution (5 mM) was injected after five monolayers of ZnS shells growth, accompanying the injection of sulfur precursor for the six monolayer. Dopant growth was allowed for 20 min and was followed by the growth of two more ZnS shells. Finally, zinc-stearate solution for the last monolayer ZnS shell growth (0.1 M, 2 mL) was injected and then the QDs were annealed at 240 °C for 30 min. The resulting Mn-doped QDs were purified by three precipitation-redispersion cycles using acetone and hexane.

*Calculation of FRET efficiency and Reabsorption:*



The simple model of the Mn-doped CdS-ZnS QDs is as illustrated above. Without mixing with diarylethene molecules, there are two processes occurring in the Mn relaxation, which are radiative decay with the rate constant  $k_R$ , and non-radiative decay with the rate constant  $k_{NR}$ . The Mn-PL QY ( $QY_1$ ) and lifetime ( $\tau_1$ ) can be expressed as the following equations:

$$QY_1 = \frac{k_R}{k_R + k_{NR}} \quad (1)$$

$$\tau_1 = \frac{1}{k_R + k_{NR}} \quad (2)$$

When mixed with diarylethene molecules, a new nonradiative transfer (i.e. FRET) occurs, with the rate constant  $k_{FRET}$ . The corresponding Mn-PL QY ( $QY_2$ , note the QY here is without considering reabsorption) and lifetime ( $\tau_2$ ) can be expressed as:

$$QY_2 = \frac{k_R}{k_R + k_{NR} + k_{FRET}} \quad (3)$$

$$\tau_2 = \frac{1}{k_R + k_{NR} + k_{FRET}} \quad (4)$$

The FRET efficiency ( $\Phi_{FRET}$ ) can be expressed as:

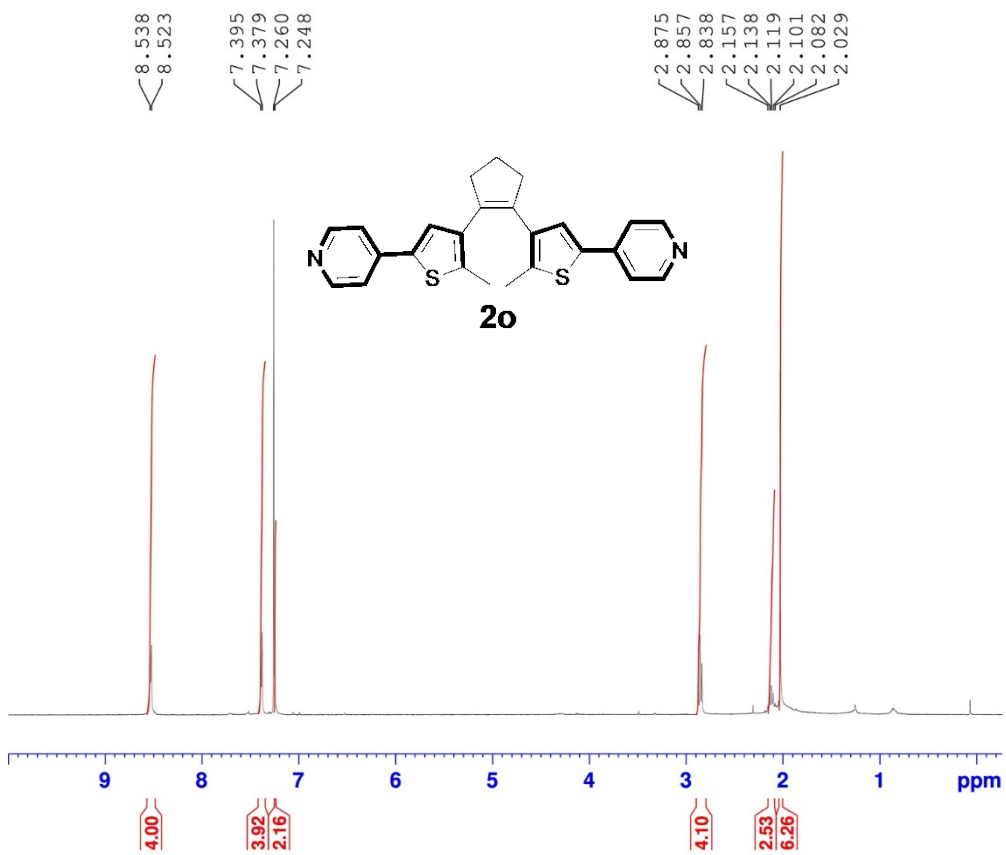
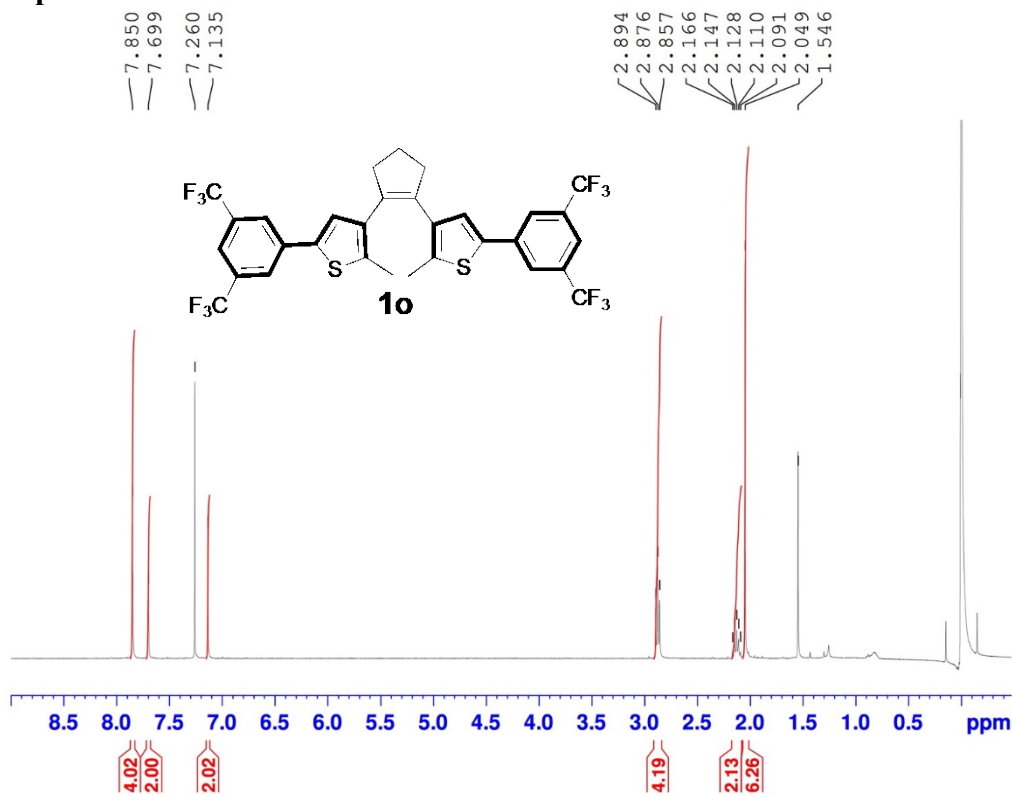
$$\Phi_{FRET} = 1 - \frac{QY_2}{QY_1} = \frac{k_{FRET}}{k_R + k_{NR} + k_{FRET}} \quad (5)$$

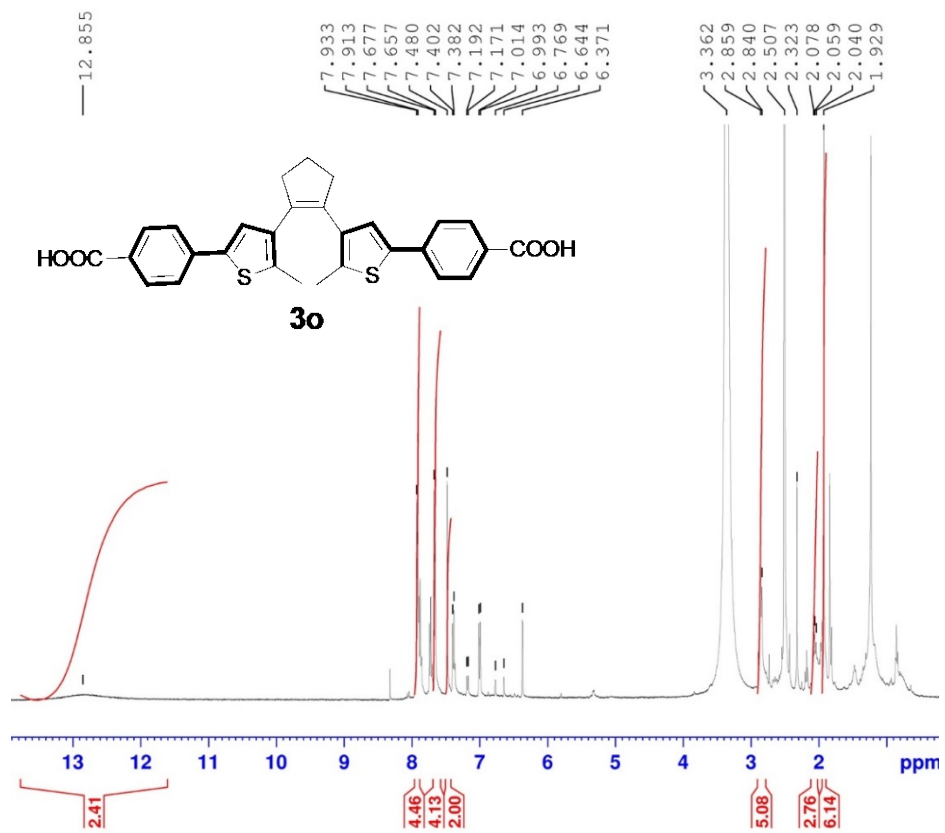
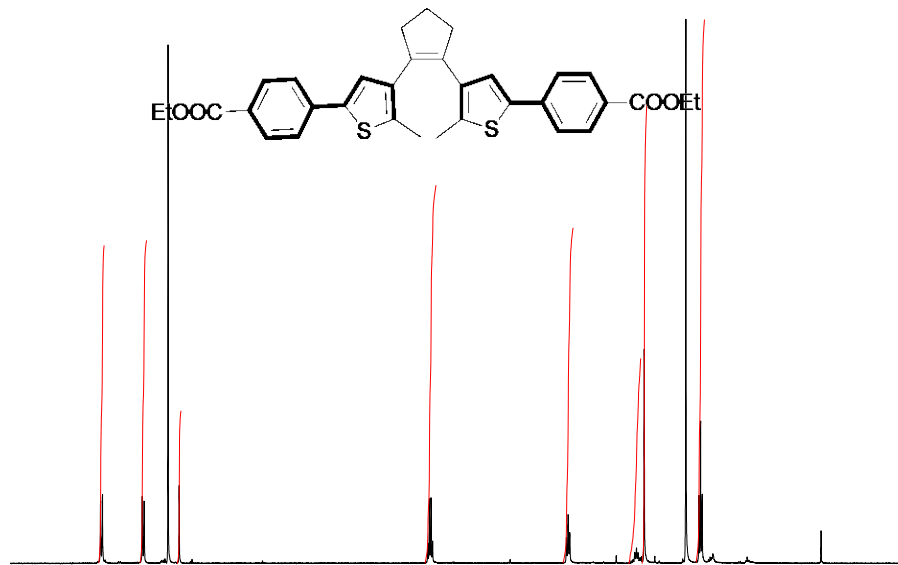
It can also be expressed as:

$$\Phi_{FRET} = 1 - \frac{\tau_2}{\tau_1} = \frac{k_{FRET}}{k_R + k_{NR} + k_{FRET}} = 1 - \frac{5.16 \text{ ms}}{5.99 \text{ ms}} = 13.9\% \quad (6)$$

In the real case, the FRET process is accompanying with the reabsorption process, the measured QY decrease (60.1%) is a combination of  $\Phi_{FRET}$  and reabsorption. So, the reabsorption fraction can be calculated as  $60.1\% - 13.9\% = 46.2\%$ .

# NMR Spectra





## References

1. Klajn, R., Spiropyran-Based Dynamic Materials. *Chem. Soc. Rev.* **2014**, *43* (1), 148-184.
2. Grinthal, A.; Aizenberg, J., Adaptive All the Way Down: Building Responsive Materials from Hierarchies of Chemomechanical Feedback. *Chem. Soc. Rev.* **2013**, *42* (17), 7072-7085.
3. Kay, E. R.; Leigh, D. A.; Zerbetto, F., Synthetic Molecular Motors and Mechanical Machines. *Angew. Chem. Int. Ed.* **2007**, *46* (1-2), 72-191.
4. Talapin, D. V.; Shevchenko, E. V., Introduction: Nanoparticle Chemistry. *Chem. Rev.* **2016**, *116* (18), 10343-10345.
5. Gilroy, K. D.; Ruditskiy, A.; Peng, H.-C.; Qin, D.; Xia, Y., Bimetallic Nanocrystals: Syntheses, Properties, and Applications. *Chem. Rev.* **2016**, *116* (18), 10414-10472.
6. Wu, L.; Mendoza-Garcia, A.; Li, Q.; Sun, S., Organic Phase Syntheses of Magnetic Nanoparticles and Their Applications. *Chem. Rev.* **2016**, *116* (18), 10473-10512.
7. Pietryga, J. M.; Park, Y.-S.; Lim, J.; Fidler, A. F.; Bae, W. K.; Brovelli, S.; Klimov, V. I., Spectroscopic and Device Aspects of Nanocrystal Quantum Dots. *Chem. Rev.* **2016**, *116* (18), 10513-10622.
8. Klajn, R.; Stoddart, J. F.; Grzybowski, B. A., Nanoparticles Functionalised with Reversible Molecular and Supramolecular Switches. *Chem. Soc. Rev.* **2010**, *39* (6), 2203-2237.
9. Qu, D.-H.; Wang, Q.-C.; Zhang, Q.-W.; Ma, X.; Tian, H., Photoresponsive Host-Guest Functional Systems. *Chem. Rev.* **2015**, *115* (15), 7543-7588.
10. Bai, F.; Li, B.; Bian, K.; Haddad, R.; Wu, H.; Wang, Z.; Fan, H., Pressure-Tuned Structure and Property of Optically Active Nanocrystals. *Adv. Mater.* **2016**, *28* (10), 1989-1993.
11. Li, B.; Bian, K.; Zhou, X.; Lu, P.; Liu, S.; Brener, I.; Sinclair, M.; Luk, T.; Schunk, H.; Alarid, L.; Clem, P. G.; Wang, Z.; Fan, H., Pressure Compression of CdSe Nanoparticles into Luminescent Nanowires. *Sci. Adv.* **2017**, *3* (5), e1602916.
12. Kundu, P. K.; Samanta, D.; Leizrowice, R.; Margulis, B.; Zhao, H.; Börner, M.; Udayabhaskararao, T.; Manna, D.; Klajn, R., Light-Controlled Self-Assembly of Non-photoresponsive Nanoparticles. *Nat. Chem.* **2015**, *7*, 646-652.
13. Roy, N.; Bruchmann, B.; Lehn, J.-M., DYNAMERS: Dynamic Polymers as Self-Healing Materials. *Chem. Soc. Rev.* **2015**, *44* (11), 3786-3807.
14. Zhang, J.; Zou, Q.; Tian, H., Photochromic Materials: More Than Meets The Eye. *Adv. Mater.* **2012**, *25* (3), 378-399.
15. Bandara, H. M. D.; Burdette, S. C., Photoisomerization in Different Classes of Azobenzene. *Chem. Soc. Rev.* **2012**, *41* (5), 1809-1825.
16. Minkin, V. I., Photo-, Thermo-, Solvato-, and Electrochromic Spiroheterocyclic Compounds. *Chem. Rev.* **2004**, *104* (5), 2751-2776.
17. Irie, M.; Fukaminato, T.; Matsuda, K.; Kobatake, S., Photochromism of Diarylethene Molecules and Crystals: Memories, Switches, and Actuators. *Chem. Rev.* **2014**, *114* (24), 12174-12277.
18. Irie, M., Diarylethenes for Memories and Switches. *Chem. Rev.* **2000**, *100* (5), 1685-1716.

19. Momotake, A.; Arai, T., Photochemistry and Photophysics of Stilbene Dendrimers and Related Compounds. *J. Photochem. Photobiol. C* **2004**, *5* (1), 1-25.
20. Mal, N. K.; Fujiwara, M.; Tanaka, Y., Photocontrolled Reversible Release of Guest Molecules from Coumarin-Modified Mesoporous Silica. *Nature* **2003**, *421* (6921), 350-353.
21. Wang, L.; Li, Q., Photochromism into Nanosystems: towards Lighting Up the Future Nanoworld. *Chem. Soc. Rev.* **2018**, *47* (3), 1044-1097.
22. Yildiz, I.; Deniz, E.; Raymo, F. M., Fluorescence Modulation with Photochromic Switches in Nanostructured Constructs. *Chem. Soc. Rev.* **2009**, *38* (7), 1859-1867.
23. Manna, D.; Udayabhaskararao, T.; Zhao, H.; Klajn, R., Orthogonal Light-Induced Self-Assembly of Nanoparticles using Differently Substituted Azobenzenes. *Angew. Chem. Int. Ed.* **2015**, *54* (42), 12394-12397.
24. Zhao, H.; Sen, S.; Udayabhaskararao, T.; Sawczyk, M.; Kučanda, K.; Manna, D.; Kundu, P. K.; Lee, J.-W.; Král, P.; Klajn, R., Reversible Trapping and Reaction Acceleration within Dynamically Self-Assembling Nanoflasks. *Nat. Nanotech.* **2015**, *11*, 82-88.
25. Mikami, R.; Taguchi, M.; Yamada, K.; Suzuki, K.; Sato, O.; Einaga, Y., Reversible Photo-Switching of the Magnetization of Iron Oxide Nanoparticles at Room Temperature. *Angew. Chem. Int. Ed. Engl.* **2004**, *43* (45), 6135-6139.
26. Min Yeo, K.; Ji Gao, C.; Ahn, K.-H.; Su Lee, I., Superparamagnetic Iron Oxide Nanoparticles with Photoswitchable Fluorescence. *Chem. Commun.* **2008**, *0* (38), 4622-4624.
27. Zhu, L.; Zhu, M.-Q.; Hurst, J. K.; Li, A. D. Q., Light-Controlled Molecular Switches Modulate Nanocrystal Fluorescence. *J. Am. Chem. Soc.* **2005**, *127* (25), 8968-8970.
28. Zhu, M.-Q.; Zhu, L.; Han, J. J.; Wu, W.; Hurst, J. K.; Li, A. D. Q., Spiropyran-Based Photochromic Polymer Nanoparticles with Optically Switchable Luminescence. *J. Am. Chem. Soc.* **2006**, *128* (13), 4303-4309.
29. Díaz, S. A.; Gillanders, F.; Jares-Erijman, E. A.; Jovin, T. M., Photoswitchable semiconductor nanocrystals with self-regulating photochromic Förster resonance energy transfer acceptors. *Nat. Commun.* **2015**, *6*, 6036.
30. Díaz, S. A.; Menéndez, G. O.; Etchehon, M. H.; Giordano, L.; Jovin, T. M.; Jares-Erijman, E. A., Photoswitchable Water-Soluble Quantum Dots: pcFRET Based on Amphiphilic Photochromic Polymer Coating. *ACS Nano* **2011**, *5* (4), 2795-2805.
31. Dolgoplova, E. A.; Rice, A. M.; Martin, C. R.; Shustova, N. B., Photochemistry and Photophysics of MOFs: Steps towards MOF-based Sensing Enhancements. *Chem. Soc. Rev.* **2018**, *47* (13), 4710-4728.
32. J. Daniel Bryan; Gamelin, D. R., Doped Semiconductor Nanocrystals: Synthesis, Characterization, Physical Properties, and Applications. In *Progress in Inorganic Chemistry*, 2005.
33. Norris, D. J.; Efros, A. L.; Erwin, S. C., Doped Nanocrystals. *Science* **2008**, *319* (5871), 1776-1779.
34. Cai, T.; Yang, H.; Hills-Kimball, K.; Song, J.-P.; Zhu, H.; Hofman, E.; Zheng, W.; Rubenstein, B. M.; Chen, O., Synthesis of All-Inorganic Cd-Doped CsPbCl<sub>3</sub> Perovskite Nanocrystals with Dual-Wavelength Emission. *J. Phys. Chem. Lett.* **2018**, *9* (24), 7079-7084.

35. Pradhan, N.; Peng, X., Efficient and Color-Tunable Mn-doped ZnSe Nanocrystal Emitters: Control of Optical Performance via Greener Synthetic Chemistry. *J. Am. Chem. Soc.* **2007**, *129* (11), 3339-3347.
36. Kroupa, D. M.; Roh, J. Y.; Milstein, T. J.; Creutz, S. E.; Gamelin, D. R., Quantum-Cutting Ytterbium-Doped CsPb(Cl<sub>1-x</sub>Br<sub>x</sub>)<sub>3</sub> Perovskite Thin Films with Photoluminescence Quantum Yields over 190%. *ACS Energy Lett.* **2018**, *3* (10), 2390-2395.
37. Bussian, D. A.; Crooker, S. A.; Yin, M.; Brynda, M.; Efros, A. L.; Klimov, V. I., Tunable Magnetic Exchange Interactions in Manganese-Doped Inverted Core-Shell ZnSe-CdSe Nanocrystals. *Nat. Mater.* **2008**, *8*, 35.
38. Yang, Y.; Chen, O.; Angerhofer, A.; Cao, Y. C., Radial-Position-Controlled Doping in CdS/ZnS Core/Shell Nanocrystals. *J. Am. Chem. Soc.* **2006**, *128* (38), 12428-12429.
39. Li, Z.-J.; Hofman, E.; Davis, A. H.; Khammang, A.; Wright, J. T.; Dzikovski, B.; Meulenberg, R. W.; Zheng, W., Complete Dopant Substitution by Spinodal Decomposition in Mn-Doped Two-Dimensional CsPbCl<sub>3</sub> Nanoplatelets. *Chem. Mater.* **2018**, *30* (18), 6400-6409.
40. Zheng, W.; Strouse, G. F., Involvement of Carriers in the Size-Dependent Magnetic Exchange for Mn:CdSe Quantum Dots. *J. Am. Chem. Soc.* **2011**, *133* (19), 7482-7489.
41. Wu, P.; Yan, X.-P., Doped Quantum Dots for Chemo/Biosensing and Bioimaging. *Chem. Soc. Rev.* **2013**, *42* (12), 5489-5521.
42. Yang, Y.; Chen, O.; Angerhofer, A.; Cao, Y. C., On Doping CdS/ZnS Core/Shell Nanocrystals with Mn. *J. Am. Chem. Soc.* **2008**, *130* (46), 15649-15661.
43. Chen, O.; Shelby, D. E.; Yang, Y.; Zhuang, J.; Wang, T.; Niu, C.; Omenetto, N.; Cao, Y. C., Excitation-Intensity-Dependent Color-Tunable Dual Emissions from Manganese-Doped CdS/ZnS Core/Shell Nanocrystals. *Angew. Chem. Int. Ed. Engl.* **2010**, *122* (52), 10330-10333.
44. Chen, H.-Y.; Maiti, S.; Son, D. H., Doping Location-Dependent Energy Transfer Dynamics in Mn-Doped CdS/ZnS Nanocrystals. *ACS Nano* **2012**, *6* (1), 583-591.
45. Pradhan, N.; Das Adhikari, S.; Nag, A.; Sarma, D. D., Luminescence, Plasmonic, and Magnetic Properties of Doped Semiconductor Nanocrystals. *Angew. Chem. Int. Ed. Engl.* **2017**, *56* (25), 7038-7054.
46. Hofman, E.; Robinson, R. J.; Li, Z.-J.; Dzikovski, B.; Zheng, W., Controlled Dopant Migration in CdS/ZnS Core/Shell Quantum Dots. *J. Am. Chem. Soc.* **2017**, *139* (26), 8878-8885.
47. Kuhn, H., A Quantum-Mechanical Theory of Light Absorption of Organic Dyes and Similar Compounds. *J. Chem. Phys.* **1949**, *17* (12), 1198-1212.
48. Yang, Y.; Chen, O.; Angerhofer, A.; Cao, Y. C., Radial-Position-Controlled Doping of CdS/ZnS Core/Shell Nanocrystals: Surface Effects and Position-Dependent Properties. *Chem. Eur. J.* **2009**, *15* (13), 3186-3197.
49. Chen, H.-Y.; Chen, T.-Y.; Son, D. H., Measurement of Energy Transfer Time in Colloidal Mn-Doped Semiconductor Nanocrystals. *J. Phys. Chem. C* **2010**, *114* (10), 4418-4423.
50. Ithurria, S.; Guyot-Sionnest, P.; Mahler, B.; Dubertret, B., Mn<sup>2+</sup> as a Radial Pressure Gauge in Colloidal Core/Shell Nanocrystal's. *Phys. Rev. Lett.* **2007**, *99* (26), 265501.
51. Medintz, I. L.; Clapp, A. R.; Mattoussi, H.; Goldman, E. R.; Fisher, B.; Mauro, J. M., Self-



- Assembled Nanoscale Biosensors Based on Quantum Dot FRET Donors. *Nat. Mater.* **2003**, *2* (9), 630-638.
52. Krivenkov, V.; Goncharov, S.; Samokhvalov, P.; Sánchez-Iglesias, A.; Grzelczak, M.; Nabiev, I.; Rakovich, Y., Enhancement of Biexciton Emission Due to Long-Range Interaction of Single Quantum Dots and Gold Nanorods in a Thin-Film Hybrid Nanostructure. *J. Phys. Chem. Lett.* **2019**, *10*, 481-486.
53. Tu, D.; Liu, L.; Ju, Q.; Liu, Y.; Zhu, H.; Li, R.; Chen, X., Time-Resolved FRET Biosensor Based on Amine-Functionalized Lanthanide-Doped NaYF<sub>4</sub> Nanocrystals. *Angew. Chem. Int. Ed. Engl.* **2011**, *123* (28), 6430-6434.
54. Gu, J.-Q.; Shen, J.; Sun, L.-D.; Yan, C.-H., Resonance Energy Transfer in Steady-State and Time-Decay Fluoro-Immunoassays for Lanthanide Nanoparticles Based on Biotin and Avidin Affinity. *J. Phys. Chem. C* **2008**, *112* (17), 6589-6593.
55. Selvin, P. R., The Renaissance of Fluorescence Resonance Energy Transfer. *Nat. Struct. Mol. Biol.* **2000**, *7*, 730.
56. Herder, M.; Schmidt, B. M.; Grubert, L.; Pätzelt, M.; Schwarz, J.; Hecht, S., Improving the Fatigue Resistance of Diarylethene Switches. *J. Am. Chem. Soc.* **2015**, *137* (7), 2738-2747.
57. Chen, O.; Chen, X.; Yang, Y.; Lynch, J.; Wu, H.; Zhuang, J.; Cao, Y. C., Synthesis of Metal-Selenide Nanocrystals Using Selenium Dioxide as the Selenium Precursor. *Angew. Chem. Int. Ed. Engl.* **2008**, *120* (45), 8766-8769.
58. Park, J.; Jiang, Q.; Feng, D.; Zhou, H.-C., Controlled Generation of Singlet Oxygen in Living Cells with Tunable Ratios of the Photochromic Switch in Metal-Organic Frameworks. *Angew. Chem. Int. Ed.* **2016**, *55* (25), 7188-7193.
59. Tam, E. S.; Parks, J. J.; Shum, W. W.; Zhong, Y.-W.; Santiago-Berrios, M. E. B.; Zheng, X.; Yang, W.; Chan, G. K. L.; Abruña, H. D.; Ralph, D. C., Single-Molecule Conductance of Pyridine-Terminated Dithienylethene Switch Molecules. *ACS Nano* **2011**, *5* (6), 5115-5123.
60. Mulder, A.; Jukovic, A.; Huskens, J.; Reinhoudt, D. N., Bis(phenylthienyl)ethene-Tethered Beta-Cyclodextrin Dimers as Photoswitchable Hosts. *Org. Biomol. Chem.* **2004**, *2* (12), 1748-1755.

## Chapter 5

# Stereoselective C–C Oxidative Coupling Reactions Photocatalyzed by Zwitterion Ligands Capped CsPbBr<sub>3</sub> Perovskite Nanocrystals

Portions of this chapter are adapted and/or reprinted from the following works. Copyright belongs to the publisher.

**Yuan, Y.**; Zhu, H.; Hills-Kimball, K.; Cai, T.; Shi, W.; Wei, Z.; Yang, H.; Candler, Y.; Wang, P.; He, J.; Chen, O.\*, Stereoselective C–C Oxidative Coupling Reactions Photocatalyzed by CsPbBr<sub>3</sub> Perovskite Nanocrystals. In preparation.

## 5.1 QDs as Catalysts in Organic Synthesis

Semiconductor QDs have been exploited in diverse practical applications including solar energy harvesting,<sup>1, 2</sup> biological imaging and labeling,<sup>3-7</sup> light-emitting diodes, and next-generation displays,<sup>8-11</sup> owing to their unique properties such as high absorbance cross sections, broad excitation spectra, tunable emission profiles, high PL QYs and superior photochemical/physical stabilities, *etc.*<sup>12-15</sup> Most recently, QDs have shown potential as good photocatalysts for organic reactions such as oxidation, reduction, and redox reactions, taking advantages of their high photo-stabilities, high absorption coefficients and long photo-generated carrier lifetimes (**Fig. 5.1**).<sup>16-34</sup> Compared to metal complexes and organic dyes as photocatalysts, colloidal QDs exhibit several advantages. Firstly, colloidal QDs can act as both photosensitizers and catalysts simultaneously, surpassing conventional photocatalytic systems where photosensitizers and catalysts are usually separated.<sup>35</sup> Secondly, unlike conventional Ru or Ir complexes, QDs (*i.e.*, CdS, CdSe, InP QDs, or perovskite NCs) do not contain precious metals. Thirdly, the surface ligands of the QDs can be easily engineered without altering the redox potentials and the absorption profiles of the QDs, in contrast to coordination compounds whose electronic structure is greatly coupled with ligand identity. Finally, the bandgap of QDs can be customized for different catalytic reactions through tuning the size and/or composition of the QDs. To date, conventional metal chalcogenide (e.g., CdSe and CdS) QDs have been heavily investigated and demonstrated as efficient photocatalysts for a series of organic reactions including C-C couplings,<sup>16, 20, 21, 30, 31, 34</sup> dehalogenations,<sup>30, 32</sup> oxidations,<sup>16, 25, 28-30</sup> polymerizations,<sup>36</sup> and cyclizations.<sup>17, 18</sup> In contrast, due to their young age as well as commonly reported instability issues, perovskite QDs have been less explored in photocatalytic reactions.<sup>37</sup> Successful examples include degradations of organic dyes,<sup>38</sup>

thiol coupling<sup>27</sup> and C-H activation reactions<sup>24, 27</sup>, and polymerizations.<sup>33</sup> Given the superior photochemical and optoelectronic properties of perovskite QDs, their full potentials in the utilizations as unique and efficient photocatalysts still need to be further investigated while resolving the major stability drawback.

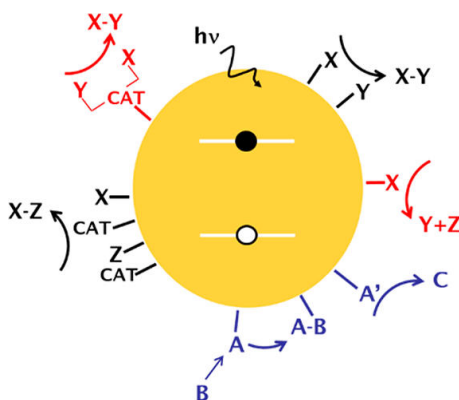


**Fig. 5.1:** Schematic illustration for different types of organic reactions photocatalyzed by semiconductor QDs. Adapted from ref 35.

Herein, we demonstrate that CsPbBr<sub>3</sub> perovskite QDs can successfully photocatalyze the stereoselective C-C oxidative homocoupling of  $\alpha$ -aryl ketonitriles under visible light (435-445 nm) illumination. Through the surface modification of CsPbBr<sub>3</sub> perovskite QDs with zwitterionic ligands, benefiting from the strong ligand chelated binding and low ligand coverage density on the particle surface, the NC stability and homocoupling reaction rate can be dramatically increased, and the stereoselectivity can be significantly improved. Our further investigation of reaction scope shows that electron-donating groups (EDGs) or large conjugated  $\pi$  system are necessary for the dimerization. Moreover, the resulting stereoselected *dl*-isomer cannot be readily accessible using other oxidants or catalysts.<sup>39, 40</sup> We propose that the reaction undergoes through radical intermediated reaction pathway on the surface of the perovskite QDs, in which a less steric hinderance leads to the favored *dl*-isomer. Our study suggests that

perovskite QDs with proper surface modification are promising photocatalysts in organic synthesis.

## 5.2 Optimization of Reaction Conditions

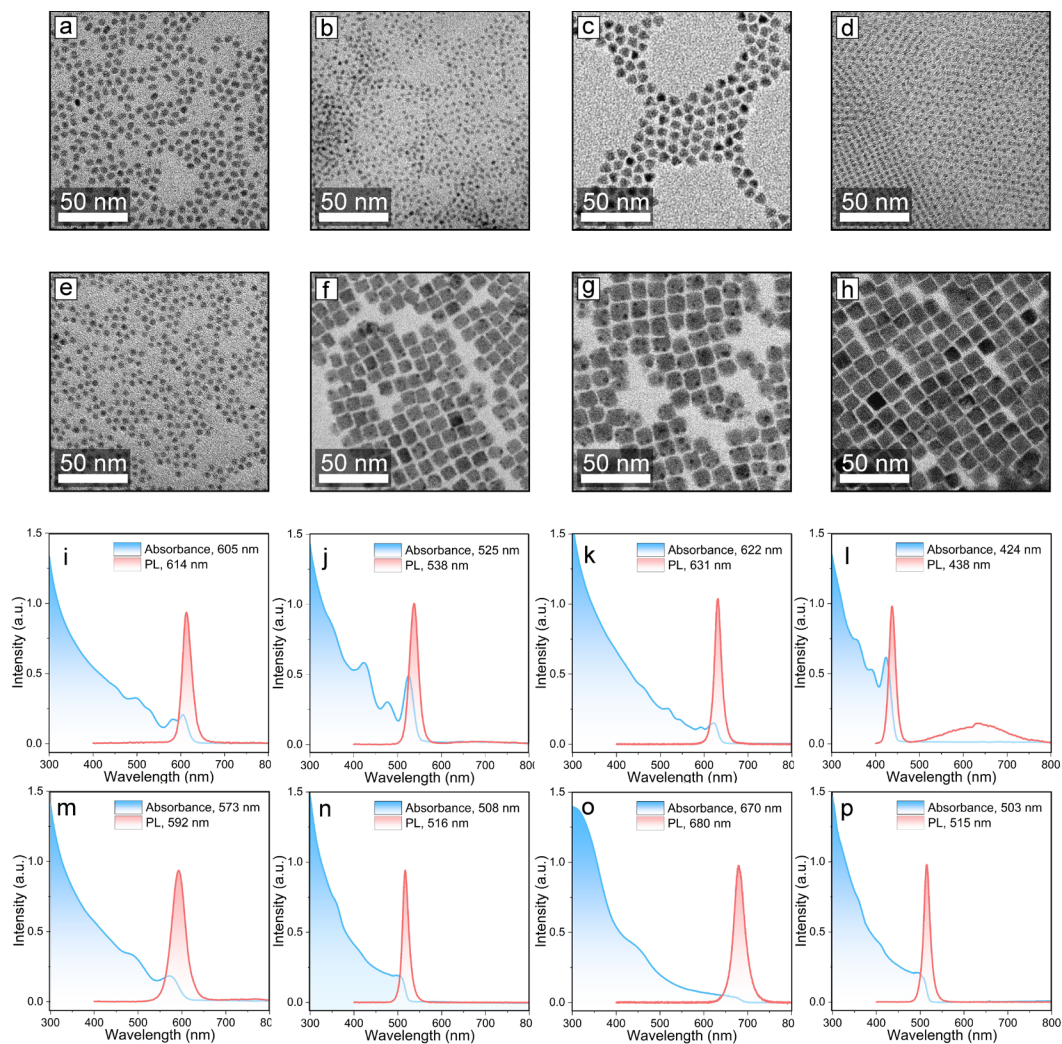


**Fig. 5.2:** TEM images, absorption (black) and PL (red) spectra for CdSe (TOP, TOPO, ODPA) (a, i), CdSe (oleate) (b, j), CdSe-CdS (oleate, OAm) (c, k), CdS (oleate) (d, l), CdS-CdSe (oleate, OAm) (e, m), CsPbBr<sub>3</sub> (oleate, OAm) (f, n), CsPbI<sub>3</sub> (oleate, OAm) (g, o), and CsPbBr<sub>3</sub> (zwitterion) (h, p) QDs, respectively.

We synthesized eight types of QDs with different compositions (*i.e.*, CdSe QDs, CdSe-CdS core-shell QDs, CdS QDs, CdS-CdSe core-shell QDs, CsPbBr<sub>3</sub> perovskite QDs, and CsPbI<sub>3</sub> perovskite QDs) and capping ligands (including TOP, ODPA, TOPO, oleate, OAm, and 3-(*N,N*- dimethyloctadecylammonio)propanesulfonate) to demonstrate

the C-C oxidative coupling of  $\alpha$ -aryl ketonitriles (See synthetic details in the Methods). All the synthesized QDs were characterized using TEM, absorption and PL spectra (**Fig. 5.2**), showing high uniformities. In particular, the zwitterionic ligand-capped colloidal CsPbBr<sub>3</sub> perovskite QDs were synthesized following a previously reported method with modifications.<sup>41</sup> The prepared CsPbBr<sub>3</sub> perovskite QDs show a cubic shape and a high morphological uniformity with an average edge length of  $10.6 \pm 1.2$  nm shown in the TEM images (**Fig. 5.2h**). The HR-TEM image shows orthogonal atomic lattice fringes with a clear visualization of the (200) plane (d-spacing of 2.9 Å) (**Fig. 5.3a**), indicating a high crystallinity of the sample with a cubic structure. The cubic perovskite crystal phase was further confirmed by the powder XRD measurement with all the Bragg diffraction peaks matching the standard peak positions (**Fig. 5.3b**). The obtained CsPbBr<sub>3</sub> perovskite QDs exhibit a narrow PL peak centered at 515 nm with a FWHM of 78 meV ( $\sim 17$  nm), similar to that of Oleate/OAm-capped CsPbBr<sub>3</sub> perovskite QDs (**Fig. 5.2o, p**).

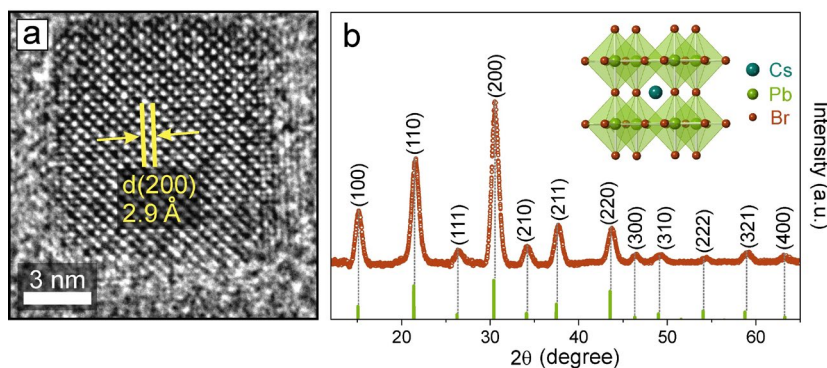
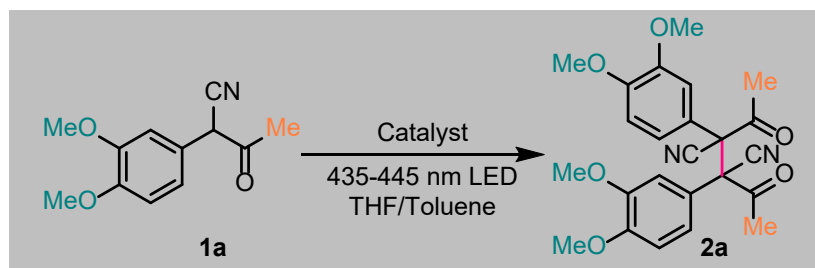


**Fig. 5.3:** Characterization of zwitterionic capped CsPbBr<sub>3</sub> perovskite QDs. (a) TEM image. Inset: edge length distribution histogram. (b) HR-TEM. (c) Absorption and emission spectra. (d) XRD patterns. The black bars show the positions of XRD peaks for bulk CsPbBr<sub>3</sub>.

With different QDs in hand, we started with 2-(3,4-dimethoxyphenyl)-3-oxobutanenitrile (**1a**) as model substrate to investigate the feasibility of the photocatalytic coupling reactions with the QDs serving as photocatalysts. With two electron-donating

methoxy groups on the phenyl ring, **1a** has been reported to convert to benzo[*b*]furan via oxidative intramolecular cyclization<sup>42</sup> or to a dimer via oxidative intermolecular C-C

**Table 5.1:** Optimization of reaction conditions.



Entry	Catalyst <sup>a</sup>	Ligands of catalyst	Time	Yield <sup>b</sup>
1	CdSe QD	TOP, TOPO,	44	99
2	CdSe QD	Oleate	15	99
3	CdSe-CdS	Oleate, OAm	63	94
4	CdS QD	Oleate	10	89
5	CdS-CdSe	Oleate, OAm	40	95
6	CsPbBr <sub>3</sub>	Oleate, OAm	1	95
7	CsPbI <sub>3</sub>	Oleate, OAm	1	97
8	CsPbBr <sub>3</sub>	Zwitterion	0.2	99
9	Zwitterion <sup>c</sup>	---	70	20
10	No	---	70	20

Reaction conditions: **1a** (0.05 mmol) in THF (0.2 mL) was added to a solution of QDs in toluene (2.8 mL) in a 4 mL vial. <sup>a</sup>The OD of absorbance was 7.7 at 440 nm for all the catalysts used. For CsPbBr<sub>3</sub> NCs, the amount was  $1.3 \times 10^{-3}$  mol%. <sup>b</sup>High performance liquid chromatography (HPLC) determined yields (**Fig. 5.4**). <sup>c</sup>0.6 mg (the calculated amount of ligand used in Entry 8).

coupling.<sup>39, 40, 43</sup> When **1a** was treated with CdSe QDs (with surface ligands of TOP, TOPO, ODPA), 99% of the dimer (**2a**) product was obtained after 44 hr of irradiation with a blue LED light source (435-445 nm). The reaction yielded a negligible amount of benzo[*b*]furan (**Table 5.1**, Entry 1). Oleate-capped CdSe QDs could shorten the reaction

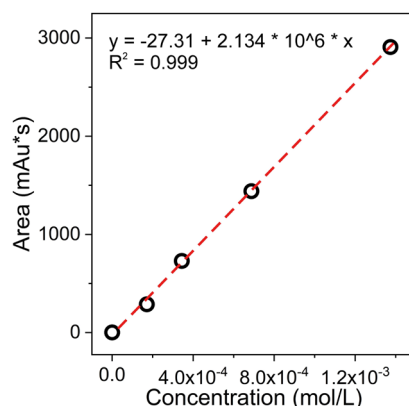


*Fig. 5.4: HPLC standard curve for product 2a. The signals were detected at 290 nm.*

time to 15 hr, which can be attributed to the increased permeability of the ligand shell (oleate compared to a combination of TOP, TOPO and ODPA) of the QDs (**Table 5.1**, Entry 2). CdSe-CdS core-shell QDs exhibited less reactivity as expected, because the photo-generated holes are largely confined in the CdSe core region due to the CdS shell passivation, limiting their accessibility to the particle surface (**Table 5.1**, Entry 3).<sup>44, 45</sup> In contrast, CdS QDs accelerated the reaction to 10 hr, while sacrificing the yield to 89% (**Table 5.1**, Entry 4). Furthermore, a CdSe shell was grown on the CdS core to form a reverse type-I structure, in which the electrons and holes generated in both CdS and CdSe can be ejected to surface shell and improve the reactivity. However, the CdS-CdSe QDs exhibited less reactivity compared to CdS QDs, which might be caused by the narrower bandgap for the CdS-CdSe (**Table 5.1**, Entry 5). In this regard, Oleate/OAm-capped CsPbX<sub>3</sub> (X = Br, and I) perovskite QDs showed a much higher reactivity compared to the conventional Cd-based QDs (**Table 5.1**, Entry 6,7). However, the instability of the CsPbI<sub>3</sub> QDs resulted in a quick particle degradation and decomposition in the reaction solution, limiting the performance of the QDs in a non-recyclable fashion. Although CsPbBr<sub>3</sub> QDs could survive in the reaction solution, we found that it is still non-feasible to recycle the CsPbBr<sub>3</sub> perovskite QD catalysts through precipitation upon addition of



poor solvent (*i.e.* ethyl acetate) due to loss of particle stability after one round of photocatalytic reaction. To overcome this stability issue, zwitterionic capping ligands attracted our attention as these types of ligands can tightly coordinate to the surface

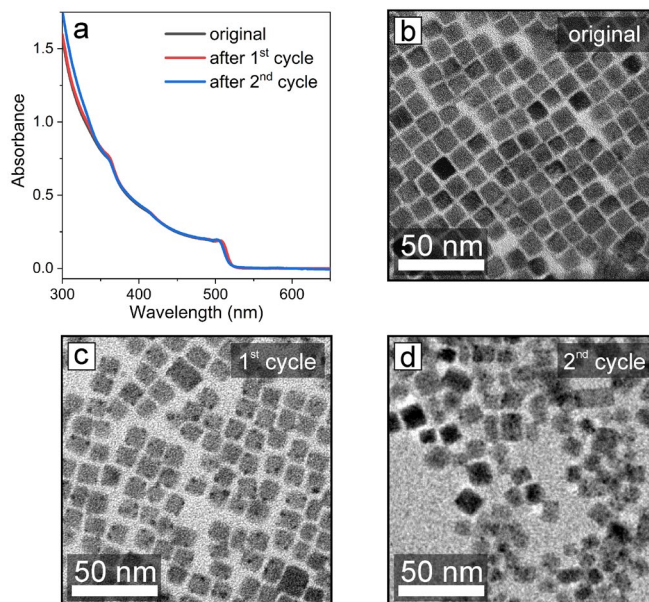


**Fig. 5.5:** Stability test of zwitterion capped CsPbBr<sub>3</sub> NCs under the optimized reaction conditions for the model reaction. (a) Absorption spectra for zwitterionic-capped CsPbBr<sub>3</sub> NCs before reaction (black), after one cycle of reaction (red), and after two cycles of reaction (blue). (b-d) TEM images for zwitterionic-capped CsPbBr<sub>3</sub> NCs before reaction (b), after one cycle of reaction (c), and after two cycles of reaction (d).

cations and anions of the perovskite QDs simultaneously.<sup>41</sup> Commercially available zwitterionic compound 3-(*N,N*-dimethyloctadecylammonio)propanesulfonate was used as the capping ligand for CsPbBr<sub>3</sub> perovskite QDs, and the resulting QD constructs were investigated for the catalytic ability. It is shown here that this zwitterionic-capped CsPbBr<sub>3</sub> QD catalyst can not only be recycled for at least three rounds of reactions without losing the particle integrity but can also significantly reduce the reaction time to merely 0.2 hr (**Table 5.1**, Entry 8 and **Fig. 5.5**). This highly enhanced reactivity can be attributed to the lower surface ligand packing density (3.0/nm<sup>2</sup> compared to 5.4/nm<sup>2</sup> for Oleate/OAm-capped CsPbBr<sub>3</sub>, see Methods for detailed characterization) and thus the

increased substrate permeability (**Fig. 5.6, 5.7**). Control experiments with the addition of only zwitterionic molecules did not show any catalytic effect, similar to control the reactions run without the addition of catalyst in the reaction system (**Table 5.1**, Entry 9,10), confirming the catalytic role played by the CsPbBr<sub>3</sub> perovskite QDs.

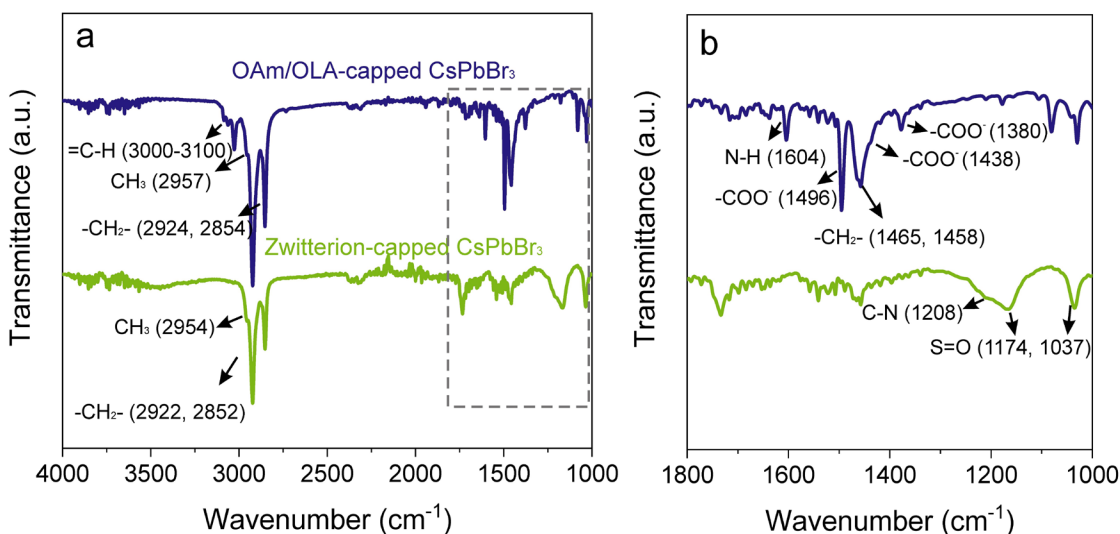


**Fig. 5.6:** FTIR spectra of zwitterion (green) and OLA/OAm (blue) capped CsPbBr<sub>3</sub> NCs. (b) Zoomed-in spectra in the dotted rectangular area in a.

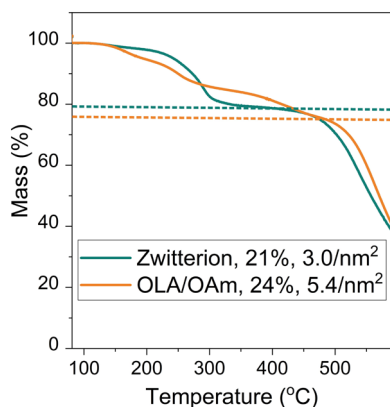


**Fig. 5.7:** TGA spectra of zwitterion (blue) and OLA/OAm (yellow) capped CsPbBr<sub>3</sub> NCs. The ligand density is ~21% for zwitterion capped CsPbBr<sub>3</sub> NCs and 24% for OLA/OAm capped CsPbBr<sub>3</sub> NCs. The calculated ligand coverage is 3.0/nm<sup>2</sup> and 5.4/nm<sup>2</sup> for zwitterion and OLA/OAm capped CsPbBr<sub>3</sub> NCs, respectively.

To unravel the catalytic role of the CsPbBr<sub>3</sub> perovskite QDs play in the coupling reaction, the reaction order was examined by monitoring the concentration evolution of

product **2a** using high performance liquid chromatography (HPLC). The concentration of **2a** increased linearly with an increase of reaction time at a reaction rate constant of  $1.167 \times 10^{-5}$  M/s during the first 10 min of the reaction and remained at  $7.4 \times 10^{-3}$  M after complete consumption of the starting material (**1a**) (**Fig. 5.8**). This result indicates that

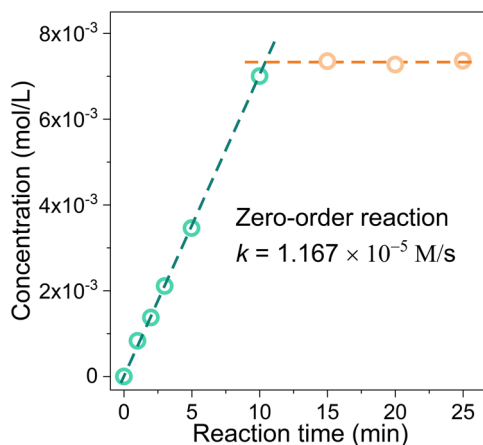


**Fig. 5.8:** HPLC-determined concentration of product **2a** vs time for the reaction under optimized reaction conditions.

the reaction is a zeroth order with respect to **1a** and demonstrates that the reaction rate is independent of the concentration of the starting substrate, thus validating the catalytic nature of this reaction (**Fig. 5.8**). It is importantly noted that all of the QDs photocatalyzed reactions studied here showed a stereoselectivity of *dl* isomer, in contrast to a mixture product of *dl*- and *meso*- isomers (*dl* : *meso* = 5 : 3, the two isomers were identified by  $^1\text{H}$  NMR spectroscopy, which will be discussed later) for the reactions without addition of QDs (see NMR data in Methods). This stereoselectivity is consistent with a previous report that the *dl*- isomer is thermodynamically more favorable than the *meso* isomer, likely caused by the attractive interaction between *gauche* cyano groups.<sup>46</sup>

### 5.3 Investigation of Reaction Scope

To explore the generality and scope of the photocatalytic reaction, various  $\alpha$ -aryl ketonitriles with different  $\text{R}^1$  and  $\text{R}^2$  groups were examined as substrates under optimized

conditions using zwitterionic ligands capped CsPbBr<sub>3</sub> perovskite QDs, and the results are summarized in **Fig. 5.9**. As EDGs and conjugated  $\pi$  systems can stabilize free radical intermediates,<sup>47</sup> we investigated the photocatalytic reactions using the substrates with

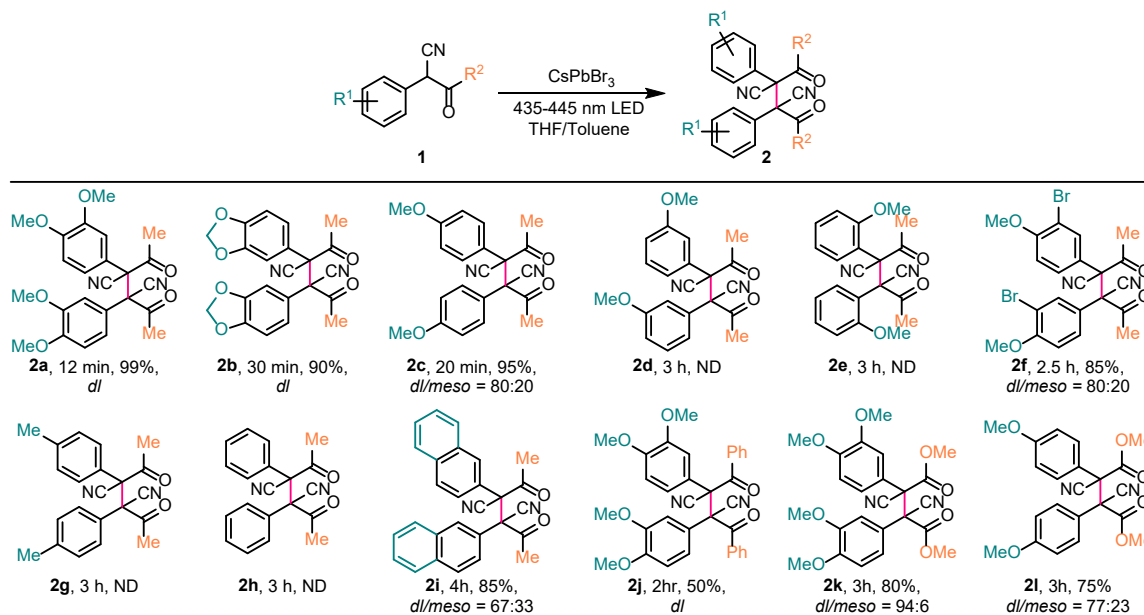


**Fig. 5.9:** Oxidative dimerization of  $\alpha$ -aryl ketonitriles photocatalyzed by zwitterionic-capped CsPbBr<sub>3</sub> NCs. General conditions: substrate **1** (0.05 mmol) in a THF (0.2 mL) was added to a solution of CsPbBr<sub>3</sub> NCs in toluene (2.8 mL, OD at 440 nm = 7.7) in a 4 mL vial, and the resulting mixture was irradiated using a blue LED (435-445 nm) light source at room temperature.

different substituents on the benzene ring (**Fig. 5.9**). The substrates bearing EDGs on the *para*-position of the benzene ring could produce corresponding dimers efficiently (**Fig. 5.9, 2a-c**), whereas no desired products were generated when EDGs were on the *ortho*- or *meta*-positions (**Fig. 5.9, 2d, e**). The less electron-donating effect from the methoxy group at *meta*-position could explain the failure of dimerization, revealing a necessity of sufficient electron-donating effect for the reaction to occur (**Fig. 5.9, 2d**). Although the methoxy group on the *ortho*-position was supposed to facilitate the reaction due to a stronger electron-donating effect, the consequently induced steric effect as the *ortho*-methoxy group is close to the benzylic position may hinder the reaction that was

responsible for the production of negligible amount of dimers (**Fig. 5.9, 2e**). For the substrates with electron-withdrawing bromo group on the *meta*-position of the benzene ring, the dimerization reaction rate was reduced with a reaction yield of 85% dimer products (*dl/meso* = 80:20) for a course of 2.5 hours reaction time (**Fig. 5.9, 2f**). For substrates with a weaker EDG (methyl group) on the *para*-position or without functional groups on the aromatic ring, no desired dimer products were obtained, confirming the requisite of strong EDGs on the benzene ring for the reaction to occur (**Fig. 5.9, 2g,h**). Expansion of the conjugated  $\pi$ -system of the substrate can also generate desired dimer products (*dl/meso* = 67:33) with a yield of 85% in a 4h reaction time (**Fig. 5.9, 2i**). We expand the reaction scope further by altering the R<sup>2</sup> from methyl group to an aryl or methoxy group (**Fig. 5.9, 2j-l**). In both cases, dimerization reaction occurred and resulted in the corresponding products with reasonable yields (**Fig. 5.9, 2j-l**). Regarding stereoselectivity, all of the successful dimerization products studied here showed a

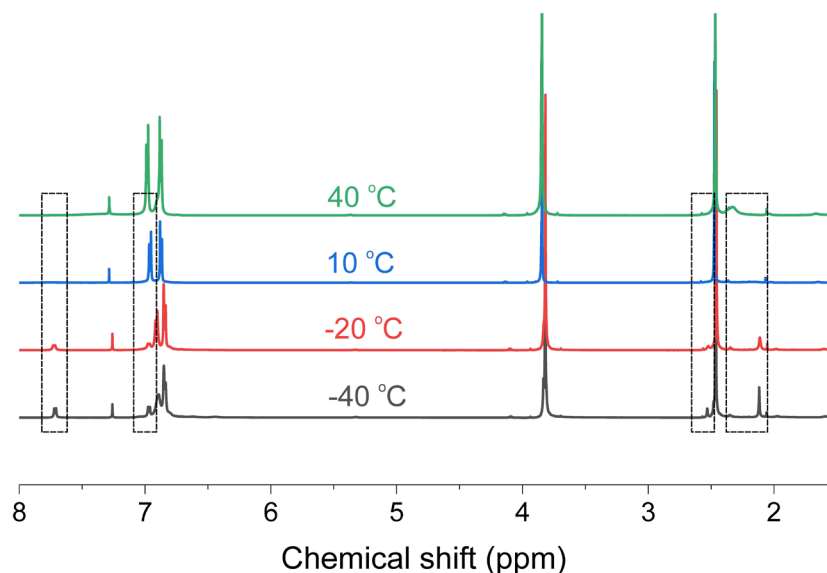


**Fig. 5.10:** Variable temperature <sup>1</sup>H NMR experiment for product 2c. At high temperature ( $\geq 10$  °C), two conformations of meso isomer exchange slower than NMR timescale, showing a broad peak for COCH<sub>3</sub> and the peaks of H<sub>arom</sub> merge together with the *dl* isomer. With the decrease of temperature, COCH<sub>3</sub> peaks of the two conformations split to two peaks (shown in the two right rectangular areas) and H<sub>arom</sub> peaks are shown in the two left rectangular areas.

avored *dl*-isomer stereoselectivity, especially for the substrates with large substituted groups on the aromatic ring, in which cases solely *dl*-isomers were obtained (Fig. 5.9, 2a, b, j).

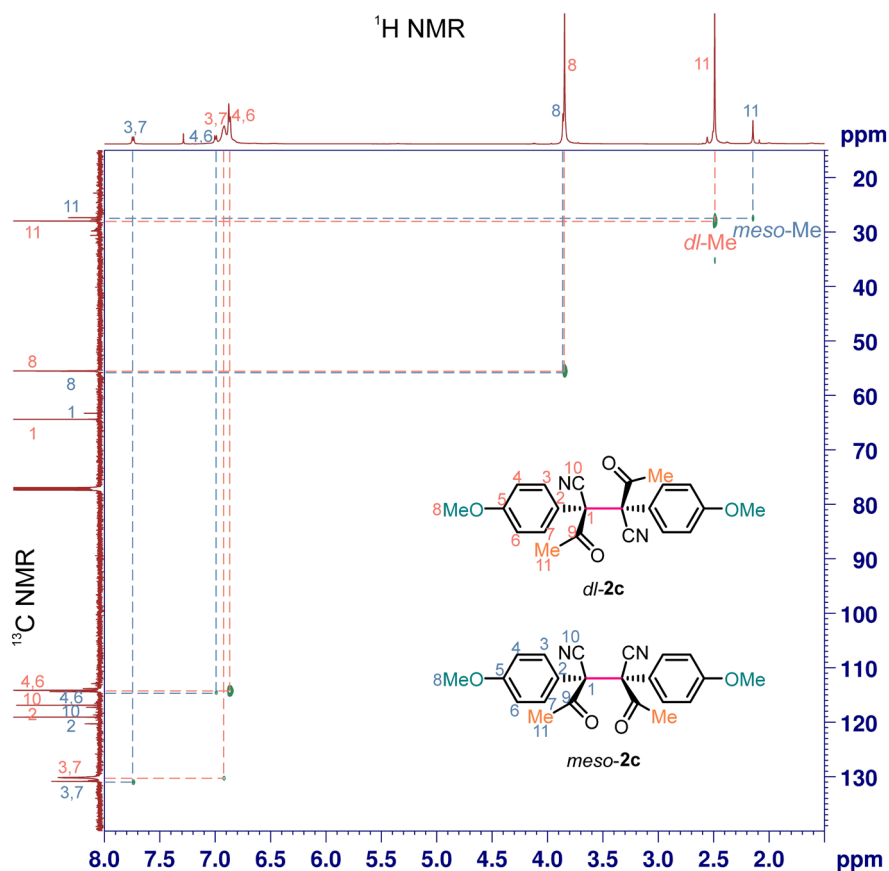


**Fig. 5.11:** Heteronuclear single quantum coherence spectroscopy (HSQC) NMR spectrum of product **2c** at  $-40\text{ }^{\circ}\text{C}$ . The correlations of carbon and hydrogens are labelled as pink for the *dl* isomer and as blue for the *meso* isomer in the 2D plot.

In the cases where a mixture of the two isomers was obtained, the two isomers could be distinguished using NMR spectroscopy. For example, in product **2c**, new peaks appeared around 2.35 ppm in the  $^1\text{H}$ -NMR spectrum for the methyl group protons in the  $\text{R}^2$  position for the *meso* isomer. This peak is very broad as it consists of two conformations of the *meso* isomer that exchange more slowly than the NMR time scale. The other peaks of the *meso* isomer in both the  $^1\text{H}$ -NMR and  $^{13}\text{C}$ -NMR spectra merged

with all of the *dl* isomer peaks at room temperature. Variable temperature NMR spectra were run for **2c**, and all of the peaks for *meso*-**2c** can be identified at -40 °C (**Fig. 5.10**). The heteronuclear single quantum coherence spectroscopy (HSQC) spectrum of **2c** at -40 °C further confirmed the characterization of *meso*-**2c** (**Fig. 5.11**).

#### 5.4 Mechanism Study and Proposed Mechanism

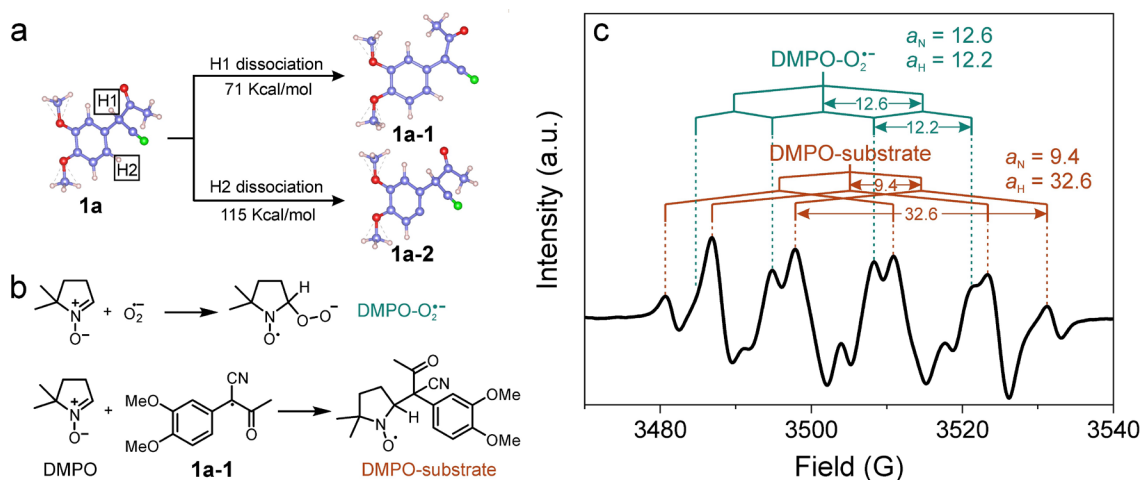


**Fig. 5.12:** Mechanism study of photo-induced oxidative coupling of 2-(3,4-dimethoxyphenyl)-3-oxobutanenitrile. (a) Comparison of bond cleavage energies of the C-H1 and C-H2 bonds of 2-(3,4-dimethoxyphenyl)-3-oxobutanenitrile. (b) Reaction schemes showing the generation of DMPO-superoxide and DMPO-substrate species upon addition of radical trapping agent DMPO. (c) EPR spectrum of a toluene/THF (2.8 mL/0.2 mL) solution of CsPbBr<sub>3</sub> NCs (OD @ 440 nm = 7.7), DMPO (0.05 mmol) and 2-(3,4-dimethoxyphenyl)-3-oxobutanenitrile (**1a**, 0.05 mmol) after irradiation for 20 min.

As mentioned above,  $\alpha$ -aryl ketonitriles can be converted to benzo[*b*]furans or dimers under oxidative conditions. However, in the current reaction system, only the dimerization products were obtained for all the substrates inspected. To scrutinize the underlining mechanism, density functional theory (DFT) calculations were performed to obtain the bond dissociation energy for the C-H1 and C-H2 bonds of **1a** to form the corresponding radicals, which are the intermediates for the two possible product, *i.e.* dimer and benzo[*b*]furan. (**Fig. 5.12a** and Methods). The DFT calculations show that the

C-H1 bond possesses a smaller bond dissociation energy of 71 Kcal/mol than that for the C-H2 bond (115 Kcal/mol), making the C-H1 bond easier to break when treated with an oxidative reagent (**Fig. 5.12a**). As a result, only dimerization occurs in the current reaction conditions. To further elucidate the mechanism and confirm the presence of the tertiary carbon radical formed from C-H1 bond cleavage (**1a-1**), EPR spectroscopy measurements were carried out using 5,5-dimethyl-pyrroline *N*-oxide (DMPO) as a radical scavenger.<sup>28</sup> It was found that with an irradiation for 20 min, a DMPO-superoxide adduct was generated in the presence of CsPbBr<sub>3</sub> perovskite QDs (**Fig. 5.13**). When substrate **1a** was added in the reaction system simultaneously, two sets of splitting peaks were obtained in the EPR spectrum, which were assigned to DMPO-superoxide species ( $a_N = 12.6$ ,  $a_H = 12.2$ ) and DMPO-substrate species ( $a_N = 9.4$ ,  $a_H = 32.6$ ) (**Fig. 5.12b, c**).<sup>20</sup> The EPR results proved that the formation of radicals and our proposed radical pathway discussed below.

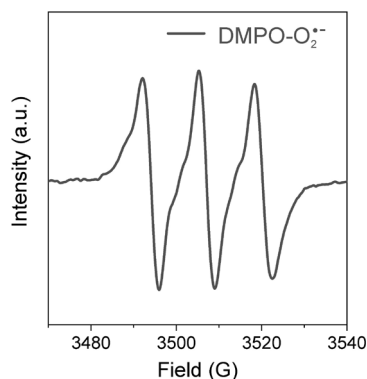


**Fig. 5.13:** EPR spectrum of toluene/THF (2.8 mL/0.2 mL) solution of CsPbBr<sub>3</sub> (OD @ 440 nm = 7.7), DMPO (0.05 mmol) after irradiation for 20 min.

Based on the reaction results and mechanistic study, a proposed mechanism describing the reaction process is illustrated in **Fig. 5.15**. Upon visible light irradiation, one electron is excited from the valence band to the conduction band in CsPbBr<sub>3</sub> perovskite QDs, which will further react with O<sub>2</sub> to form a superoxide radical.



Meanwhile, the hole left in the valence band of the CsPbBr<sub>3</sub> QDs oxidizes the substrate to form a radical intermediate, two of which then come together to form a dimer. In addition, X-ray photoelectron spectroscopy (XPS) analysis shows the coexistence of Pb-Br bond and Pb-zwitterion bond, indicating that the CsPbBr<sub>3</sub> perovskite QDs possess a Pb-rich

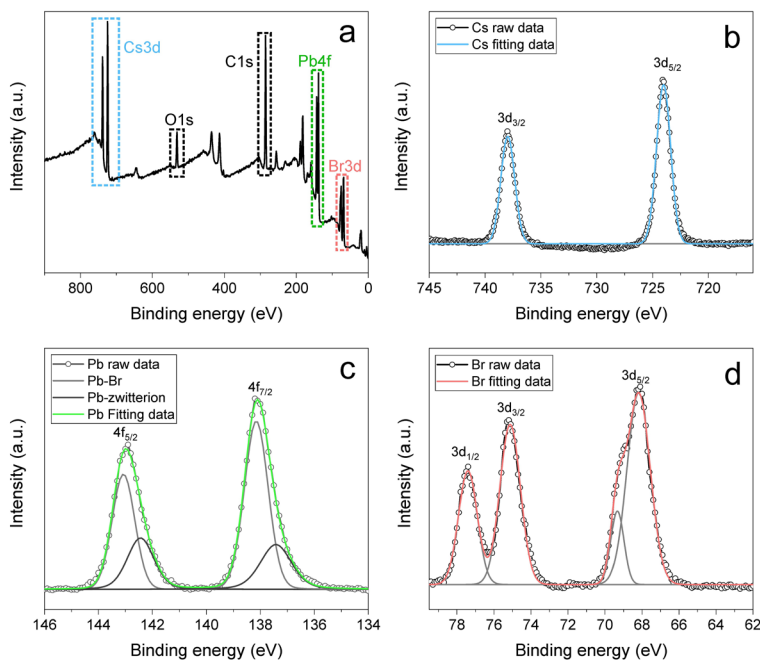


**Fig. 5.14:** (a) An XPS survey spectrum of the zwitterionic ligand capped CsPbBr<sub>3</sub> NCs. (b) Cs 3d spectrum. (c) Pb 4f spectrum. (d) Br 3d spectrum.

surface, agrees with previous reports (Fig. 5.14).<sup>48</sup> Thus, we propose that the oxygen atom of the carbonyl group of the radical intermediate can serve as a L-type of ligands and dynamically attach on surface Pb atoms through donating a lone pair electrons of oxygen (Fig. 5.15). Consequently, *dl*- or *meso*-isomers can be formed depending on the relative configuration of the two radical intermediates. In this case, the trans-arrangement of the two radicals exhibits less steric hinderance from the large aryl groups during the C-C bond-formation process, making the *dl*- configuration more favorable compared to the *meso*-isomer (Fig. 5.15). This proposed mechanism explains well the stereoselective dimerization reaction observed in our experiments (Fig. 5.9). To validate the proposed

mechanism and prove that the hole, rather than the superoxide formed during the reaction,

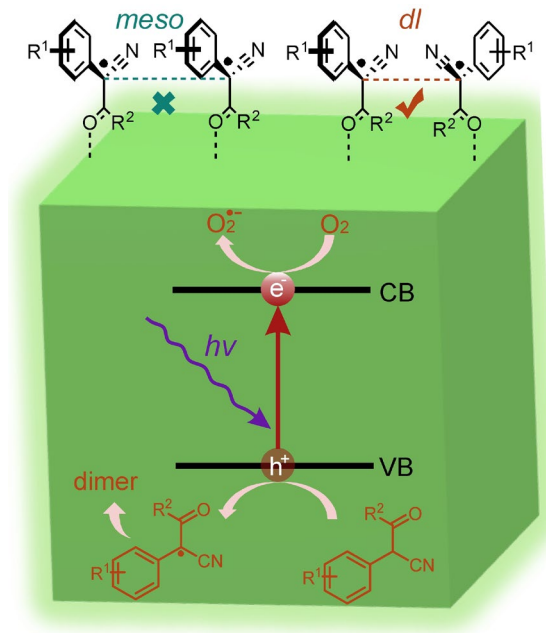


**Fig. 5.15:** Proposed mechanism for the stereoselective dimerization of  $\alpha$ -aryl ketonitriles photocatalyzed by zwitterionic-capped CsPbBr<sub>3</sub> perovskite NCs.

is acting as the oxidative reagent for the dimerization, substrate **1a** was directly treated with superoxide, resulting, however, no detectable desired dimer products (see Methods for reaction details). This control experiment result further supports our proposed free-radical based reaction pathway.

In conclusion, we demonstrate the stereoselective C-C oxidative dimerization of  $\alpha$ -aryl ketonitriles photocatalyzed by various QDs under visible light illumination. Upon optimization of reaction conditions, zwitterionic ligand capped CsPbBr<sub>3</sub> perovskite QDs are chosen as the desired photocatalyst, exhibiting high stability and reactivity. Kinetic study shows a zeroth order reaction with respect to substrate concentration, indicative of the catalytic capability of the CsPbBr<sub>3</sub> perovskite QDs. By employing zwitterionic-capped CsPbBr<sub>3</sub> NCs as photocatalysts, various starting materials with different substituents on the aryl ring and varied functional moieties were investigated, showing

EDG (OMe) on the *para*-position of the aryl ring or an extended conjugated  $\pi$  system is necessary for dimerization under current reaction conditions. Mechanistic studies through both DFT calculations and EPR measurements prove a free-radical based dimerization reaction pathway for this photocatalytic reaction. We propose that the observed stereoselectivity is attributed to the steric hinderance effect from the large aryl groups of the applied substrats during the dimerization process on the QD surface. Our study shows that Pb-halide perovskite QDs with an optimized surface modification hold the potential to bring a series of new insights in a range of photochemical synthesis.

## Methods

\* (for UV-Vis absorption measurements, PL, lifetime and QY measurements, TEM measurements, and XRD measurements, see Ch.2)

### *Chemicals:*

All chemicals were used without further purification unless otherwise specified.

*Chemicals for syntheses of QDs:* Cadmium oxide (CdO, 99.998%), 1-octadecene (ODE, technical grade, 90%), trioctylphosphine oxide (TOPO 99%), trioctylphosphine (TOP, 97%), oleylamine (OAm, technical grade, 70%), 1-octanethiol (> 98.5%), selenium dioxide (SeO<sub>2</sub>,  $\geq$  99.9% trace metal basis)sulfur powder (99.98%), cesium carbonate (Cs<sub>2</sub>CO<sub>3</sub>, 99.9%), lead(II) bromide (PbBr<sub>2</sub>, 99.999%) and 3-(*N,N*-dimethyloctadecylammonio)propanesulfonate ( $\geq$  99.0%) were obtained from Sigma Aldrich; selenium powder (Se, 99.999%), oleic acid (OLA, technical grade, 90%), and lead(II) iodide (PbI<sub>2</sub>, 98.5%) were purchased from Alfa Aesar; n-octadecylphosphonic acid (ODPA, > 99%) was purchased from PCI Synthesis. *Chemicals for syntheses of organic compounds:* (3,4-dimethoxyphenyl)acetonitrile (98%), 3-methoxyphenylacetonitrile (99%), 4-methoxyphenylacetonitrile (97), 4-methylbenzyl cyanide (98%), benzyl cyanide (98%), 2-naphthylacetonitrile (97%), dimethyl carbonate

(ReagentPlus, 99%), sodium hydride (60 % dispersion in mineral oil), and potassium superoxide (KO<sub>2</sub>, power) were obtained from Sigma Aldrich; 3-bromo-4-methoxyphenylacetonitrile (99%), and ethyl benzoate (99%) were purchased from Alfa Aesar; 2-methoxyphenylacetonitrile (98%) and tetrabutylammonium perchlorate (TBAP, > 98%) were purchased from TCI Chemicals; tetrahydrofuran (THF), ethyl acetate (EtOAc), and toluene were purchased from Fisher Scientific. THF and toluene were sparged for 20 min with dry Ar and dried using a commercial two-column solvent purification system (LC Technologies).

*Synthesis of CdSe (TOP, HPA, ODPa capped) core QDs:*

CdSe core QDs were synthesized by a hot-injection method as previously reported.<sup>12</sup> Typically, CdO (120 mg, 0.934 mmol), ODPa (560 mg, 1.674 mmol) and TOPO (6 g) were loaded into a 100 mL flask. The resulting mixture was heated to 150 °C and was degassed for 1 hour under vacuum with stirring. The reaction solution was then heated to 360 °C under nitrogen to form a colorless clear solution. After adding 4.0 mL TOP, the temperature was increased to 380 °C and a freshly prepared Se/TOP (120 mg Se (1.520 mmol) in 1.0 mL TOP) solution was swiftly injected into the flask. The reaction was quenched by removing the heating mantle and by blowing cool air after 90 seconds. The resulting CdSe core QDs were diluted in hexane as stock.

*Synthesis of CdSe-CdS core-shell QDs:*

Synthesis of CdSe-CdS core-shell QDs was carried out following previous a procedure with minor modifications.<sup>44</sup> Typically, 200 nmol of CdSe (TOP, HPA, ODPa capped) core QDs (purified one time by acetone) were loaded into a 50 mL 3-neck flask with a solvent mixture of 2 mL ODE and 2 mL OAm. The reaction mixture was

degassed under vacuum at room temperature for 1 hour and 120 °C for 10 min to remove hexane, water and oxygen. The reaction mixture was then heated to 310 °C under nitrogen for shell growth. When temperature reached 220 °C, a desired amount of Cd-oleate (0.1 M in ODE) and 1.2 equivalence of 1-octanethiol (0.12 M in ODE) were injected slowly into the reaction mixture simultaneously using a syringe pump with a rate of two monolayers of CdS shell per hour. The reaction was stopped by removing the heating mantle and cooling down to room temperature after one hour. The synthesized CdSe-CdS QDs were purified by three rounds of precipitation and redispersion using acetone/methanol and hexane. The particles were finally suspended in toluene as stock.

*Synthesis of CdSe (oleate capped) core QDs:*

Oleate capped CdSe core QDs were synthesized by a heating-up method as previously reported.<sup>49</sup> Cadmium myristate (0.1 mmol) and SeO<sub>2</sub> (0.1 mmol) were added to ODE (6 mL) in a three-neck flask. The resulting mixture was pumped for 5 min at room temperature and then heated to 240 °C, at which temperature the reaction stayed for 20 min. The reaction was stopped by removing the heating mantle. After cooling down to room temperature, the resulting NCs were purified by three rounds of precipitation and redispersion using acetone/methanol and hexane. 1 mL of OLA was added to help dissolve and stabilize the NCs in the second round of purification. The particles were finally suspended in toluene as stock.

*Synthesis of CdS core QDs:*

CdS core QDs were prepared following a previously published approach with minor modification.<sup>50</sup> Typically, CdO (12.9 mg 0.1 mmol) and OLA (508.4 mg, 1.8 mmol) were mixed with ODE (4.4 mL) in a 25 mL three-neck flask. The resulting

solution was pumped for 10 min at room temperature and then was heated to 260 °C under N<sub>2</sub> to dissolve CdO completely. After that, 1 mL sulfur/ODE (0.05 M) was injected into the solution, and the reaction solution was kept at 230 °C for 7 min. The reaction was stopped by removing the heating mantle. The unreacted precursors were separated by extraction of the reaction mixtures dissolved in hexanes with methanol for 3 times. After reaction, the CdS NCs were precipitated with acetone and then redispersed in toluene for shell growth.

*Synthesis of CdS-CdSe core-shell QDs:*

CdS-CdSe core-shell QDs were synthesized following a previously published approach with minor modification.<sup>50</sup> CdS core QDs (50 nmol), ODE (3 mL) and OAm (1 mL) were loaded into a 50 mL three-neck flask. The resulting solution was pumped at room temperature for 1 hr and 120 °C for 10 min to remove the hexanes and air. Then the reaction mixture was heated to 220 °C under N<sub>2</sub> for the shell growth layer by layer. Cd-oleate (0.2 M in ODE) and selenium (0.2 M in ODE, suspension) were injected into the reaction solution simultaneously, and the reaction time was 20 min after each injection. Two monolayers of CdSe were grown in this reaction. The synthesized CdS-CdSe QDs were purified by three rounds of precipitation and redispersion using acetone/methanol and hexane. The particles were finally suspended in toluene as stock.

*Syntheses of CsPbX<sub>3</sub> (X = Br, I) perovskite QDs:*

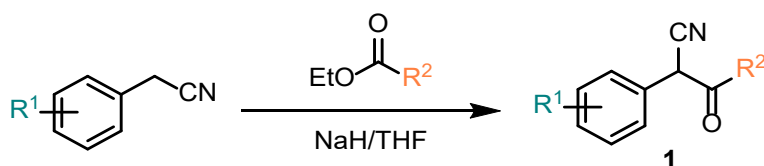
CsPbX<sub>3</sub> perovskite QDs were synthesized following a modified literature procedure.<sup>51</sup> ODE (5 mL), OAm (0.5 mL), OLA (0.5 mL) and PbX<sub>2</sub> (0.188 mmol, 70.0 mg PbBr<sub>2</sub> or 86.7 mg PbI<sub>2</sub>) were loaded into a 25 mL three-neck flask and the reaction mixture was pumped at 120 °C for 1 hr. Then the temperature was raised to 180 °C and

0.4 mL of a Cs-oleate solution (0.125 M in ODE) was injected swiftly and the reaction mixture was cooled by an ice-water bath. The prepared NCs were separated by centrifugation. After centrifugation, the supernatant was discarded and the perovskite NCs were redispersed in toluene as stock.

*Synthesis of 3-(N,N-dimethyloctadecylammonio)propanesulfonate capped CsPbBr<sub>3</sub> QDs:*

The zwitterionic ligands capped colloidal CsPbBr<sub>3</sub> QDs were synthesized following a previously reported method with minor modification.<sup>41</sup> For the typical synthesis, Cs-oleate (2.4 mL, 0.4 M), Pb-oleate (3.0 mL, 0.5 M), 3-(N,N-dimethyloctadecylammonio)propanesulfonate (252 mg, 0.6 mmol), and ODE (30 mL) were added to a 100 mL three-neck flask, the resulting mixture of which was purged three times and then heated to 160 °C under N<sub>2</sub>, at which temperature, TMS-Br (380 μL, 2.9 mmol) was injected. The resulting crude solution was immediately cooled-down to room temperature by immersion in an ice-water bath. The impurities were centrifuged down while the supernatant was collected and was purified by addition of EtOAc and centrifugation. The prepared NCs were re-dispersed in toluene for further use.

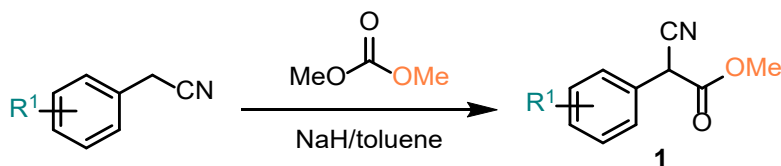
*General procedure I for the syntheses of α-aryl ketonitriles (1a-1j):*



The syntheses of α-aryl ketonitriles followed a previously reported method.<sup>52</sup> Generally, NaH (13 mmol) was added to a solution of substituted cyanide (10 mmol) in dry THF (30 mL) slowly under flowing N<sub>2</sub> with stirring in an ice-water bath. The ice-water bath was removed after the addition of NaH and the reaction mixture was stirred at

room temperature for 1hr, followed by addition of carboxylic ester (12 mmol). The resulting mixture was then heated to 60 °C and kept at this temperature until full consumption of the substituted cyanide occurred. After, the reaction was cooled to room temperature and the insoluble salts were collected on a Buchner funnel and washed with ethyl acetate, and then were dissolved in cold water (100 mL) with vigorous stirring. Then, HCl solution (1 mmol/L in water) was added to the solution to precipitate the  $\alpha$ -aryl ketonitriles. The precipitate was collected on the Buchner funnel and washed with water ( $3 \times 15$  mL). The residual water was removed by pumping at 45 °C overnight, and the products could be used without further purification. In cases where no insoluble salts were generated, the reaction mixture was dissolved in cold water (50 mL), followed by addition of 1 N HCl solution dropwise under vigorous stirring until the solution was neutral. EtOAc ( $3 \times 30$  mL) was then used to extract the  $\alpha$ -aryl ketonitriles. The organic layers were combined and dried with anhydrous  $\text{Na}_2\text{SO}_4$ , followed by evaporation to remove the solvent under vacuum. The residues were purified by flash column chromatography.

*General procedure II for the syntheses of  $\alpha$ -aryl ketonitriles (2k, 2l):*



Compounds **2k** and **2l** were synthesized following a previous reported method with minor modification.<sup>53</sup>  $\text{NaH}$  (20 mmol) was slowly added to a solution of substituted cyanide (10 mmol) and dimethyl carbonate (50 mmol) in dry toluene (20 mL) under vigorous stirring in an ice-water bath. Then the resulting mixture was heated to 80 °C and was kept at this temperature for 5 hr. After cooling to room temperature, 1N HCl solution



was added dropwise to the reaction mixture to dissolve the solid formed during the reaction. Then the product was extracted with EtOAc (3 × 30 mL). The combined organic extracts were dried over anhydrous Na<sub>2</sub>SO<sub>4</sub> and concentrated under vacuum. The residues were purified by flash column chromatography.

*General procedure for the dimerization of  $\alpha$ -aryl ketonitriles photocatalyzed by QDs:*

A solution of QDs in toluene (2.8 mL, absorbance at 440 nm = 7.7 AU) was added to a solution of  $\alpha$ -aryl ketonitrile **1** (0.05 mmol) in a THF (0.2 mL) in a 4 mL vial. The resulting solution was irradiated under stirring using a micro photochemical reactor (blue LED lights, 435-445 nm, Sigma Aldrich, ALDKIT001-1EA,) until the TLC indicated that the total consumption of the  $\alpha$ -aryl ketonitrile **1**. Six vials of same reaction were usually run simultaneously. After consumption of the substrate completely, the mixtures in the six vials were combined and 18 mL of EtOAc was added to the mixture to precipitate QDs. QDs were recycled by centrifugation with a speed of 6000 rpm for 5 min. The product in supernatant was treated with water (30 mL) and then extracted with EtOAc (3 × 30 mL). The organic phase was combined and washed with brine (1 × 30 mL), then dried over anhydrous Na<sub>2</sub>SO<sub>4</sub>. The desired pure product was obtained by silica gel chromatography using a mixture of hexanes and EtOAc as eluent.

*Reaction with superoxide:*

KO<sub>2</sub> salt was used as the source for the generation of superoxide, with the addition of TBAP to increase the solubility of KO<sub>2</sub>.<sup>54</sup> The reaction was run in the glovebox. KO<sub>2</sub> (0.05 mmol) and TBAP (0.3 mmol) were added to MeCN (3 mL) in a 4 mL vial, generating a clear solution, followed by addition of substrate **1a** (0.05 mmol)

with stirring. After 30 min, the reaction mixture was taken out of the glovebox and diluted with DMSO, then was treated with a dilute HCl solution. There was only substrate and no desired product detected with TLC.

*XPS measurement of zwitterionic ligand capped CsPbBr<sub>3</sub> QDs:*

XPS spectra were measured on a Thermo Scientific KAlpha+ instrument operating on Al K $\alpha$ =1486.6 eV radiation with a spot size of  $\sim 200 \mu\text{m}$ . Sample dispersed in toluene was dropped on silicon wafers and the toluene was allowed to evaporate with gentle heating.

*TGA of CsPbBr<sub>3</sub> QDs:*

The ligand density of CsPbBr<sub>3</sub> NCs was measured by a thermogravimetric analyzer (TA Instruments model Q500) under a nitrogen atmosphere. The samples were first dissolved in hexane and were then transferred to a TGA platinum pan and dried in air. In order to totally remove the residual solvent, the samples were first heated up to 80 °C at a heating rate of 10 °C/min and kept isothermal for 60 minutes. The weight loss of the samples was then recorded by heating up to 600 °C with a rate of 6 °C/min.

*DFT calculations:*

DFT calculations were performed with Vienna *ab initio* Simulation Package (VASP) code<sup>55, 56</sup> with the projector augmented wave (PAW) potentials method<sup>57</sup> to describe the electron-ion interaction. The generalized gradient approximation (GGA) in the scheme of Perdew–Burke–Ernzerhof (PBE) was used to describe the exchange and correlation interactions.<sup>58</sup> The plane-wave cut-off energy was set to 520 eV, and a  $\Gamma$ -centered  $k$ -point mesh with  $7 \times 7 \times 1$  was employed for sampling the Brillouin zone. The lattice parameters and atomic positions were fully relaxed until the force on each atom

was smaller than  $0.01 \text{ eV/\AA}$ , the convergence threshold of energy for the self-consistent was  $10^{-6} \text{ eV}$ .

The cleavage energy ( $E_c$ ) of the hydrogen ions was determined by using following equation,

$$E_c = E_{M-H} + E_H - E_M$$

where  $E_{M-H}$ ,  $E_H$ , and  $E_M$  are the total energies of removing a H atom from M, one H atom, and a M molecule.

*NMR spectroscopy:*

$^1\text{H}$  and  $^{13}\text{C}$  NMR spectra were acquired on 400 or 600 MHz Bruker NMR instruments at  $25 \text{ }^\circ\text{C}$  unless otherwise specified. NMR chemical shifts are reported in ppm and are referenced to the residual solvent peak for  $\text{CDCl}_3$  ( $\delta = 7.26 \text{ ppm}$ ,  $^1\text{H}$  NMR;  $\delta = 77.16 \text{ ppm}$ ,  $^{13}\text{C}$  NMR) as an internal standard. Data are reported as follows: chemical shift, multiplicity (s = singlet, d = doublet, t = triplet, dd = doublet of doublets, m = multiplet, br = broad). Coupling constants ( $J$ ) are reported in Hertz (Hz).

*HRMS measurements:*

HRMS was obtained on a Q-TOF micro spectrometer equipped with an electrospray (ESI) ionization source.

*HPLC measurements:*

HPLC data were acquired on Agilent 1260 Infinite LC. This system consisted of a quaternary pump, autosampler, thermostatted column compartment, diode array detector (190–950 nm), and fraction collector.

*Ligand density calculations:*

$$\text{Density} = \frac{\frac{m_{\text{ligand}}}{M_{\text{ligand}}} \times 6.02 \times 10^{23} / \text{mol}}{A}} = \frac{\frac{m_{\text{particle}}}{\%_{\text{particle}}} \times \%_{\text{ligand}}}{M_{\text{ligand}}} \times 6.02 \times 10^{23} / \text{mol}}{A}$$

In which,  $m_{\text{ligand}}$  is the mass of ligand per nanoparticle,  $M_{\text{ligand}}$  is the molar mass of ligand,  $m_{\text{particle}}$  is the mass of per inorganic CsPbBr<sub>3</sub> particle,  $\%_{\text{particle}}$  and  $\%_{\text{ligand}}$  are the percentage of inorganic core and organic ligand shell, and  $A$  is the surface area for one nanoparticle.

$$m_{\text{particle}} = \rho \times V = 4.42 \text{ g/cm}^3 \times (10.6 \text{ nm})^3 = 5.26 \times 10^{-18} \text{ g}$$

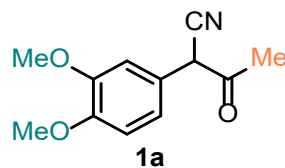
$$A = 10.6 \text{ nm} \times 10.6 \text{ nm} = 674.16 \text{ nm}^2$$

$$\text{Density}_{\text{zwitterion}} = \frac{\frac{\frac{5.26 \times 10^{-18} \text{ g} \times 21\%}{79\%}}{419.71 \text{ g/mol}} \times 6.02 \times 10^{23} / \text{mol}}{674.16 \text{ nm}^2} = 3.0 / \text{nm}^2$$

$$\text{Density}_{\text{OLA/OAm}} = \frac{\frac{\frac{5.26 \times 10^{-18} \text{ g} \times 24\%}{76\%}}{274.98 \text{ g/mol}} \times 6.02 \times 10^{23} / \text{mol}}{674.16 \text{ nm}^2} = 5.4 / \text{nm}^2$$

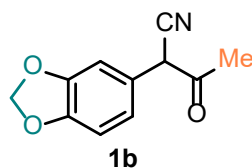
## NMR Characterization Data

### 2-(3,4-Dimethoxyphenyl)-3-oxobutanenitrile (1a)<sup>59</sup>



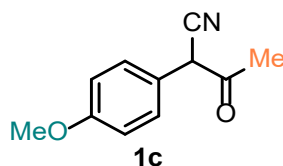
Following the general procedure I, **1a** was obtained after drying. Yield: 90%, 1.9 g, white solid. <sup>1</sup>H NMR (400 MHz, CDCl<sub>3</sub>) Enol:  $\delta$  6.95 (dd,  $J$  = 8.2, 1.9 Hz, 1H, H<sub>arom</sub>), 6.91 (d,  $J$  = 8.2 Hz, 1H, H<sub>arom</sub>), 6.89 (d,  $J$  = 1.9 Hz, 1H, H<sub>arom</sub>), 6.27 (s, 1H, OH), 3.90 (s, 3H, OCH<sub>3</sub>), 3.90 (s, 3H, OCH<sub>3</sub>), 2.32 (s, 3H, COCH<sub>3</sub>).

### 2-(Benzo[*d*][1,3]dioxol-5-yl)-3-oxobutanenitrile (1b)<sup>60</sup>



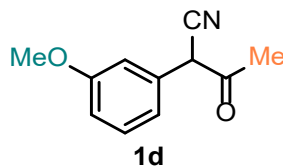
Following the general procedure I, **1b** was obtained after drying. Yield: 85%, 1.7 g, white solid.  $^1\text{H}$  NMR (400 MHz,  $\text{CDCl}_3$ ) Enol:  $\delta$  6.85-6.83 (m, 3H,  $\text{H}_{\text{arom}}$ ), 6.33 (s, 1H, OH), 6.00 (s, 2H,  $\text{OCH}_2\text{O}$ ), 2.31 (s, 3H,  $\text{COCH}_3$ ). Keto:  $\delta$  6.85-6.83 (m, 3H,  $\text{H}_{\text{arom}}$ ), 6.01 (s, 2H,  $\text{OCH}_2\text{O}$ ), 4.57 (s, 1H, CH), 2.26 (s, 3H,  $\text{COCH}_3$ ).

### 2-(4-Methoxyphenyl)-3-oxobutanenitrile (1c)<sup>61</sup>



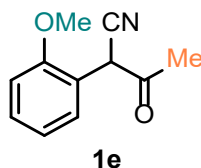
Following the general procedure I, **1c** was obtained after drying. Yield: 92%, 1.7 g, white solid.  $^1\text{H}$  NMR (400 MHz,  $\text{CDCl}_3$ ) Enol:  $\delta$  7.35-7.29 (m, 2H,  $\text{H}_{\text{arom}}$ ), 6.97-6.94 (m, 2H,  $\text{H}_{\text{arom}}$ ), 6.27 (s, 1H, OH), 3.82 (s, 3H,  $\text{OCH}_3$ ), 2.32 (s, 3H,  $\text{COCH}_3$ ). Keto: 7.35-7.29 (m, 2H,  $\text{H}_{\text{arom}}$ ), 6.97-6.94 (m, 2H,  $\text{H}_{\text{arom}}$ ), 4.61 (s, 1H, CH), 3.82 (s, 3H,  $\text{OCH}_3$ ), 2.24 (s, 3H,  $\text{COCH}_3$ ).

### 2-(3-Methoxyphenyl)-3-oxobutanenitrile (1d)<sup>62</sup>



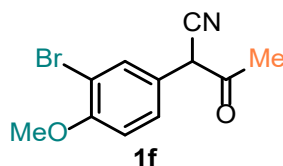
Following the general procedure I, **1d** was obtained after drying. Yield: 91%, 1.7 g, white solid.  $^1\text{H}$  NMR (400 MHz,  $\text{CDCl}_3$ ) Enol:  $\delta$  7.36 (t, 1H,  $J = 8.0$  Hz,  $\text{H}_{\text{arom}}$ ), 6.99 (d,  $J = 7.6$  Hz, 1H,  $\text{H}_{\text{arom}}$ ), 6.96 (s, 1H,  $\text{H}_{\text{arom}}$ ), 6.99 (dd,  $J = 8.4, 2.2$  Hz, 1H,  $\text{H}_{\text{arom}}$ ), 6.58 (s, 1H, OH), 3.82 (s, 3H,  $\text{OCH}_3$ ), 2.34 (s, 3H,  $\text{COCH}_3$ ).

### 2-(2-Methoxyphenyl)-3-oxobutanenitrile (1e)



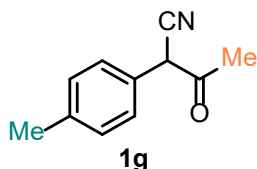
Following the general procedure I, **1e** was obtained after drying. Yield: 86%, 1,6 g, white solid.  $^1\text{H}$  NMR (400 MHz,  $\text{CDCl}_3$ ) Keto: 7.41-7.35 (m, 2H,  $\text{H}_{\text{arom}}$ ), 7.03 (td,  $J = 7.6, 1.0$  Hz, 1H,  $\text{H}_{\text{arom}}$ ), 6.95 (d,  $J = 8.3$  Hz, 1H,  $\text{H}_{\text{arom}}$ ), 5.01 (s, 1H, CH), 3.88 (s, 3H,  $\text{OCH}_3$ ), 2.23 (s, 3H,  $\text{COCH}_3$ ).  $^{13}\text{C}$  NMR (150 MHz,  $\text{CDCl}_3$ )  $\delta$  197.0, 156.4, 131.0, 129.8, 121.6, 119.2, 116.5, 111.4, 55.9, 45.8, 27.6.

### 2-(3-Bromo-4-methoxyphenyl)-3-oxobutanenitrile (1f)<sup>42</sup>



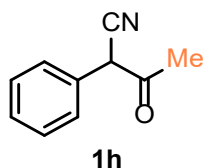
Following the general procedure I, **1f** was purified by silica gel chromatography (EtOAc/hexanes = 1/2). Yield: 84%, 2.2 g, white solid.  $^1\text{H}$  NMR (600 MHz,  $\text{DMSO-}d_6$ ) Enol:  $\delta$  11.78 (s, 1H, OH), 7.83 (d,  $J = 2.3$  Hz, 1H,  $\text{H}_{\text{arom}}$ ), 7.54 (dd,  $J = 8.8, 2.3$  Hz, 1H,  $\text{H}_{\text{arom}}$ ), 6.89 (d,  $J = 8.8$  Hz, 1H,  $\text{H}_{\text{arom}}$ ), 3.84 (s, 3H,  $\text{OCH}_3$ ), 2.31 (s, 3H,  $\text{COCH}_3$ ).

### 3-Oxo-2-(p-tolyl)butanenitrile (1g)<sup>62</sup>



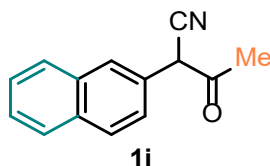
Following the general procedure I, **1g** was purified by silica gel chromatography (EtOAc/hexanes = 1/2). Yield: 90%, 1.6 g, white solid.  $^1\text{H}$  NMR (400 MHz,  $\text{CDCl}_3$ ) Enol:  $\delta$  7.31 (d,  $J = 8.0$  Hz, 2H,  $\text{H}_{\text{arom}}$ ), 7.25 (d,  $J = 8.0$  Hz, 2H,  $\text{H}_{\text{arom}}$ ), 6.35 (s, 1H, OH), 2.37 (s, 3H,  $\text{CH}_3$ ), 2.33 (s, 3H,  $\text{COCH}_3$ ).

### 3-oxo-2-phenylbutanenitrile (1h)<sup>63</sup>



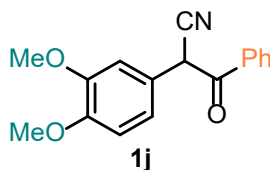
Following the general procedure I, **1h** was purified by silica gel chromatography (EtOAc/hexanes = 1/3). Yield: 91%, 1.4 g, white solid. <sup>1</sup>H NMR (400 MHz, CDCl<sub>3</sub>) Enol: δ 7.45-7.33 (m, 5H, H<sub>arom</sub>), 6.44 (s, 1H, OH), 2.35 (s, 3H, COCH<sub>3</sub>). Keto: 7.45-7.33 (m, 5H, H<sub>arom</sub>), 4.68 (s, 1H, CH), 2.27 (s, 3H, COCH<sub>3</sub>).

**2-(Naphthalen-2-yl)-3-oxobutanenitrile (1i)**<sup>62</sup>



Following the general procedure I, **1i** was purified by silica gel chromatography (EtOAc/hexanes = 1/3). Yield: 80%, 1.7 g, white solid. <sup>1</sup>H NMR (400 MHz, CDCl<sub>3</sub>) Keto: 7.92-7.87 (m, 4H, H<sub>arom</sub>), 7.57-7.55 (m, 2H, H<sub>arom</sub>), 7.43 (dd, *J* = 8.6, 1.8 Hz, 1H, H<sub>arom</sub>), 4.84 (s, 1H, CH), 2.29 (s, 3H, COCH<sub>3</sub>).

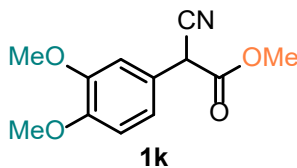
**2-(3,4-Dimethoxyphenyl)-3-oxo-3-phenylpropanenitrile (1j)**



Following the general procedure I, **1j** was purified by silica gel chromatography (EtOAc/hexanes = 1/2). Yield: 82%, 2.3 g, white solid. <sup>1</sup>H NMR (600 MHz, CDCl<sub>3</sub>) Enol: δ 7.87 (d, *J* = 7.0 Hz, 2H, H<sub>arom</sub>), 7.51-7.47 (m, 3H, H<sub>arom</sub>), 7.14 (dd, *J* = 8.3, 1.2 Hz, 1H, H<sub>arom</sub>), 7.07 (s, 1H, H<sub>arom</sub>), 6.95 (d, *J* = 8.3 Hz, 1H, H<sub>arom</sub>), 6.45 (s, 1H, OH), 3.92 (s, 3H, OCH<sub>3</sub>), 3.91 (s, 3H, OCH<sub>3</sub>). Keto: δ 7.94 (d, *J* = 7.4 Hz, 2H, H<sub>arom</sub>), 7.38-7.33 (m, 3H, H<sub>arom</sub>), 7.29 (d, *J* = 7.6 Hz, 1H, H<sub>arom</sub>), 6.89 (s, 1H, H<sub>arom</sub>), 6.84 (d, *J* = 8.4 Hz, 1H, H<sub>arom</sub>), 6.77-6.71 (m, 1H, H<sub>arom</sub>), 5.53 (s, 1H, CH), 3.86 (s, 3H, OCH<sub>3</sub>), 3.85 (s, 3H, OCH<sub>3</sub>). <sup>13</sup>C NMR (150 MHz, CDCl<sub>3</sub>) Enol: δ 164.1, 150.1, 149.6, 131.4,

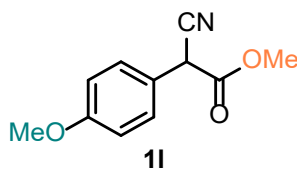
128.8, 128.3, 123.8, 121.4, 120.1, 112.0, 111.9, 89.0, 56.1, 56.1, 46.5. Keto:  $\delta$  189.2, 134.5, 133.1, 130.9, 129.4, 129.1, 128.7, 122.2, 121.1, 112.6, 111.3, 110.9, 56.1, 56.0, 55.7.

**Methyl 2-cyano-2-(3,4-dimethoxyphenyl)acetate (1k)<sup>64</sup>**



Following the general procedure II, **1k** was purified by silica gel chromatography (EtOAc/hexanes = 1/2). Yield: 80%, 1.9 g, light yellow oil. <sup>1</sup>H NMR (400 MHz, CDCl<sub>3</sub>) Keto: 6.98 (dd,  $J$  = 8.3 Hz, 2.1 Hz, 1H, H<sub>arom</sub>), 6.91 (d,  $J$  = 2.1 Hz, 1H, H<sub>arom</sub>), 6.85 (d,  $J$  = 8.3 Hz, 1H, H<sub>arom</sub>), 4.67 (s, 1H, CH), 3.88 (s, 3H, OCH<sub>3</sub>), 3.86 (s, 3H, OCH<sub>3</sub>), 3.78 (s, 3H, COOCH<sub>3</sub>).

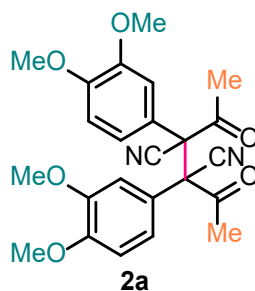
**Methyl 2-cyano-2-(4-methoxyphenyl)acetate (1l)**



Following the general procedure II, **1l** was purified by silica gel chromatography (EtOAc/hexanes = 1/3). Yield: 81%, 1.7 g, light yellow oil. <sup>1</sup>H NMR (600 MHz, CDCl<sub>3</sub>) Keto:  $\delta$  7.36 (d,  $J$  = 8.4 Hz, 2H, H<sub>arom</sub>), 6.92 (d,  $J$  = 8.4 Hz, 2H, H<sub>arom</sub>), 4.68 (s, 1H, CH), 3.80 (s, 3H, OCH<sub>3</sub>), 3.78 (s, 3H, COOCH<sub>3</sub>). <sup>13</sup>C NMR (150 MHz, CDCl<sub>3</sub>)  $\delta$  165.9, 160.3, 129.3, 121.8, 115.9, 114.8, 55.5, 53.9, 42.8.

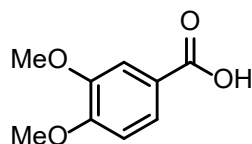
**2,3-Diacetyl-2,3-bis(3,4-dimethoxyphenyl)succinonitrile (2a)**





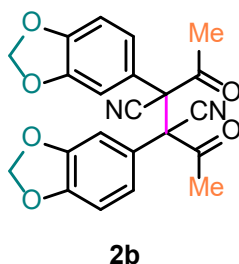
Following the general procedure for dimerization photocatalyzed by QDs, **2a** was purified by silica gel chromatography (EtOAc/hexanes = 1/2). Yield: 99%, 130 mg, white solid.  $^1\text{H}$  NMR (400 MHz,  $\text{CDCl}_3$ ) *dl*:  $\delta$  6.82 (d,  $J=8.5$  Hz, 1H,  $\text{H}_{\text{arom}}$ ), 6.65 (dd,  $J=8.5, 2.2$  Hz, 1H,  $\text{H}_{\text{arom}}$ ), 6.48 (d,  $J=1.8$  Hz, 1H,  $\text{H}_{\text{arom}}$ ), 3.89 (s, 3H,  $\text{OCH}_3$ ), 3.70 (s, 3H,  $\text{OCH}_3$ ), 2.48 (s, 3H,  $\text{COCH}_3$ ). *meso* (observed when no QDs added):  $\delta$  7.14 (dd,  $J=8.4, 2.2$  Hz, 1H,  $\text{H}_{\text{arom}}$ ), 6.95 (d,  $J=2.2$  Hz, 1H,  $\text{H}_{\text{arom}}$ ), 6.91 (d,  $J=8.4$  Hz, 1H,  $\text{H}_{\text{arom}}$ ), 3.90 (s, 3H,  $\text{OCH}_3$ ), 3.89 (s, 3H,  $\text{OCH}_3$ ), 2.32 (s, 3H,  $\text{COCH}_3$ ).  $^{13}\text{C}$  NMR (100 MHz,  $\text{CDCl}_3$ ) *dl*:  $\delta$  197.9, 150.5, 148.9, 121.9, 120.1, 117.2, 111.9, 111.0, 65.2, 56.1, 56.0, 27.8. HRMS (ESI) *m/z* calculated for  $\text{C}_{24}\text{H}_{28}\text{N}_3\text{O}_6$  [ $\text{M} + \text{NH}_4^+$ ] 454.1973, found 454.1956.

### 3,4-Dimethoxybenzoic acid



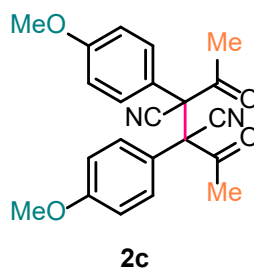
3,4-Dimethoxybenzoic acid was generated in dimerization of **1a** with  $\text{O}_2$ .  $^1\text{H}$  NMR (400 MHz,  $\text{CDCl}_3$ )  $\delta$  9.73 (br s, 1H, OH), 7.87 (dd,  $J=8.4, 2.1$  Hz, 1H,  $\text{H}_{\text{arom}}$ ), 7.52 (d,  $J=2.1$  Hz, 1H,  $\text{H}_{\text{arom}}$ ), 7.02 (d,  $J=8.4$  Hz, 1H,  $\text{H}_{\text{arom}}$ ), 4.02 (s, 3H,  $\text{OCH}_3$ ), 3.96 (s, 3H,  $\text{OCH}_3$ ).

### 2,3-Diacetyl-2,3-bis(benzo[*d*][1,3]dioxol-5-yl)succinonitrile (2b)



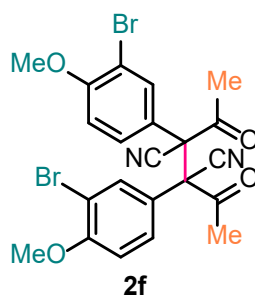
Following the general procedure for dimerization photocatalyzed by QDs, **2b** was purified by silica gel chromatography (EtOAc/hexanes = 1/2). Yield: 90%, 109 mg, white solid. <sup>1</sup>H NMR (600 MHz, CDCl<sub>3</sub>) *dl*: δ 6.77 (d, *J* = 8.8 Hz, 1H, H<sub>arom</sub>), 6.58-6.57 (m, 2H, H<sub>arom</sub>), 6.03 (d, *J* = 1.0 Hz, 2H, CH<sub>2</sub>), 2.46 (s, 3H, COCH<sub>3</sub>). <sup>13</sup>C NMR (150 MHz, CDCl<sub>3</sub>) *dl*: δ 197.7, 149.4, 148.4, 123.6, 121.4, 117.0, 109.3, 108.6, 102.1, 65.0, 27.8. HRMS (ESI) *m/z* calculated for C<sub>22</sub>H<sub>20</sub>N<sub>3</sub>O<sub>6</sub> [M + NH<sub>4</sub><sup>+</sup>] 422.1347, found 422.1348.

**2,3-Diacetyl-2,3-bis(4-methoxyphenyl)succinonitrile (2c)**



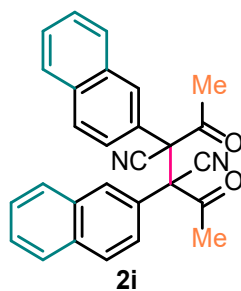
Following the general procedure for dimerization photocatalyzed by QDs, **2c** was purified by silica gel chromatography (EtOAc/hexanes = 1/2). Yield: 95%, 107 mg, white solid. <sup>1</sup>H NMR (400 MHz, CDCl<sub>3</sub>) *dl*: δ 6.95 (d, *J* = 9.2 Hz, 2H, H<sub>arom</sub>), 6.85 (d, *J* = 9.2 Hz, 2H, H<sub>arom</sub>), 3.82 (s, 3H, OCH<sub>3</sub>), 2.45 (s, 3H, COCH<sub>3</sub>). *meso*: δ 6.95 (d, *J* = 9.2 Hz, 2H, H<sub>arom</sub>), 6.85 (d, *J* = 9.2 Hz, 2H, H<sub>arom</sub>), 3.82 (s, 3H, OCH<sub>3</sub>), 2.33 (br s, 3H, COCH<sub>3</sub>). <sup>13</sup>C NMR (100 MHz, CDCl<sub>3</sub>) *dl*: δ 198.0, 161.0, 130.5, 119.8, 117.1, 114.4, 64.9, 55.5, 27.8. *meso*: δ 198.0, 160.9, 130.5, 119.8, 117.1, 114.4, 64.9, 55.5, 27.8. <sup>1</sup>H NMR (-40 °C, 600 MHz, CDCl<sub>3</sub>) *dl*: δ 6.89 (br s, 2H, H<sub>arom</sub>), 6.84 (d, *J* = 8.3 Hz, 2H, H<sub>arom</sub>), 3.82 (s, 3H, OCH<sub>3</sub>), 2.46 (s, 3H, COCH<sub>3</sub>). *meso*: δ 7.71 (d, *J* = 8.7 Hz, 2H, H<sub>arom</sub>), 6.97 (d, *J* = 8.7 Hz, 2H, H<sub>arom</sub>), 3.83 (s, 3H, OCH<sub>3</sub>), 2.53 (s, 3/4H, COCH<sub>3</sub>), 2.12 (s, 9/4H, COCH<sub>3</sub>). <sup>13</sup>C NMR (-40 °C, 150 MHz, CDCl<sub>3</sub>) *dl*: δ 198.3, 160.5, 130.2, 119.1, 116.9, 114.2, 64.4, 55.5, 28.0. *meso*: δ 195.5, 160.5, 130.9, 130.7, 120.3, 117.3, 114.4, 113.8, 63.3, 55.6, 27.4. HRMS (ESI) *m/z* calculated for C<sub>22</sub>H<sub>24</sub>N<sub>3</sub>O<sub>4</sub> [M + NH<sub>4</sub><sup>+</sup>] 394.1761, found 394.1759.

**2,3-Diacetyl-2,3-bis(3-bromo-4-methoxyphenyl)succinonitrile (2f)**



Following the general procedure for dimerization photocatalyzed by QDs, **2f** was purified by silica gel chromatography (EtOAc/hexanes = 1/2). Yield: 85%, 136 mg, white solid.  $^1\text{H}$  NMR (400 MHz,  $\text{CDCl}_3$ ) *dl*:  $\delta$  7.11 (d,  $J = 2.4$  Hz, 1H,  $\text{H}_{\text{arom}}$ ), 6.99 (dd,  $J = 8.8, 2.4$  Hz, 1H,  $\text{H}_{\text{arom}}$ ), 6.89 (d,  $J = 8.8$  Hz, 1H,  $\text{H}_{\text{arom}}$ ), 3.94 (s, 3H,  $\text{OCH}_3$ ), 2.48 (s, 3H,  $\text{COCH}_3$ ). *meso*:  $\delta$  7.11 (d,  $J = 2.4$  Hz, 1H,  $\text{H}_{\text{arom}}$ ), 6.99 (dd,  $J = 8.8, 2.4$  Hz, 1H,  $\text{H}_{\text{arom}}$ ), 6.89 (d,  $J = 8.8$  Hz, 1H,  $\text{H}_{\text{arom}}$ ), 3.94 (s, 3H,  $\text{OCH}_3$ ), 2.37 (br s, 3H,  $\text{COCH}_3$ ).  $^{13}\text{C}$  NMR (100 MHz,  $\text{CDCl}_3$ ) *dl*:  $\delta$  197.4, 157.7, 134.0, 129.2, 120.9, 116.4, 112.5, 111.8, 64.3, 56.6, 27.9. *meso*:  $\delta$  197.4, 157.5, 134.0, 129.2, 120.9, 116.4, 112.5, 111.8, 64.3, 56.6, 27.9. HRMS (ESI)  $m/z$  calculated for  $\text{C}_{22}\text{H}_{22}\text{Br}_2\text{N}_3\text{O}_4$  [ $\text{M} + \text{NH}_4^+$ ] 549.9972, found 549.9963.

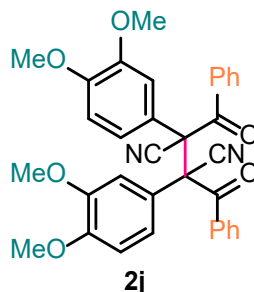
### 2,3-Diacetyl-2,3-di(naphthalen-2-yl)succinonitrile (2i)



Following the general procedure for dimerization photocatalyzed by QDs, **2i** was purified by silica gel chromatography (EtOAc/hexanes = 1/2). Yield: 85%, 96 mg, light yellow solid.  $^1\text{H}$  NMR (600 MHz,  $\text{CDCl}_3$ ) *dl*:  $\delta$  7.85 (d,  $J = 8.2$  Hz, 2H,  $\text{H}_{\text{arom}}$ ), 7.76 (d,  $J = 8.7$  Hz, 1H,  $\text{H}_{\text{arom}}$ ), 7.70 (d,  $J = 8.2$  Hz, 1H,  $\text{H}_{\text{arom}}$ ), 7.60-7.51 (m, 2 H,  $\text{H}_{\text{arom}}$ ), 7.05 (d,  $J = 7.9$  Hz, 1H,  $\text{H}_{\text{arom}}$ ), 2.54 (s, 3H,  $\text{COCH}_3$ ). *meso*:  $\delta$  7.86 (d,  $J = 8.2$  Hz, 1H,  $\text{H}_{\text{arom}}$ ), 7.60-7.50 (m, 6 H,  $\text{H}_{\text{arom}}$ ), 2.34 (br s, 3H,  $\text{COCH}_3$ ).  $^{13}\text{C}$  NMR (150 MHz,  $\text{CDCl}_3$ ) *dl*:  $\delta$  197.8, 133.6, 132.7, 129.6, 129.0, 128.8, 128.1, 127.7, 127.3, 125.4, 125.2, 117.0, 65.5, 28.0. *meso*:  $\delta$  197.8, 133.6, 132.7, 129.6, 128.9, 128.8, 128.1, 127.7, 127.2, 125.4, 125.2, 117.0, 65.5, 28.0. HRMS (ESI)  $m/z$  calculated for  $\text{C}_{28}\text{H}_{24}\text{N}_3\text{O}_2$

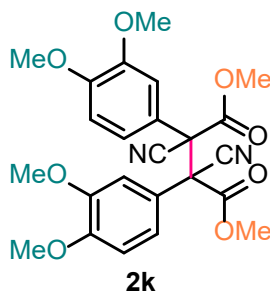
[M + NH<sub>4</sub><sup>+</sup>] 434.1863, found 434.1861.

**2,3-Dibenzoyl-2,3-bis(3,4-dimethoxyphenyl)succinonitrile (2j)**



Following the general procedure for dimerization photocatalyzed by QDs, **2j** was purified by silica gel chromatography (EtOAc/hexanes = 1/2). Yield: 50%, 84 mg, white solid. <sup>1</sup>H NMR (600 MHz, CDCl<sub>3</sub>) *dl*: δ 7.81 (d, *J* = 7.6 Hz, 2H, H<sub>arom</sub>), 7.55 (t, *J* = 7.0 Hz, 1H, H<sub>arom</sub>), 7.38 (t, *J* = 7.5 Hz, 1H, H<sub>arom</sub>), 6.85 (d, *J* = 8.1 Hz, 1H, H<sub>arom</sub>), 6.78 (s, 1H, H<sub>arom</sub>), 6.58 (s, 1H, H<sub>arom</sub>), 3.90 (s, 3H, OCH<sub>3</sub>), 3.67 (s, 3H, OCH<sub>3</sub>). <sup>13</sup>C NMR (150 MHz, CDCl<sub>3</sub>) *dl*: δ 190.6, 150.4, 148.9, 134.1, 133.8, 130.5, 128.6, 122.6, 121.5, 118.1, 112.5, 111.1, 64.4, 56.1, 56.0. HRMS (ESI) *m/z* calculated for C<sub>34</sub>H<sub>32</sub>N<sub>3</sub>O<sub>6</sub> [M + NH<sub>4</sub><sup>+</sup>] 578.2286, found 578.2281.

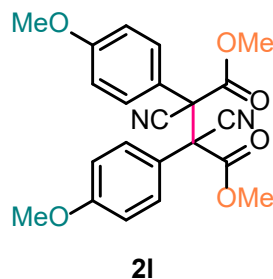
**Dimethyl 2,3-dicyano-2,3-bis(3,4-dimethoxyphenyl)succinate (2k)**



Following the general procedure for dimerization photocatalyzed by QDs, **2k** was purified by silica gel chromatography (EtOAc/hexanes = 1/2). Yield: 80%, 112 mg, white solid. <sup>1</sup>H NMR (400 MHz, CDCl<sub>3</sub>) *dl*: δ 6.81 (d, *J* = 8.5 Hz, 1H, H<sub>arom</sub>), 6.74 (dd, *J* = 8.5, 2.4 Hz, 1H, H<sub>arom</sub>), 6.54 (d, *J* = 2.4 Hz, 1H, H<sub>arom</sub>), 3.95 (s, 3H, COOCH<sub>3</sub>), 3.88 (s, 3H, OCH<sub>3</sub>), 3.69 (s, 3H, OCH<sub>3</sub>). *meso*: δ 6.81 (d, *J* = 8.5 Hz, 1H, H<sub>arom</sub>), 6.74 (dd, *J* = 8.5, 2.4 Hz, 1H, H<sub>arom</sub>), 6.54 (d, *J* = 2.4 Hz, 1H, H<sub>arom</sub>), 3.89 (s, 3H, OCH<sub>3</sub>), 3.82 (s, 3H, COOCH<sub>3</sub>), 3.77 (s, 3H, OCH<sub>3</sub>). <sup>13</sup>C NMR (150 MHz, CDCl<sub>3</sub>) δ 166.9, 150.6, 148.6, 121.6, 120.9, 115.7, 111.9, 110.8, 60.4, 56.1, 56.0, 54.9. HRMS

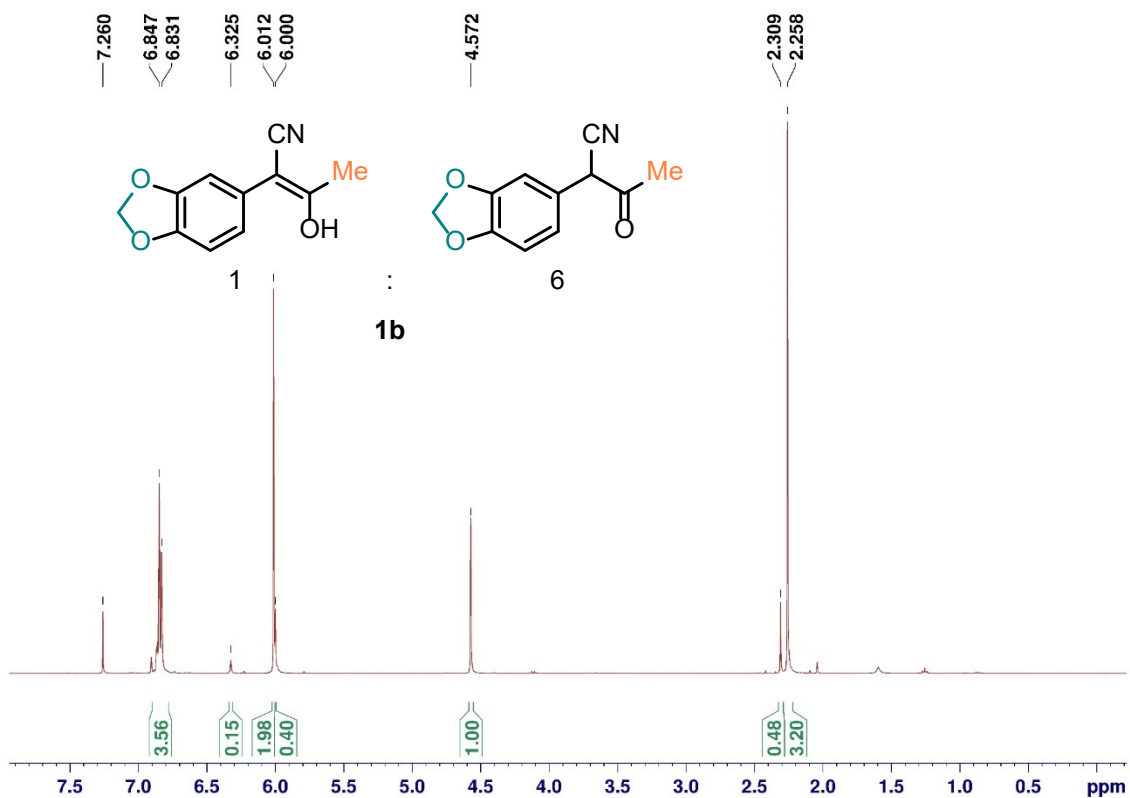
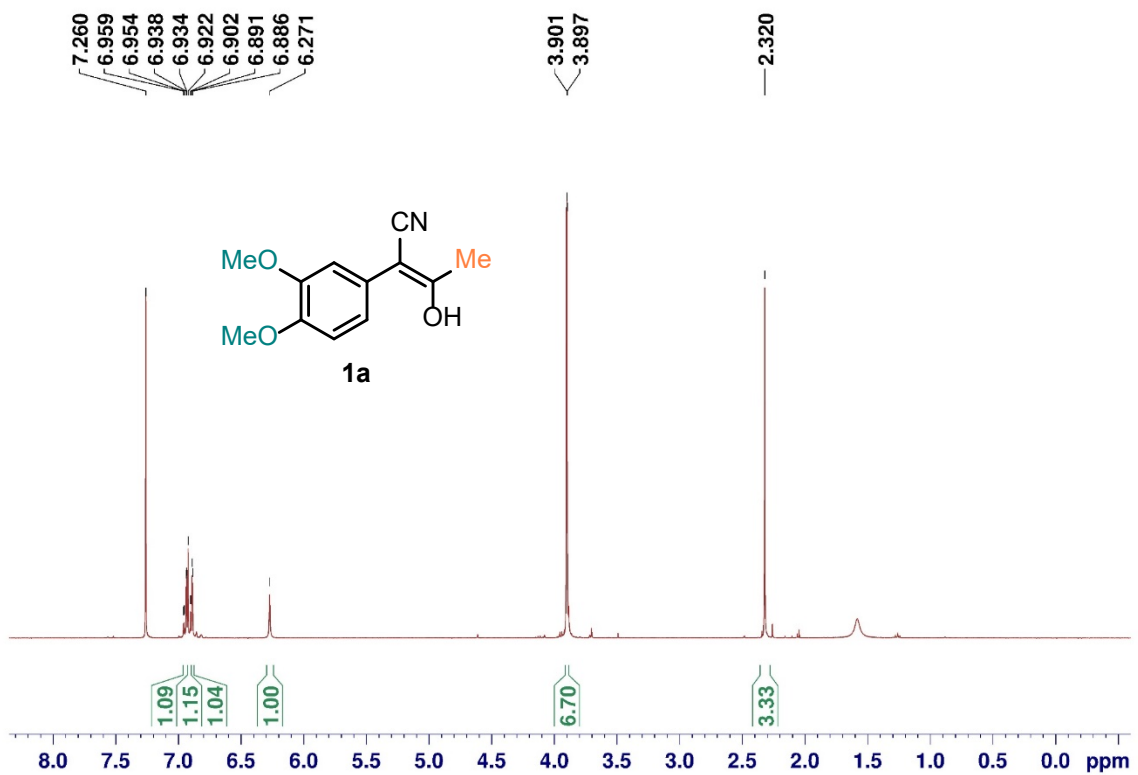
(ESI)  $m/z$  calculated for  $C_{24}H_{28}N_3O_8$   $[M + NH_4^+]$  486.1871, found 486.1867.

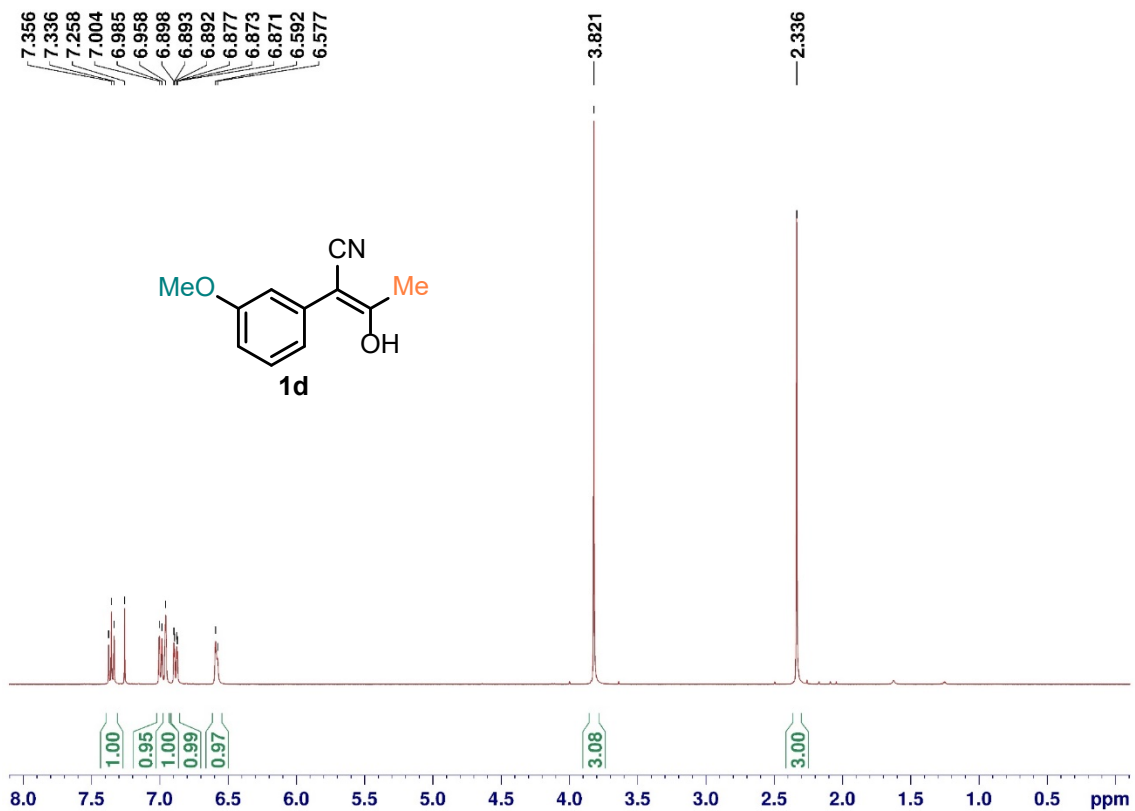
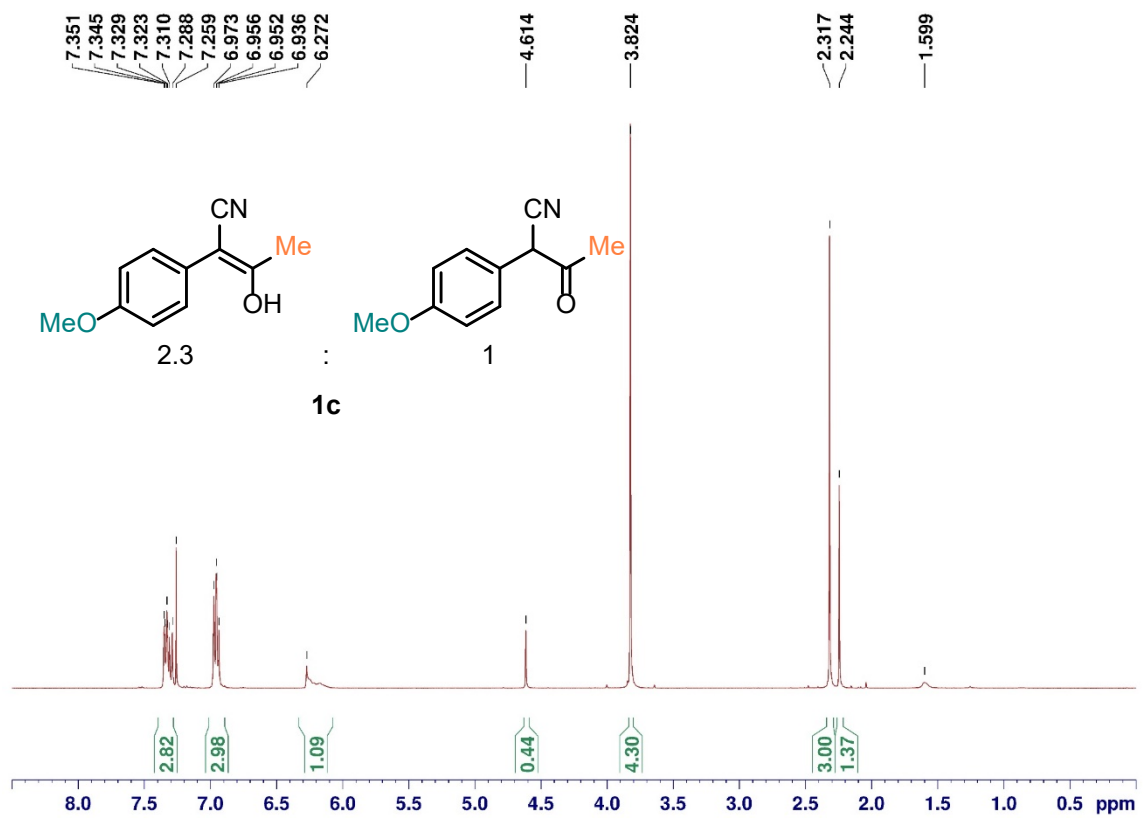
**Dimethyl 2,3-dicyano-2,3-bis(4-methoxyphenyl)succinate (21)**

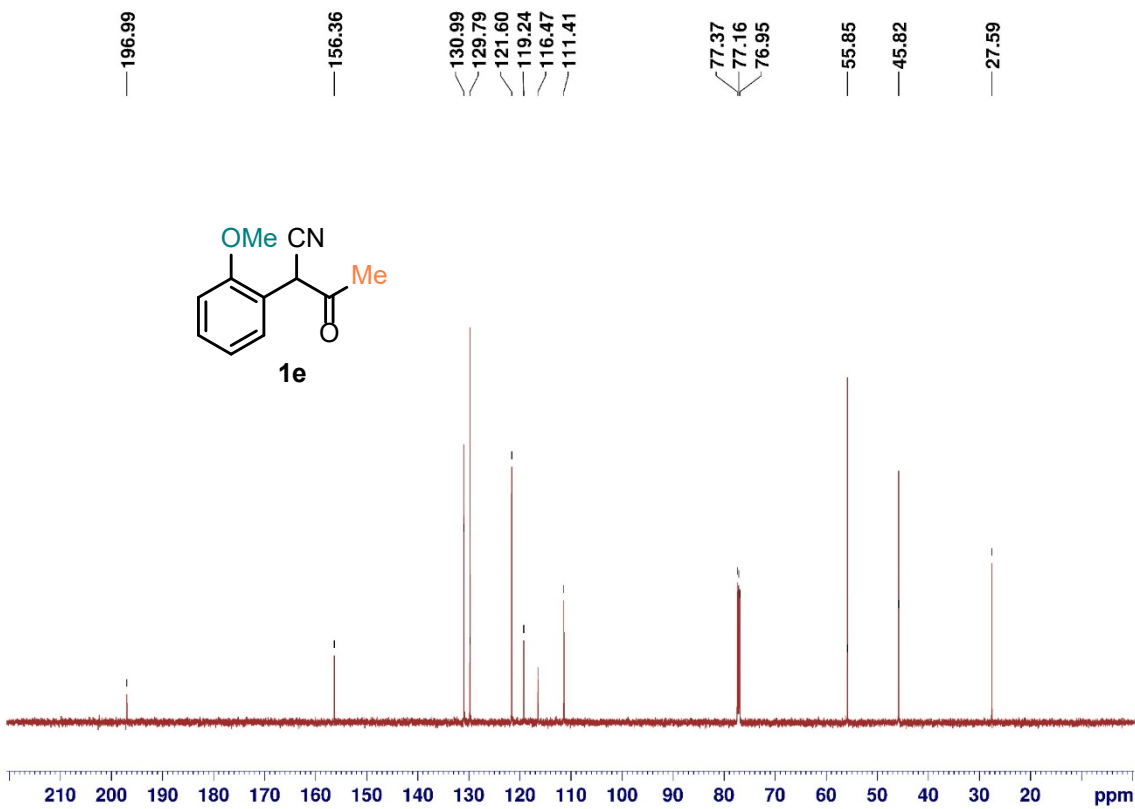
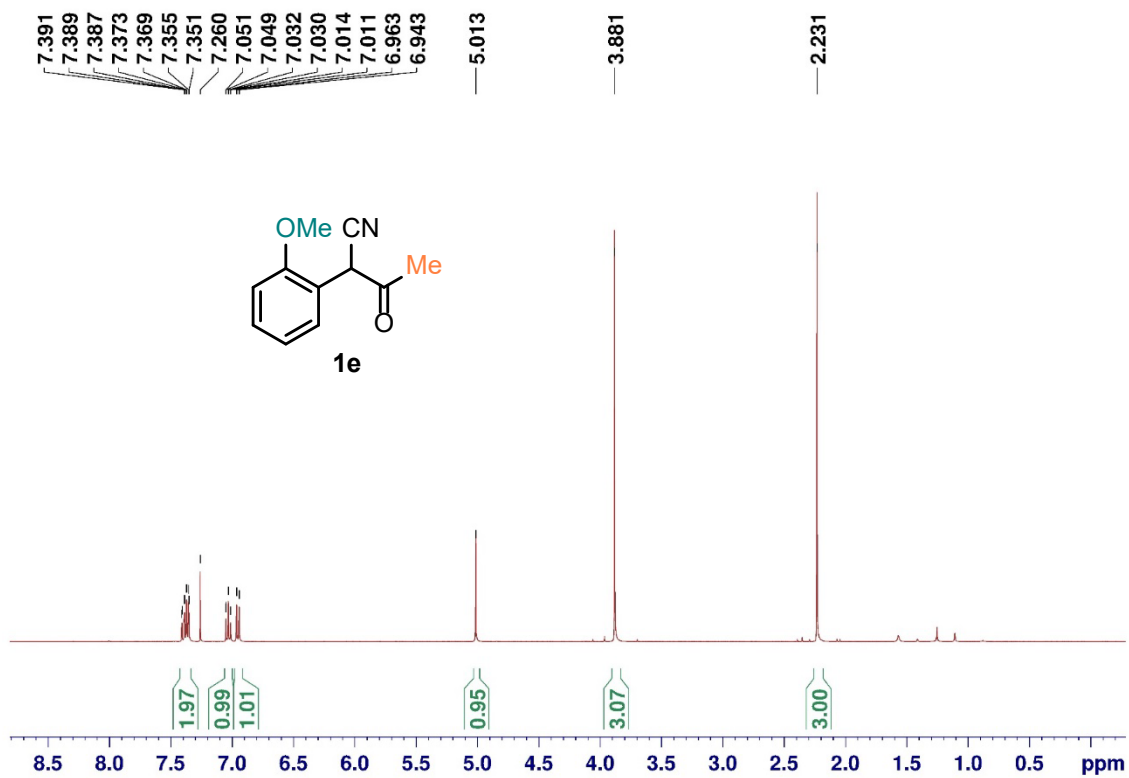


Following the general procedure for dimerization photocatalyzed by QDs, **21** was purified by silica gel chromatography (EtOAc/hexanes = 1/3). Yield: 75%, 92 mg, white solid.  $^1H$  NMR (600 MHz,  $CDCl_3$ ) *dl*:  $\delta$  7.02 (d,  $J = 8.9$  Hz, 2H,  $H_{arom}$ ), 6.83 (d,  $J = 8.9$  Hz, 2H,  $H_{arom}$ ), 3.94 (s, 3H,  $COOCH_3$ ), 3.82 (s, 3H,  $OCH_3$ ). *meso*:  $\delta$  7.31 (d,  $J = 8.6$  Hz, 2H,  $H_{arom}$ ), 6.86-6.82 (m, 2H,  $H_{arom}$ ), 3.82 (s, 3H,  $COOCH_3$ ), 3.82 (s, 3H,  $OCH_3$ ).  $^{13}C$  NMR (150 MHz,  $CDCl_3$ ) *dl*:  $\delta$  167.0, 161.0, 130.2, 120.6, 115.7, 114.1, 60.1, 55.5, 54.9. *meso*:  $\delta$  167.0, 161.0, 130.9, 120.6, 115.7, 113.8, 60.1, 55.5, 54.6. HRMS (ESI)  $m/z$  calculated for  $C_{22}H_{24}N_3O_6$   $[M + NH_4^+]$  426.1660, found 426.1656.

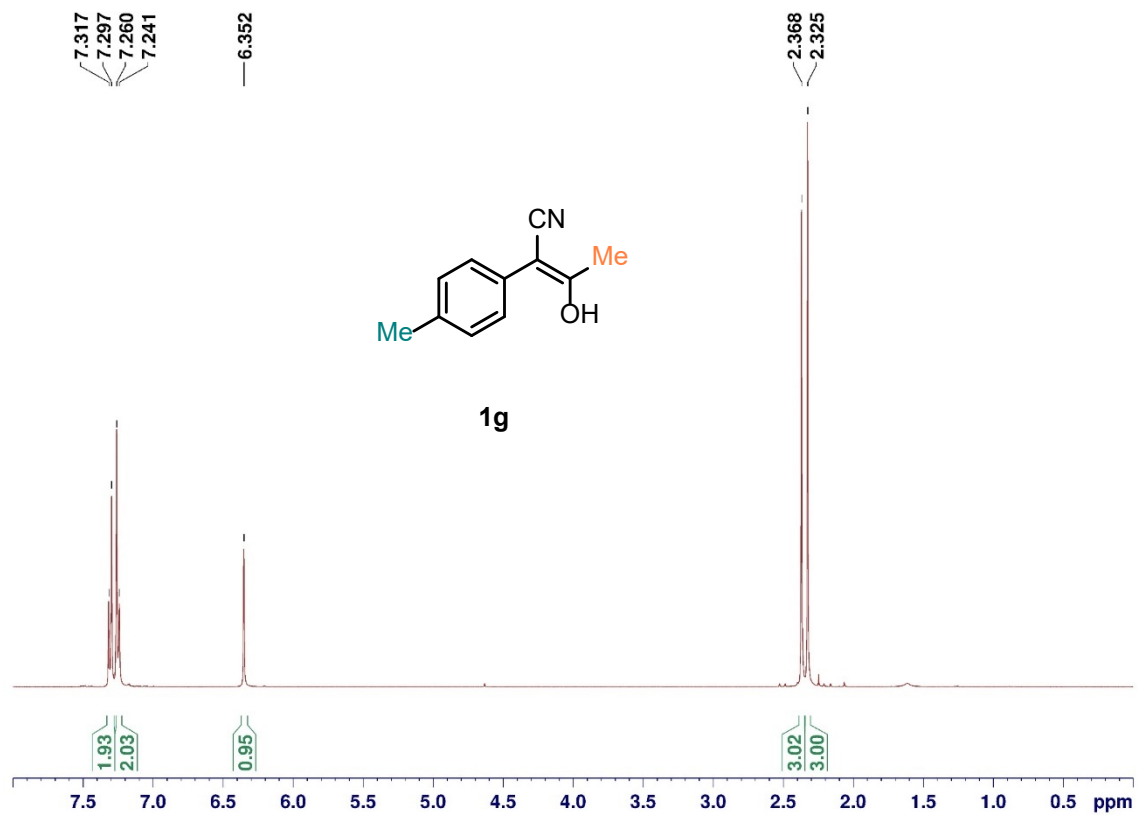
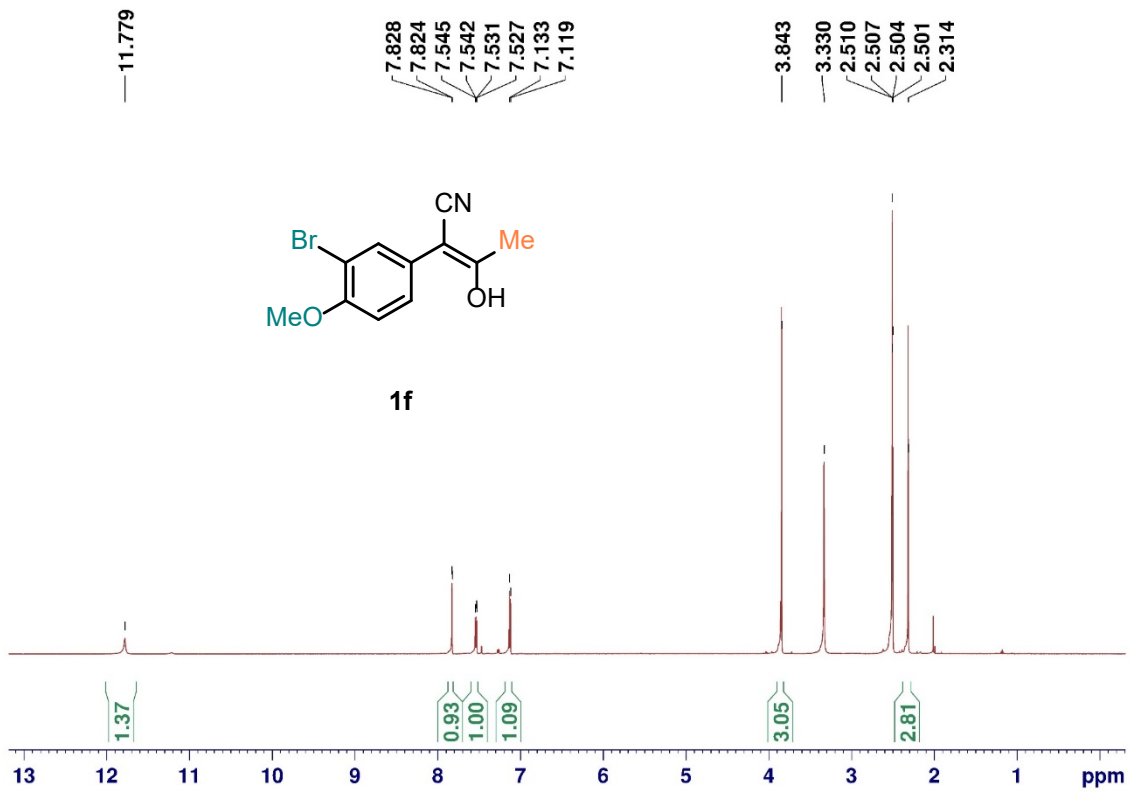
# NMR Spectra

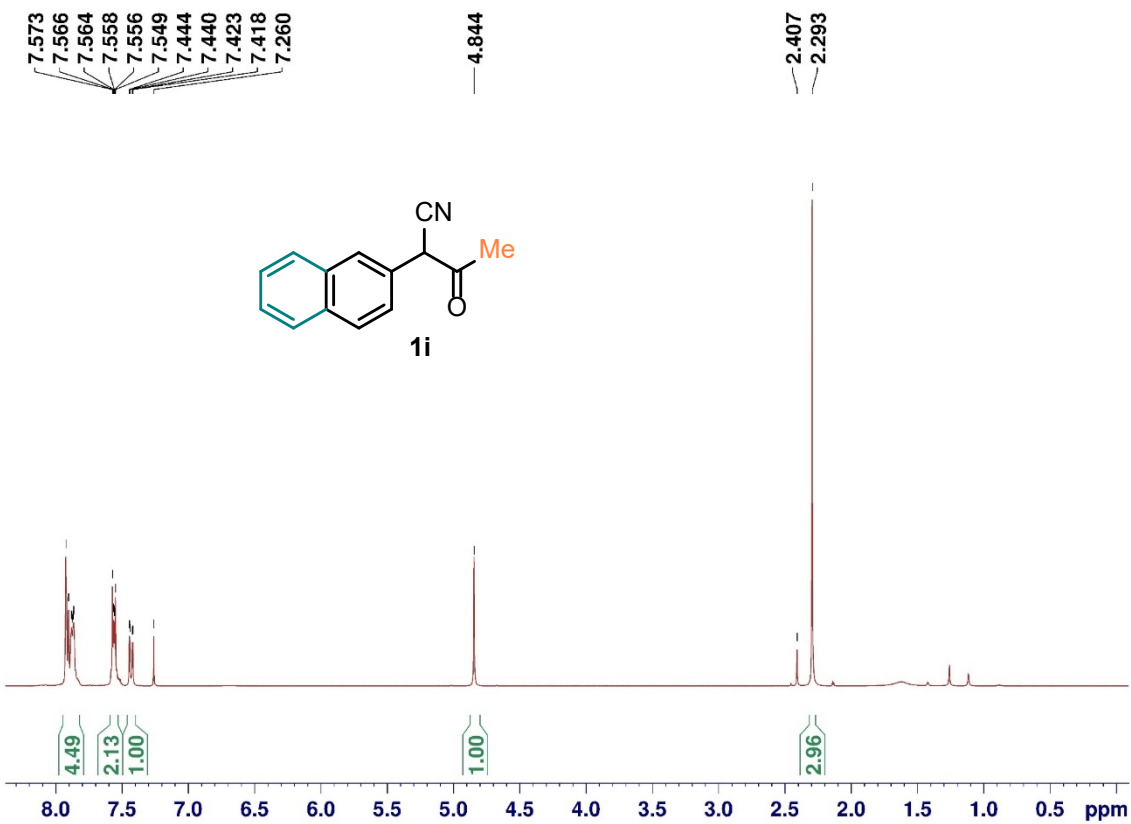
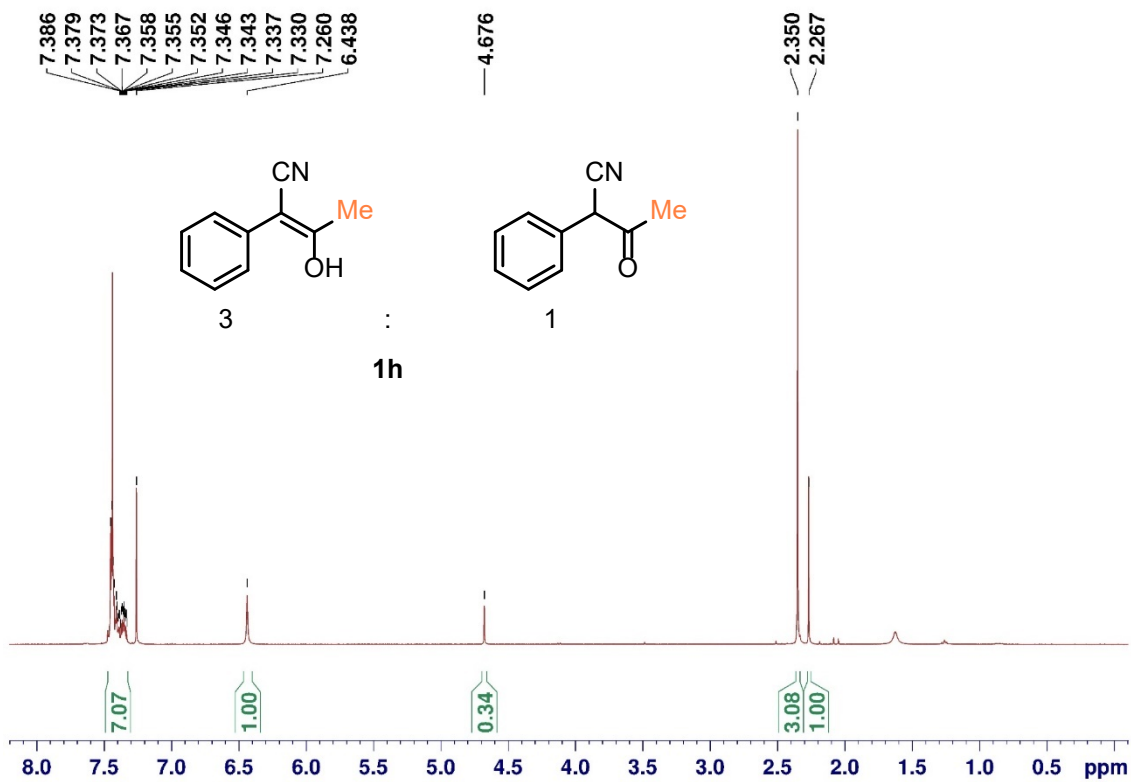


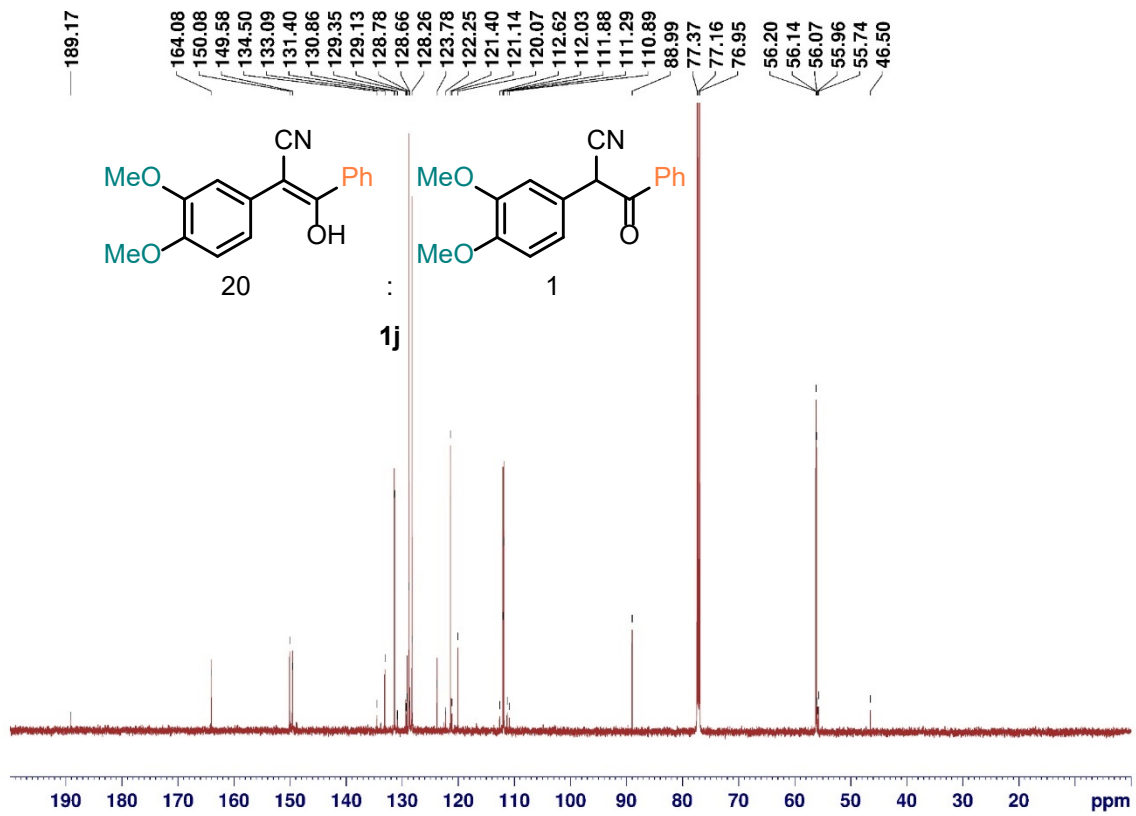
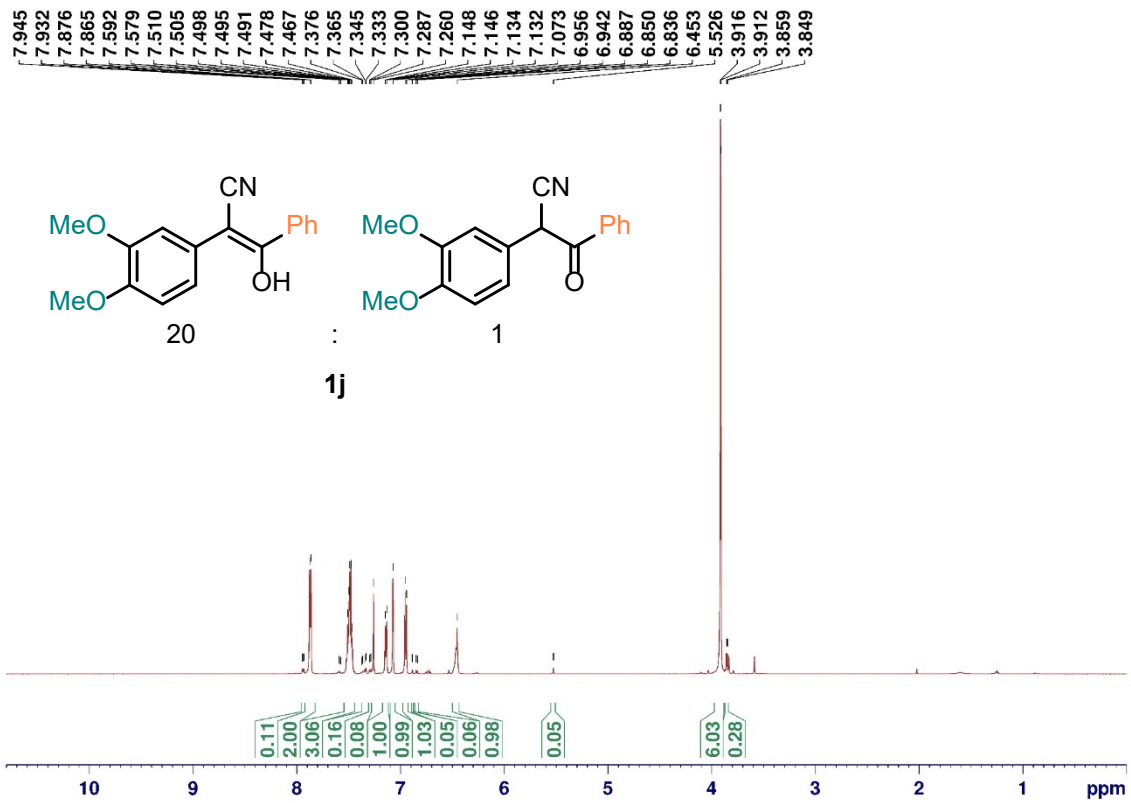


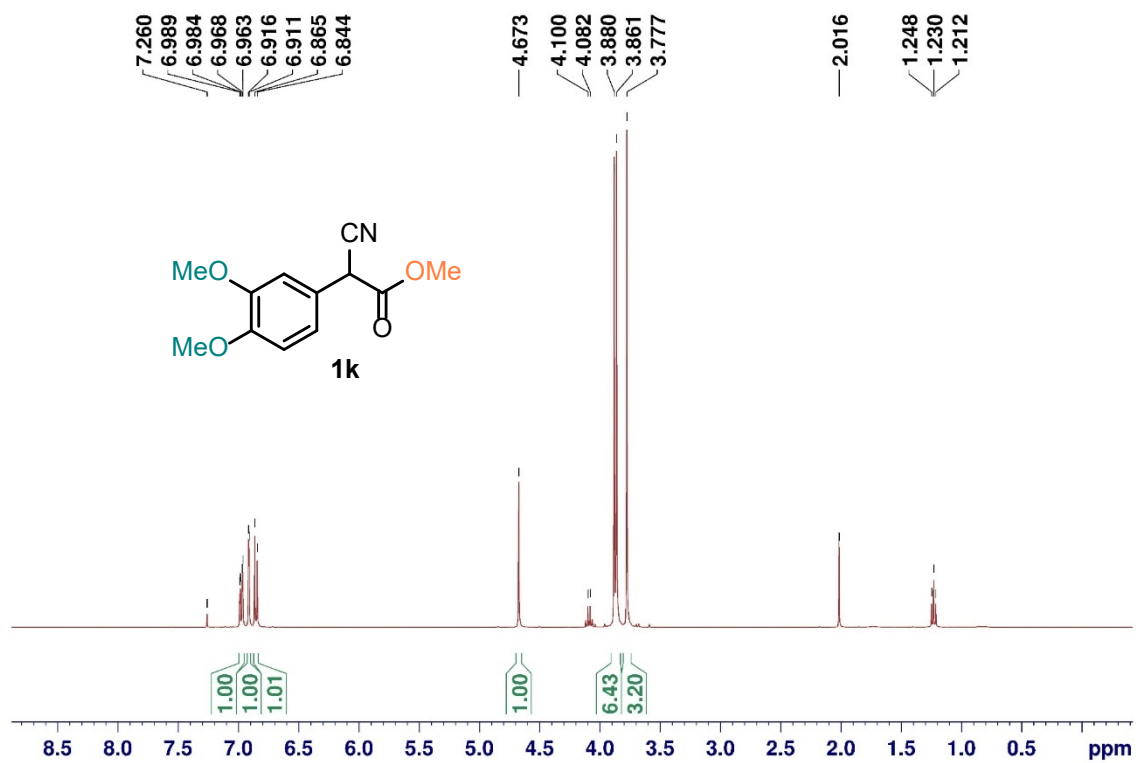


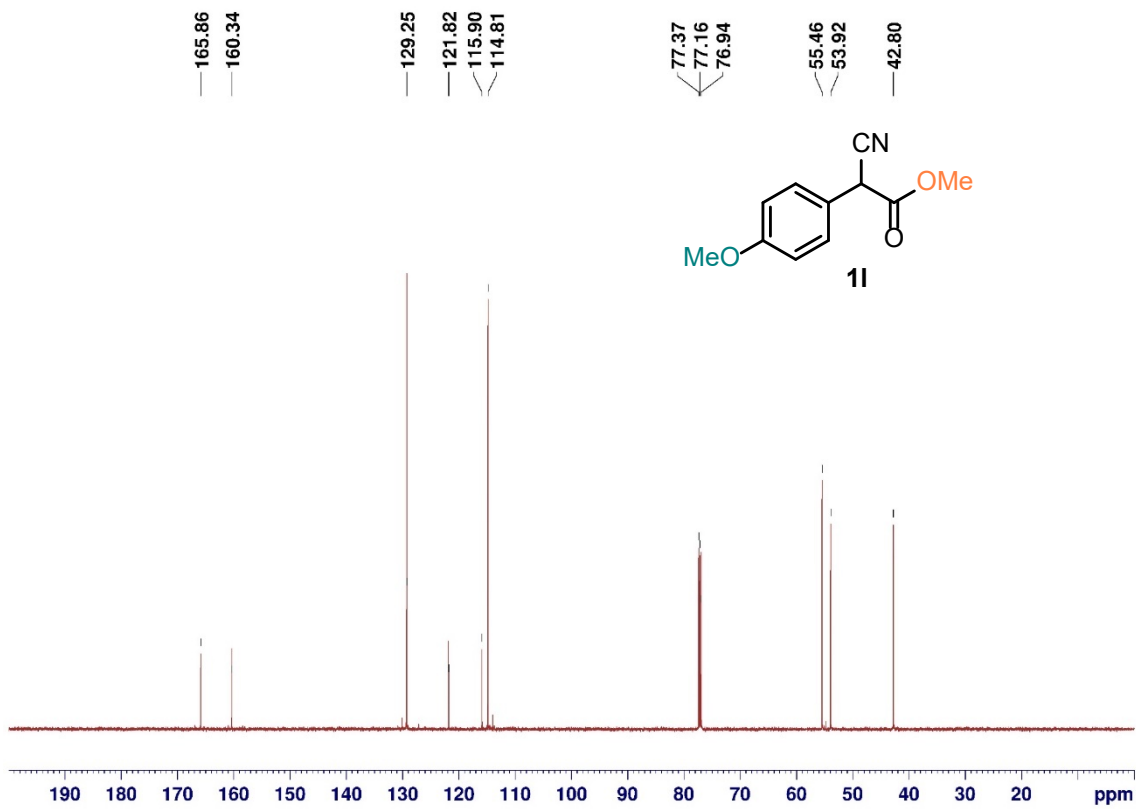
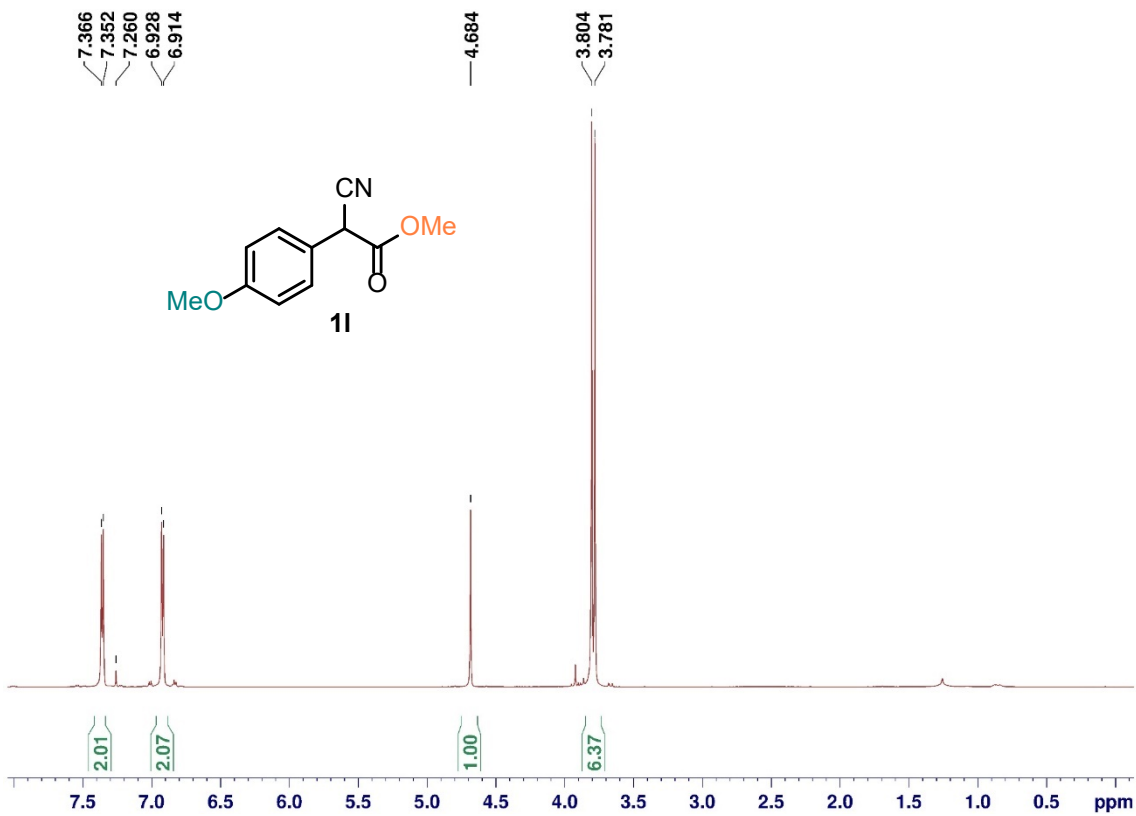


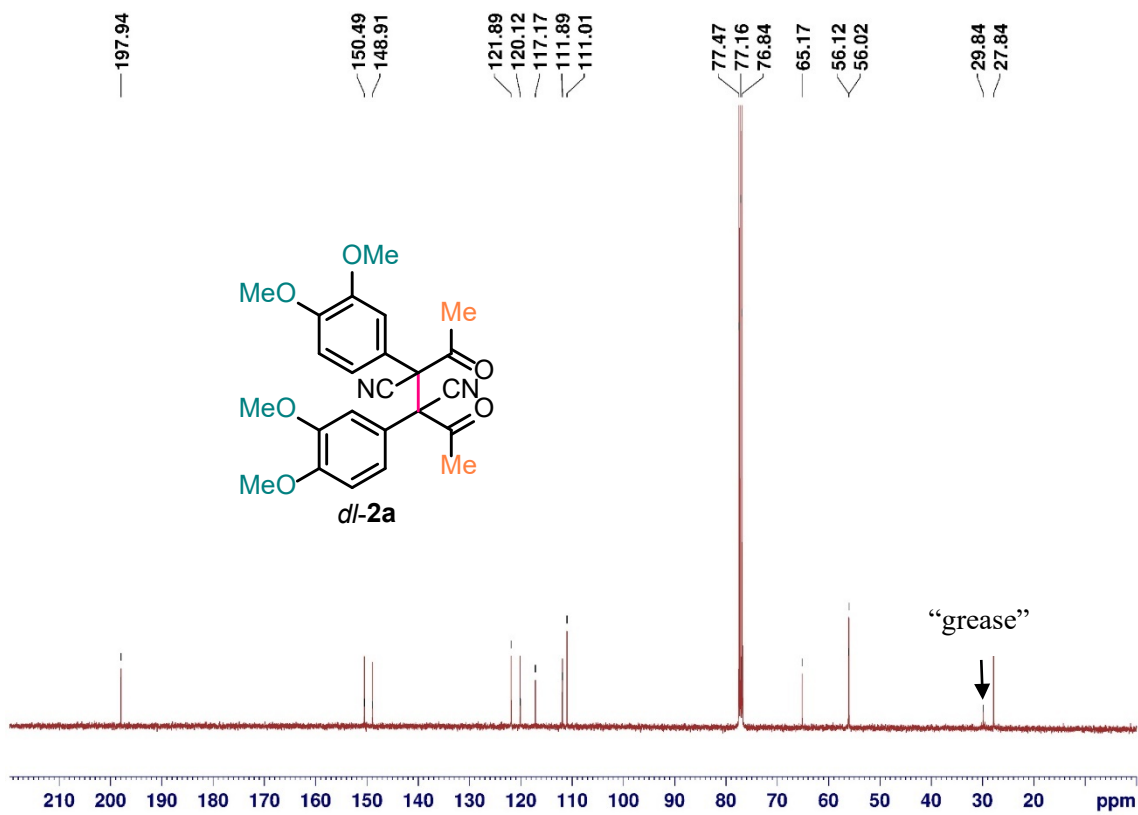
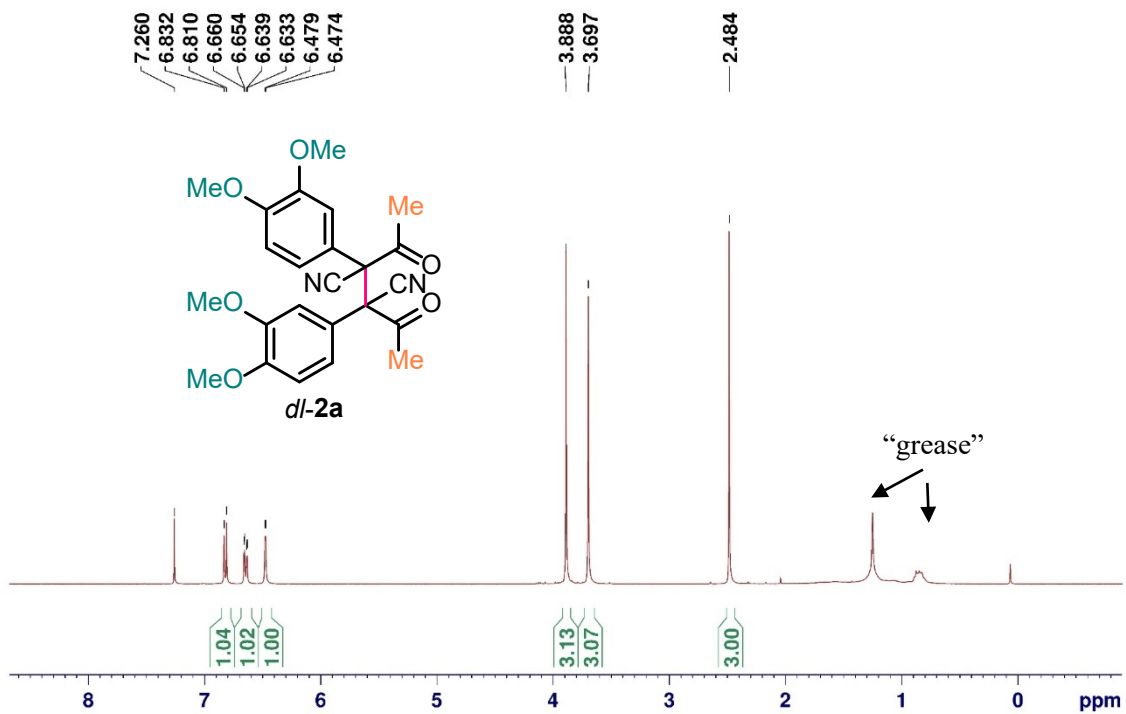


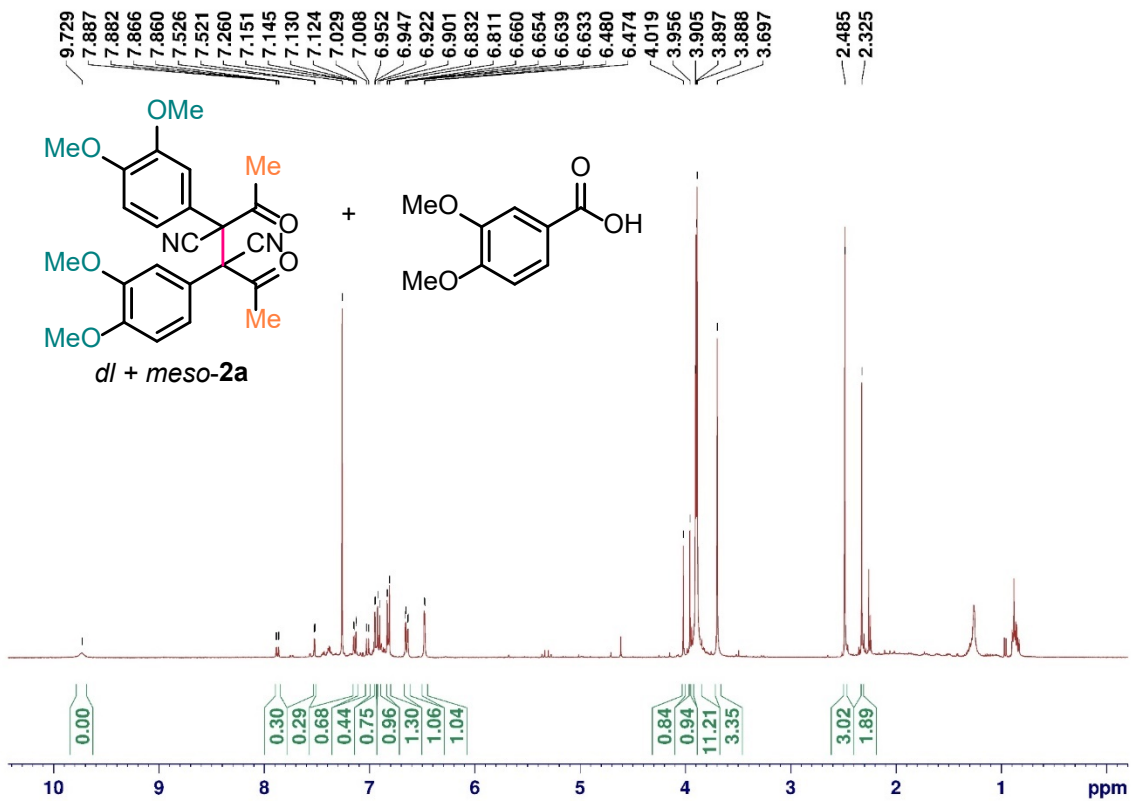


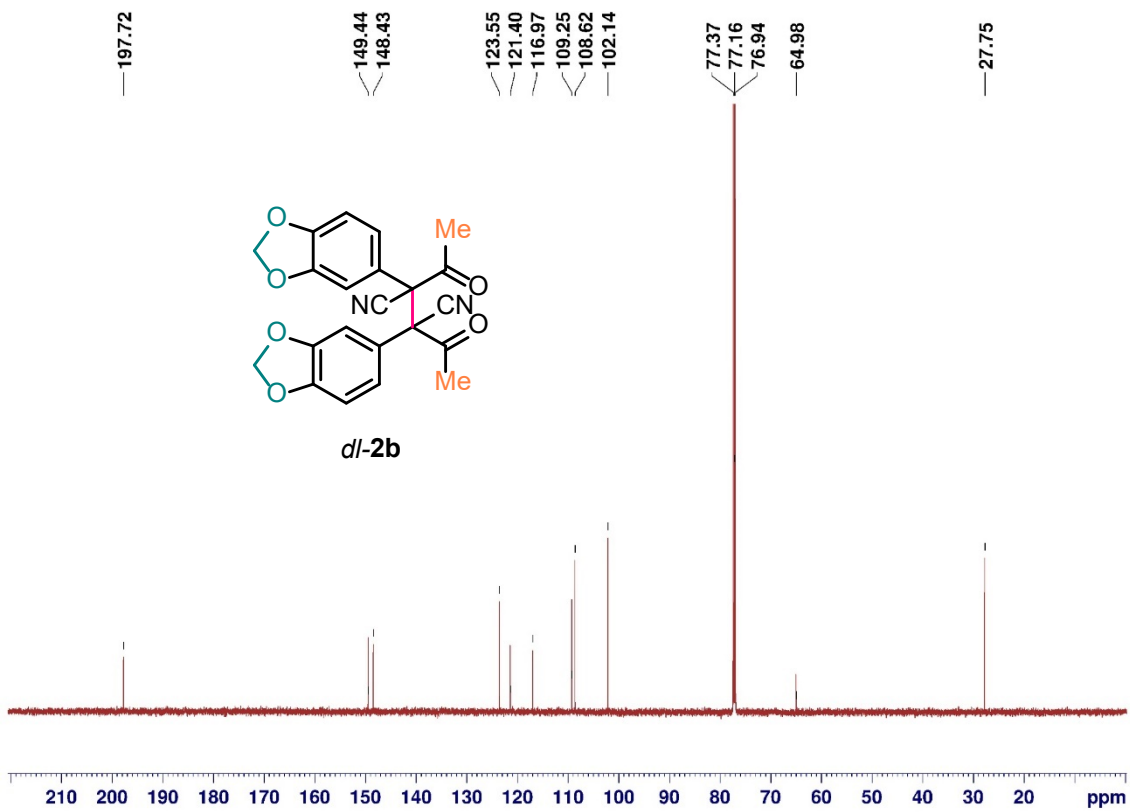
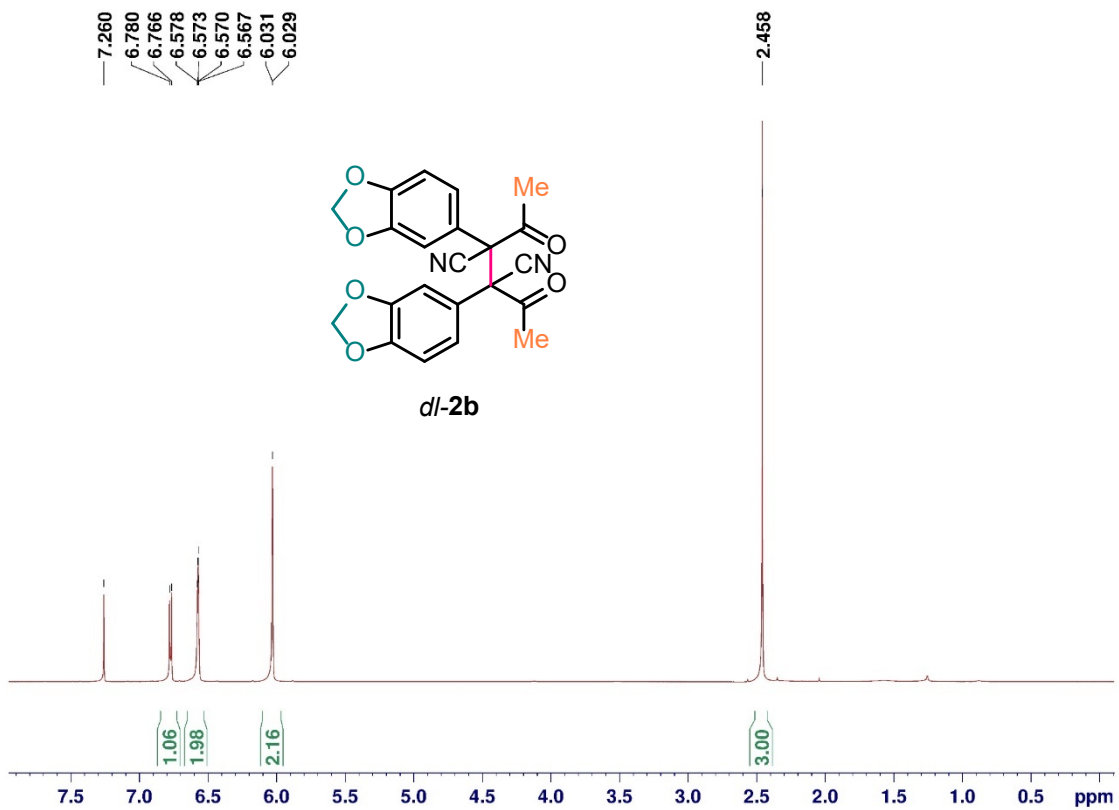




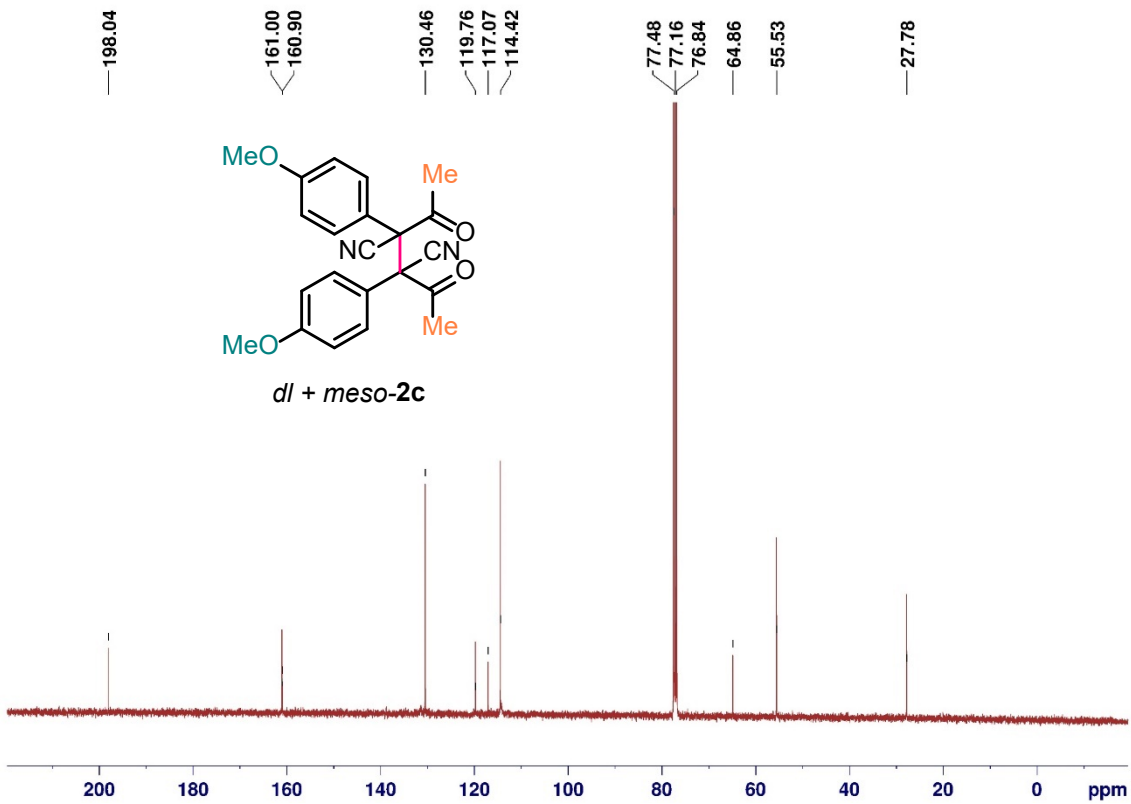
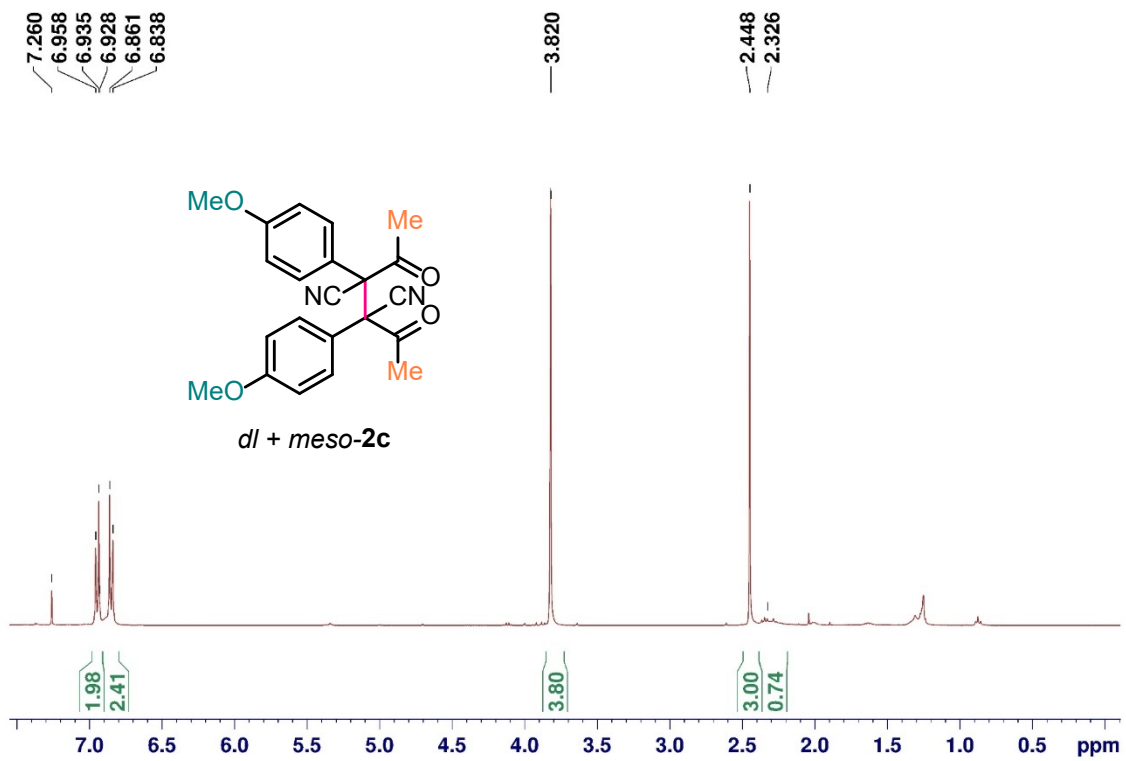


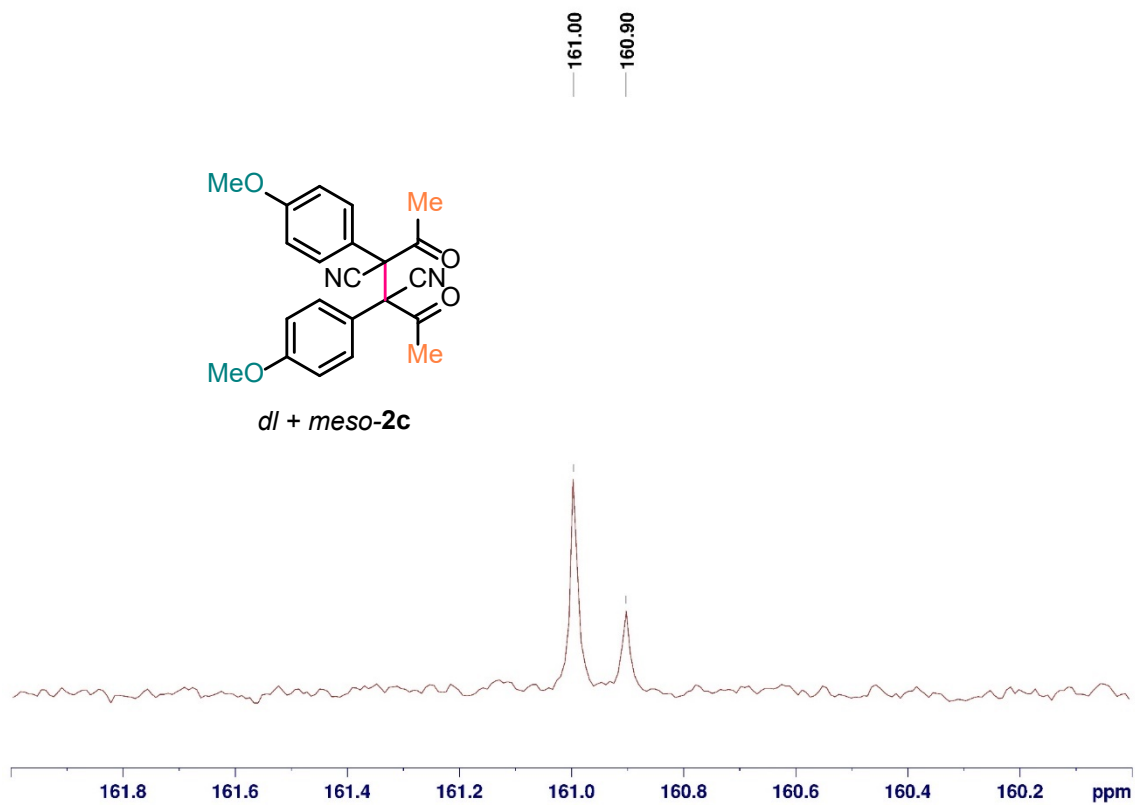


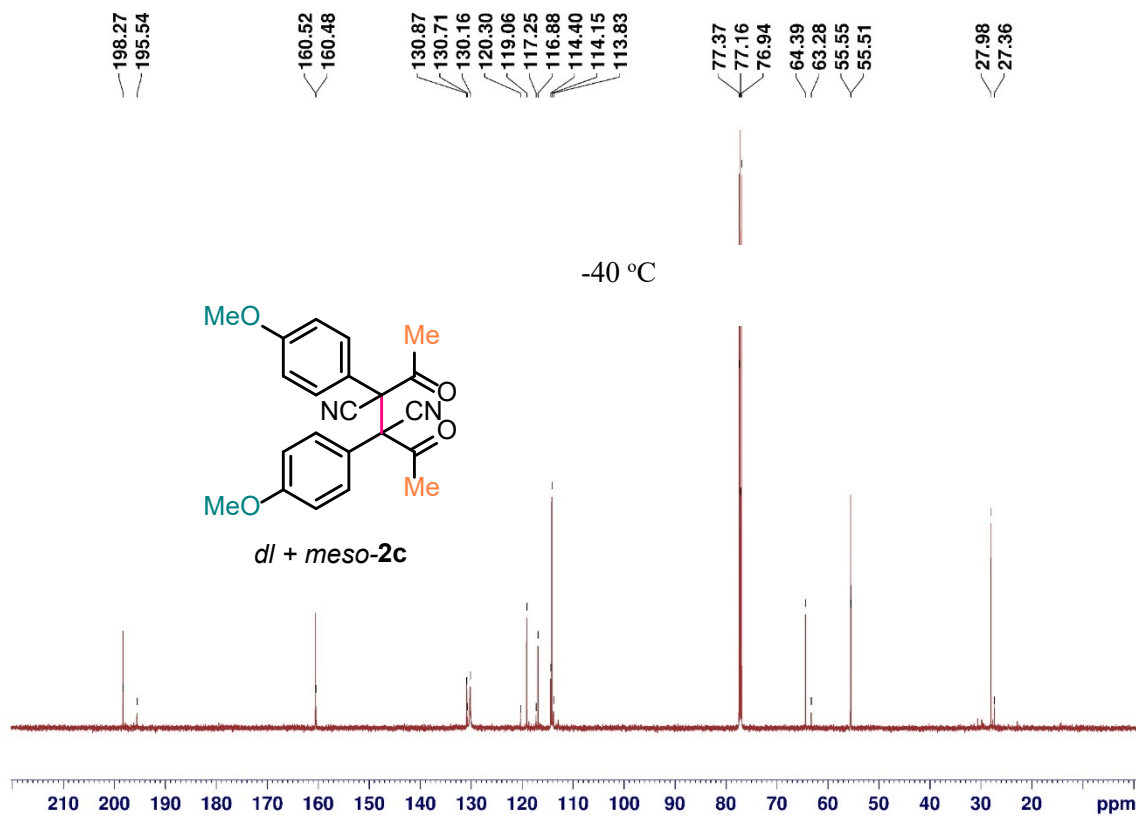
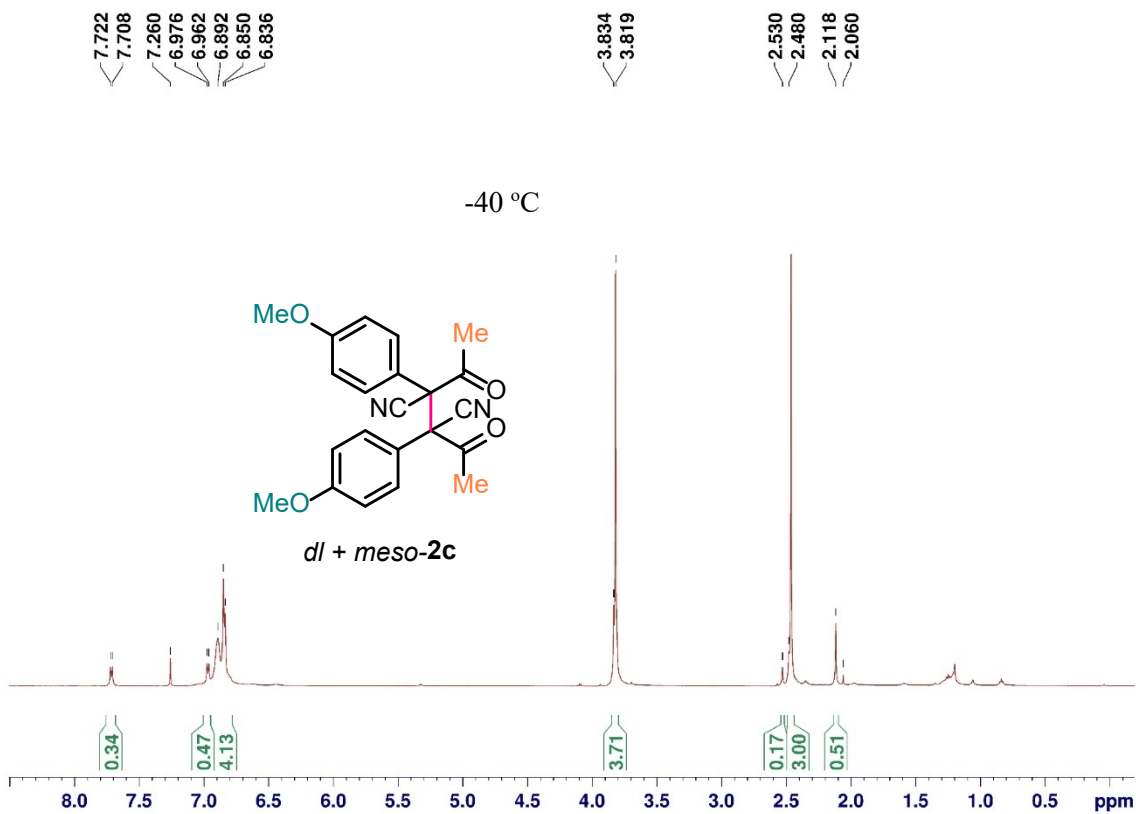


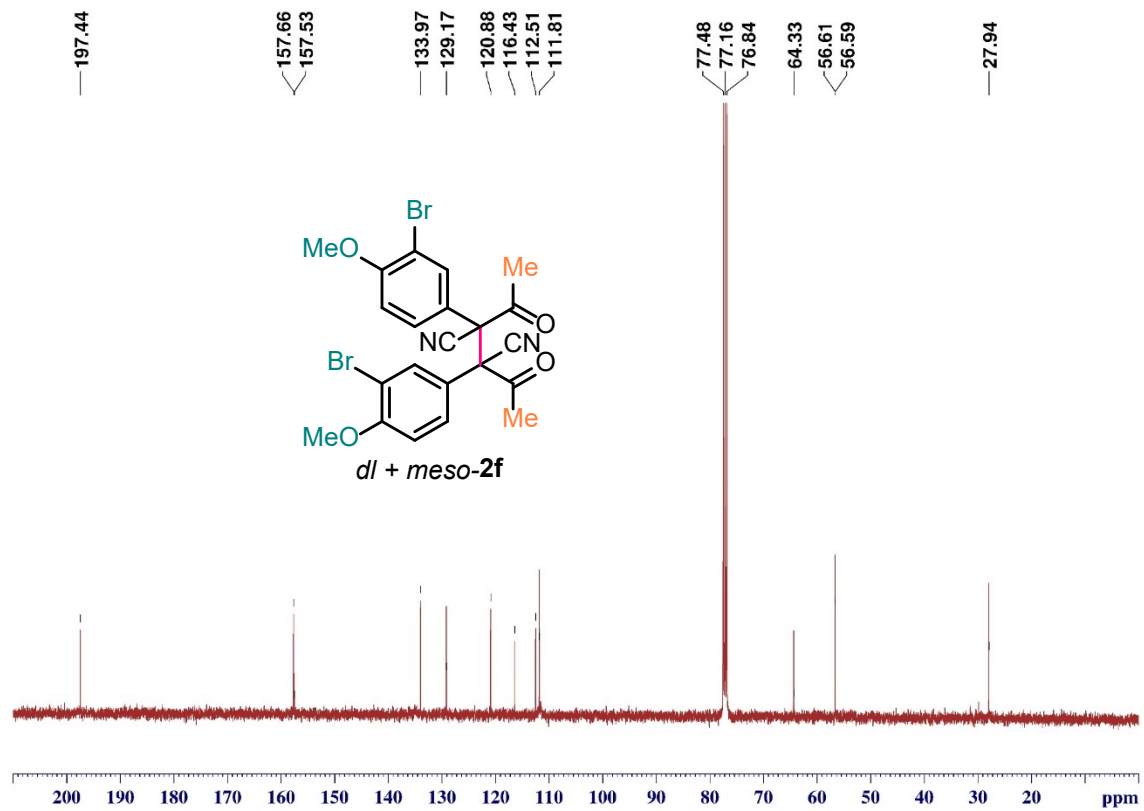
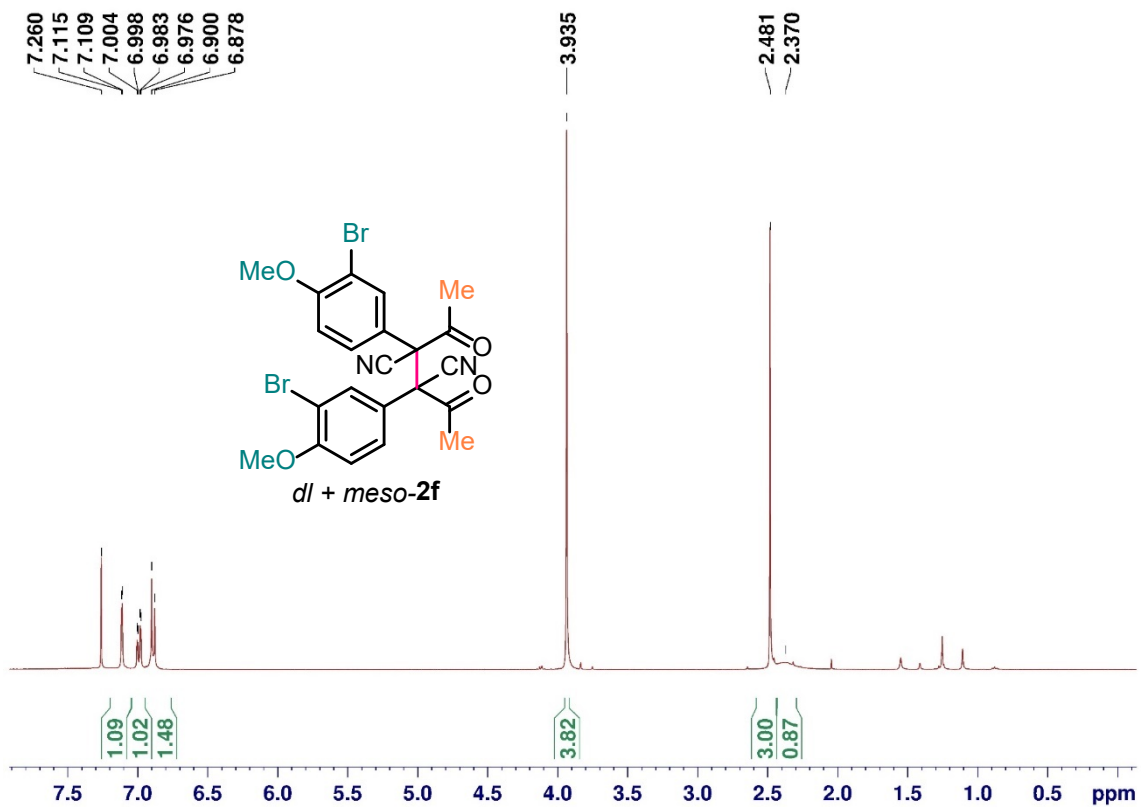


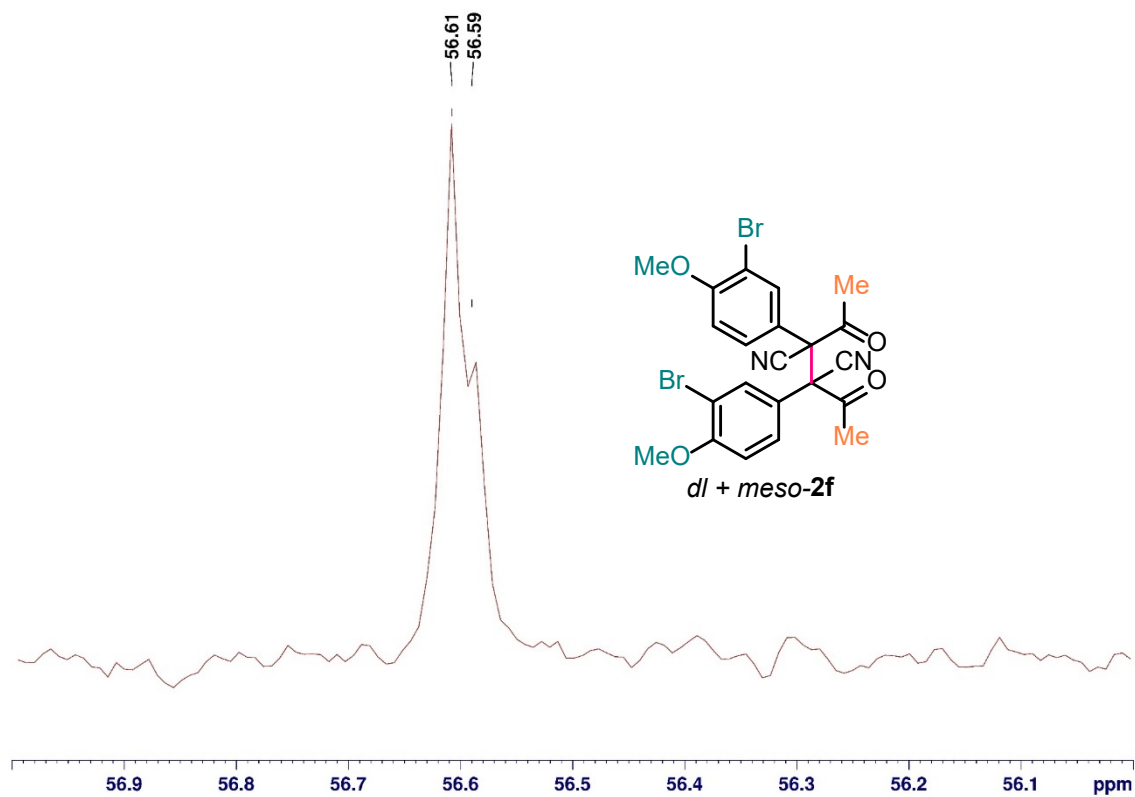
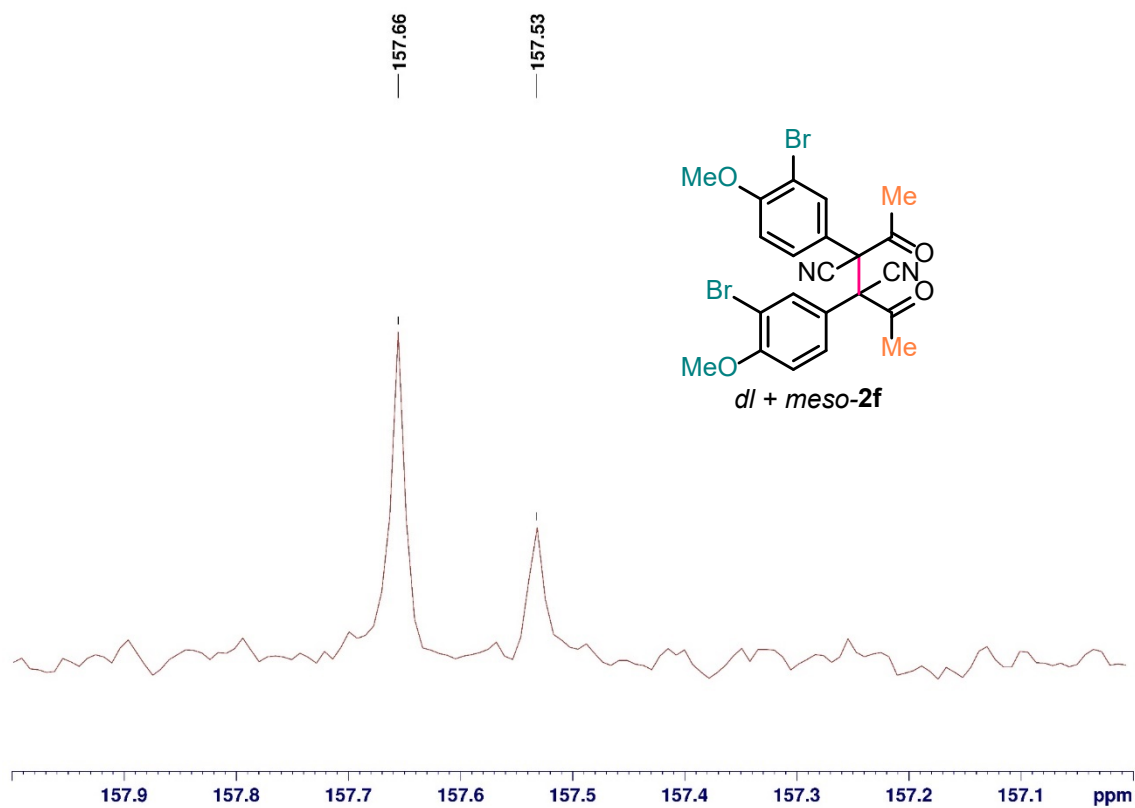


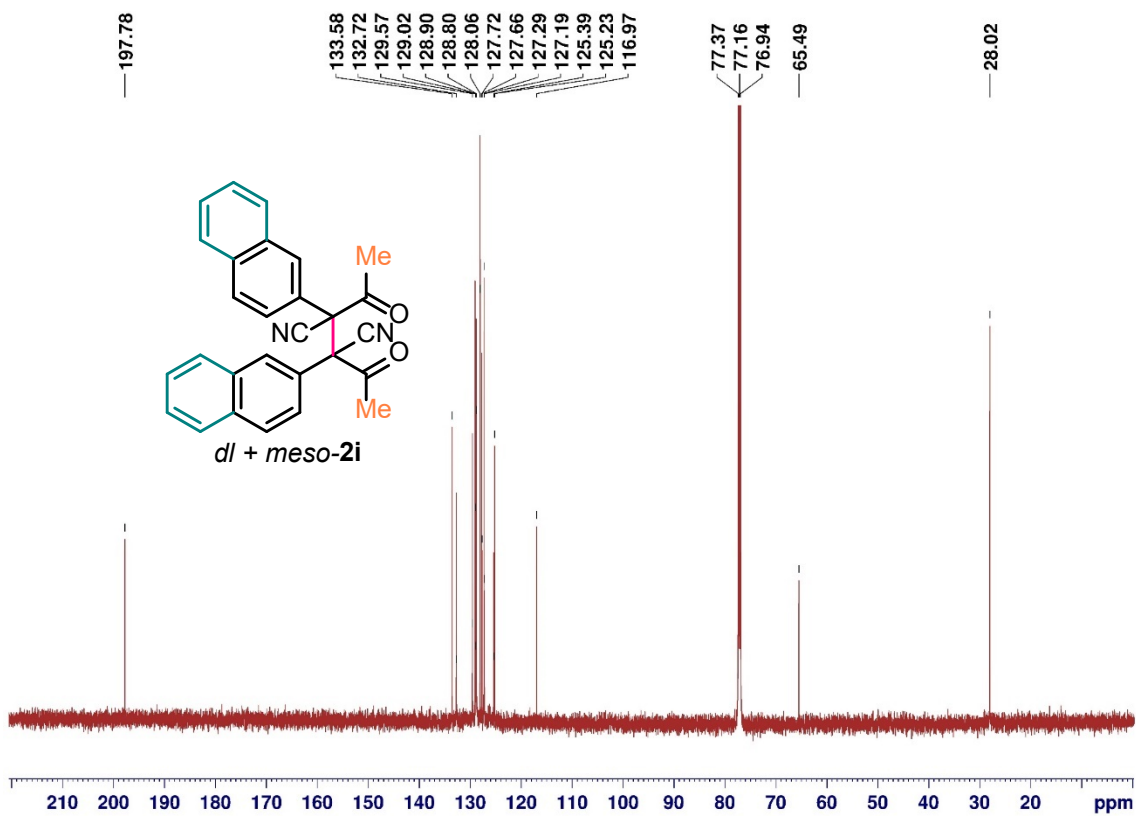
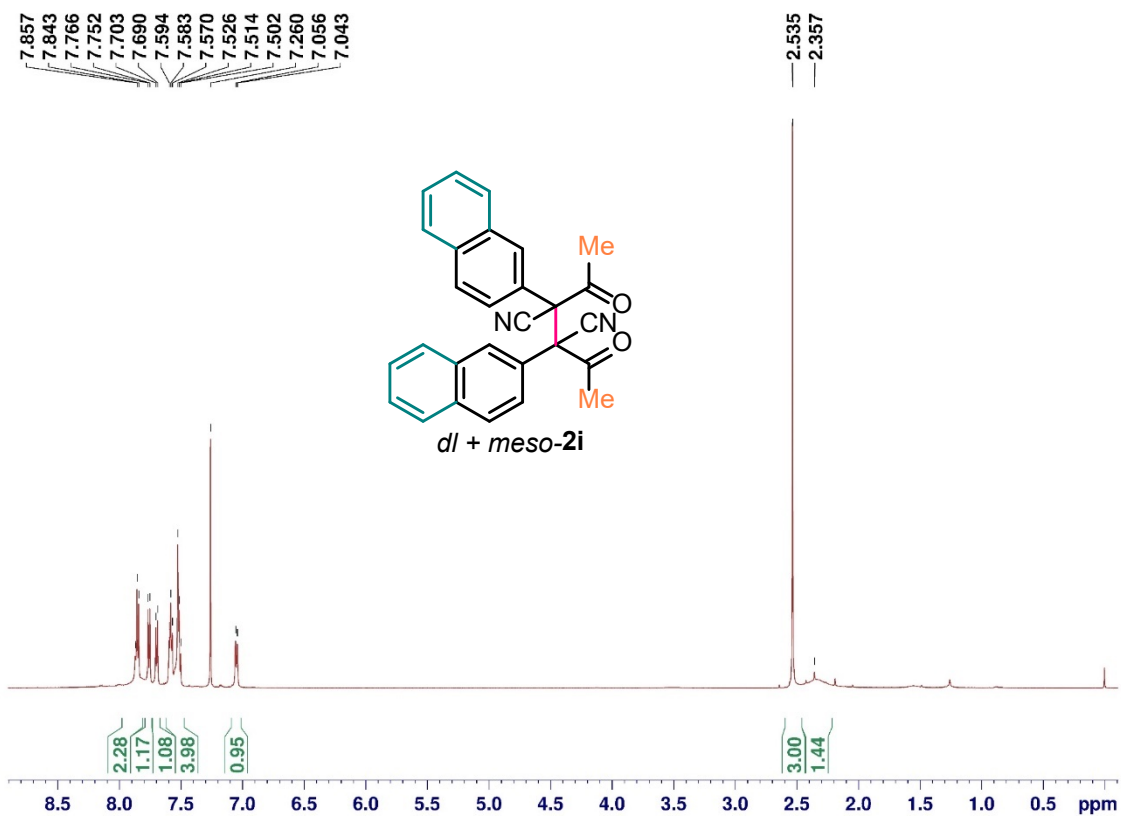


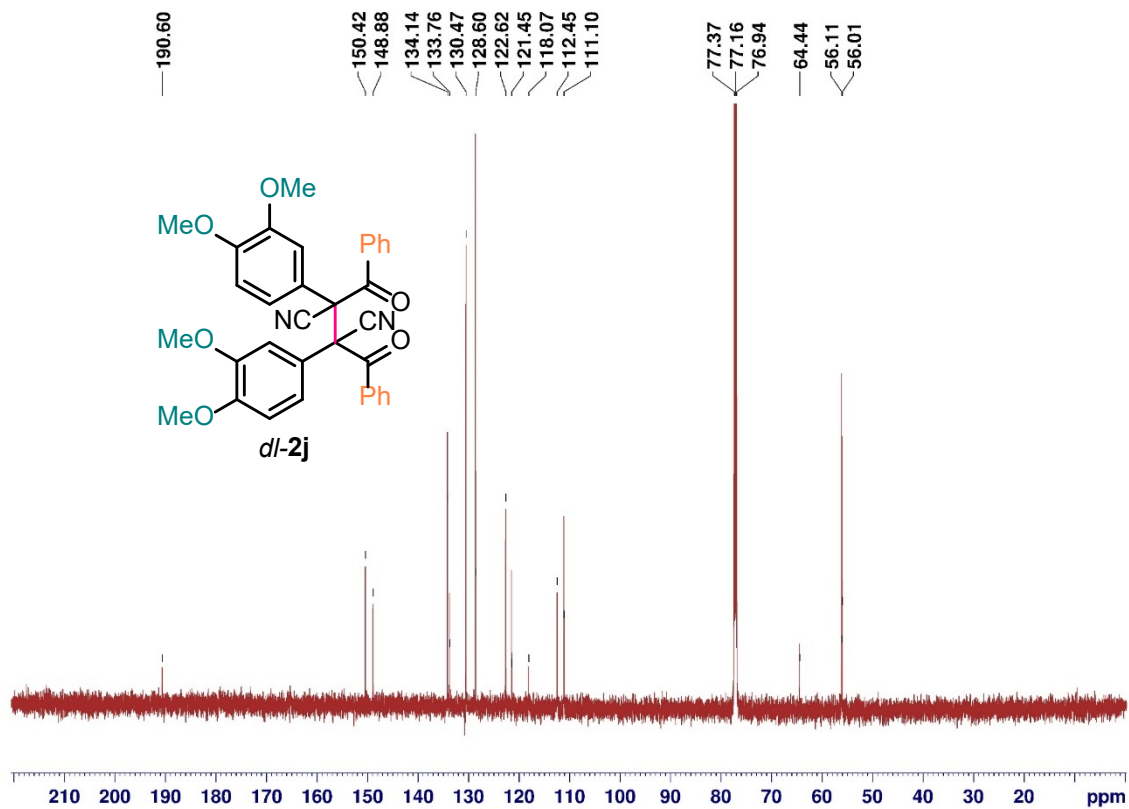
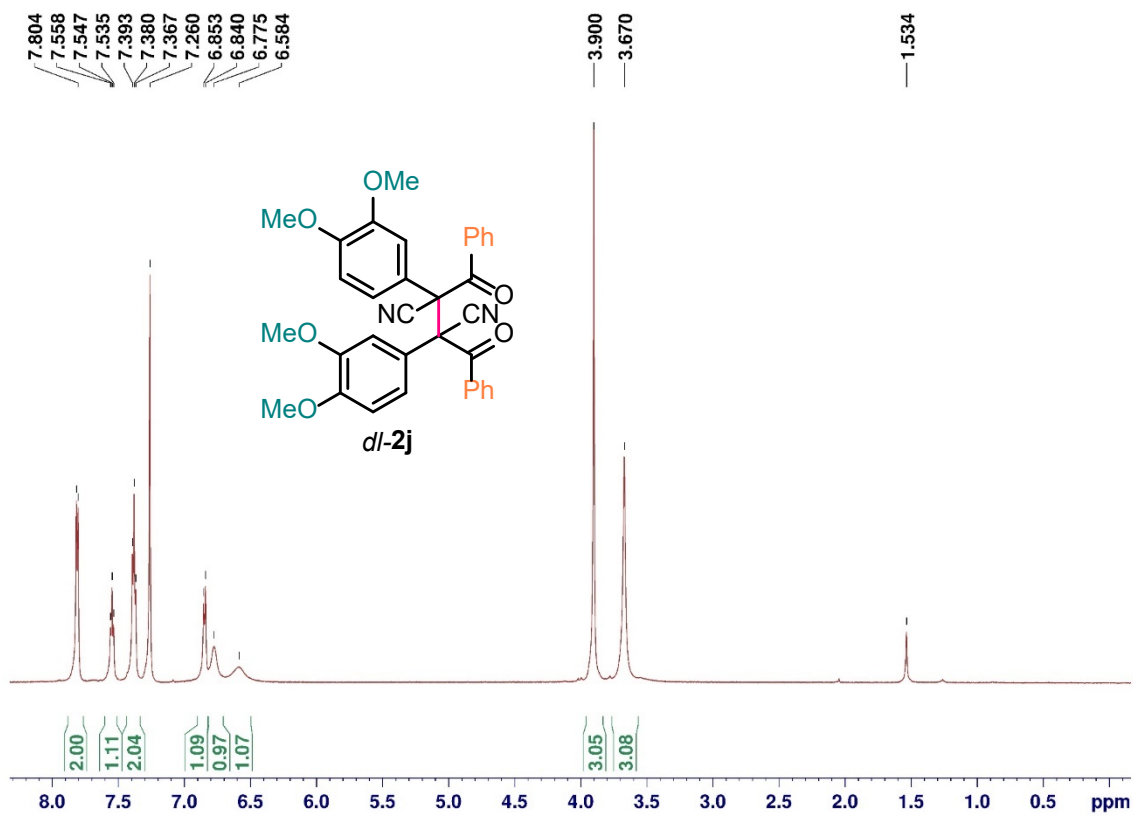


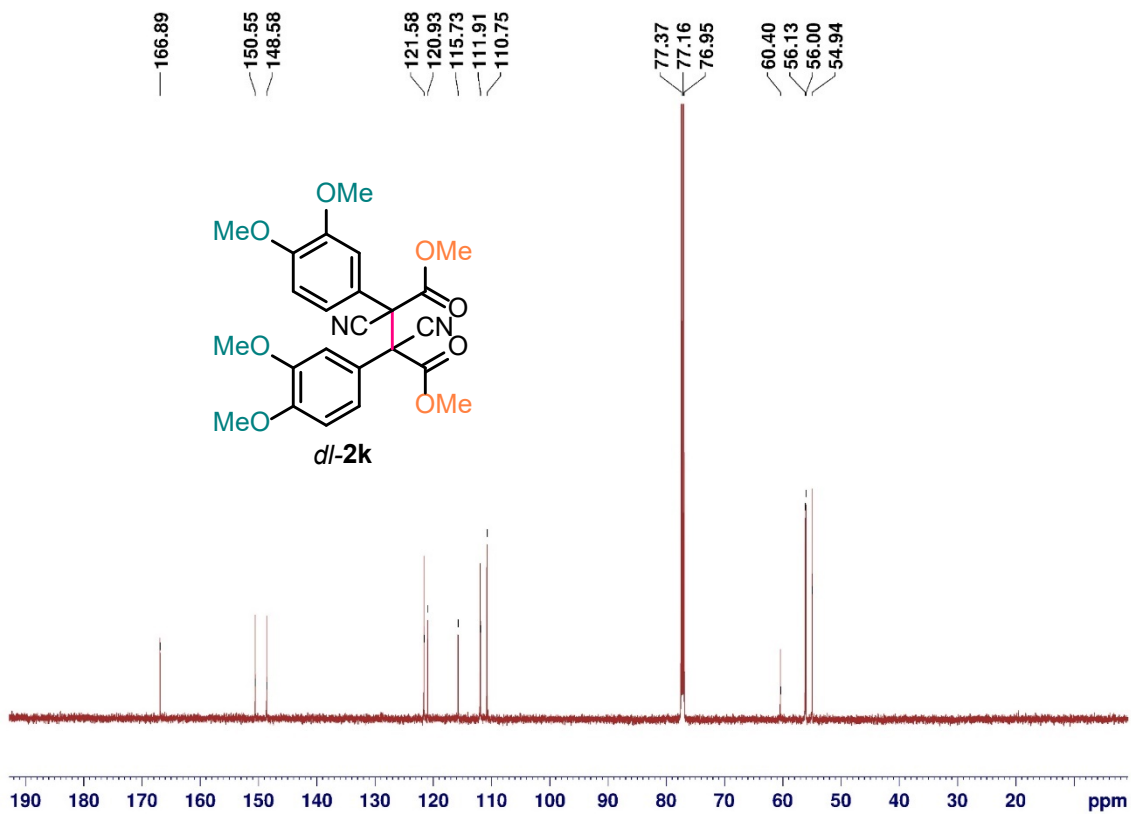
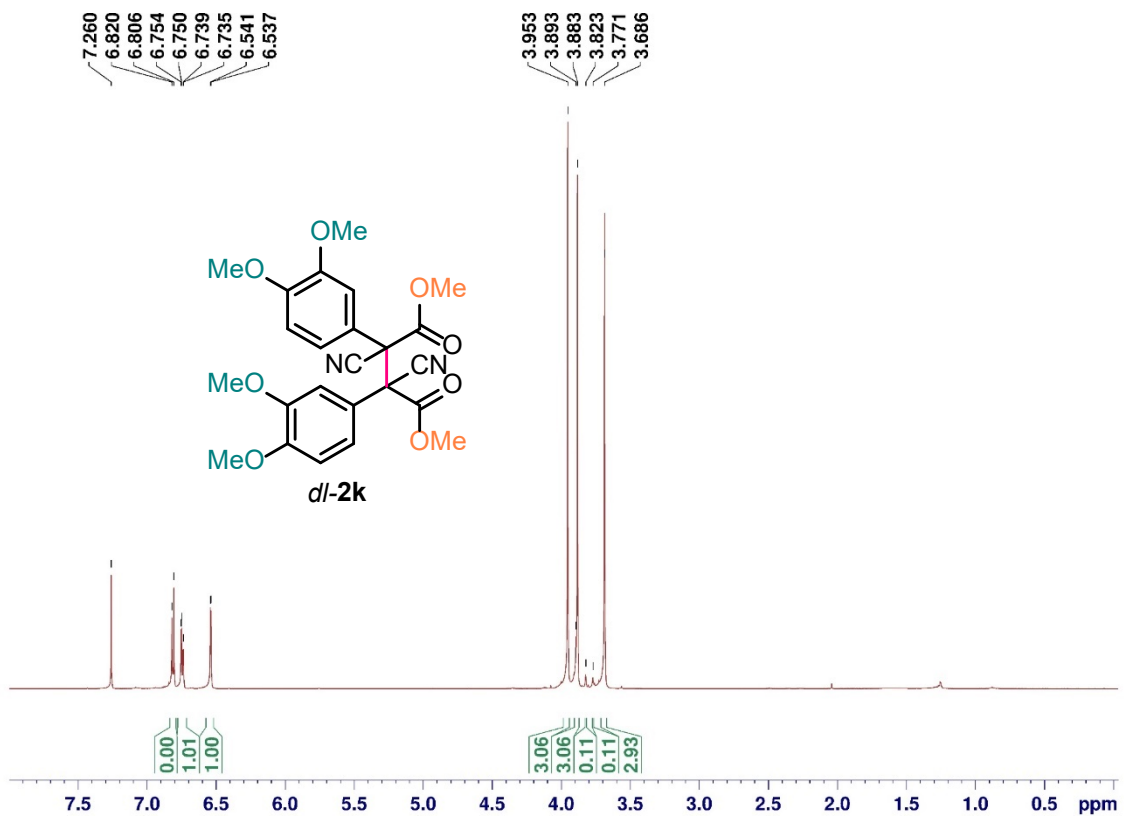




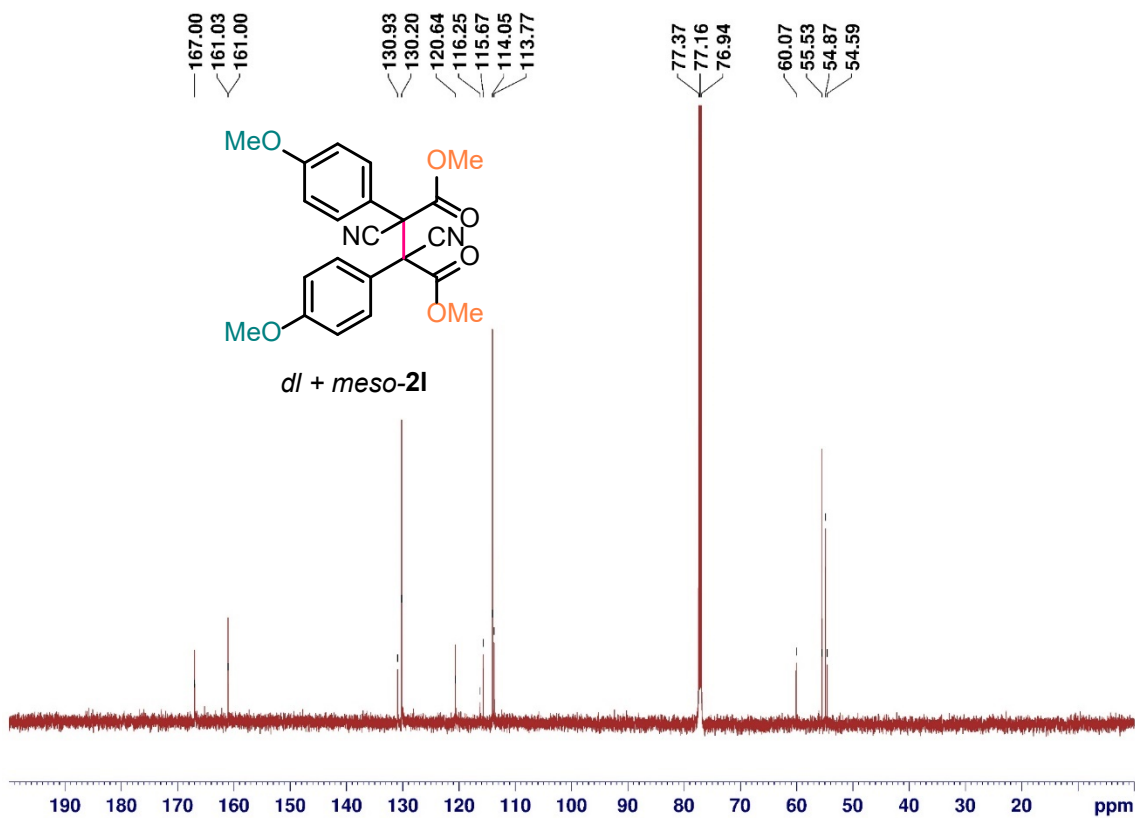
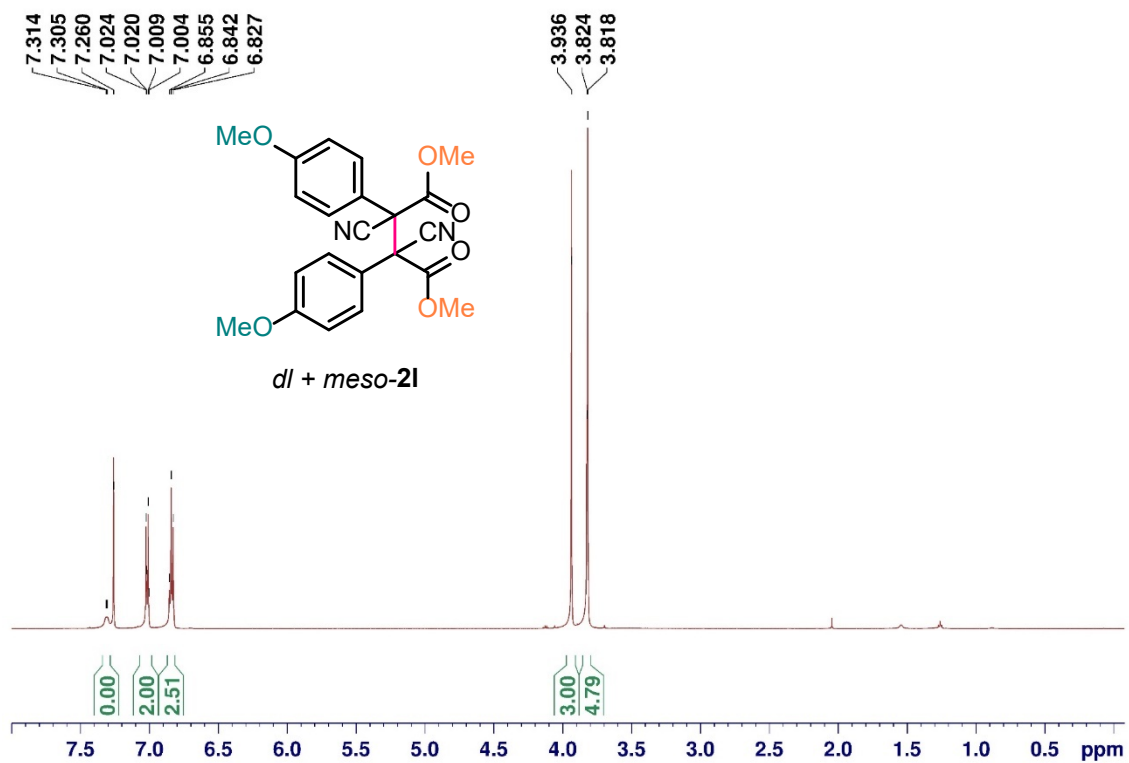


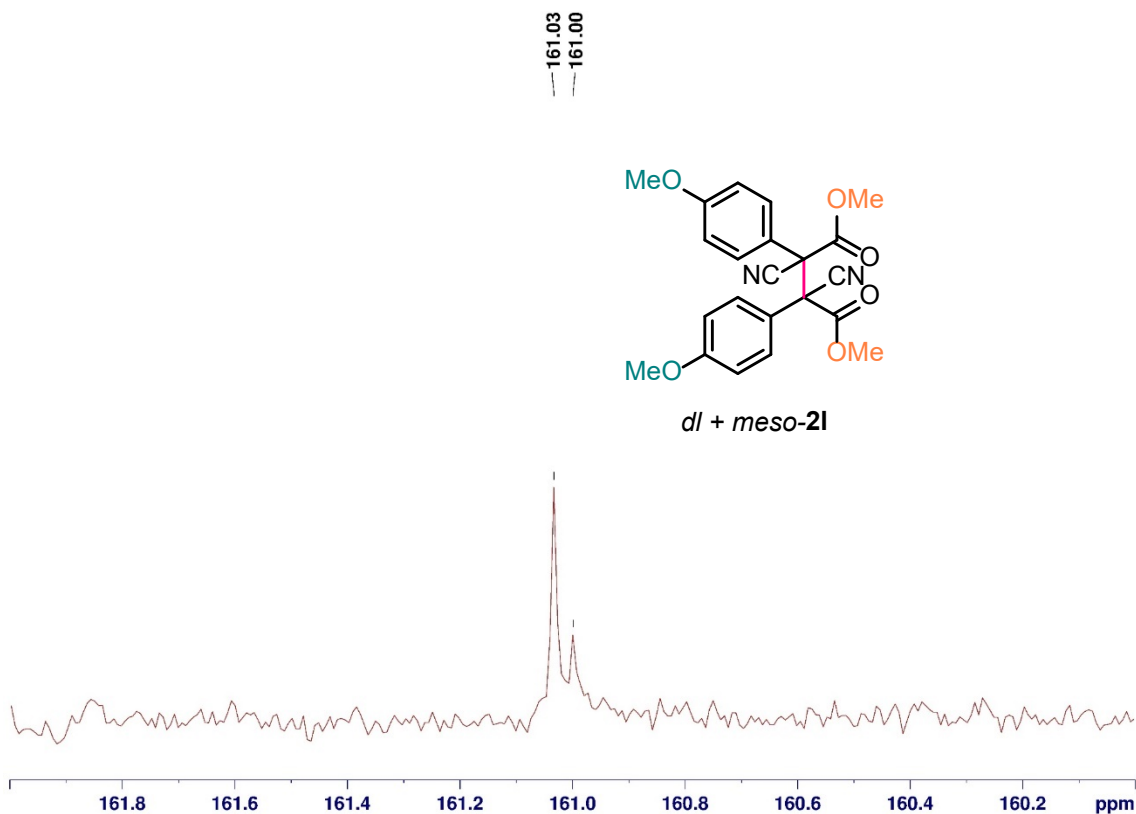












## References

1. Wang, J.; Yuan, Y.; Zhu, H.; Cai, T.; Fang, Y.; Chen, O., Three-Dimensional Macroporous Photonic Crystal Enhanced Photon Collection for Quantum Dot-Based Luminescent Solar Concentrator. *Nano Energy* **2020**, *67*, 104217.
2. Carey, G. H.; Abdelhady, A. L.; Ning, Z.; Thon, S. M.; Bakr, O. M.; Sargent, E. H., Colloidal Quantum Dot Solar Cells. *Chem. Rev.* **2015**, *115* (23), 12732-12763.
3. Medintz, I. L.; Uyeda, H. T.; Goldman, E. R.; Mattoussi, H., Quantum Dot Bioconjugates for Imaging, Labelling and Sensing. *Nat. Mater.* **2005**, *4* (6), 435-446.
4. Jaiswal, J. K.; Simon, S. M., Potentials and Pitfalls of Fluorescent Quantum Dots for Biological Imaging. *Trends Cell Biol.* **2004**, *14* (9), 497-504.
5. So, M.-K.; Xu, C.; Loening, A. M.; Gambhir, S. S.; Rao, J., Self-Illuminating Quantum Dot Conjugates for *in vivo* Imaging. *Nat. Biotechnol.* **2006**, *24* (3), 339-343.
6. Heine, M.; Fischer, A. W.; Schlein, C.; Jung, C.; Straub, L. G.; Gottschling, K.; Mangels, N.; Yuan, Y.; Nilsson, S. K.; Liebscher, G.; Chen, O.; Schreiber, R.; Zechner, R.; Scheja, L.; Heeren, J., Lipolysis Triggers a Systemic Insulin Response Essential for Efficient Energy Replenishment of Activated Brown Adipose Tissue in Mice. *Cell Metab.* **2018**, *28* (4), 644-655.
7. Bruns, O. T.; Bischof, T. S.; Harris, D. K.; Franke, D.; Shi, Y.; Riedemann, L.; Bartelt, A.;

- Jaworski, F. B.; Carr, J. A.; Rowlands, C. J.; Wilson, M. W. B.; Chen, O.; Wei, H.; Hwang, G. W.; Montana, D. M.; Coropceanu, I.; Achorn, O. B.; Kloepper, J.; Heeren, J.; So, P. T. C.; Fukumura, D.; Jensen, K. F.; Jain, R. K.; Bawendi, M. G., Next-Generation *in vivo* Optical Imaging with Short-Wave Infrared Quantum Dots. *Nat. Biomed. Eng.* **2017**, *1* (4), 0056.
8. Sun, Q.; Wang, Y. A.; Li, L. S.; Wang, D.; Zhu, T.; Xu, J.; Yang, C.; Li, Y., Bright, Multicoloured Light-Emitting Diodes Based on Quantum Dots. *Nat. Photonics* **2007**, *1* (12), 717-722.
9. Dai, X.; Zhang, Z.; Jin, Y.; Niu, Y.; Cao, H.; Liang, X.; Chen, L.; Wang, J.; Peng, X., Solution Processed, High-Performance Light-Emitting Diodes Based on Quantum Dots. *Nature* **2014**, *515* (7525), 96-99.
10. Qian, L.; Zheng, Y.; Xue, J.; Holloway, P. H., Stable and Efficient Quantum-Dot Light-Emitting Diodes Based on Solution-Processed Multilayer Structures. *Nat. Photonics* **2011**, *5* (9), 543-548.
11. Won, Y.-H.; Cho, O.; Kim, T.; Chung, D.-Y.; Kim, T.; Chung, H.; Jang, H.; Lee, J.; Kim, D.; Jang, E., Highly Efficient and Stable InP/ZnSe/ZnS Quantum Dot Light-Emitting Diodes. *Nature* **2019**, *575* (7784), 634-638.
12. Yuan, Y.; Zhu, H.; Wang, X.; Cui, D.; Gao, Z.; Su, D.; Zhao, J.; Chen, O., Cu-Catalyzed Synthesis of CdZnSe–CdZnS Alloy Quantum Dots with Highly Tunable Emission. *Chem. Mater.* **2019**, *31* (7), 2635-2643.
13. Chen, O.; Wei, H.; Maurice, A.; Bawendi, M.; Reiss, P., Pure Colors from Core–Shell Quantum Dots. *MRS Bull.* **2013**, *38* (9), 696-702.
14. Kovalenko, M. V.; Manna, L.; Cabot, A.; Hens, Z.; Talapin, D. V.; Kagan, C. R.; Klimov, V. I.; Rogach, A. L.; Reiss, P.; Milliron, D. J.; Guyot-Sionnest, P.; Konstantatos, G.; Parak, W. J.; Hyeon, T.; Korgel, B. A.; Murray, C. B.; Heiss, W., Prospects of Nanoscience with Nanocrystals. *ACS Nano* **2015**, *9* (2), 1012-1057.
15. Gao, L.; Quan, L. N.; García de Arquer, F. P.; Zhao, Y.; Munir, R.; Proppe, A.; Quintero-Bermudez, R.; Zou, C.; Yang, Z.; Saidaminov, M. I.; Voznyy, O.; Kinge, S.; Lu, Z.; Kelley, S. O.; Amassian, A.; Tang, J.; Sargent, E. H., Efficient Near-Infrared Light-Emitting Diodes Based on Quantum Dots in Layered Perovskite. *Nat. Photonics* **2020**, *14*, 227-233.
16. McClelland, K. P.; Weiss, E. A., Selective Photocatalytic Oxidation of Benzyl Alcohol to Benzaldehyde or C–C Coupled Products by Visible-Light-Absorbing Quantum Dots. *ACS Appl. Energy Mater.* **2019**, *2* (1), 92-96.
17. Jiang, Y.; Wang, C.; Rogers, C. R.; Kodaimati, M. S.; Weiss, E. A., Regio- and Diastereoselective Intermolecular [2+2] Cycloadditions Photocatalysed by Quantum Dots. *Nat. Chem.* **2019**, *11* (11), 1034-1040.
18. Hu, J.; Pu, T.-J.; Xu, Z.-W.; Xu, W.-Y.; Feng, Y.-S., Cadmium Sulfide Quantum-Dot-Photocatalyzed Cascade Cyclization of Functionalized Difluoromethyl Chlorides with Unactivated Olefins. *Adv. Synth. Catal.* **2019**, *361* (4), 708-713.
19. Hao, H.; Lang, X., Metal Sulfide Photocatalysis: Visible-Light-Induced Organic Transformations. *ChemCatChem* **2019**, *11* (5), 1378-1393.

20. Guo, Q.; Liang, F.; Li, X.-B.; Gao, Y.-J.; Huang, M.-Y.; Wang, Y.; Xia, S.-G.; Gao, X.-Y.; Gan, Q.-C.; Lin, Z.-S.; Tung, C.-H.; Wu, L.-Z., Efficient and Selective CO<sub>2</sub> Reduction Integrated with Organic Synthesis by Solar Energy. *Chem* **2019**, *5* (10), 2605-2616.
21. Chakraborty, I. N.; Roy, S.; Devatha, G.; Rao, A.; Pillai, P. P., InP/ZnS Quantum Dots as Efficient Visible-Light Photocatalysts for Redox and Carbon–Carbon Coupling Reactions. *Chem. Mater.* **2019**, *31* (7), 2258-2262.
22. Dai, Y.; Tüysüz, H., Lead-Free Cs<sub>3</sub>Bi<sub>2</sub>Br<sub>9</sub> Perovskite as Photocatalyst for Ring-Opening Reactions of Epoxides. *ChemSusChem* **2019**, *12* (12), 2587-2592.
23. Zhu, X.; Lin, Y.; Sun, Y.; Beard, M. C.; Yan, Y., Lead-Halide Perovskites for Photocatalytic  $\alpha$ -Alkylation of Aldehydes. *J. Am. Chem. Soc.* **2019**, *141* (2), 733-738.
24. Zhu, X.; Lin, Y.; San Martin, J.; Sun, Y.; Zhu, D.; Yan, Y., Lead Halide Perovskites for Photocatalytic Organic Synthesis. *Nat. Commun.* **2019**, *10* (1), 2843.
25. Xie, S.; Shen, Z.; Deng, J.; Guo, P.; Zhang, Q.; Zhang, H.; Ma, C.; Jiang, Z.; Cheng, J.; Deng, D.; Wang, Y., Visible Light-Driven C–H Activation and C–C Coupling of Methanol into Ethylene Glycol. *Nat. Commun.* **2018**, *9* (1), 1181.
26. Xi, Z.-W.; Yang, L.; Wang, D.-Y.; Pu, C.-D.; Shen, Y.-M.; Wu, C.-D.; Peng, X.-G., Visible-Light Photocatalytic Synthesis of Amines from Imines via Transfer Hydrogenation Using Quantum Dots as Catalysts. *J. Org. Chem.* **2018**, *83* (19), 11886-11895.
27. Wu, W.-B.; Wong, Y.-C.; Tan, Z.-K.; Wu, J., Photo-Induced Thiol Coupling and C–H Activation Using Nanocrystalline Lead-Halide Perovskite Catalysts. *Catal. Sci. Technol.* **2018**, *8* (16), 4257-4263.
28. Schünemann, S.; van Gastel, M.; Tüysüz, H., A CsPbBr<sub>3</sub>/TiO<sub>2</sub> Composite for Visible-Light-Driven Photocatalytic Benzyl Alcohol Oxidation. *ChemSusChem* **2018**, *11* (13), 2057-2061.
29. Huang, H.; Yuan, H.; Janssen, K. P. F.; Solís-Fernández, G.; Wang, Y.; Tan, C. Y. X.; Jonckheere, D.; Debroye, E.; Long, J.; Hendrix, J.; Hofkens, J.; Steele, J. A.; Roeffaers, M. B. J., Efficient and Selective Photocatalytic Oxidation of Benzylic Alcohols with Hybrid Organic–Inorganic Perovskite Materials. *ACS Energy Lett.* **2018**, *3* (4), 755-759.
30. Huang, C.; Li, X.-B.; Tung, C.-H.; Wu, L.-Z., Photocatalysis with Quantum Dots and Visible Light for Effective Organic Synthesis. *Chem. Eur. J.* **2018**, *24* (45), 11530-11534.
31. Zhang, Z.; Edme, K.; Lian, S.; Weiss, E. A., Enhancing the Rate of Quantum-Dot-Photocatalyzed Carbon–Carbon Coupling by Tuning the Composition of the Dot’s Ligand Shell. *J. Am. Chem. Soc.* **2017**, *139* (12), 4246-4249.
32. Pal, A.; Ghosh, I.; Sapra, S.; König, B., Quantum Dots in Visible-Light Photoredox Catalysis: Reductive Dehalogenations and C–H Arylation Reactions Using Aryl Bromides. *Chem. Mater.* **2017**, *29* (12), 5225-5231.
33. Chen, K.; Deng, X.; Dodekatos, G.; Tüysüz, H., Photocatalytic Polymerization of 3,4-Ethylenedioxythiophene over Cesium Lead Iodide Perovskite Quantum Dots. *J. Am. Chem. Soc.* **2017**, *139* (35), 12267-12273.
34. Caputo, J. A.; Frenette, L. C.; Zhao, N.; Sowers, K. L.; Krauss, T. D.; Weix, D. J., General and

- Efficient C–C Bond Forming Photoredox Catalysis with Semiconductor Quantum Dots. *J. Am. Chem. Soc.* **2017**, *139* (12), 4250-4253.
35. Kodaimati, M. S.; McClelland, K. P.; He, C.; Lian, S.; Jiang, Y.; Zhang, Z.; Weiss, E. A., Viewpoint: Challenges in Colloidal Photocatalysis and Some Strategies for Addressing Them. *Inorg. Chem.* **2018**, *57* (7), 3659-3670.
36. Huang, Y.; Zhu, Y.; Egap, E., Semiconductor Quantum Dots as Photocatalysts for Controlled Light-Mediated Radical Polymerization. *ACS Macro Lett.* **2018**, *7* (2), 184-189.
37. De Roo, J.; Ibáñez, M.; Geiregat, P.; Nedelcu, G.; Walravens, W.; Maes, J.; Martins, J. C.; Van Driessche, I.; Kovalenko, M. V.; Hens, Z., Highly Dynamic Ligand Binding and Light Absorption Coefficient of Cesium Lead Bromide Perovskite Nanocrystals. *ACS Nano* **2016**, *10* (2), 2071-2081.
38. Zhang, Z.; Liang, Y.; Huang, H.; Liu, X.; Li, Q.; Chen, L.; Xu, D., Stable and Highly Efficient Photocatalysis with Lead-Free Double-Perovskite of Cs<sub>2</sub>AgBiBr<sub>6</sub>. *Angew. Chem. Int. Ed.* **2019**, *58* (22), 7263-7267.
39. De Jongh, H. A. P.; De Jonge, C. R. H. I.; Mijs, W. J., Oxidative Carbon-Carbon Coupling. I. Oxidative Coupling of  $\alpha$ -Substituted Benzylcyanides. *J. Org. Chem.* **1971**, *36* (21), 3160-3168.
40. Du, Y.; Zhang, Y.; Wang, S.; Zhao, K., Highly Stereoselective Dimerization of 3-Alkoxyimino-2-aryl-alkylnitriles via Oxidative Carbon–Carbon Bond Formation. *Synlett* **2009**, *2009* (11), 1835-1841.
41. Krieg, F.; Ochsenbein, S. T.; Yakunin, S.; ten Brinck, S.; Aellen, P.; Süess, A.; Clerc, B.; Guggisberg, D.; Nazarenko, O.; Shynkarenko, Y.; Kumar, S.; Shih, C.-J.; Infante, I.; Kovalenko, M. V., Colloidal CsPbX<sub>3</sub> (X = Cl, Br, I) Nanocrystals 2.0: Zwitterionic Capping Ligands for Improved Durability and Stability. *ACS Energy Lett.* **2018**, *3* (3), 641-646.
42. Liang, Z.; Hou, W.; Du, Y.; Zhang, Y.; Pan, Y.; Mao, D.; Zhao, K., Oxidative Aromatic C–O Bond Formation: Synthesis of 3-Functionalized Benzo[*b*]furans by FeCl<sub>3</sub>-Mediated Ring Closure of  $\alpha$ -Aryl Ketones. *Org. Lett.* **2009**, *11* (21), 4978-4981.
43. Liu, L.; Fan, Y.; He, Q.; Zhang, Y.; Zhang-Negrerie, D.; Huang, J.; Du, Y.; Zhao, K., Synthesis of Functionalized Fluorescent Indenes from Electron-Rich  $\alpha$ -Aryl Ketonitriles. *J. Org. Chem.* **2012**, *77* (8), 3997-4004.
44. Chen, O.; Zhao, J.; Chauhan, V. P.; Cui, J.; Wong, C.; Harris, D. K.; Wei, H.; Han, H.-S.; Fukumura, D.; Jain, R. K.; Bawendi, M. G., Compact High-Quality CdSe–CdS Core–Shell Nanocrystals with Narrow Emission Linewidths and Suppressed Blinking. *Nat. Mater.* **2013**, *12*, 445.
45. Tan, R.; Yuan, Y.; Nagaoka, Y.; Eggert, D.; Wang, X.; Thota, S.; Guo, P.; Yang, H.; Zhao, J.; Chen, O., Monodisperse Hexagonal Pyramidal and Bipyramidal Wurtzite CdSe–CdS Core–Shell Nanocrystals. *Chem. Mater.* **2017**, *29* (9), 4097-4108.
46. Peterson, L. I., Meso-dl Isomerization of 2,3-Dimethyl-2,3-diphenylsuccinonitrile. *J. Am. Chem. Soc.* **1967**, *89* (11), 2677-2681.
47. Griller, D.; Ingold, K. U., Persistent Carbon-Centered Radicals. *Acc. Chem. Res.* **1976**, *9* (1), 13-19.
48. Woo, J. Y.; Kim, Y.; Bae, J.; Kim, T. G.; Kim, J. W.; Lee, D. C.; Jeong, S., Highly Stable Cesium Lead Halide Perovskite Nanocrystals through in Situ Lead Halide Inorganic Passivation. *Chem. Mater.*

2017, 29 (17), 7088-7092.

49. Chen, O.; Chen, X.; Yang, Y.; Lynch, J.; Wu, H.; Zhuang, J.; Cao, Y. C., Synthesis of Metal–Selenide Nanocrystals Using Selenium Dioxide as the Selenium Precursor. *Angew. Chem. Int. Ed.* **2008**, 47 (45), 8638-8641.

50. Wang, P.; Wang, M.; Zhang, J.; Li, C.; Xu, X.; Jin, Y., Shell Thickness Engineering Significantly Boosts the Photocatalytic H<sub>2</sub> Evolution Efficiency of CdS/CdSe Core/Shell Quantum Dots. *ACS Appl. Mater. Interfaces* **2017**, 9 (41), 35712-35720.

51. Protesescu, L.; Yakunin, S.; Bodnarchuk, M. I.; Krieg, F.; Caputo, R.; Hendon, C. H.; Yang, R. X.; Walsh, A.; Kovalenko, M. V., Nanocrystals of Cesium Lead Halide Perovskites (CsPbX<sub>3</sub>, X = Cl, Br, and I): Novel Optoelectronic Materials Showing Bright Emission with Wide Color Gamut. *Nano Lett.* **2015**, 15 (6), 3692-3696.

52. Du, Y.; Liu, R.; Linn, G.; Zhao, K., Synthesis of N-Substituted Indole Derivatives via PIFA-Mediated Intramolecular Cyclization. *Org. Lett.* **2006**, 8 (26), 5919-5922.

53. Zhang, D.; Lian, M.; Liu, J.; Tang, S.; Liu, G.; Ma, C.; Meng, Q.; Peng, H.; Zhu, D., Preparation of O-Protected Cyanohydrins by Aerobic Oxidation of  $\alpha$ -Substituted Malononitriles in the Presence of Diarylphosphine Oxides. *Org. Lett.* **2019**, 21 (8), 2597-2601.

54. Hayyan, M.; Hashim, M. A.; AlNashief, I. M., Superoxide Ion: Generation and Chemical Implications. *Chem. Rev.* **2016**, 116 (5), 3029-3085.

55. Kresse, G.; Furthmüller, J., Efficient Iterative Schemes for ab initio Total-Energy Calculations using a Plane-Wave Basis Set. *Phys. Rev. B* **1996**, 54 (16), 11169-11186.

56. Kresse, G.; Joubert, D., From Ultrasoft Pseudopotentials to the Projector Augmented-Wave Method. *Phys. Rev. B* **1999**, 59 (3), 1758-1775.

57. Blöchl, P. E., Projector Augmented-Wave Method. *Phys. Rev. B* **1994**, 50 (24), 17953-17979.

58. Perdew, J. P.; Burke, K.; Ernzerhof, M., Generalized Gradient Approximation Made Simple. *Phys. Rev. Lett.* **1996**, 77 (18), 3865-3868.

59. Catalano, J. G.; Gaitonde, V.; Beesu, M.; Leivers, A. L.; Shotwell, J. B., Phenoxide Leaving Group SNAr Strategy for the Facile Preparation of 7-Amino-3-aryl pyrazolo[1,5-a]pyrimidines from a 3-Bromo-7-phenoxy pyrazolo[1,5-a]pyrimidine Intermediate. *Tetrahedron Lett.* **2015**, 56 (44), 6077-6079.

60. Wei, M.-X.; Wang, C.-T.; Du, J.-Y.; Qu, H.; Yin, P.-R.; Bao, X.; Ma, X.-Y.; Zhao, X.-H.; Zhang, G.-B.; Fan, C.-A., Enantioselective Synthesis of Amaryllidaceae Alkaloids (+)-Vittatine, (+)-epi-Vittatine, and (+)-Buphanisine. *Chem. Asian J.* **2013**, 8 (9), 1966-1971.

61. Kern, J. M.; Sauer, J. D.; Federlin, P., Determination de pK<sub>a</sub> d'acides conjugués de carbanions dans le DMSO anhydre. Reexamen des corrélations entre ces pK<sub>a</sub> et les potentiels d'oxydation E<sub>ox</sub> déterminés dans le même solvant. *Tetrahedron* **1982**, 38 (20), 3023-3033.

62. Kurz, M. E.; Baru, V.; Nguyen, P. N., Aromatic Acetylation Promoted by Manganese(III) and Cerium(IV) Salts. *J. Org. Chem.* **1984**, 49 (9), 1603-1607.

63. Chan, C.-K.; Chang, M.-Y., BF<sub>3</sub>·OEt<sub>2</sub>-Mediated [1,2]-Aryl Shift: Synthesis of Functionalized  $\alpha$ -Arylnitriles via the Bromination/Cyanation/Deformylation of Substituted Deoxybenzoin. *Tetrahedron*

2017, 73 (34), 5207-5213.

64. Honan, M. C.; Balasuryia, A.; Cresp, T. M., Total Synthesis of Sericenin. *J. Org. Chem.* **1985**, 50 (22), 4326-4329.

## Chapter 6

# Quantification of the Photon Absorption, Scattering, and On-resonance Emission Properties of CdSe-CdS Core-Shell Nanocrystals

Portions of this chapter are adapted and/or reprinted from the following works. Copyright belongs to the publisher.

Xu, J. X.; **Yuan, Y.**; Zou, S.; Chen, O.; Zhang, D\*., A Divide-and-Conquer Strategy for Quantification of Light Absorption, Scattering, and Emission Properties of Fluorescent Nanomaterials in Solutions. *Anal. Chem.* **2019**, *91* (13), 8540-8548.

Xu, J. X.; **Yuan, Y.**; Liu, M. Zou, S.; Chen, O.; Zhang, D\*., Quantification of the Photon Absorption, Scattering, and On-resonance Emission Properties of CdSe/CdS Core/Shell Quantum Dots: Effect of Shell Geometry and Volumes. *Anal. Chem.* **2020**, *92* (7), 5346-5353.



## 6.1 Background of Quantification of NCs Optical Properties

Fluorescent QDs have demonstrated their diverse applications in bioimaging,<sup>1-3</sup> lasing,<sup>4, 5</sup> optical devices<sup>6, 7</sup> and energy conservations<sup>8-10</sup> owing to their exceptional fluorescence properties. Understanding the optical properties of fluorescent nanomaterials is important for rational material design and applications. However, reliable quantifications of fluorophore photon absorption, scattering, and fluorescence activities can be challenging due to the complex interplay of the photon absorption, scattering, and emission. As an example, the UV–Vis spectrophotometric measurements quantify the sample total photon extinction, the combined contributions by material photon absorption and scattering. It is, however, a widespread practice for researchers to explicitly label or interpret the experimental UV–Vis extinction spectra as absorbance spectra. This approach can be highly problematic for nanoscale materials whose light scattering is likely significant.<sup>11-16</sup> In cases where light scattering was considered, some researchers assume that fluorescent NPs are Rayleigh scatterers in the long wavelength region and then compute the fluorophore scattering activities in the short wavelength by assuming its scattering cross-section linearly-proportional to  $\lambda^{-4}$ .<sup>17</sup> The validity of this approach has not been examined, to our knowledge. Indeed, light scattering is a universal material property because all materials have nonzero polarizability.<sup>18, 19</sup> Furthermore, only nonabsorbing materials with sizes significantly smaller than excitation wavelengths can be approximated as Rayleigh scatterers.<sup>20</sup> Resonance light scattering can occur for light-absorbing materials in the wavelength region where the sample absorbs.<sup>19</sup> Such resonance light scattering has been extensively demonstrated in nanoscale fluorophore aggregates such as self-assembled porphyrins.<sup>21-25</sup> While there are many analytical techniques for detecting sample light scattering intensity, scant information is available

on material scattering cross-sections. As an example, light scattering cross-section spectra of common organic solvents have been made available only very recently.<sup>26</sup> Compared to solvents, most of which are approximately pure scatters with no significant photon absorption and emission in the UV–Vis region, quantification of optical properties of fluorescent materials is drastically more difficult. A series of challenges must be simultaneously addressed in order to reliably determine their light scattering cross-section spectra. The first is the sample inner filter effect (IFE) induced by the sample photon absorption.<sup>27, 28</sup> The second is the interference of light scattering by solvent and sample holders. The third is the under-sampling issue arising from the fact that a spectrofluorometer collects only a small fraction of the scattered and/or emitted photons that are distributed in the three-dimensional space.<sup>29</sup> Critically, the fraction of the collected photons versus the total number of scattered or emitted photons depends not only on the instrument setups (e.g., acceptance angle, detection geometry, detection polarization bias) but also on the sample light scattering and fluorescence depolarization. Indeed, one must quantify the material light scattering and fluorescence depolarization in order to determine its light scattering and fluorescence activities.<sup>29</sup> The fourth is the interference of fluorophore fluorescence on light scattering detection. Such fluorescence interference arises from the fact that, when excited in the wavelength region it both absorbs and emits, a fluorophore can produce both fluorescence emission and light scattering under resonance excitation and detection conditions.<sup>29-31</sup>

A recent advance in the experimental quantification of the material optical properties is the polarized resonance synchronous spectroscopic (PRS2) technique (**Fig. 6.1**).<sup>29, 32</sup> Like the conventional resonance synchronous spectroscopic (RSS) method, PRS2 spectrum is also acquired with spectrofluorometers under resonance excitation and

detection conditions. Unlike the RSS method that uses plane polarized light (also commonly referred to as collimated nonpolarized light) for excitation and detection, however, the excitation and detection photons in PRS2 measurements are both linearly polarized.<sup>29</sup> For nonfluorescent materials, the IFE-corrected sample PRS2 signal is due completely to sample light scattering.<sup>29</sup> However, the IFE-corrected PRS2 spectra of fluorescent samples can contain both fluorescence and light scattering.<sup>29</sup> Therefore, one needs to decompose the fluorophore PRS2 spectra into its PRS2 scattering and fluorescence component spectra before quantification of the fluorophore light scattering and fluorescence cross sections and depolarizations.

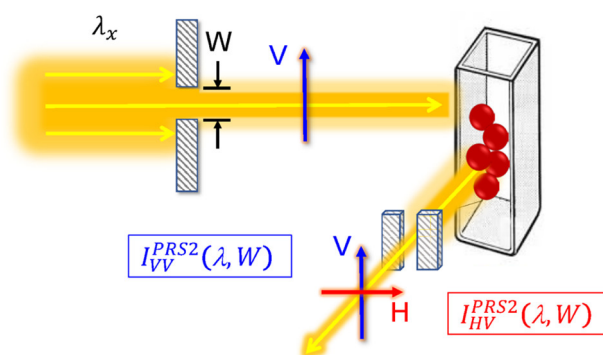


*Fig. 6.1: Schematic illustration of PRS2, adopt from ref 32.*

Understanding the origin of the light scattering signal in PRS2 spectra is straightforward. However, identifying the sources of the fluorescence signal in the sample PRS2 spectrum has proven challenging. As an example, beguiled by the fact the PRS2 is acquired under resonance excitation and detection conditions, we attributed the fluorescence signal in the PRS2 spectrum all to the fluorophore ORF in our initial PRS2 work.<sup>29</sup> Later on, we discovered that the fluorescence signal in the PRS2 spectrum is proportional to the square of the excitation and detection monochromator bandwidth while the light signal in the PRS2 spectrum is linearly proportional to the monochromator

bandwidth.<sup>32</sup> This observation leads to the realization that off-resonance fluorescence must also contribute to the fluorescence signal detected under the resonance excitation and detection conditions.<sup>32</sup> Unfortunately, however, we attributed such off-resonance fluorescence completely to fluorophore Stokes-shifted fluorescence (SSF).<sup>32</sup> The possible contribution by the fluorophore anti-Stokes-shifted fluorescence (ASSF) to the fluorescence signal in the PRS2 spectra has not been studied.

Using a new polarized anti-Stokes-shifted, on-resonance, and Stokes-shifted (PAOS) spectroscopic method developed in this work, we provide direct visual evidence that, besides ORF and SSF, fluorophore ASSF also contributes to its PRS2 fluorescence signal. An individual PAOS spectrum is acquired by keeping the excitation wavelength fixed but varying the detection wavelengths from the anti-Stokes' side to the Stokes side of the excitation wavelength. As will be shown later in this work, by acquiring a set of PAOS spectra as a function of excitation wavelength, one can reconstruct the fluorophore PRS2 spectrum and the fluorophore PRS2 light scattering and PRS2 fluorescence component spectra. While the PAOS spectral acquisition enables visual examination and facile separation of the fluorophore fluorescence and light scattering signal detected under resonance excitation and detection conditions, it can be time-consuming if the PAOS spectral acquisition is implemented crossing the entire UV–Vis spectral region. To resolve this issue, we devised a divide-and-conquer approach so that relatively tedious PAOS spectral acquisition is limited to the fluorophore emission wavelength region. This divide-and-conquer strategy divides a fluorophore UV–Vis spectrum into a blue and a red wavelength region. The blue wavelength region spans from 300 nm to the blue-edge of the fluorophore SSF peak. The fluorophores in this wavelength region are simultaneous photon absorbers and scatterers, but not emitters under the resonance excitation and

detection conditions. The fluorophore red-wavelength region spans from the blue-edge of the fluorophore SSF peak to the red-edge of its SSF peak. In this region, the IFE-corrected PRS2 spectrum can contain fluorophore ASSF, ORF, and SSF emission and light scattering features, as will be demonstrated later.

## 6.2 Quantification of Fluorescent Nanomaterials in Solutions

The five model fluorophores used in this work comprise three NP fluorophores: fluorescence polystyrene NPs (fPSNP), rod-shaped fluorescent quantum dots (RQD), spherical fluorescence quantum dots (SQD), and two molecular fluorophores: Rhodamine 6G (R6G) and Eosin Y (EY). These fluorophores differ significantly in their light scattering, absorption, and ORF activities. Therefore, they serve a representative set of model analytes for testing the utility of the designed methods. For discussion simplicity, all PRS2 and PAOS spectra will be represented as PRS2 XD and PAOS XD, respectively. The first letter X indicates the polarization direction of the excitation linear polarizer, while the second letter D stands for the detection polarizer. Both X and D can take values “N,” “V,” and “H,” where “N” indicates no linear polarizer is used; “V” represents that the light is vertically polarized, i.e, the electrical field of the electromagnetic wave is perpendicular to the spectrofluorometer plane defined by the excitation lamp, sample chamber, and detector; and “H” indicates the linear polarizer is parallel to the instrument plane.

Dividing fluorophore UV-Vis spectra into its blue and red wavelength regions is straightforward on the basis of the experimental UV-Vis extinction and SSF spectrum (**Fig. 6.2f–j**). The wavelength region below the blue-edge of the SSF peak (highlighted in light blue) is the blue wavelength region. The spectral region covering SSF emission wavelengths is referred to as red-wavelength region (highlighted red in **Fig. 6.2f–j**).

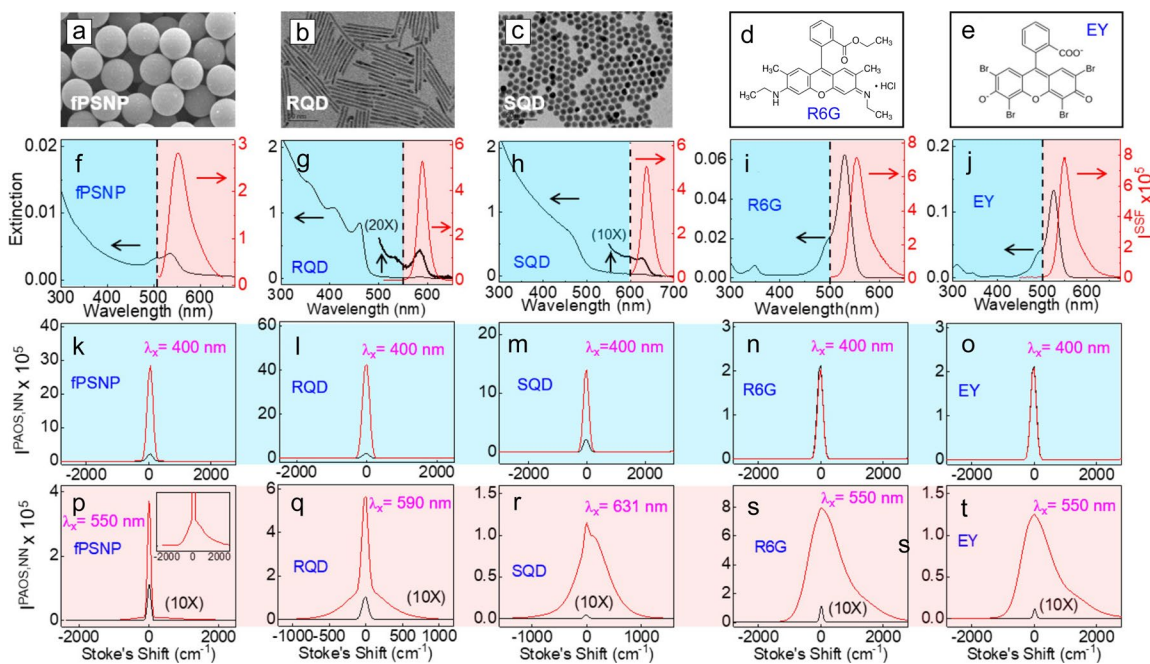


**Fig. 6.2:** Structures, UV-Vis, fluorescence, and PAOS spectra obtained with (1st column) fPSNP, (2nd column) RQD, (3rd column) SQD, (4th column) R6G, and (5th column) EY. (1st row; a) SEM images of fPSNP. (1st row; b, and c) TEM images of RQD, and SQD, respectively. (d and e) R6G and EY molecular structures, respectively. (2nd row; black) UV-Vis extinction and (red) SSF spectra. The dashed lines divide the blue and red wavelength regions shadowed with blue and pink, respectively. (3rd row and 4th row): Example PAOS spectra obtained with an excitation wavelength in the (3rd row) blue- and (4th row) red-wavelength region. The spectra in red and black are the as-acquired sample and solvent PAOS spectrum, respectively. The solvent PAOS spectra in p–t is scaled by a factor of 10. The inset in P is the zoom-in of the data showing the fPSNP fluorescence signal.

In their blue wavelength region, the NP fluorophores fPSNP, RQD, and SQD are simultaneously photon absorbers and scatterers but not emitters, while the two molecular fluorophores R6G and EY are predominantly light absorbers with no significant photon scattering or emissions under the resonance excitation and detection conditions. The light scattering of the NP fluorophores is evident from the intense sharp peak centered at detection wavelength with zero Stokes-shift from excitation wavelength (the red curve in **Fig. 6.2k–m**). This peak shares the same shape with the solvent light scattering peak but with drastically higher intensity. In contrast, there is no detectable fluorophore light scattering in the AOS spectra obtained with R6G and EY in their respective blue

wavelength regions (**Fig. 6.2n–o**). The light scattering peaks in these two sample solutions are due almost entirely to light scattering from the solvent and sample-holder background. In their red wavelength region, NP fluorophores are all simultaneous photon absorbers, scatterers, and fluorescence emitters (**Fig. 6.2p–r**), while the R6G and EY are simultaneous photon absorbers and emitters with, again, no significant photon scattering (**Fig. 6.2s,t**). The absence of detectable photon scattering by R6G and EY is not surprising because of their small sizes. For these two molecular fluorophores, their UV–Vis extinction cross-section spectra were directly taken as their respective absorption cross-section spectrum.

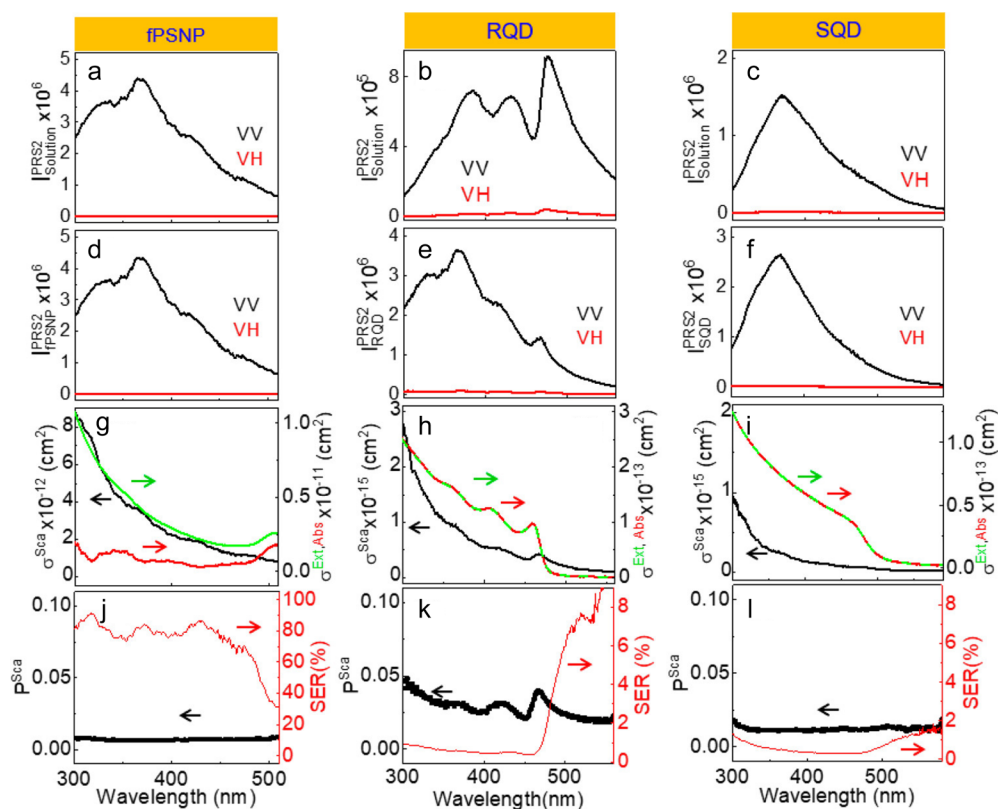


**Fig. 6.3:** Decomposition of NP fluorophore UV–Vis extinction cross-section spectra into the absorption and scattering component spectra for (1st column) fPSNP, (2nd column) RQD, and (3rd column) SQD in their blue wavelength region. (1st row) As-acquired PRS2 (black) VV and (red) VH spectra of the sample solutions. (2nd row) Fluorophore-specific PRS2 (black) VV and (red) VH spectra. (3rd row) UV–Vis (green) extinction, (red) absorption, and (black) scattering cross-section spectra. (4th row; red) the fluorophore scattering-to-extinction ratio (SER) and (black) scattering depolarization spectrum.

For the NP fluorophores, however, their photon scattering contribution to their UV–Vis extinction spectra should be considered in quantification of their photon absorption activities. In other words, one needs to decompose the NP UV–Vis extinction spectra into its absorption and scattering component spectra. The fluorophore PRS2 spectra obtained in their blue wavelength region are due exclusively to the fluorophore light scattering with no fluorescence contribution (**Fig. 6.2k–o**). As such, one calculates the fluorophore light scattering depolarization spectrum and, subsequently, its scattering cross-section spectra using the experimental PRS2 VV and VH spectra (**Fig. 6.3**). The procedures for converting the as-acquired solution PRS2 VV and VH spectra (**Fig. 6.3a–c**) to their respective fluorophore-specific PRS2 spectra (**Fig. 6.3d–f**), the calculations of the fluorophore light scattering depolarization spectra (**Fig. 6.3j–l**), and cross-section spectra (**Fig. 6.3g–i**) are shown in earlier works.<sup>24, 45</sup> After quantification of the fluorophore extinction cross-section spectra (**Fig. 6.3g–i**) on the basis of the fluorophore UV–Vis extinction spectra (**Fig. 6.2f–h**), the fluorophore UV–Vis absorption cross-section spectra (**Fig. 6.3g–i**) were obtained by subtracting the scattering cross-section spectrum from the fluorophore UV–Vis extinction cross-section spectrum.

Several observations are worth noting: First, with only the exception of the fPSNP that is predominantly a photon scatterer in its blue wavelength region, the QD and molecular fluorophores are all strong photon absorbers in their respective blue wavelength regions. The highest scattering-to-extinction ratio is more than 80% for fPSNP (**Fig. 6.3g**) but 8% (**Fig. 6.3h**) and 2% (**Fig. 6.3i**) for RQD and SQD, respectively. These indicate that the examined QDs are predominant photo absorbers. Second, the fPSNPs can be approximated as Rayleigh scatterers, and their experimental cross-section spectra can be treated approximately as  $\sigma(\lambda) = a\lambda^{-4}$  where  $a$  is a constant. However,



neither RQDs nor SQDs are Rayleigh scatterers as assumed in earlier work.<sup>34</sup> Third, the light scattering depolarization of the RQD is significantly higher than both SQDs and fPSNPs. This phenomenon is consistent with the observations that the rod-shaped solvent molecules and gold NPs (AuNPs) invariably have higher light scattering depolarization than their respective spherical counterparts.<sup>26, 45</sup>

Comparing and contrasting the RQD depolarization spectrum with that for rod-shaped molecule CS<sub>2</sub> and AuNPs is instructive. The scattering depolarization of CS<sub>2</sub> is totally wavelength-independent, and it is 0.5 crossing the entire UV–Vis region,<sup>26</sup> while the scattering depolarization of gold nanorods is strongly wavelength-dependent,<sup>45</sup> so is that of RQD (**Fig. 6.3K**). However, the peak scattering depolarizations of the rod-shaped AuNPs and QDs are vastly different. The peak scattering depolarization is 0.4 in a gold nanorod with an AR as small as 3.<sup>45</sup> In contrast, the peak scattering depolarization of the RQD is only 0.05 even when its AR is as large as 16.8 (**Fig. 6.2B** and **Fig. 6.3K**). The fundamental mechanism governing the QD light scattering depolarization features is currently unclear. Nonetheless, the data obtained with the RQDs and SQDs provide further evidence that light scattering depolarization is sensitive to the scatterers' geometries.

Consistent with what has been observed in their blue wavelength regions, the UV–Vis extinction spectra of molecular fluorophores R6G and EY in their red wavelength region can also be directly taken as their respective absorbance spectrum since there are no detectable scattering features in the R6G and EY PAOS spectra obtained in their red wavelength regions (**Fig. 6.2S,T**). In contrast, PAOS spectra (**Fig. 6.2P–R**) obtained with the NP fluorophores contain both fluorophore light scattering and fluorescence signals. This conclusion is further supported by the PAOS spectra obtained

for all the model fluorophores in their red wavelength regions (**Fig. 6.4**).

Comparing and contrasting the fluorophore PRS2 and PAOS spectra (**Fig. 6.4**) is instructive. The experimental PRS2 spectra overlap nearly perfectly with that of the reconstructed PRS2 (**Fig. 6.4**). The reconstructed PRS2 spectra (blue dots in the plots in **Fig. 6.4**) were obtained by taking the PAOS spectral intensities at each excitation wavelength as the intensity of the reconstructed PRS2 spectrum. The excellent agreement between the experimental and reconstructed PRS2 spectra highlights the reproducibility of the PRS2 and PAOS measurements.

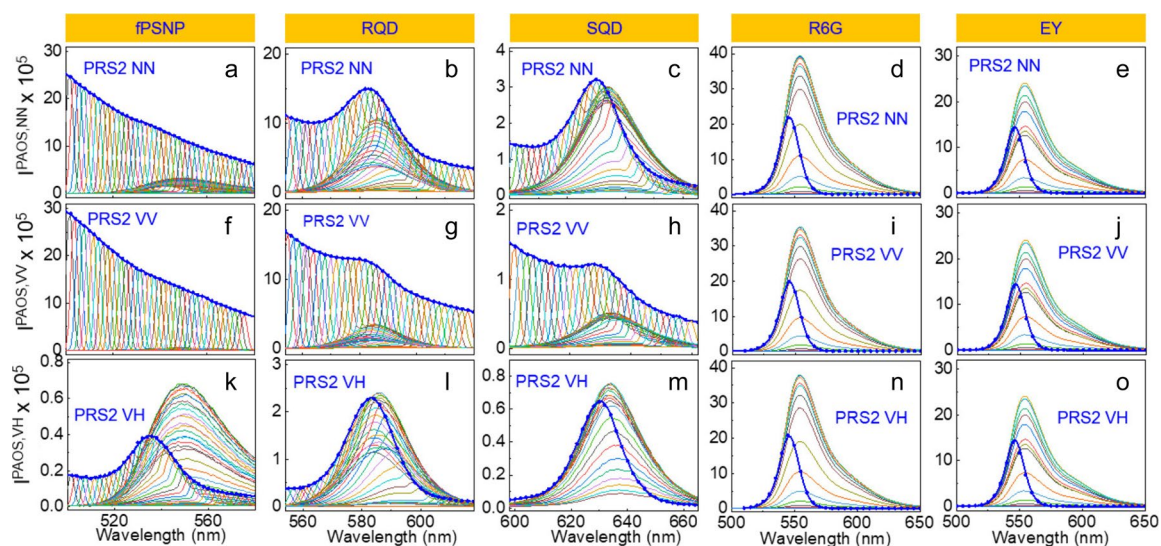


**Fig. 6.4:** Comparisons of (1st row) as-acquired PAOS NN and PRS2 NN spectra, (2nd row) PAOS VV and PRS2 VV spectra, (3rd row) PAOS VH and PRS2 VH spectra for (1st column) fPSNP, (2nd column) RQD, (3rd column) SQD, (4th column) R6G, and (5th column) EY in their red wavelength region. The solid blue line is the experimental PRS2 spectrum, and the blue dots are the PRS2 spectra reconstructed by taking the PAOS intensity at each excitation wavelength as the intensity of the reconstructed PRS2 spectrum at the resonance excitation and detection wavelength.

The PAOS-based PRS2 reconstruction method holds two key advantages over the direct experimental PRS2 acquisitions. First, the PAOS spectra used for the PRS2 reconstruction provide direct visual evidence that both light scattering and fluorescence can contribute to the fluorophore PRS2 spectra. In contrast, one can deduce the

fluorescence and light scattering contribution to PRS2 signal through only indirect evidence either by the difference in the depolarization between fluorescence and light scattering<sup>45</sup> or by the difference in intensity dependence on the monochromator bandwidth between the fluorescence and light scattering signal.<sup>32</sup> Second, the PAOS spectra enable one to directly separate the light scattering and fluorescence contribution to the experimental PRS2 spectrum and subsequently reconstruct the fluorophore PRS2 light scattering and fluorescence component spectra (**Fig. 6.5**). This light scattering peak is invariably centered at excitation wavelength and with a peak shape identical to the scattering peak observed in the PAOS spectra obtained with a pure scatterer such as the solvents and PSNP (**Fig. 6.2k–o**). The decomposition of the fluorophore PAOS spectrum into its polarized fluorescence and light scattering component spectra (**Fig. 6.5**) was performed by subtracting the scaled PSNP PAOS spectra from fluorophore PAOS spectrum. The criterion for determining the scaling factor is that the resulting difference spectrum should contain no residual sharp peak on top of a broad fluorescence peak. Since there are no detectable light scattering features in the PAOS spectra obtained with R6G and EY (**Fig. 6.4**), their experimental or reconstructed PRS2 spectra are their PRS2 fluorescence spectra. Third, the PAOS spectra offer direct evidence that when excited in the wavelength region the fluorophore both absorbs and emits; light scattering, ASSF, ORF, and SSF can all concurrently occur (**Fig. 6.2p–t** and **Fig. 6.4**).

The relative fluorescence and scattering contribution to the PRS2 spectra of the NP fluorophores depends strongly on the excitation and detection polarization (**Fig. 6.5**). The scattering/fluorescence intensity ratio decreases from PRS2 VV, PRS2 NN, and then to PRS2 VH (**Fig. 6.5**). This observation is consistent with the fact that fluorescence depolarization for fluorophores in solution is usually very high, close to unity for most

small molecular fluorophores,<sup>27</sup> but the light scattering depolarization is commonly very small, as shown in **Fig. 6.3**. The absence of a detectable scattering feature in the SQD PAOS VH is also consistent with spherical scatterers usually having negligible light scattering depolarization.<sup>26, 45</sup>

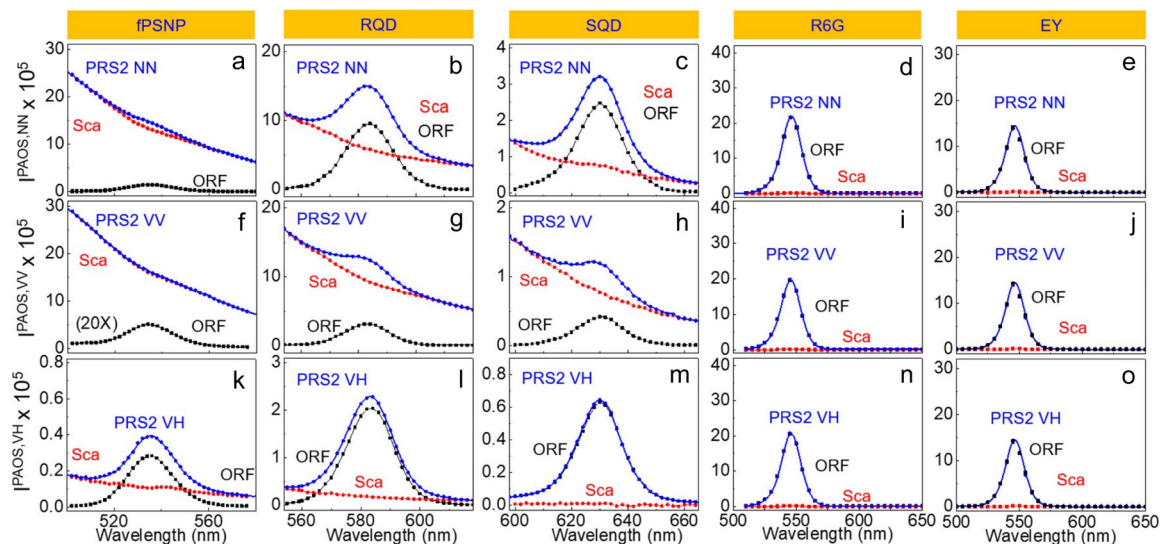


**Fig. 6.5:** (Black) PRS2 fluorescence and (red) scattering component spectra derived from the experimental (blue) PAOS spectra for (1st column) fPSNP, (2nd column) RQD, (3rd column) SQD, (4th column) R6G, and (5th column) EY. The data in the first, second, and third rows are derived from the PAOS spectra acquired with excitation and detection polarization of NN, VV, and VH, respectively.

The fluorophore PRS2 fluorescence spectra and fluorophore PRS2 scattering spectra are shown in **Fig. 6.5**, the light scattering and ORF cross-section spectra were quantified for the three NP fluorophores (**Fig. 6.6**). The fluorophore absorption cross-section spectrum is quantified by subtracting the fluorophore light scattering cross-section spectrum from its extinction cross-section spectrum (**Fig. 6.6a–c**). The fluorophore ORF quantum yield spectrum (QY) is determined using the equation  $ORF\ QY(\lambda) = \sigma^{ORF}(\lambda)/\sigma^{abs}(\lambda)$ , the ratio between the fluorophore ORF fluorescence cross-section spectrum versus absorption cross-section spectrum in the wavelength region that the fluorophore both absorbs and emits. Since the signals of R6G and EY PRS2 spectra

are completely dominated by the fluorescence feature, their IFE- and solvent-background- corrected PRS2 spectra were used directly for calculating the fluorophore ORF depolarization, cross-sections, and QY. The fluorophore ORF and light scattering depolarization spectra (**Fig. 6.6g–i**) are computed.

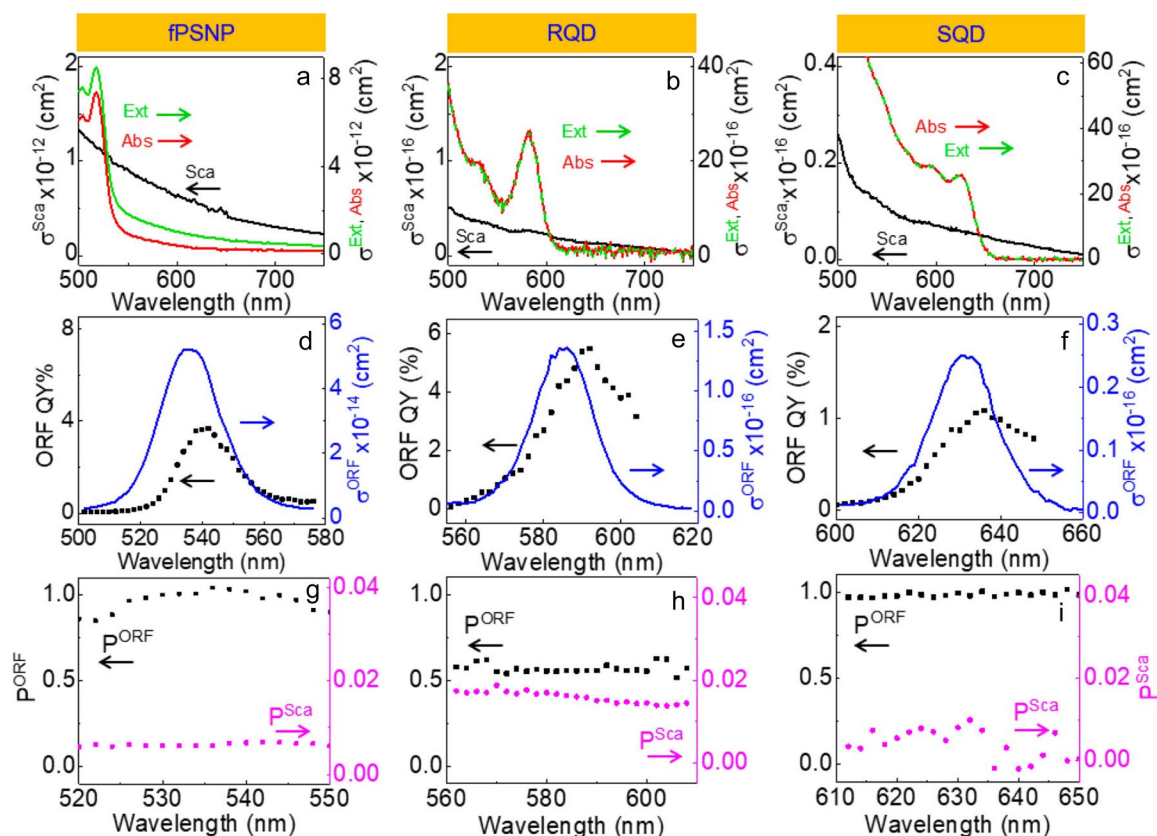


**Fig. 6.6:** Optical constants of (1st column) *fPSNP*, (2nd column) *RQD*, and (3rd column) *SQD* in their respective red wavelength region. (1st row) UV–Vis (green) extinction, (red) absorption, and (black) scattering cross-sections. (2nd row) ORF emission (blue) cross-sections and (black) ORF quantum yield (*QY*) spectrum. (3rd row) (red) scattering and (black) ORF depolarization. The spectra, axis, and name for each optical parameter are encoded with the same color.

Several observations from **Fig. 6.6** are worth noting. *fPSNP* has drastically higher extinction, scattering, and absorption and ORF emission cross-sections than their respective counterparts for the QDs (**Fig. 6.6**). The scattering cross-section of *fPSNP* at 500 nm excitation wavelength is more than 4 orders of magnitude higher than that for the *RQD* and *SQD* (**Fig. 6.6a–c**), which is due most likely to the fact that *fPSNP* is much

larger than both RQDs and SQDs. The average ORF depolarization of the RQDs in its ORF active region is  $0.6 \pm 0.06$  (**Fig. 6.6h**), which is significantly smaller than that of other model fluorophores including the SQDs (**Fig. 6.6i**). The ORF depolarizations for the other fluorophores are all close to unity crossing their entire ORF-active region. Fluorescence depolarization is related to the fluorophore mobility and fluorescence lifetime.<sup>33-37</sup> A detailed reason why RQDs have such a small ORF depolarization is currently unclear. However, this result suggests that the fluorescence depolarization can be an effective spectral marker for differentiating RQDs and SQDs. The fact that the RQDs have higher light scattering depolarization than both SQDs and fPSNPs (**Fig. 6.6g-i**) in their red wavelength region is consistent again with the fact that rod-shape scatterers have higher scattering depolarization than the spherical ones.

Up to date, we have presented three methods for differentiating and separating light scattering and fluorescence contributions to the sample PRS2 spectra. The first is the spectral subtraction method that works only under the assumption that the fluorophore PRS2 VH features are due entirely to its fluorescence. This assumption is valid only for well-dispersed molecular fluorophores that have no detectable light scattering features in their PRS2 VH spectrum, but it is unreliable for the NP fluorophores used in this work. The second is the recent bandwidth varied-PRS2 (BV-PRS2) method. While the BV-PRS2 technique is a self-sufficient method enabling one to compute light scattering and ORF cross-sections and depolarization regardless of the fluorophore fluorescence and light scattering depolarization, it provides no insights to the origins of the fluorescence detected in the PRS2. The third, which is the current PAOS-based approach, is also a self-sufficient method. The key advantage of this PAOS-based method is that it enables direct visualization and separation of the light scattering and fluorescence contribution to

fluorophore PRS2 spectra. This visualization has been critical for revealing the fact that the fluorescence in the PRS2 spectra comprises ASSF, ORF, and SSF contributions, not just ORF in the initial PRS2 technique, or only ORF and SSF assumed in the BV-PRS2 technique.

### 6.3 Quantification of the QD Optical Spectra

A total of eight CdSe-CdS core-shell fluorescent QDs, four spherical and four rod-shaped, are employed as the model QDs. All SQDs have the same spherical core (4.3 nm in diameter), but with varying shell thicknesses that result in QD diameters of 5.6 nm, 7.4, 9.2, and 10.8 nm, respectively. For the sake of discussion convenience, these SQDs are referred to as SQD5.6, SQD7.4, SQD9.2, and SQD10.8, respectively. The CdSe core used for the preparation of the rod-shaped QDs (RQDs) are also spherical, but with a smaller diameter (3.0 nm in diameter). The four RQDs all have the same width (4.4 nm) but with different lengths that result in different AR. These RQDs are referred to as RQD4.8, RQD9.3, RQD12.8, and RQD16.8, respectively, where the number specifies the AR of the RQDs.

The TEM images of the CdSe-CdS core-shell QDs are shown in **Fig. 6.7**. Based on the structural analyses of seeded-grown QDs performed in previous works,<sup>38, 39</sup> the CdSe cores are located at the center in SQDs while at one end in the. The width of all RQDs are essentially the same based on their TEM images (**Fig. 6.7**) and the thermal gravimetric analysis (TGA) (**Fig. 6.8**). The percentage mass losses due to the ligand evaporation in the TGA thermograms are approximately the same for all RQDs (**Fig. 6.8b**), which indicates the surface-to-volume ratios are very similar for the RQDs and is consistent with the fact that the RODs have the same width but different lengths (**Table 6.1**). In contrast, the ligand evaporation-induced mass loss for the SQDs decreases with



increasing QD diameter (**Fig. 6.8a**), which is again consistent with the fact that for SQDs, their surface-to-volume ratios decrease with increasing particle sizes (**Table 6.1**).

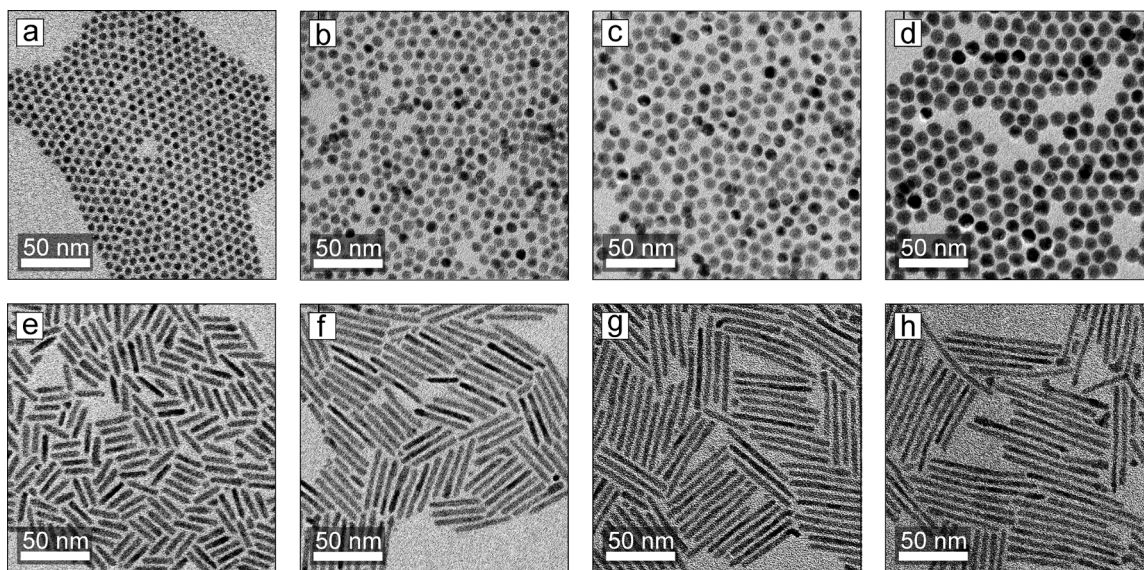


**Fig. 6.7:** TEM images of (a) SQD5.6, (b) SQD7.4, (c) SQD9.2, (d) SQD10.8, (e) RQD4.8, (f) RQD9.3, (g) RQD12.8, and (h) RQD16.8.

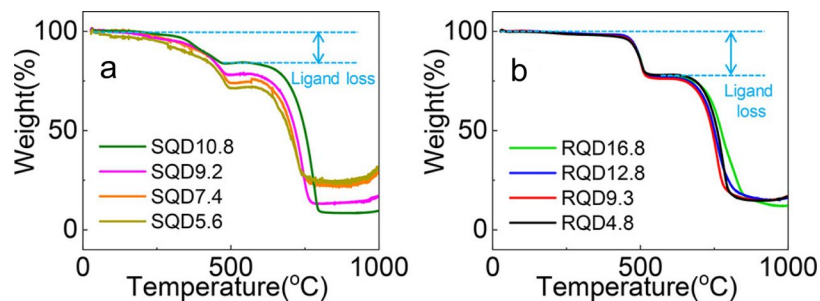


**Fig. 6.8:** TGA thermograms of (a) SQDs and (b) RQDs. The weight loss range highlighted with blue dashed lines are ligand loss percentages for SQD10.8 in (a) and RQD16.8 in (b) as examples.



**Table. 6.1:** Summary of QD dimensions and calculation of QD Molarity.

Sample	Core Abs (nm)	Core Diameter (nm)	Core Volume (nm <sup>3</sup> )	Core mass (mg)	Core/Shell Diameter (nm)	Core/Shell volume (nm <sup>3</sup> )	Shell Volume (nm <sup>3</sup> )	Shell mass (mg)	Core/shell mass (mg)	Core/shell mass% from TGA (%)	QD particle mass (mg)	# particle per mg	QD stock molality (mg/ml)	QD stock molarity (mol/L)
SQD5.6	593	4.29	41	2.41E-16	5.6	91	50	2.41E-16	4.82E-16	71.8%	6.71E-16	1.49E+15	3.0	7.42E-06
SQD7.4	593	4.29	41	2.41E-16	7.4	212	170	8.19E-16	1.06E-15	74.3%	1.43E-15	7.02E+14	0.94	1.09E-06
SQD9.2	593	4.29	41	2.41E-16	9.2	407	366	1.76E-15	2.00E-15	78.2%	2.56E-15	3.91E+14	0.98	6.37E-07
SQD10.8	593	4.29	41	2.41E-16	10.8	659	617	2.97E-15	3.21E-15	83.4%	3.85E-15	2.60E+14	5.5	2.37E-06
RQD4.8	549	3.02	14	8.39E-17	22.2; 4.6	369	354	1.71E-15	1.79E-15	78.1%	2.29E-15	4.36E+14	5.97	4.33E-06
RQD9.3	549	3.02	14	8.39E-17	39.2; 4.2	543	528	2.54E-15	2.63E-15	76.1%	3.46E-15	2.89E+14	3.91	1.88E-06
RQD12.8	549	3.02	14	8.39E-17	56.5; 4.4	858	844	4.07E-15	4.15E-15	76.5%	5.42E-15	1.84E+14	4.60	1.41E-06
RQD16.8	549	3.02	14	8.39E-17	73.8; 4.4	1121	1107	5.34E-15	5.42E-15	76.5%	7.08E-15	1.41E+14	7.89	1.85E-06
R core	549	3.02	14	8.39E-17	N/A	N/A	N/A	N/A	N/A	57%	1.48E-16	6.76E+15	13.78	1.55E-04
S core	593	4.29	41	2.41E-16	N/A	N/A	N/A	N/A	N/A	58%	4.19E-16	2.39E+15	17.83	7.07E-05

The shell geometry has enormous impact on the QD fluorescence depolarization or fluorescence anisotropy. Fluorescence depolarization and anisotropy can be readily converted into each other.<sup>40</sup> We choose to use fluorescence depolarization instead of anisotropy because depolarization is far more commonly used in light scattering literatures. Currently fluorescence depolarization or anisotropy has been mostly investigated using a single excitation or emission wavelength. We devised in this work a total fluorescence depolarization method to probe how the fluorescence depolarization varies as a function of the excitation and detection wavelengths (**Fig. 6.9a, b**). Evidently the RQD fluorescence depolarization depends strongly on the RQD sizes and the excitation wavelengths (**Fig. 6.9c**), while the SQDs have near unity fluorescence depolarization regardless of the SQD sizes and the excitation and detection wavelengths (**Fig. 6.9d**).

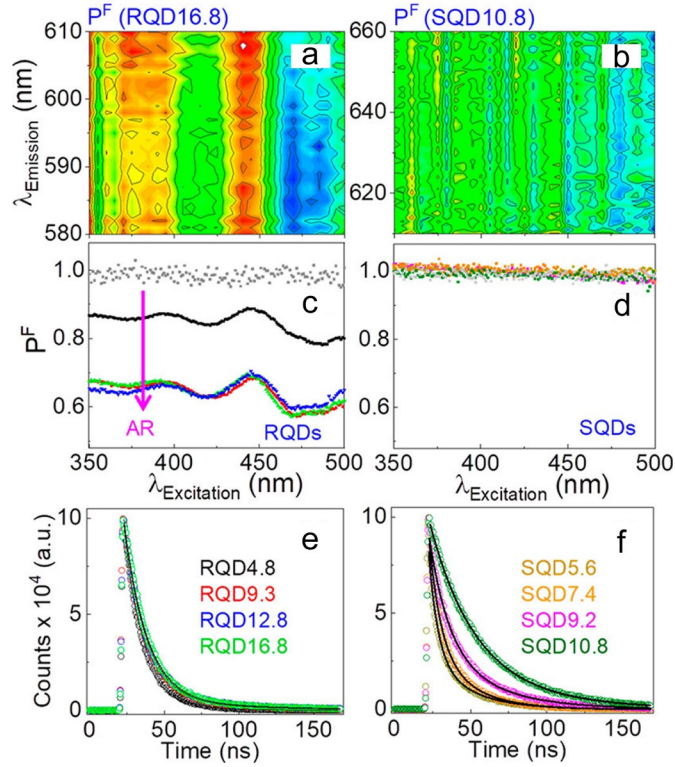


**Fig. 6.9:** (a) and (b) show example total fluorescence depolarization ( $P^F$ ) spectra of RQD16.8 and SQD10.8. (c) and (d) show fluorescence excitation depolarization spectra of SQDs and RQDs. (e) and (f) are fluorescence lifetime data of SQDs and RQDs, respectively. The circles are experimental data and the black traces are exponential fitting, which follows the two-exponential decay model.

The difference between RQDs and SQDs in their fluorescence depolarization is most likely due to rotational diffusion rate. Fluorescence depolarization is a function of fluorophore rotational correlation time and the fluorescence lifetime.<sup>41</sup> When the fluorophore rotational correlation time is much shorter than its fluorescence emission lifetime, the fluorescence emission dipoles can adopt any angle related to the excitation polarization after fast fluorophore rotations. In this case, the fluorescence emission is isotropic, which results in unity of fluorescence depolarization ( $P^F = 1$ ). In contrast, if the fluorophore rotational correlation time is longer than fluorescence lifetime, the polarizations of the emitted photons will mostly remain oriented towards emission dipole direction, leading to anisotropic emission ( $P^F \neq 1$ ). Since RQDs and SQDs have similar

fluorescence lifetimes (**Fig. 6.9e** and **f**), the fact that RQDs, especially the ones with large ARs, deviate significantly from unity strongly suggests that RQDs have longer rotational correlation time than SQDs.

The scattering depolarizations of both RQDs and SQDs are negligibly small at the QD emission wavelength region, which is manifested by the fact that no observable light scattering signal in the PAOS VH spectra obtained with the QDs (**Fig. 6.10q–t**). Since the fluorescence depolarizations of SQDs are unity, the efficient PRS2 method is directly applicable for decomposition of the SQD PRS2 spectra into their scattering and ORF component spectra, and subsequently the SQD UV-Vis extinction spectra into their absorption and scattering extinction component spectra.<sup>40</sup> In contrast, the PAOS spectra is necessary for quantifications of RQD light absorption, scattering, and ORF activities in its ORF active region because the RQD fluorescence depolarization is strongly excitation wavelength dependent (**Fig. 6.9**). The wavelength region where PAOS analysis is necessary can be readily identified by comparing UV-Vis, SSF, and PRS2 VH spectra of individual RQD samples (**Fig. 6.10a–d**). PRS2 VH refers to the PRS2 spectra taken under condition where the excitation polarization is vertical (V), but the detection polarization is horizontal (H) to the plane defined by the excitation source, sample chamber, and the detector. Only the wavelength region where all three spectra overlap can ORF occurs, and thereby PAOS spectral acquisitions are required. The PAOS VV spectra acquired in the ORF-active wavelength region contain both light scattering, and anti-stokes-shifted fluorescence, on-resonance fluorescence, and stokes-shifted fluorescence (**Fig. 6.10 e–h**). In contrast, the PAOS VH spectra are dominated by the RQD fluorescence with relatively small light scattering contribution (**Fig. 6.10m–p**). Using the method described in the PAOS publication,<sup>42</sup> the RQD PRS2 VV and PRS2

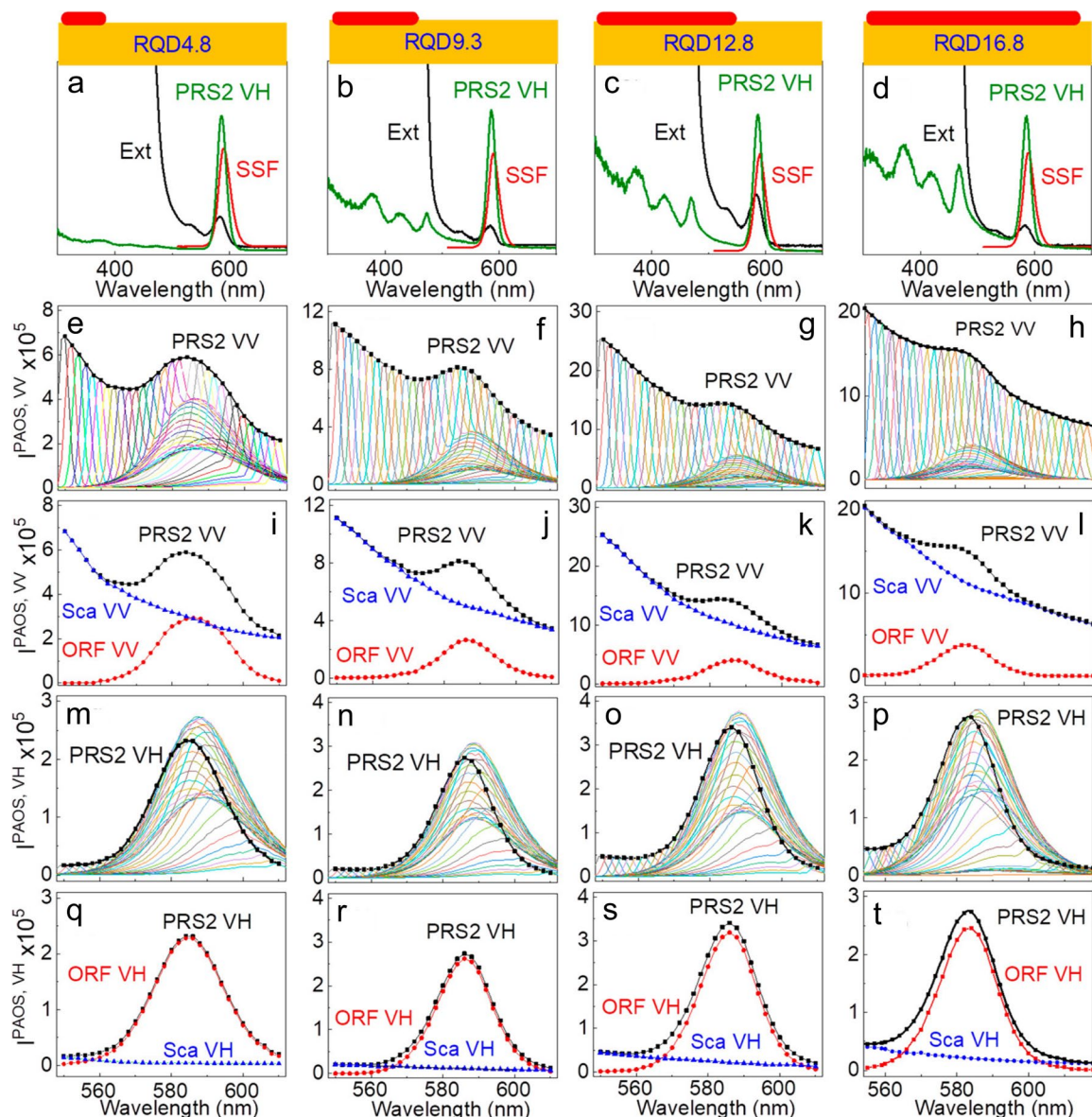


**Fig. 6.10:** (1st row) (black) RQD UV–Vis extinction (*Ext*) spectra, (red) Stokes’s Shifted Fluorescence (*SSF*) spectra, and (green) PRS2 VH spectra of (a) RQD4.8, (b) RQD9.3, (c) RQD12.8, (d) RQD16.8. (2nd row) PAOS VV spectra in the ORF-active region for (e) RQD4.8, (f) RQD9.3, (g) RQD12.8, (h) RQD16.8. (3rd row) Separation of scattering and ORF component in the PRS2 VV spectra with PAOS in the ORF-active wavelength region for (i) RQD4.8, (j) RQD9.3, (k) RQD12.8, (l) RQD16.8. (4th row) PAOS VH spectra in the ORF-active region for (m) RQD4.8, (n) RQD9.3, (o) RQD12.8, (p) RQD16.8. (5th row) Separation of scattering and ORF component in the PRS2 VH spectra with PAOS in the ORF-active wavelength region for (q) RQD4.8, (r) RQD9.3, (s) RQD12.8, (t) RQD16.8.

VH spectra are decomposed into their respectively ORF and light scattering component spectra. (Fig. 6.10i-l, and Fig. 6.10q-4t).

## 6.4 Effect of Shell Sizes and Geometries on Shell Scattering and Absorption Cross-sections

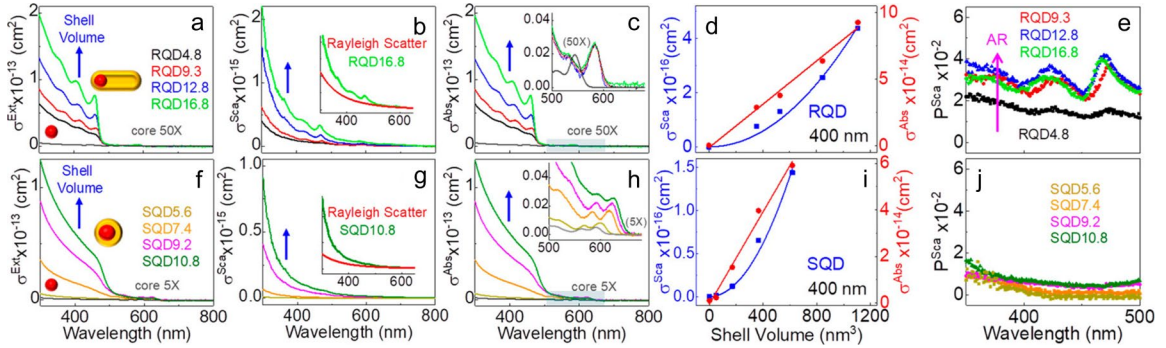


**Fig. 6.11:** Optical constant spectra of (upper row) RQDs and (bottom row) SQDs and their respective cores. (a, f), (b, g), and (c, h) are the QD total extinction, scattering, and absorption cross-section spectra, respectively. The insets in (c) and (h) are the zoomed-in in the longer wavelength region highlighted in blue in (c) and (h). (d) RQD (blue dots) scattering cross-sections and (red dots) absorption cross-sections as a function of shell volume at the excitation wavelength of 400 nm. (i) SQD (blue dots) scattering cross-sections and (red dots) absorption cross-sections as a function of shell volume at the excitation wavelength of 400 nm. Both scattering cross-sections are fitted quadratically and absorption cross-sections linearly. Scattering depolarization spectra of (e) RQDs and (j) SQDs.

The UV-Vis extinction spectral features of CdSe-CdS core-shell QDs below 500 nm are dominantly contributed from the CdS shell, while those above 500 nm are predominantly from the CdSe core.<sup>39</sup> It has been known that QD photon extinction increases with increasing the shell volume, but the fractional contributions by the shell light scattering and absorption have not been investigated. By decomposition of the QD UV-Vis extinction spectra into their absorption and scattering component spectra, this work enables us to systematically evaluate the shell size and geometry to the QD absorption and scattering activity. There are several notable observations. First, while all QDs exhibit relatively high scattering intensity in the wavelength region attributed to the CdS shell (**Fig. 6.11b** and **g**), the QDs are predominant light absorbers in this wavelength region since their absorption cross-sections are two orders of magnitude higher than their scattering cross-sections (**Fig. 6.11 b, c, g** and **h**). Second, none of the QDs can be approximated



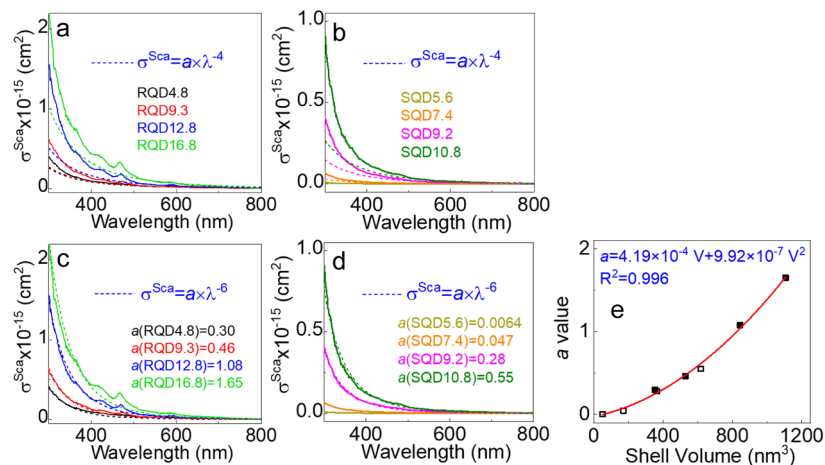


**Fig. 6.12:** (dashed lines) Curve fitting with an empirical equation  $\sigma = a\lambda^{-4}$  for (solid lines) the experimental scattering cross-section spectra of (a) RQDs and (b) SQDs. (dashed lines) Curve fitting with an empirical equation  $\sigma = a\lambda^{-6}$  for (solid lines) the experimental scattering cross-section spectra of (c) RQDs and (d) SQDs. The  $a$  values of  $\sigma = a\lambda^{-6}$  for each QD are highlighted in the graphs. (e) Polynomial fitting of  $a$  values from  $\sigma = a\lambda^{-6}$  for (hollow square) SQDs and (filled square) RQDs as a function of shell volume with the highest power of 2.

as Rayleigh scatterers ( $\sigma = a\lambda^{-4}$ ) (insets in **Fig. 6.11b, g**, and **Fig. 6.12a, b**) as assumed in a recent work,<sup>43</sup> despite they are all in the Rayleigh scattering size domain with dimensions significantly smaller than the excitation wavelengths from 300 to 800 nm. This observation is in sharp contrast to the small polystyrene nanoparticles (100 nm in diameter) and solvent molecules that can all be approximated as Rayleigh scatterers.<sup>44</sup> Instead, the wavelength dependence of SQD and RQD scattering cross-sections can be approximated with the equation of  $\sigma = a\lambda^{-6}$  (**Fig. 6.12c, d**) where the fitting coefficient  $a$  increases quadratically with increasing particle sizes. Third, regardless of their geometry, the absorption cross-section of CdS shell on the SQD and RQD is linearly proportional to the shell volume, while their light scattering cross-section increases quadratically with the latter (**Fig. 6.11d** and **i**).

The most surprising observation is the remarkably small light scattering depolarization ( $P^{Sca} < 0.1$ ) of the RQDs (**Fig. 6.11e**). Earlier works performed with the rod-shaped (CS<sub>2</sub>) and spherical shape (CCl<sub>4</sub>) molecules,<sup>44</sup> as well as the spherical and rod-shaped gold nanoparticles (AuNPs)<sup>45</sup> revealed that light scattering depolarization is very sensitive to scatterers' shapes. While the spherical scatterers have negligibly small light scattering depolarization ( $P^{Sca} < 0.02$ ),

the scattering depolarization of the rod-shaped scatterers can be as high as 0.5. As an example, the light scattering depolarization for the rod shaped CS<sub>2</sub> molecular is 0.5 from 400 nm to 600 nm region, while the peak light scattering depolarization of the rod-shaped AuNP increases with increasing AR.<sup>44, 45</sup> The peak scattering depolarization of the gold nanorod with an AR of 3.2 is 0.45. While the similar trend is observed for the spherical and rod shaped QDs that the light scattering depolarizations of the SQDs are smaller than that of the RQDs, the peak RQD scattering depolarizations remain very small. The maximum light scattering depolarization is 0.04 for the RQD with an AR as large as 16.8. Computational simulations of the QD depolarizations agree well with the experimental results (**Fig. 6.13**).

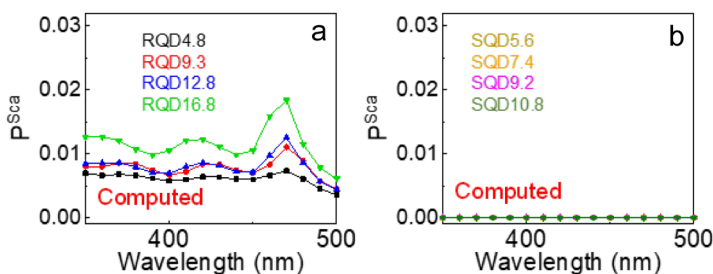


**Fig. 6.13:** Computational simulation of scattering depolarization spectra of (a) RQDs and (b) SQDs.

## 6.5 Effect of Shell Sizes and Geometries on the Core Optical Properties

The QD spectral features above the 500 nm are due predominantly to the CdSe core. Earlier work established that shell coating enhances core UV-Vis extinction and fluorescence emission.<sup>46</sup> However, the enhanced UV-Vis extinction can be due to the increased photon absorption, scattering, or both, while enhanced fluorescence emission can be due to the increased QD photon absorbance, fluorescence quantum yield, or both. The quantitative decomposition of the QD UV-Vis extinction spectra into their absorption extinction (absorbance) and scattering extinction spectrum enabled us to pinpoint the physical origins of the increased core UV-Vis and fluorescence intensity caused by the shell coating.

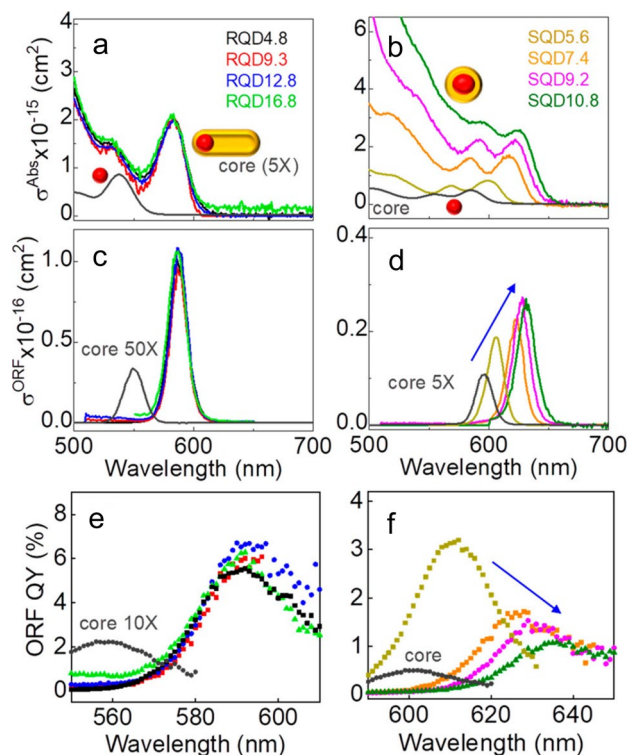


**Fig. 6.14:** Optical properties in QD core region (500–700 nm). Absorption cross-section spectra of (a) RQDs and (b) SQDs. The gray curves represent data of the corresponding cores. ORF cross-section spectra of (c) RQDs and (d) SQDs. ORF QY spectra ( $ORF\ QY(\lambda) = \sigma_{ORF}(\lambda)/\sigma_{Abs}(\lambda) \times 100\%$ ) of (e) RQDs and (f) SQDs.

The shell coating enhances UV-Vis absorption (**Fig. 6.14a, b**) and ORF (**Fig. 6.14 c, d**) cross-sections of the CdSe cores in both RQDs and SQDs QDs. However, despite all their large difference in their shell volumes, all RQDs have approximately the same UV-Vis cross-sections, ORF cross-sections, and ORF fluorescence quantum yields (**Fig. 16a, c, e**). In contrast, both the absorption and ORF cross-sections of the CdSe cores inside SQDs increase with increasing shell volume. These results indicate that only the initial layer of CdS shell on the CdSe core in RQDs is effective in enhancing the core photon absorption and on-resonance fluorescence. Once the CdS thickness on the RQDs surpasses a critical volume, further growing the CdS shell has no impact on either CdSe photon absorption or ORF activities. In contrast, absorption and ORF activities of the CdSe cores inside SQDs monotonically increases with increasing CdS shell thickness.



This trend is observed even when the thickness of the shell is as large as 3.3 nm in SQD10.8, which is equivalent to 9.6 monolayers of wurtzite CdS.

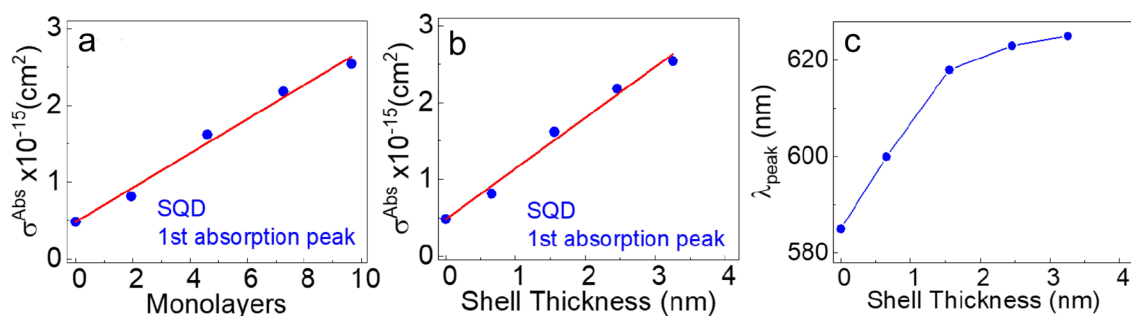


**Fig. 6.15:** Absorption cross-sections of the 1st absorption peak of SQDs as a function of shell (a) monolayers and (b) thickness. The monolayers are calculated based on wurtzite CdS using relationship of “0.3378 nm thickness = 1 monolayers”. The red line is linear fitting of the 1st absorption peak intensity of SQDs as a function of shell monolayers or thickness. The data points at 0 shell thickness are data of the CdSe core. (c) Peak wavelengths of the 1st absorption peak of SQDs as a function of shell thickness.

The difference in the shell volume dependence of the CdSe core optical properties between the RQDs and SQDs can be explained by their different shell geometric characteristics. On the RQDs, only the initial CdS shell grows three-dimensionally surrounding the CdSe (**Fig. 6.14a**), further CdS elongation at one end of the rod is essentially zero dimensional. Therefore, only the initial three-dimensional CdS coating, which is the same for all RQDs with different ARs, is effective in enhancing the CdSe core photon absorption and fluorescence activities, the subsequent CdS coatings that define the AR of the RQDs have no significant effect on the optical property of the core. As such, the CdSe core photon absorption and emission properties are the same in all RQDs despite of their difference in the AR and the shell volume.

The quantifications of the UV-Vis absorption and ORF cross-section enable us to determine the QD ORF QY spectrum, which is the ratio between the QD ORF and absorption cross-section at the same excitation wavelengths. Comparing and contrasting the shell thickness dependence of the core UV-Vis absorption cross-section, ORF cross-section, and ORF QY for the

SQDs is revealing. The peak UV-Vis absorption cross-section of the core increases linearly with further shell coating (**Fig. 16.4b** and **Fig. 16.5**), but the peak ORF cross-section increases most effectively with the initial CdS coating. Further increasing the CdS shell thickness has no significant effect on the RQD ORF cross-section (**Fig. 16.4d**). The ORF QY of the CdSe core in SQDs increases significantly with the initial CdS coating. However, further increasing the thickness of the shell reduces the core ORF QY (**Fig. 16.4f**). The data for SQDs indicate only the initial thin layer CdS shell coating are effective in enhancing both the core UV-Vis photon absorption and ORF QY. Further increasing the shell thickness can more effectively increase the SQD photon absorption but be less effective in increasing their ORF emission due to the reduced ORF QY. While the fundamental mechanism for this experimental observation will be subjected to further investigation, the finding is important for optimizing QD fluorescence QY by design.

Fluorescent QDs are among most optically complicated materials because they can simultaneously absorb, scatter, and emit photons under resonance excitation and detection conditions. This work quantified for the first time a series of fundamental optical constant spectra for a series of RQDs and SQDs that include their scattering, absorption and ORF cross-section spectra, scattering and ORF depolarization spectra, and ORF QY spectra. The QD shell scattering cross-section follows, empirically,  $\sigma = a\lambda^{-6}$  where the value of coefficient  $a$  increases quadratically as a function of shell volume, while the shell absorption cross-section increases linearly with the shell volume for both the RQDs and SQDs. The shell geometry has significant impact on the QD fluorescence depolarization. All SQDs of different sizes all have negligible light scattering depolarization, but unity fluorescence depolarization in the entire UV-Vis region. The RQD fluorescence and light scattering depolarization depends strongly on the shell size and the excitation wavelengths. Furthermore, varying CdS shell size has no significant effect on the core light absorption, scattering, and ORF fluorescence activities for the

investigated RQDs, but increasing the shell thickness introduce systematic change in the optical property of the core in SQDs. Besides providing quantitative insights to the optical properties of CdSe/CdS core/shell nanoparticles, the methodology such as the total fluorescence depolarization measurements, PRS2, and PAOS techniques presented in this work should be important for a wide range of material characterization applications.

## Methods

\* (for CdSe and CdSe-CdS core-shell QDs synthesis, see Ch. 2)

\* (for CdSe-CdS core-shell NRs synthesis, see Ch. 3)

### *UV-Vis, fluorescence, PRS2, and PAOS spectral acquisitions:*

The UV-Vis extinction spectra were measured with a Thermo Scientific Evolution 300 UV-Vis spectrometer, while the SSF, fluorescence excitation, PRS2, and PAOS spectra were acquired with a Horiba FluoroMax-4 spectrofluorometer equipped with an excitation and detection linear polarizer. Detailed PRS2 and PAOS spectral acquisition and analysis has been demonstrated before.<sup>47</sup> Unless indicated otherwise, all the spectrofluorometer-based spectra were acquired with an intergration time 0.3 s, and a slit width 2 nm for both the excitation and detection monochromators. The normailzed spectra were used where the signal intensity was normailzed by the signal from the sample detector and reference detector (S1/R1) to eliminate light source fluctuations.

### *Computational simulations:*

The QD scattering depolarization spectra were computational simulated by the Kramers-Kronig transformation method<sup>48, 49</sup> combined with the Discrete Dipole Approximation (DDA) method.<sup>50, 51</sup> Kramers-Kronig transformation method was used to calculate the index of refraction of QDs, with the experimentally measured absorption spectra, concentrations, and volumes of the QDs. Since the index of refraction of the QD is significantly different from its environment, herein we consider the wavelength change of the incident light due to the index of refraction of

QD itself instead of pure solvent in the Kramers-Kronig transformation method. Discrete Dipole Approximation (DDA) method was then used to calculate the scattering depolarization spectra based on the QD geometric parameters.

## References

1. Kuo, W.-S.; Shao, Y.-T.; Huang, K.-S.; Chou, T.-M.; Yang, C.-H., Antimicrobial Amino-Functionalized Nitrogen-Doped Graphene Quantum Dots for Eliminating Multidrug-Resistant Species in Dual-Modality Photodynamic Therapy and Bioimaging under Two-Photon Excitation. *ACS Appl. Mater. Interfaces* **2018**, *10* (17), 14438-14446.
2. Kang, S.; Kim, K. M.; Jung, K.; Son, Y.; Mhin, S.; Ryu, J. H.; Shim, K. B.; Lee, B.; Han, H.; Song, T., Graphene Oxide Quantum Dots Derived from Coal for Bioimaging: Facile and Green Approach. *Sci. Rep.* **2019**, *9* (1), 4101.
3. Zebibula, A.; Alifu, N.; Xia, L.; Sun, C.; Yu, X.; Xue, D.; Liu, L.; Li, G.; Qian, J., Ultrastable and Biocompatible NIR-II Quantum Dots for Functional Bioimaging. *Adv. Funct. Mater.* **2018**, *28* (9), 1703451.
4. De Liberato, S., Lasing from Dressed Dots. *Nat. Photonics* **2018**, *12* (1), 4-6.
5. Samuel, I., Colloidal Nanocrystals: Electrifying Quantum Dots for Lasers. *Nat. Mater.* **2017**, *17*(1), 9-10.
6. Li, Y.; Hou, X.; Dai, X.; Yao, Z.; Lv, L.; Jin, Y.; Peng, X., Stoichiometry-Controlled InP-Based Quantum Dots: Synthesis, Photoluminescence, and Electroluminescence. *J. Am. Chem. Soc.* **2019**, *141* (16), 6448-6452.
7. Mei, S.; Liu, X.; Zhang, W.; Liu, R.; Zheng, L.; Guo, R.; Tian, P., High-Bandwidth White-Light System Combining a Micro-LED with Perovskite Quantum Dots for Visible Light Communication. *ACS Appl. Mater. Interfaces* **2018**, *10* (6), 5641-5648.
8. Wu, K.; Li, H.; Klimov, V. I., Tandem luminescent solar concentrators based on engineered quantum dots. *Nat. Photonics* **2018**, *12* (2), 105-110.
9. Wang, W.; Feng, W.; Du, J.; Xue, W.; Zhang, L.; Zhao, L.; Li, Y.; Zhong, X., Cosensitized Quantum Dot Solar Cells with Conversion Efficiency over 12%. *Adv. Mater.* **2018**, *30* (11), 1705746.
10. Zhou, Y.; Zhao, H.; Ma, D.; Rosei, F., Harnessing the Properties of Colloidal Quantum Dots in Luminescent Solar Concentrators. *Chem. Soc. Rev.* **2018**, *47* (15), 5866-5890.
11. Zhou, Z.; Liu, X.; Yue, L.; Willner, I., Controlling the Catalytic and Optical Properties of Aggregated Nanoparticles or Semiconductor Quantum Dots Using DNA-Based Constitutional Dynamic Networks. *ACS Nano* **2018**, *12* (11), 10725-10735.
12. Böhm, M. L.; Jellicoe, T. C.; Tabachnyk, M.; Davis, N. J. L. K.; Wisnivesky-Rocca-Rivarola, F.; Ducati, C.; Ehrler, B.; Bakulin, A. A.; Greenham, N. C., Lead Telluride Quantum Dot Solar Cells Displaying External Quantum Efficiencies Exceeding 120%. *Nano Lett.* **2015**, *15* (12), 7987-7993.
13. Kim, S.; Marshall, A. R.; Kroupa, D. M.; Miller, E. M.; Luther, J. M.; Jeong, S.; Beard, M. C., Air-Stable and Efficient PbSe Quantum-Dot Solar Cells Based upon ZnSe to PbSe Cation-Exchanged Quantum

- Dots. *ACS Nano* **2015**, *9* (8), 8157-8164.
14. Bhattacharyya, B.; Pandey, A., CuFeS<sub>2</sub> Quantum Dots and Highly Luminescent CuFeS<sub>2</sub> Based Core/Shell Structures: Synthesis, Tunability, and Photophysics. *J. Am. Chem. Soc.* **2016**, *138* (32), 10207-10213.
15. Chai, J.; Yang, S.; Lv, Y.; Chen, T.; Wang, S.; Yu, H.; Zhu, M., A Unique Pair: Ag<sub>40</sub> and Ag<sub>46</sub> Nanoclusters with the Same Surface but Different Cores for Structure–Property Correlation. *J. Am. Chem. Soc.* **2018**, *140* (46), 15582-15585.
16. Origuchi, S.; Kishimoto, M.; Yoshizawa, M.; Yoshimoto, S., A Supramolecular Approach to the Preparation of Nanographene Adlayers Using Water-Soluble Molecular Capsules. *Angew. Chem. Int. Ed.* **2018**, *57* (47), 15481-15485.
17. Geißler, D.; Würth, C.; Wolter, C.; Weller, H.; Resch-Genger, U., Excitation Wavelength Dependence of the Photoluminescence Quantum Yield and Decay Behavior of CdSe/CdS Quantum Dot/Quantum Rods with Different Aspect Ratios. *Phys. Chem. Chem. Phys.* **2017**, *19* (19), 12509-12516.
18. Hulst, H. C.; van de Hulst, H. C., *Light Scattering by Small Particles*. Courier Corporation: 1981.
19. Andrews, D. L.; Dávila Romero, L. C.; Stedman, G. E., Polarizability and the Resonance Scattering of Light: Damping Sign Issues. *Phys. Rev. A* **2003**, *67* (5), 055801.
20. Johnson, R. C.; Li, J.; Hupp, J. T.; Schatz, G. C., Hyper-Rayleigh Scattering Studies of Silver, Copper, and Platinum Nanoparticle Suspensions. *Chem. Phys. Lett.* **2002**, *356* (5), 534-540.
21. Pasternack, R.; Collings, P., Resonance Light Scattering: A New Technique for Studying Chromophore Aggregation. *Science* **1995**, *269* (5226), 935-939.
22. Arteaga, O.; Canillas, A.; El-Hachemi, Z.; Crusats, J.; Ribó, J. M., Structure vs. Excitonic Transitions in Self-Assembled Porphyrin Nanotubes and Their Effect on Light Absorption and Scattering. *Nanoscale* **2015**, *7* (48), 20435-20441.
23. Gangemi, C. M. A.; D'Agostino, B.; Randazzo, R.; Gaeta, M.; Fragalà, M. E.; Purrello, R.; D'Urso, A., Interaction of Spermine Derivative Porphyrin with DNA. *J. Porphyrins Phthalocyanines* **2018**, *22* (07), 581-587.
24. Yue, Q.; Tao, L.; Hou, Y.; Zhang, C.; Wang, Y.; Hong, M.; Li, C.-Z., Assay of miRNA in Cell Samples Using Enhanced Resonance Light Scattering Technique Based on Self Aggregation of Magnetic Nanoparticles. *Nanomedicine* **2018**, *13* (18), 2301-2310.
25. Zhang, L.-M.; Cui, Y.-X.; Zhu, L.-N.; Chu, J.-Q.; Kong, D.-M., Cationic Porphyrins With Large Side Arm Substituents as Resonance Light Scattering Ratiometric Probes for Specific Recognition of Nucleic Acid G-quadruplexes. *Nucleic Acids Res.* **2019**, *47* (6), 2727-2738.
26. Athukorale, S. A.; Zhou, Y.; Zou, S.; Zhang, D., Determining the Liquid Light Scattering Cross Section and Depolarization Spectra Using Polarized Resonance Synchronous Spectroscopy. *Anal. Chem.* **2017**, *89* (23), 12705-12712.
27. Nettles, C. B.; Hu, J.; Zhang, D., Using Water Raman Intensities To Determine the Effective Excitation and Emission Path Lengths of Fluorophotometers for Correcting Fluorescence Inner Filter Effect. *Anal. Chem.* **2015**, *87* (9), 4917-4924.

28. Xu, J. X.; Vithanage, B. C. N.; Athukorale, S. A.; Zhang, D., Scattering and Absorption Differ Drastically in Their Inner Filter Effects on Fluorescence, Resonance Synchronous, and Polarized Resonance Synchronous Spectroscopic Measurements. *Analyst* **2018**, *143* (14), 3382-3389.
29. Siriwardana, K.; Vithanage, B. C. N.; Zou, S.; Zhang, D., Quantification of the Depolarization and Anisotropy of Fluorophore Stokes-Shifted Fluorescence, On-Resonance Fluorescence, and Rayleigh Scattering. *Anal. Chem.* **2017**, *89* (12), 6686-6694.
30. Williams, P. F.; Rousseau, D. L.; Dworetzky, S. H., Resonance Fluorescence and Resonance Raman Scattering: Lifetimes in Molecular Iodine. *Phys. Rev. Lett.* **1974**, *32* (5), 196-199.
31. Wu, F. Y.; Grove, R. E.; Ezekiel, S., Investigation of the Spectrum of Resonance Fluorescence Induced by a Monochromatic Field. *Phys. Rev. Lett.* **1975**, *35* (21), 1426-1429.
32. Xu, J. X.; Hu, J.; Zhang, D., Quantification of Material Fluorescence and Light Scattering Cross Sections Using Ratiometric Bandwidth-Varied Polarized Resonance Synchronous Spectroscopy. *Anal. Chem.* **2018**, *90* (12), 7406-7414.
33. Jameson, D. M.; Ross, J. A., Fluorescence Polarization/Anisotropy in Diagnostics and Imaging. *Chem. Rev.* **2010**, *110* (5), 2685-2708.
34. Tice, D. B.; Weinberg, D. J.; Mathew, N.; Chang, R. P. H.; Weiss, E. A., Measurement of Wavelength-Dependent Polarization Character in the Absorption Anisotropies of Ensembles of CdSe Nanorods. *J. Phys. Chem. C* **2013**, *117* (25), 13289-13296.
35. Zhang, Y.; Miao, L.; Wang, H.-F., Fluorescence Anisotropy as a Reliable Discrimination of Ligand-Asymmetric and Symmetric Mn-Doped ZnS Quantum Dots. *Anal. Chem.* **2016**, *88* (19), 9714-9719.
36. Gawęłczyk, M.; Syperek, M.; Maryński, A.; Mrowiński, P.; Dusanowski, Ł.; Gawarecki, K.; Misiewicz, J.; Somers, A.; Reithmaier, J. P.; Höfling, S.; Sęk, G., Exciton Lifetime and Emission Polarization Dispersion in Strongly in-Plane Asymmetric Nanostructures. *Phys. Rev. B* **2017**, *96* (24), 245425.
37. Hadar, I.; Philbin, J. P.; Panfil, Y. E.; Neyshtadt, S.; Lieberman, I.; Eshet, H.; Lazar, S.; Rabani, E.; Banin, U., Semiconductor Seeded Nanorods with Graded Composition Exhibiting High Quantum-Yield, High Polarization, and Minimal Blinking. *Nano Lett.* **2017**, *17* (4), 2524-2531.
38. Chen, O.; Zhao, J.; Chauhan, V. P.; Cui, J.; Wong, C.; Harris, D. K.; Wei, H.; Han, H.-S.; Fukumura, D.; Jain, R. K.; Bawendi, M. G., Compact High-Quality CdSe–CdS Core–Shell Nanocrystals with Narrow Emission Linewidths and Suppressed Blinking. *Nat. Mater.* **2013**, *12* (5), 445-451.
39. Carbone, L.; Nobile, C.; De Giorgi, M.; Sala, F. D.; Morello, G.; Pompa, P.; Hytch, M.; Snoeck, E.; Fiore, A.; Franchini, I. R.; Nadasan, M.; Silvestre, A. F.; Chiodo, L.; Kudera, S.; Cingolani, R.; Krahn, R.; Manna, L., Synthesis and Micrometer-Scale Assembly of Colloidal CdSe/CdS Nanorods Prepared by a Seeded Growth Approach. *Nano Lett.* **2007**, *7* (10), 2942-2950.
40. Siriwardana, K.; Vithanage, B. C. N.; Zou, S.; Zhang, D., Quantification of the Depolarization and Anisotropy of Fluorophore Stokes-Shifted Fluorescence, On-Resonance Fluorescence, and Rayleigh Scattering. *Anal. Chem.* **2017**, *89* (12), 6686-6694.
41. Jameson, D. M.; Ross, J. A., Fluorescence Polarization/Anisotropy in Diagnostics and Imaging. *Chem.*

- Rev.* **2010**, *110* (5), 2685-2708.
42. Xu, J. X.; Yuan, Y.; Zou, S.; Chen, O.; Zhang, D., A Divide-and-Conquer Strategy for Quantification of Light Absorption, Scattering, and Emission Properties of Fluorescent Nanomaterials in Solutions. *Anal. Chem.* **2019**, *91* (13), 8540-8548.
43. Geißler, D.; Würth, C.; Wolter, C.; Weller, H.; Resch-Genger, U., Excitation Wavelength Dependence of the Photoluminescence Quantum Yield and Decay Behavior of CdSe/CdS Quantum Dot/Quantum Rods with Different Aspect Ratios. *Phys. Chem. Chem. Phys.* **2017**, *19* (19), 12509-12516.
44. Athukorale, S. A.; Zhou, Y.; Zou, S.; Zhang, D., Determining the Liquid Light Scattering Cross Section and Depolarization Spectra Using Polarized Resonance Synchronous Spectroscopy. *Anal. Chem.* **2017**, *89* (23), 12705-12712.
45. Xu, J. X.; Siriwardana, K.; Zhou, Y.; Zou, S.; Zhang, D., Quantification of Gold Nanoparticle Ultraviolet–Visible Extinction, Absorption, and Scattering Cross-Section Spectra and Scattering Depolarization Spectra: The Effects of Nanoparticle Geometry, Solvent Composition, Ligand Functionalization, and Nanoparticle Aggregation. *Anal. Chem.* **2018**, *90* (1), 785-793.
46. Pietryga, J. M.; Park, Y.-S.; Lim, J.; Fidler, A. F.; Bae, W. K.; Brovelli, S.; Klimov, V. I., Spectroscopic and Device Aspects of Nanocrystal Quantum Dots. *Chem. Rev.* **2016**, *116* (18), 10513-10622.
47. Xu, J. X.; Yuan, Y.; Zou, S.; Chen, O.; Zhang, D., A Divide-and-Conquer Strategy for Quantification of Light Absorption, Scattering, and Emission Properties of Fluorescent Nanomaterials in Solutions. *Anal. Chem.* **2019**.
48. Haes, A. J.; Zou, S.; Zhao, J.; Schatz, G. C.; Van Duyne, R. P., Localized Surface Plasmon Resonance Spectroscopy near Molecular Resonances. *J. Am. Chem. Soc.* **2006**, *128* (33), 10905-10914.
49. Yang, W.; Reed, J. M.; Wang, H.; Zou, S., Surface-Plasmon-Assisted Electromagnetic Wave Propagation. *Phys. Chem. Chem. Phys.* **2010**, *12* (39), 12647-52.
50. Draine, B. T., Discrete-Dipole Approximation and its Application to Interstellar Graphite Grains. *Astrophys. J.* **1988**, 848-872.
51. Draine, B. T.; Flatau, P. J., Discrete-Dipole Approximation For Scattering Calculations. *J. Opt. Soc. Am. A* **1994**, *11* (4), 1491-1499.

# **Chapter 7**

## Conclusions and Perspectives



In this research, colloidal QDs were investigated from four different perspectives. Considering the synthesis methodologies, inspired by the formation of compact spherical CdSe-CdS core-shell QDs, anisotropic HP and HBP CdSe-CdS core-shell QDs were prepared for the first time by manipulating the surface passivation. Compared to their spherical counterparts, high multi-exciton emission, prolonged ensemble, and single-QD PL lifetimes, and high cellular uptakes associated with low cytotoxicity were observed. In addition, a Cu-catalyzed solid solution alloying strategy was explored to fabricate CdZnSe-CdZnS core-shell alloy QDs and NRs. The resulting emission profiles covered the entire visible spectral range while maintaining uniformity and high QYs. With the advancements for the Cd-based QDs, our next step is Cd-free QDs (Fig. 7.1).<sup>1</sup> The recent synthesis of high-quality InP-based QDs also was based on high-temperature shell growth,<sup>2</sup> similar to the Cd-based system. I believe that non-toxic QDs with optical properties comparable to those of the Cd-based QDs can be synthesized based on the experience that was gained from the study of Cd-based QDs.

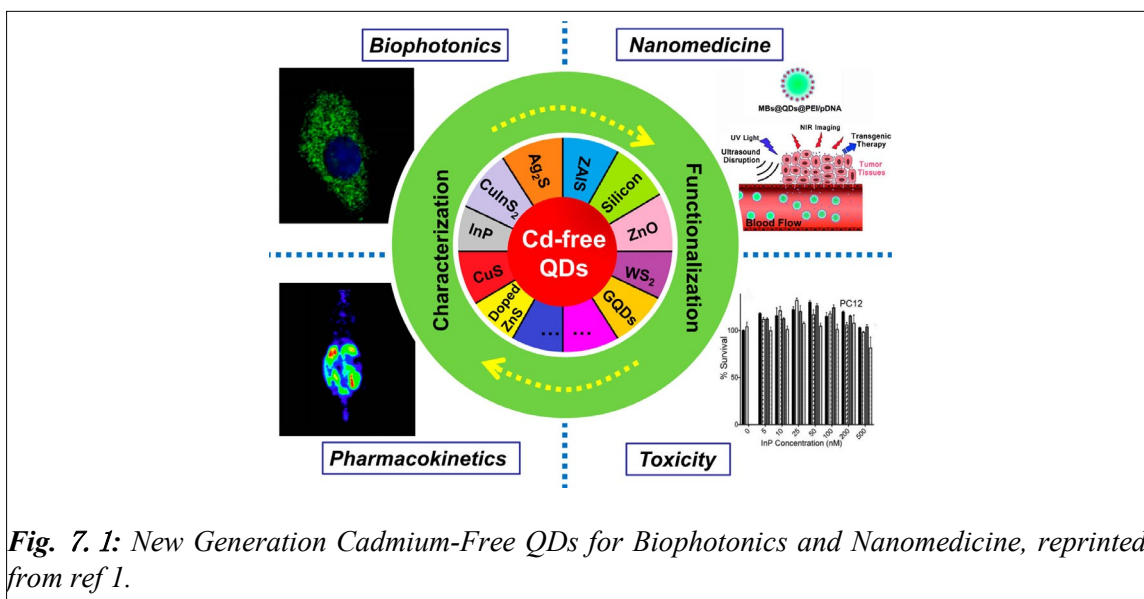


**Fig. 7. 1:** New Generation Cadmium-Free QDs for Biophotonics and Nanomedicine, reprinted from ref 1.

In terms of photo-switching, a highly-reversible, dynamic hybrid system with

excellent fatigue resistance was established by mixing well-designed, dual-color emitting, Mn-doped CdS-ZnS QDs with photo-switchable diarylethene molecules. Photo-switching of the system between blue and pink can be induced mainly by selective quenching/recovering of the Mn-PL of the QDs. I expect that this type of “smart” dynamic materials could be used in various practical applications, such as self-erasing paper and super-resolution fluorescence imaging.

Regarding photocatalysis, zwitterionic-capped CsPbBr<sub>3</sub> perovskite QDs were used with a series of  $\alpha$ -aryl ketonitriles, which were converted into their dimers under the illumination of visible light, with a stereoselectivity of *dl*-isomers. As a new member of the solar energy harvesting family, there are ample opportunities as well as challenges for photocatalysis using QDs. First, more comprehensive understandings of the catalytic process and the physical properties of QDs are needed. Second, future studies should focus on optimizing ligands to ensure permeability, solubility, colloidal stability, and selective interaction with co-catalysts. Third, CO<sub>2</sub> reduction or H<sub>2</sub> generation may be integrated to fully use both the electrons and holes with the photocatalytically oxidative organic reactions. In this case, plastic wastes are one possible choice for the oxidative half path, which can feed two birds with one stone.

With respect to spectroscopy, we experimentally quantified the photon scattering, absorption, and ORF activities of CdSe-CdS core-shell QDs as a function of the shell sizes and geometries. The future design, characterization, and applications of QDs will be guided by the differentiating and detailed analysis of their complicated optical properties. In addition, the methodology presented in this work is directly applicable for quantifying the optical activities of optically complex materials for which the common UV-vis spectrometry and fluorescence spectroscopy are inadequate.

Overall, with all of the efforts that have been made during the past four decades, a lot has been accomplished. However, QD technology is still young, and new, imaginative. Discoveries and applications of QDs continue to emerge. There is still much work to be done in this field in the future, and cooperative work with researchers in other fields also is likely to be beneficial and productive.

## References

1. Xu, G.; Zeng, S.; Zhang, B.; Swihart, M. T.; Yong, K.-T.; Prasad, P. N., New Generation Cadmium-Free Quantum Dots for Biophotonics and Nanomedicine. *Chem. Rev.* **2016**, *116* (19), 12234-12327.
2. Won, Y.-H.; Cho, O.; Kim, T.; Chung, D.-Y.; Kim, T.; Chung, H.; Jang, H.; Lee, J.; Kim, D.; Jang, E., Highly Efficient and Stable InP/ZnSe/ZnS Quantum Dot Light-Emitting Diodes. *Nature* **2019**, *575* (7784), 634-638.